PLACING HIGH-REDSHIFT QUASARS IN PERSPECTIVE: UNIFYING DISTANT QUASARS WITH THEIR LOWER REDSHIFT COUNTERPARTS THROUGH NEAR-INFRARED SPECTROSCOPY

Brandon M. Matthews, M.S.

Dissertation Prepared for the Degree of

DOCTOR OF PHILOSOPHY

UNIVERSITY OF NORTH TEXAS

May 2023

APPROVED:

Ohad Shemmer, Major Professor
Yuan Li, Committee Member
Chris L. Littler, Committee Member
Duncan Weathers, Committee Member
Jingbiao Cui, Chair of the Department of Physics
John Quintanilla, Dean of the College of Science
Victor R. Prybutok, Dean of the Toulouse Graduate School

Matthews, Brandon M. *Placing High-Redshift Quasars in Perspective: Unifying Distant Quasars with Their Lower Redshift Counterparts through Near-Infrared Spectroscopy*. Doctor of Philosophy (Physics), May 2023, 190 pp., 16 tables, 33 figures, 229 numbered references.

I present spectroscopic measurements for 260 sources from the Gemini Near Infrared Spectrograph–Distant Quasar Survey (GNIRS-DQS). Being the largest uniform, homogeneous survey of its kind, it represents a flux-limited sample of Sloan Digital Sky Survey (SDSS) quasars at $1.5 < z < 3.5$. A combination of the GNIRS and SDSS spectra covers principal quasar diagnostic features, chiefly the C IV λ1549, Mg II λλ2798, 2803, Hβ λ4861, and [O III] λλ4959, 5007 emission lines, in each source. The spectral inventory is utilized primarily to develop prescriptions for obtaining more accurate and precise redshifts, black hole masses, and accretion rates for all quasars. Additionally, the measurements facilitate an understanding of the dependence of rest-frame ultraviolet–optical spectral properties of quasars on redshift, luminosity, and Eddington ratio, and test whether the physical properties of the quasar central engine evolve over cosmic time.

ACKNOWLEDGEMENTS

I would like to thank my research advisor, Dr. Ohad Shemmer, whom was always available to provide guidance, advice, and assistance throughout my time at UNT with respect to a myriad of factors and situations, and whose mentorship will undoubtedly prove invaluable in my future endeavours. I would also like to thank Dr. Yuan Li, whom provided additional support and much needed advice and professional experience. Additionally, I would like to extend gratitude to the members of my defense committee: Chris L. Littler and Duncan Weathers, for their willingness to participate in the proposal and defense of this dissertation, along with the help they provided during my graduate studies. I would like to thank my colleague, Cooper Dix, whom I worked alongside for the majority of my time at UNT, and, finally, I would like to express sincere thanks to my family and friends whose help, knowledge, and support I could not have done any of this without.

TABLE OF CONTENTS

LIST OF TABLES

LIST OF FIGURES

CHAPTER 1

INTRODUCTION

1.1. Active Galactic Nuclei

Active galactic nuclei (AGN) are compact regions at the center of galaxies which exhibit energies orders of magnitude higher than normal galaxies (i.e., the Milky Way). These "central engines" emit over a large span of wavelengths in a manner that cannot be attributed to stellar emission [1]. Galaxies that host AGN are referred to as active galaxies, and these objects differ from normal galaxies in that the large amounts of energy generated in active galaxies is believed to be primarily from the influence of supermassive black holes (SMBHs), as opposed to predominantly stellar nucleosynthesis that illuminates galaxies like our own [2].

This fundamental difference in what fuels AGN leads to distinct features that can be observed in these objects. While the specifics are debated, it is believed that AGN continua can be defined by some form of power-law in both the rest-frame UV-optical and X-ray bands, and typically have strong, broad emission lines of characteristic elements [3, 4]. Some AGN can exhibit unusually low luminosities with respect to the general population [5], while others can exhibit strong radio emission [6], in addition to absorption features [7]. This variety of effects is believed to be primarily due to line-of-sight observation and inclination angle of the AGN structure itself (see [8] and Figure 1.1). While AGN can have many different, overlapping classifications based on observational parameters, there is one classification of AGN that will be the focus of this dissertation: quasars.

In the 1920s, a variety of studies demonstrated that certain objects that were believed to be within our own galaxy exhibited spectral properties that physically placed them at distances thought to be outside of our own galaxy [9, 10, 11]. It was determined that these objects could have their large distances explained by the fact that they were, themselves, other galaxies outside of our own Milky Way. A few of these objects, such as the "extra-galactic spirals" Carl Seyfert described in 1943 [5], had distinctly different properties from similar objects in the sky, such as strong, broad nuclear emission lines present only in the galaxy's core. These objects, known as Seyfert galaxies, were very bright galaxies that were

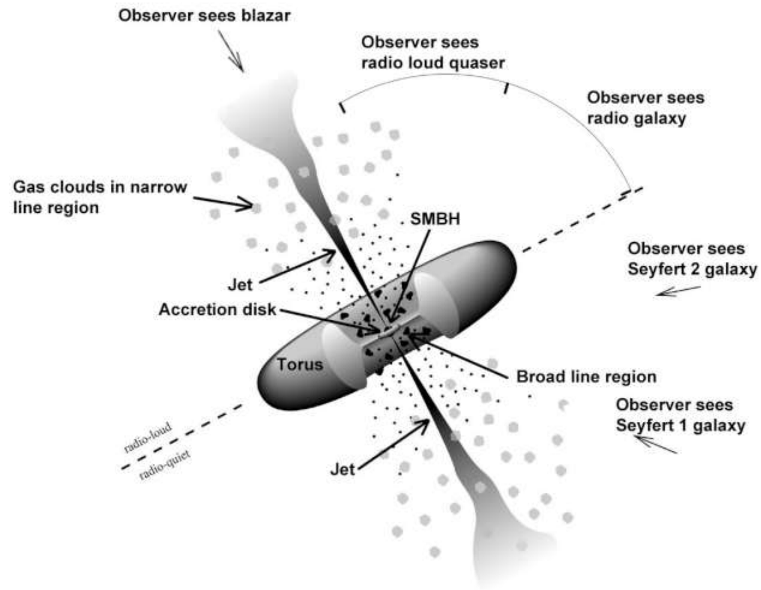

FIGURE 1.1. The unification model of AGN (see Torres & Anchordoqui 2004; [8]). The unification model demonstrates that the different classifications of AGN arise from orientation of the source. A Seyfert 1 galaxy [5] is observed if the orientation angle is $\sim$ 30 degrees, making both the narrow and broad line regions visible, whereas larger angular offsets will mask the broad line region via the toroidal structure surrounding the accretion disk, showing to an observer the properties of a Seyfert 2 galaxy. Blazars are seen when observing down the line of sight of the relativistic jets eminating from the central engine, and orthogonal observation to the jets, along the disk structure itself, presents an ordinary radio galaxy.

host to large amounts of activity originating at the galaxy center, and are now known as one of the many types of AGN that astronomers recognize today. In 1959, Cambridge published the Third Cambridge Catalog of Radio Sources, also known as “3C”, with a revised version in 1962 [12]. Within this source catalog, there were more than a few interesting objects, and many objects that were recorded as radio sources, but did not have any optical counterparts

[13]. One object in the survey, 3C 48, had an optical counterpart identified, which appeared to be a faint blue star, and a spectrum was obtained. However, this spectrum was considered anomalous and unreliable by the community, as it contained many unknown broad emission lines. It wasn't until 1962 when another interesting source, 3C 273, was predicted to undergo several lunar occultations, allowing astronomers Cyril Hazard and John Bolton to accurately record a position for optical followup. Using the precise position, Maarten Schmidt identified its optical counterpart, again appearing to be a faint stellar source, and recorded its spectrum, which produced the same oddities observed in 3C 48. Schmidt realized that the emission lines present in the spectrum of 3C 273 were hydrogen (Balmer series) emission lines, and concluded that the redshift of this object was $z = 0.158$ [14]. This value was baffling to astronomers. If this redshift was due to the motion of a star, it would mean it was receding at a rate of $47,000$ km s^{-1}, which was orders of magnitude beyond any known star. If the redshift was cosmological, its distance would imply an object both more luminous and more compact than any observed galaxy. 3C 273 appeared as an unresolved point source with both unusual radio emission and Balmer emission that defied explanation. Upon further investigation, it was also discovered that 3C 273 was bright enough that it appeared in archival photographs from the early 20th century, and further observations showed that its luminosity was variable on yearly timescales, which implied that a large percentage of the light was being emitted from an extremely small region that would be minuscule compared to the size of a galaxy. Despite no concrete explanation, the floodgates were opened, and many more spectra were taken and interpreted in a similar manner, including a retroactive acceptance of 3C 48. In 1964 the term "quasar" was coined, dubbed such from a portmanteau of "quasi-stellar radio sources", and QSO, or ""quasi-stellar object".

As further speculation and studies were undertaken, it was determined that these quasars were indeed compact, as interferometry and further optical observations demonstrated no ability to spatially resolve them. Because of their compact size, it meant that the amount of power generated would have to be enormous, especially at the redshifts indicated by their spectra. In 1964, it was suggested by Edwin Salpeter and Yakov Zel'dovich that

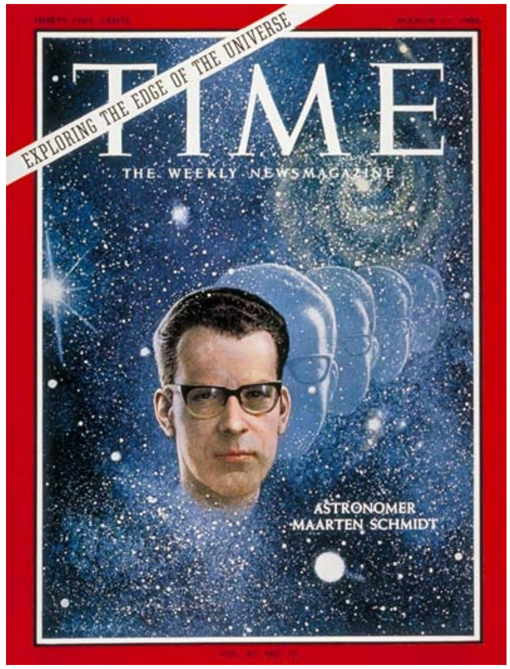

FIGURE 1.2. TIME Magazine cover, March 11, 1966, featuring Maarten Schmidt.

the amount of powert being generated by these objects could be due to an accretion disk surrounding a SMBH [15]. This explanation, while widely accepted today, was met with apprehension at the time due to the still speculative existence of black holes. The 1970s proved fruitful for quasar understanding, as black hole physics became more widely accepted and understood, X-ray observations were made of quasars, and modern cosmological modeling began to take form [15]. Eventually, quasars became established science, and the field of quasarology evolved. Distances such as those originally recorded by Maarten Schmidt have now been dwarfed, as quasars up to $z > 7$ have been observed [16].

Quasars are the most luminous type of AGN, along with being the most luminous objects in the known universe, with characteristic bolometric luminosities of $L_{bol} \sim 10^{45} - 10^{48}$ erg s^{-1}. Quasars share certain spectral features with other types of AGN, such as prominent Lyα emission, alongside other broad line emitting regions in the rest-frame UV-optical band. Despite what the name might imply, future surveys revealed that the majority of the quasar population lacked strong radio emission [17], with only $\sim 10\%$ of quasars being classified as radio-loud [18]. Quasars themselves are powered by accretion onto a central SMBH of

$\sim 10^7 - 10^9\ M_\odot$, which is believed to be surrounded by a geometrically thin, optically thick accretion disk structure in the case of radio-quiet sources [19]. This structure enables thermal UV-optical emission, while X-ray emission is caused by Compton upscattering of photons in the disk. In addition to the accretion disk, these objects have powerful jets of relativistic material orthogonal to the plane of the accretion disk [20]. Quasars can also exhibit severe absorption in the form of broad absorption lines (BALs; [21, 22, 23]). It is spectral properties such as these that define the role of observational astronomy with respect to studying these objects.

1.2. Quasar Spectroscopy

Vanden Berk (2001; [24]) presents a composite of $\sim$ 2000 Sloan Digital Sky Survey (SDSS) quasars (presented here in Figure 1.3). This spectrum shows the typical layout of an average, "ordinary" quasar in the rest-frame UV-optical band. Within this figure is shown a steep UV power-law continuum from $\sim 1216 - 5600$ Å, and a shallow optical power-law from $\sim 5600 - 8000$ Å. The physical motivation behind the use of the power-laws is the thermal emission onto the accretion disk surrounding the SMBH [25], and the breaking of a continuous power-law could be caused by a variety of factors, such as the ratio of Balmer emission to Fe II emission, and reddening effects such as the presence of molecular gas, absorption by the host galaxy, and extinction [26]. Changes of spectral slopes over redshift could provide information on quasar evolution and co-evolution with the quasar host galaxy.

Quasar spectra typically contain a set of prominent narrow and broad emission lines. Permitted lines, such as Lyα, C IV, Mg II, Hβ, and Hα are usually broad, with larger measurable full width at half maximum intensities (FWHMs), whereas forbidden lines, such as [O III], are usually narrow with FWHM values below $\sim$ 1000 km s^{-1}. Narrow lines cannot form in the same region of the quasar as broad emission lines due to high densities in the broad line region (BLR) being much larger than the critical density required for these forbidden transitions. Semi-forbidden lines can be both broad and narrow.

Due to the emission mechanisms of broad lines, and the high density region they originate from, these lines are susceptible to (sometimes severe) shifting effects, i.e., blueshifts,

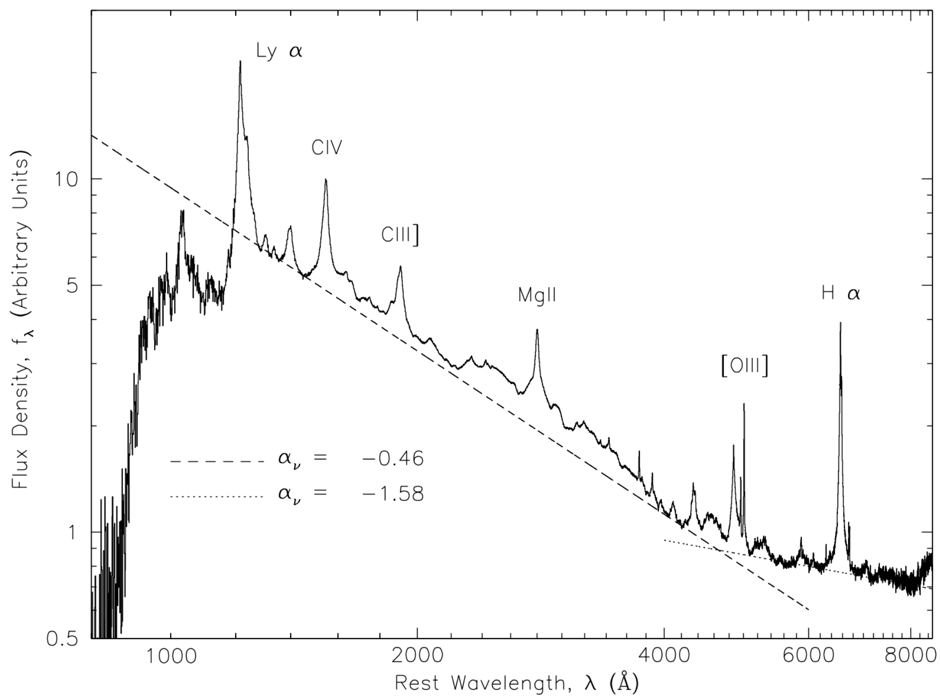

FIGURE 1.3. A quasar composite spectrum using ∼ 2000 SDSS quasar spectra taken from Vanden Berk (2001; [24]). This spectrum showcases two power-law continua, prominent Fe III+Fe II emission, and several important diagnostic broad emission lines.

with respect to the rest frame of the quasar, which implies that broad emission line gases are directly impacted by outflows from the AGN [27, 28, 22, 29, 30, 24, 31, 32]. Certain broad lines (i.e., C IV and Hβ) can be comprised of a narrow "core" component and a broad component, which can cause measurement of their central wavelengths to be offset. This feature of certain broad emission lines, combined with photoionization theory, implies that the BLR contains layers within the overall region, implying a stratified structure [33, 30, 24, 34]. Conversely, narrow lines show little to no shifting effects due to the fact that the narrow line region is located much farther away from the accretion disk, and is therefore subjected to much less interference from quasar outflows [35].

Spectroscopy is critical to understand quasars and their interactions with the host galaxy, as certain emission lines can be used as diagnostic indicators of specific behaviors in the environment surrounding the AGN. Lines such as Hβ and Mg II can be used as indicators for M_{BH} and accretion rate probes, and lines such as [O III] are accurate measures of redshift. However, due to the high redshifts that many of these objects exist at, these lines, which accurately identify the features and properties of quasars, are shifted out of the UV-optical regime. As we "chase" these emission lines, we must go to redder wavelengths, and the need for IR and radio data increases. Throughout recent history, there have been a few mini near-infrared (NIR) surveys, but none of substantial size. To this end, we desire to take a comprehensive approach to building the largest uniform survey of NIR high redshift quasars to create the ultimate go-to inventory of such data so that it might be used as a goalpost for rest-frame optical high redshift quasars.

In this dissertation, we use a multi-wavelength approach across a large range of redshifts to investigate quasar redshifts, black hole masses ($M_{\rm BH}$), and spectral properties. In Chapter 2, we overview the Gemini Near-Infrared Spectrograph - Distant Quasar Survey (GNIRS-DQS), which includes technical details concerning observation and data reduction to produce quasar spectra, along with measurements of both primary quasar diagnostic lines and supplementary lines present in the survey sample. In Chapter 3, we supplement the GNIRS-DQS sample with additional objects, and provide new measurements for quantifying Fe II emission strength, which is becoming an increasingly important diagnostic for quasars. Additionally, we utilize linear regression analysis to improve rest-frame UV-optical-based quasar redshifts via the GNIRS-DQS sample, and search for any possible redshift dependence. In Chapter 4, we search for new methods to correct for quasar $M_{\rm BH}$ using GNIRS-DQS as a diagnostic, and compare our result to those presented in other works. In Chapter 5, we use a combination of spectral inventories, including GNIRS-DQS, in order to investigate the properties of weak emission line quasars, and how they fit in a unified spectroscopic UV-optical parameter space, which can show that these objects might not be as unique as previously thought. In Chapter 6, we summarize the work and results stemming from GNIRS-DQS, along with presenting further avenues of investigation for future works.

CHAPTER 2

A CATALOG OF SPECTROSCOPIC PROPERTIES FROM THE GEMINI NEAR INFRARED SPECTROGRAPH - DISTANT QUASAR SURVEY

2.1. Introduction

A persistent problem in extragalactic astrophysics is understanding how supermassive black holes (SMBHs) and their host galaxies co-evolve over cosmic time [36, 37, 38, 39]. This problem touches upon several aspects of galaxy evolution, including the SMBH mass ($M_{\rm BH}$), which correlates with properties of the host galaxy, such as the bulge mass and stellar velocity dispersion [40, 41, 42, 43, 44, 45], the accretion rate, which probes the accretion flow and efficiency of the accretion process, [46, 47, 48], and the kinematics of material outflowing from the vicinity of the SMBH, which may affect star formation in the host galaxy [49, 50, 51]. For nearby ($z \lesssim 1$) active galactic nuclei (AGNs) or quasars, most of the parameters required for exploring these topics can be most reliably estimated using optical diagnostics, namely the broad Hβ λ4861 and narrow [O III] $\lambda\lambda$4959, 5007 emission lines. However, at $z \gtrsim 1$, which includes the epoch of peak quasar activity (from $z = 1-3$), these diagnostic emission lines are redshifted beyond $\lambda_{\rm obs} \sim 1\mu$m, firmly into the near-infrared (NIR) regime. Since the vast majority of large spectroscopic quasar surveys have been limited to $\lambda_{\rm obs} \lesssim 1\mu$m, investigations of large samples of quasars at $z \gtrsim 1$ are usually forced to use spectroscopic proxies for Hβ and [O III]. Using indirect proxies can lead not only to inaccurate redshifts [27, 52, 53, 32, 54], but also to systematically biased and imprecise estimates of fundamental parameters such as $M_{\rm BH}$ and accretion rate [55, 56, 57].

NIR spectra have been obtained for a few hundred quasars at $z \gtrsim 1$, but these spectra constitute a heterogeneous collection of relatively small samples ($\approx 10-100$ sources) that span wide ranges of source-selection criteria, instrument properties, spectral band and resolution, and signal-to-noise ratio (S/N) [30, 58, 59, 60, 61, 56, 62, 63, 64, 35, 65]. Thus,

This entire chapter is reproduced from BM Matthews, O Shemmer, C Dix, MS Brotherton, AD Myers, I Andruchow, WN Brandt, GA Ferrero, SC Gallagher, R Green. Placing high-redshift quasars in perspective: A catalog of spectroscopic properties from the gemini near infrared spectrograph–distant quasar survey. Astrophysical Journal Supplement Series 252 (2021), no. 2, 15-26. DOI 10.3847/1538-4365/abc705, with permission from IOP Publishing.

the current NIR spectroscopic inventory for high-redshift quasars is biased in a multitude of selection criteria, and none of these mini-surveys are capable of providing a coherent picture of SMBH growth across cosmic time.

To mitigate the various systematic biases present in the current NIR spectroscopic inventory, we have obtained NIR spectra of 272 quasars at high redshift using the Gemini Near-Infrared Spectrograph (GNIRS, [66]), at the Gemini-North Observatory, with a Gemini Large and Long Program[1]. By utilizing spectroscopy in the ~ 0.8–$2.5\ \mu$m band of a uniform, flux-limited sample of optically selected quasars at $1.5 \lesssim z \lesssim 3.5$, our Distant Quasar Survey (GNIRS-DQS) was designed to produce spectra that, at a minimum, encompass the essential Hβ and [O III] region in each source while having sufficient S/N in the NIR band to obtain meaningful measurements of this region. This survey assembles the largest uniform sample of $z \gtrsim 1$ quasars with rest-frame optical spectroscopic coverage. The spectral inventory presented in this catalog will allow development of single-epoch prescriptions, as opposed to C IV reverberation mapping, for rest-frame ultraviolet (UV) analogs of key properties such as $M_{\rm BH}$ and accretion rate, along with revised redshifts based primarily on emission lines in the rest-frame optical band.

This paper describes the GNIRS observations and structure of the catalog; subsequent investigations will present the scientific analyses enabled by this catalog. Section 2.2 describes the target selection, and Section 2.3 describes the GNIRS observations, and the spectroscopic data processing. Section 2.4 presents the catalog of basic spectral properties, along with a smaller catalog of additional features that can be measured reliably in some of the spectra. Section 3.4 summarizes the main properties of our catalog as well as comments on its future applications. Throughout this paper we adopt a flat ΛCDM cosmology with $\Omega_\Lambda = 1 - \Omega_0 = 0.7$ and $H_0 = 70$ kms^{-1}Mpc^{-1} [67].

2.2. Target Selection

The GNIRS-DQS targets were selected from the spectroscopic quasar catalog of the Sloan Digital Sky Survey (SDSS; [68]), primarily from SDSS Data Release 12 [69] and sup-

[1] http://www.gemini.edu/node/12726

plemented by SDSS Data Release 14 (DR14; [70]). Sources were selected to lie in three narrow redshift intervals, $1.55 \lesssim z \lesssim 1.65$, $2.10 \lesssim z \lesssim 2.40$, and $3.20 \lesssim z \lesssim 3.50$, in order to cover the Hβ+[O III] emission complex, and in order of decreasing NIR brightness, down to $m_i \sim 19.0$, a limit at which the SDSS is close to complete in each of those redshift intervals [71]. Figure 2.1 displays the luminosity-redshift distribution of GNIRS-DQS sources with respect to sources from the SDSS DR14 catalog. For the redshift distributions in the selected intervals, shown in Figure 3.1 along with their respective magnitude distributions, the Hβ+[O III] emission complex reaches the highest S/N in the centers of the J, H, and K bands, respectively. The selected redshift intervals also ensure coverage of sufficient continuum emission and Fe II line emission flanking the Hβ+[O III] complex, enabling accurate fitting of these features. We visually inspected the SDSS spectrum of each candidate and removed sources having spurious redshifts, instrumental artifacts, and other anomalies. The combined SDSS-GNIRS spectroscopic coverage of each source includes, at a minimum, the C IV λ1549, Mg II $\lambda\lambda$2796, 2803, Hβ, and [O III] emission lines; the Hα λ6563 emission line is present in all sources at $1.55 \lesssim z \lesssim 2.50$, representing $\sim$ 87% of our sample. We note that the $2.10 \lesssim z \lesssim 2.40$ redshift bin comprises $\sim$ 67% of our entire sample, given that this redshift bin is three times wider than that of the lower redshift bin, and sources in this bin are brighter than the sources in the higher redshift bin.

In summary, the GNIRS-DQS sources constitute an optically-selected, NIR flux limited sample of quasars, spanning wide ranges in rest-frame UV spectral properties, including broad absorption line (BAL) and non-radio quiet quasars[2] (comprising $\sim$ 30%[3] and $\sim$ 12% of the sample, respectively [70]. Figure 2.3 shows the radio loudness distribution of the GNIRS-DQS sources. The GNIRS-DQS sample is broadly representative of the general quasar population of luminous, high-redshift quasars during the epoch of most intense quasar activity [72, 73, 74].

[2]We consider radio-quiet quasars to have $R < 10$, where R is the radio loudness, defined as $R = f_\nu(5\text{ GHz})$ / f_ν (4400 Å), where $f_\nu(5\text{ GHz})$ and $f_\nu(4400\text{ Å})$ are the flux densities at rest-frame frequencies of 5 GHz and 4400 Å, respectively [17]. Non-radio quiet quasars include radio-intermediate ($10 < R < 100$) and radio-loud ($R > 100$) sources, respectively.

[3]Quasars flagged as BAL quasars in [70] (see, Table 3.1).

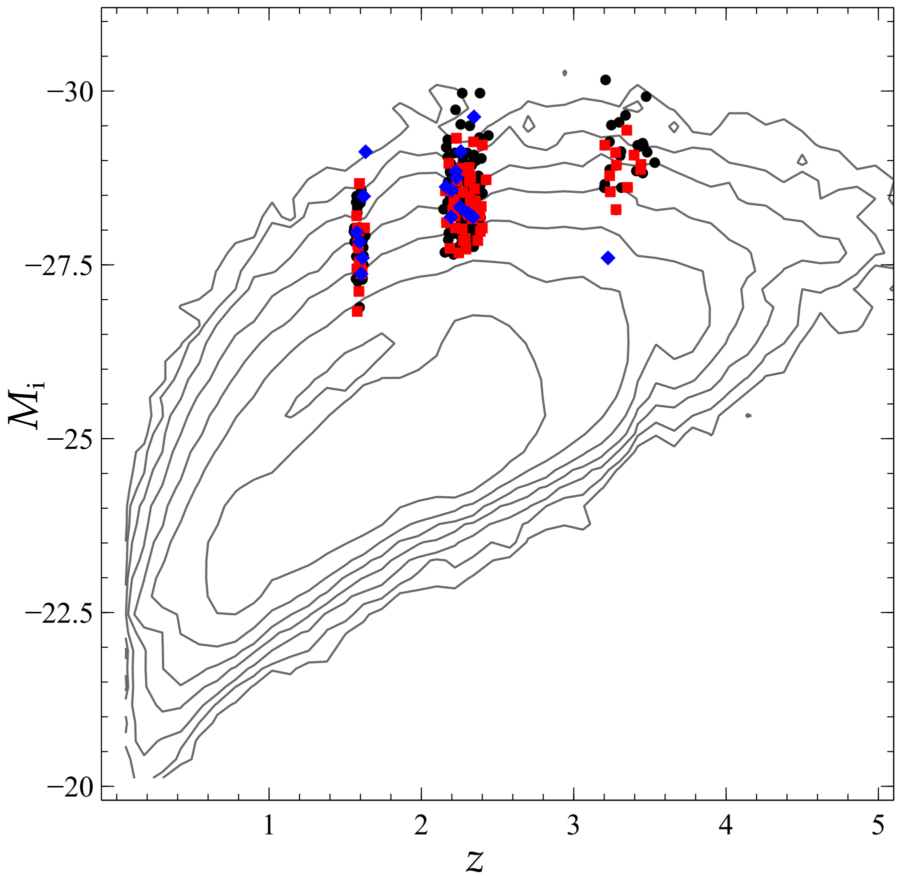

FIGURE 2.1. Distribution of SDSS quasars from DR14 (contours) and the 272 objects in the GNIRS-DQS sample (symbols) in the luminosity-redshift plane, where M_i is the absolute i-band luminosity (BAL quasars are represented by red squares, and non-radio quiet quasars are represented by blue diamonds). Most, but not all, quasars in DR14 are represented via contour lines, for clarity. Redshift ranges were chosen to ensure the prominent emission lines of Hβ and [O III] would be centered in the J, H, or K band. The final sample is representative of the quasar population within our selection criteria.

2.3. Observations, and Data Reduction

The observations were designed to yield data of roughly comparable quality, in terms of both S/N and spectral resolution, to the respective SDSS spectra at $\lambda_{\mathrm{obs}} \sim 5000$ Å. The GNIRS spectra were thus required to have a ratio of ~ 40 between the mean flux density and

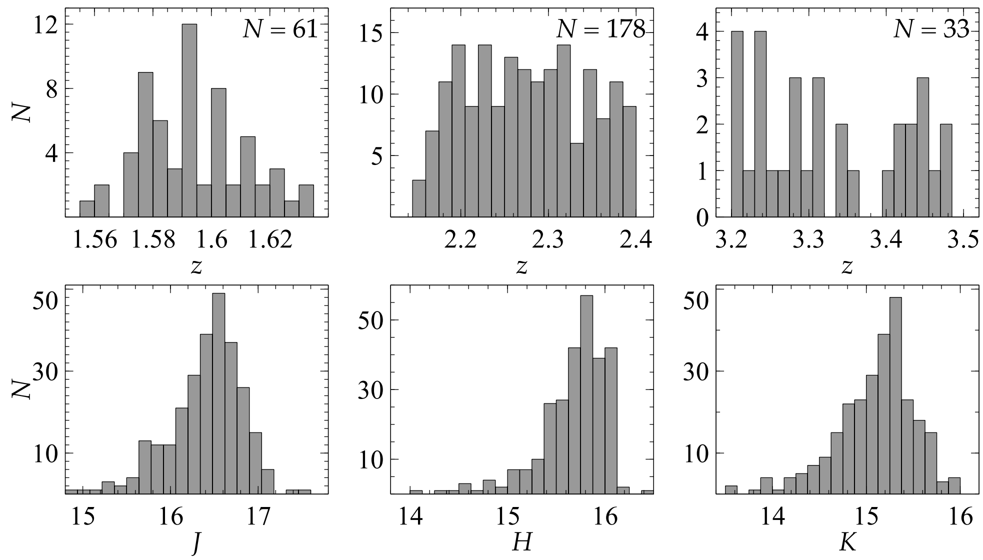

FIGURE 2.2. Redshift distribution in each redshift interval from SDSS (top), and corresponding magnitude distribution of the 272 objects in our sample (bottom). The three redshift bins correspond to the Hβ and [O III] lines appearing at the center of the J, H, or K photometric bands.

the standard deviation of that flux density in a rest-frame wavelength interval spanning 100 Å around $\lambda_{\rm rest} = 5100$ Å, and a spectral resolution of $R \sim 1100$ across the entire GNIRS band. These requirements enable accurate measurements of redshift based on [O III] line peaks, with the high S/N contributing to reducing the uncertainties below the spectral resolution limit, ~ 300 km s^{-1} [32]. As explained below in Section 2.4, we determine that, on average, our spectra produce uncertainties on the measured line peak of [O III] $\lambda5007$ of order ~ 50 km s^{-1}, stemming from pixel-to-wavelength calibration and our fitting procedures.

All spectra were obtained in queue observing mode with GNIRS configured to use the Short Blue camera (0.15" pix^{-1}), the 32 lines mm^{-1} grating in cross-dispersed mode, and the 0.45"-wide slit. This configuration covers the observed-frame ~0.8–2.5 μm band in each source, simultaneously, in six spectral orders with overlapping spectral coverage. Our observing strategy utilized an ABBA method of slit nodding to enable sky subtraction. Exposure times ranged from $\sim 10-40$ minutes for each object, with an additional 15 minutes of overhead per source. Each observation included calibration exposures, and either one or

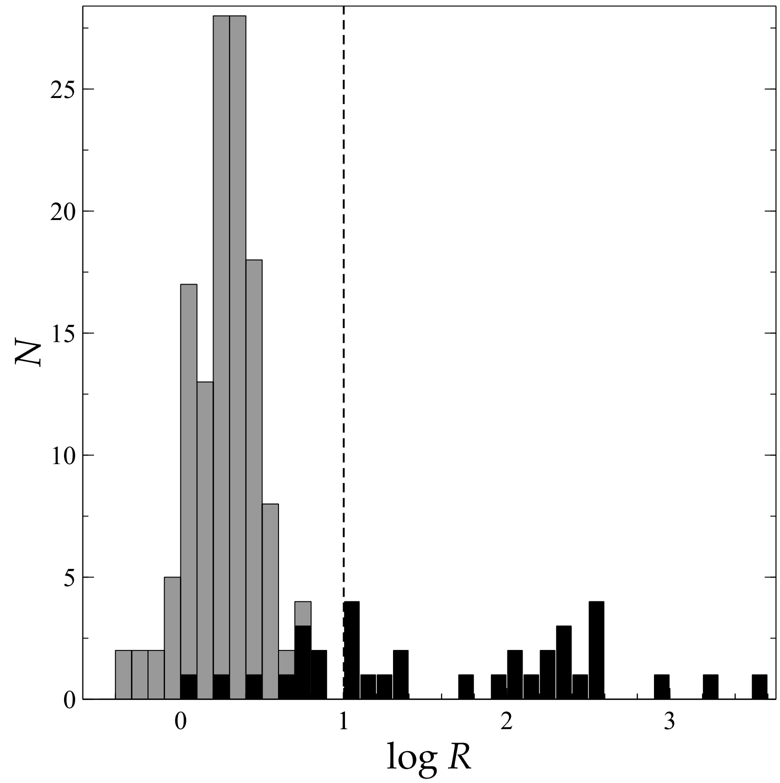

FIGURE 2.3. Radio loudness distribution of the GNIRS-DQS sources; the shaded (grey) columns represent upper limits on R for radio undetected sources based on the [70] catalog, and the dashed line at $\log R = 1$ incidates the threshold for radio quiet quasars. This distribution is generally similar to that of the SDSS quasar population [74].

two ABBA sequences depending on source brightness. We also observed a telluric standard star either immediately before or after the observation in a spectral range of B8 V to A4 V, with $8200\,\mathrm{K} \lesssim T_{\mathrm{eff}} \lesssim 13000\,\mathrm{K}$, and typically within $\approx 10^{\circ} - 15^{\circ}$ from each quasar.

The observation log of the original 272 sources appears in Table 3.1. Column (1) is the SDSS designation of the quasar. Column (2) provides the most reliable reported redshift estimate from SDSS (Table A1, column 9 "Z" [70]). Columns (3), (4), and (5) list the respective J, H, and K magnitudes of each quasar from the Two Micron All Sky Survey (2MASS; [75]). Columns (6) and (7) give the observation date and semester, respectively. Column (8) is the net science exposure time, Column (9) provides comments, if any, concerning the observation, Column (10) provides a flag for whether or not the quasar is a BAL quasar (as defined in [70]), and Column (11) provides a flag for whether or not the quasar is considered non-radio quiet (see, footnote 2).

We classify an acceptable observing night for this survey based on our programs' approved observing conditions including no greater than 50% cloud cover and 85% image quality[4], however some objects were observed under worse conditions, and are noted as such in Table 3.1. Additionally, 12 sources were observed over two observing sessions. These additional observations are recorded separately and immediately follow the initial observation in Table 3.1 (which brings the total number of lines in that Table to 284). For these objects, all available observations were utilized in the reduction process.

Quasar	$z_{\rm SDSS}$ [a]	J [mag]	H [mag]	K [mag]	Obs. Date	Semester	Net Exp. [s]	Comments	BAL	RL
(1)	(2)	(3)	(4)	(5)	(6)	(7)	(8)	(9)	(10)	(11)
SDSS J000544.71−044915.2	2.322	16.94	16.09	16.66	2019 Oct 18	2019B	1800	4	...	...
SDSS J000730.94−095831.5	2.223	17.09	15.94	15.37	2019 Jan 06	2018B	1800	4	1	...
SDSS J001249.89+285552.6	3.236	16.51	15.71	15.49	2017 Sep 09	2017B	1800	...	1	...
SDSS J001355.10−012304.0	3.396	16.71	16.05	15.46	2019 Jan 05	2018B	900	...	1	...
	...	...	...	...	2019 Jan 07	2018B	900	...	...	...
SDSS J001453.20+091217.6	2.338	16.65	15.92	15.14	2017 Sep 19	2017B	2025	1	...	...
SDSS J001813.30+361058.6	2.316	16.15	15.65	14.75	2017 Aug 31	2017B	1800	...	...	...
SDSS J001914.46+155555.9	2.271	16.72	15.81	15.14	2017 Sep 01	2017B	1800	...	...	...
SDSS J002634.46+274015.5	2.250	17.05	15.92	15.25	2018 Dec 20	2018B	1800	...	...	...
SDSS J003416.61+002241.1	1.632	16.48	15.86	15.68	2017 Sep 01	2017B	1800	...	...	...
SDSS J004300.26+045718.6	2.362	16.22	15.65	14.89	2018 Dec 21	2018B	1800	4	1	...
SDSS J004719.71+014813.9	1.590	16.57	16.06	15.25	2018 Dec 24	2018B	1800	...	...	...
SDSS J005233.67+014040.8	2.301	15.99	15.22	14.59	2019 Jul 04	2019B	900	...	...	...
SDSS J005408.29+020751.6	1.590	16.53	15.90	15.50	2018 Nov 25	2018B	2250	1,4	1	...
SDSS J010113.72+032427.0	1.579	16.23	15.38	15.25	2018 Dec 21	2018B	1800	...	...	1
SDSS J010328.72−110414.4	2.195	16.90	15.86	15.47	2017 Sep 04	2017B	1800	...	...	1
SDSS J010447.39+101031.6	2.361	17.36	16.07	15.46	2019 Oct 18	2019B	1800	...	...	1
SDSS J010500.72+194230.4	2.320	16.73	15.76	15.00	2017 Sep 04	2017B	1800	...	...	...
SDSS J010615.93+101043.0	2.350	17.09	16.09	15.30	2019 Nov 26	2019B	1920	...	...	...
SDSS J010643.23−031536.4	2.242	16.58	15.75	15.19	2018 Dec 24	2018B	1800	...	...	...

[4] https://www.gemini.edu/observing/telescopes-and-sites/sites#Constraints

SDSS J011218.07+353011.7	2.305	17.06	16.04	15.69	2019 Nov 29	2019B	1800	4	1	...
SDSS J011515.84+110651.1	2.280	16.92	16.01	14.94	2019 Nov 29	2019B	1800	4	...	...
SDSS J011538.72+242446.0	2.374	16.55	15.74	15.09	2019 Jan 06	2018B	1800	...	...	...
SDSS J013012.36+153157.9	2.349	16.43	15.82	14.71	2017 Sep 04	2017B	1800	...	1	...
SDSS J013113.25+085245.5	3.532	16.63	16.16	15.32	2017 Sep 01	2017B	1800	...	...	...
SDSS J013136.44+130331.0	1.594	16.29	15.43	15.61	2018 Aug 30	2018B	2025	1	...	...
SDSS J013417.81−005036.2	2.254	16.64	15.85	15.16	2018 Dec 24	2018B	1800	...	...	...
SDSS J013647.96−062753.6	3.285	16.46	16.03	15.47	2018 Nov 25	2018B	1800	...	...	...
SDSS J013652.52+122501.5	2.393	16.64	15.78	14.73	2017 Oct 29	2017B	1800	...	1	1
SDSS J014018.20−013805.8	2.235	16.10	15.42	14.58	2018 Nov 25	2018B	900	...	1	...
SDSS J014128.26+070606.1	2.265	17.01	16.08	15.24	2019 Nov 26	2019B	1920	1	...	...
	...	...	...	...	2019 Nov 29	2019B	1920	...	...	...
SDSS J014206.86+025713.0	2.315	15.75	14.92	13.99	2018 Nov 26	2018B	900	...	1	...
SDSS J014932.06+152754.0	2.389	16.82	16.06	15.29	2019 Nov 27	2019B	1920	...	...	...
SDSS J021259.21+132618.8	1.619	16.49	15.67	15.59	2017 Sep 25	2017B	1800	3	...	...
SDSS J022007.64−010731.1	3.441	16.90	16.19	15.36	2017 Sep 01	2017B	1800	...	1	...
SDSS J024318.99+025746.6	3.280	16.47	15.92	15.68	2019 Dec 04	2019B	1800	4	1	...
SDSS J025042.45+003536.7	2.387	16.72	15.77	15.25	2017 Sep 09	2017B	1800	...	1	...
SDSS J035150.97−061326.4	2.221	16.21	15.74	15.17	2017 Oct 30	2017B	1800	...	...	...
SDSS J072517.52+434553.4	1.594	16.14	15.50	15.01	2017 Oct 20	2017B	1880	1	...	...
SDSS J072928.48+252451.8	2.306	16.67	15.67	14.95	2017 Nov 05	2017B	1800	...	...	...
SDSS J073519.68+240104.6	3.278	16.81	16.45	15.35	2017 Sep 21	2017B	1800	...	1	...
SDSS J073900.90+485159.0	1.620	16.62	15.81	15.63	2018 Dec 23	2018B	1800	...	...	...
SDSS J073913.65+461858.5	1.581	16.22	15.71	15.22	2018 Dec 17	2018B	1800	...	...	...
SDSS J074941.16+262715.9	1.592	16.53	15.60	15.35	2017 Nov 06	2017B	1800	...	...	...
SDSS J075115.43+505439.1	2.300	15.89	15.55	14.90	2019 Oct 02	2019B	1800	...	...	...
SDSS J075136.36+432732.4	2.250	16.67	15.75	15.22	2018 Dec 17	2018B	1800	...	...	...
SDSS J075405.08+280339.6	2.271	16.49	15.96	15.27	2018 Dec 24	2018B	1800	...	...	...
SDSS J075547.83+220450.1	2.314	16.08	15.50	14.74	2017 Nov 02	2017B	1880	...	...	...
SDSS J075837.62+135733.7	2.198	16.37	15.56	14.48	2018 Dec 20	2018B	1800	...	...	1
SDSS J080036.01+501044.3	1.621	15.84	15.41	15.12	2017 Nov 04	2017B	940	...	...	1
SDSS J080117.79+521034.5	3.209	15.71	15.34	14.61	2017 Nov 04	2017B	1880	...	...	...
SDSS J080413.66+251633.9	2.298	16.27	15.68	14.89	2019 Jan 03	2018B	1800	...	...	1
SDSS J080937.55+263729.6	2.260	16.69	16.02	15.61	2019 Oct 27	2019B	1800	4	...	...
SDSS J081019.47+095040.9	2.218	16.58	15.87	15.06	2017 Dec 29	2017B	1800	...	...	...
SDSS J081056.96+120914.8	2.259	16.16	15.45	14.68	2017 Dec 29	2017B	1410	1	...	...
SDSS J081114.66+172057.4	2.323	16.19	15.49	14.65	2017 Nov 04	2017B	940	...	1	...
SDSS J081127.44+461812.9	2.257	15.96	15.64	14.88	2017 Nov 14	2017B	1880	...	...	...
SDSS J081342.09+344235.3	2.245	17.14	16.01	15.23	2019 Oct 27	2019B	1800	4	1	...

SDSS J081410.76+443706.9	2.277	16.83	16.03	15.11	2019 Dec 04	2019B	2250	...	...	...
SDSS J081558.35+154055.2	2.230	16.39	15.63	14.90	2019 Jan 03	2018B	1800	...	...	...
SDSS J081940.58+082357.9	3.204	16.80	15.80	15.70	2019 Oct 27	2019B	1800	...	...	...
SDSS J082507.67+360411.1	1.579	15.52	14.79	14.75	2017 Dec 30	2017B	940	3	...	...
SDSS J082603.32+342800.6	2.307	16.50	15.80	15.17	2018 Dec 20	2018B	1800	...	...	...
SDSS J082613.85+495019.3	2.180	16.49	16.08	15.27	2019 Dec 09	2019B	1880	4	...	...
SDSS J082643.45+143427.6	2.308	16.88	16.00	15.63	2019 Nov 16	2019B	1800	...	...	1
SDSS J082644.66+163549.0	2.189	15.89	15.32	14.28	2018 Nov 25	2018B	1125	1	...	...
SDSS J082736.89+061812.1	2.192	15.99	15.19	14.21	2018 Nov 20	2018B	900	1	...	...
	...	...	...	...	2018 Dec 23	2018B	900	...	...	...
SDSS J082852.67−042938.9	2.275	16.70	16.07	15.41	2019 Dec 11	2019B	1800	4	1	...
SDSS J083255.63+182300.7	2.274	15.90	15.43	14.68	2018 Dec 20	2018B	900	...	...	...
SDSS J083417.12+354833.1	2.163	15.71	15.29	14.60	2017 Nov 13	2017B	940	...	...	...
SDSS J083745.74+052109.4	2.355	16.43	15.85	15.15	2019 Jan 11	2018B	1800	...	1	...
SDSS J084029.97+465113.7	1.572	15.90	15.20	15.03	2017 Nov 10	2017B	940	...	...	...
SDSS J084133.15+200525.7	2.342	15.09	14.41	13.62	2019 Feb 03	2019A	900	1	1	...
SDSS J084526.75+550546.8	1.618	16.33	15.65	15.18	2018 Jan 05	2017B	1800	1,4	...	...
SDSS J084729.52+441616.7	2.347	16.61	15.51	15.01	2019 Jan 03	2018B	1800	...	1	...
SDSS J084846.11+611234.6	2.258	15.38	14.73	13.89	2017 Nov 02	2017B	640	...	...	...
SDSS J085046.17+522057.4	2.230	15.94	15.45	14.55	2019 Sep 30	2019B	900	...	1	...
SDSS J085337.36+121800.3	2.196	16.06	15.65	14.80	2017 Dec 30	2017B	2350	1	...	...
SDSS J085344.17+354104.5	2.175	16.79	16.02	15.30	2019 Oct 27	2019B	1800	...	...	...
SDSS J085443.10+075223.2	1.604	16.62	15.62	15.51	2019 Jan 21	2019A	1800	...	...	...
SDSS J085726.94+331317.1	2.339	16.26	15.60	15.19	2019 Jan 01	2018B	1800	...	...	1
SDSS J085856.00+015219.4	2.172	16.87	15.78	15.06	2018 Jan 02	2017B	1800	3	...	...
SDSS J085946.79+603702.1	2.276	16.71	15.97	15.11	2019 Nov 16	2019B	450	...	...	...
	...	...	...	...	2019 Dec 11	2019B	1800	...	...	...
SDSS J090247.57+304120.7	1.560	15.74	15.08	14.89	2017 Oct 20	2017B	940	...	...	...
SDSS J090444.33+233354.0	2.259	15.77	15.25	14.21	2018 Jan 02	2017B	940	...	...	1
SDSS J090646.98+174046.8	1.579	16.25	15.47	15.20	2019 Jan 01	2018B	1800	...	...	...
SDSS J090709.89+250620.8	3.310	16.24	15.71	15.08	2018 Dec 21	2018B	1800	...	...	...
SDSS J090710.36+430000.2	2.189	15.88	15.41	14.67	2018 Jan 05	2017B	940	3	...	...
SDSS J091000.56+401158.5	2.176	16.81	16.06	15.36	2019 Dec 11	2019B	1920	4	...	...
SDSS J091054.17+375914.9	2.162	16.45	15.85	15.12	2019 Mar 16	2019A	1800	3	...	1
SDSS J091118.02+202254.7	3.225	16.96	16.08	15.30	2017 Nov 03	2017B	1305	3	...	1
SDSS J091301.01+422344.7	2.315	16.07	15.50	14.43	2018 Jan 02	2017B	1880	...	1	...
SDSS J091328.22+394443.9	1.582	16.40	15.85	15.32	2018 Jan 01	2017B	1800	...	1	1
SDSS J091716.79+461435.4	1.626	16.33	15.61	15.33	2018 Jan 05	2017B	1800	3	1	...
SDSS J091941.26+253537.7	2.267	16.81	16.02	15.96	2019 Dec 10	2019B	1800	...	...	...

SDSS J092216.04+160526.4	2.373	16.47	15.94	15.05	2017 Dec 29	2017B	1800	...	...	...
SDSS J092325.25+453222.2	3.452	16.44	16.02	15.64	2019 Dec 10	2019B	1800	...	...	...
SDSS J092456.66+305354.7	3.457	16.39	16.04	15.33	2019 Jun 19	2019A	1800	...	...	...
	...	...	...	...	2019 Dec 10	2019B	1800	...	...	...
SDSS J092523.24+214119.8	2.364	16.66	15.79	15.13	2019 Jan 03	2018B	1800	...	...	...
SDSS J092555.05+490338.2	2.343	16.77	16.01	15.50	2019 Dec 11	2019B	1800	...	...	...
SDSS J093251.98+023727.0	2.165	16.85	15.85	15.28	2018 Dec 21	2018B	1800	...	1	...
SDSS J093533.88+235720.5	2.306	16.67	15.93	15.29	2019 Jan 09	2018B	1800	...	...	...
SDSS J093952.61+195838.3	1.580	15.81	15.00	14.85	2018 Jan 06	2017B	1880	4	1	...
SDSS J094140.16+325703.2	3.453	16.55	15.81	15.24	2018 Jan 06	2017B	1800	4	...	...
SDSS J094214.40+034100.3	1.583	16.62	15.99	15.53	2019 Dec 16	2019B	1880	...	...	...
SDSS J094328.94+140415.6	2.400	16.63	15.86	14.88	2018 Jan 03	2017B	900	1	1	...
	...	...	...	...	2018 Jan 06	2017B	900	...	...	...
SDSS J094347.02+690818.4	1.598	16.62	15.74	15.68	2019 Jan 03	2018B	1800	...	...	...
SDSS J094427.27+614424.6	2.333	16.41	15.61	14.72	2019 Dec 12	2019B	2250	...	1	...
SDSS J094602.31+274407.0	2.440	15.87	15.28	14.55	2017 Nov 10	2017B	940	...	...	1
SDSS J094637.83−012411.5	2.214	16.99	15.72	15.34	2017 Nov 13	2017B	1800	...	...	...
SDSS J094646.94+392719.0	2.220	16.70	16.08	15.57	2019 Oct 24	2019B	1920	...	...	...
SDSS J094648.59+171827.7	2.294	16.90	15.87	15.01	2019 Mar 09	2019A	1800	...	...	...
SDSS J094902.38+531241.5	1.611	16.61	16.07	15.96	2019 Jan 01	2018B	1800	...	1	...
SDSS J095058.76+263424.6	2.401	16.61	15.94	15.64	2018 Dec 19	2018B	1800	...	...	...
SDSS J095327.95+322551.6	1.575	16.13	15.28	14.81	2019 Feb 06	2019A	1800	...	...	1
SDSS J095330.36+353223.1	2.385	16.93	15.90	15.69	2018 Dec 17	2018B	1800	...	...	...
SDSS J095544.26+182546.9	3.482	16.80	15.83	15.58	2019 Jan 10	2018B	1800	...	...	...
SDSS J095707.82+184739.9	2.380	16.54	15.68	15.37	2018 Jan 03	2017B	1800	...	...	...
SDSS J095746.75+565800.7	1.575	16.08	15.31	15.04	2017 Nov 03	2017B	900	1,3	1	...
	...	...	...	...	2018 Jan 04	2017B	900	...	...	...
SDSS J095823.07+371218.3	2.280	16.33	15.81	15.33	2018 Jan 02	2017B	1800	...	...	...
SDSS J095852.19+120245.0	3.298	16.29	15.70	14.98	2018 Jan 02	2017B	940	...	...	...
SDSS J100212.63+520800.2	1.613	16.52	15.96	15.98	2019 Jan 03	2018B	1800	...	...	...
SDSS J100610.55+370513.8	3.204	16.30	15.69	15.27	2017 Nov 04	2017B	940	...	1	...
	...	...	...	...	2017 Nov 10	2017B	940	...	...	...
SDSS J100653.26+011938.7	2.298	16.80	15.92	15.20	2019 Jan 10	2018B	1800	...	1	...
SDSS J100850.06−023831.6	2.259	17.05	15.92	15.50	2019 Jan 03	2018B	1800	...	...	...
SDSS J101106.74+114759.4	2.248	17.03	15.87	15.04	2019 Jan 02	2018B	1800	...	...	...
SDSS J101211.44+330926.4	2.254	16.59	15.85	15.17	2017 Dec 04	2017B	1350	...	...	1
	...	...	...	...	2018 Jan 03	2017B	900	...	...	...
SDSS J101353.43+244916.4	1.634	15.03	14.06	13.90	2018 Jan 02	2017B	640	...	...	1
SDSS J101425.11+032003.7	2.146	16.61	15.82	15.17	2018 Jan 03	2017B	1800	...	...	...

SDSS J101429.57+481938.4	1.571	16.25	15.53	15.32	2018 Jan 03	2017B	1800	...	...	...
SDSS J101542.04+430455.6	2.425	16.49	16.05	15.34	2019 Dec 18	2019B	1800	...	1	...
SDSS J101724.26+333403.3	1.573	16.49	15.84	15.40	2018 Jan 03	2017B	1800	1,4	...	...
SDSS J101921.62+354036.7	1.557	16.24	15.66	15.77	2017 Nov 03	2017B	1305	4	...	...
SDSS J102154.00+051646.3	3.439	16.75	16.06	15.33	2018 Dec 16	2018B	1800	...	1	...
SDSS J102537.69+211509.1	2.252	16.30	15.90	14.89	2018 Dec 19	2018B	1800	3	...	...
SDSS J102648.15+295410.9	2.335	16.61	15.54	15.09	2018 Jan 02	2017B	940	4	...	...
SDSS J102731.49+541809.7	1.593	16.55	15.72	15.71	2019 Jan 04	2018B	900	...	...	...
	...	...	...	...	2019 Jan 13	2018B	900	...	...	...
SDSS J102907.09+651024.6	2.175	15.88	15.41	14.57	2018 Mar 29	2018A	920	...	...	...
SDSS J103209.78+385630.6	1.584	16.21	15.86	15.49	2019 Apr 15	2019A	1800	...	...	...
SDSS J103236.98+230554.1	2.379	16.99	16.09	15.41	2019 Dec 16	2019B	1920	...	...	...
SDSS J103246.19+323618.0	2.380	17.02	15.90	15.41	2019 Dec 16	2019B	1800	...	1	...
SDSS J103405.73+463545.4	2.215	16.74	15.96	15.13	2018 Jan 08	2018B	1800	...	1	...
SDSS J103546.02+110546.4	2.359	15.70	15.13	14.23	2017 Nov 17	2017B	940	4	...	...
SDSS J103718.23+302509.1	2.293	16.94	15.69	15.57	2019 Mar 03	2019A	1350	1	1	...
SDSS J104018.51+572448.1	3.411	16.96	15.97	15.30	2019 Jan 01	2018B	1800	...	...	1
SDSS J104330.09+441051.5	2.215	16.63	15.76	15.52	2018 Dec 19	2018B	1800	...	...	...
SDSS J104336.73+494707.6	2.194	16.34	15.78	14.78	2018 Dec 20	2018B	1800	...	...	...
SDSS J104621.57+483322.6	1.577	16.38	16.06	15.52	2019 Jan 07	2018B	1800	...	1	...
SDSS J104716.50+360654.0	2.291	16.68	15.88	15.25	2018 Dec 21	2018B	1800	...	...	1
SDSS J104743.57+661830.5	2.171	16.43	15.64	15.20	2019 Jan 03	2018B	1800	...	...	...
SDSS J104911.34+495113.6	1.606	15.40	14.58	14.28	2017 Oct 28	2017B	640	...	...	...
SDSS J104941.58+522348.9	2.384	17.01	15.91	15.27	2019 Dec 12	2019B	1800	...	1	...
SDSS J105045.72+544719.2	2.173	15.85	15.38	14.45	2019 Mar 09	2019A	920	...	...	...
SDSS J105714.82+440323.8	3.340	16.14	15.70	15.01	2019 Feb 03	2019A	470	4	...	...
SDSS J105902.04+580848.6	2.248	16.61	15.93	15.00	2019 Jan 03	2018B	900	...	...	...
SDSS J105926.43+062227.4	2.199	16.00	15.27	14.71	2019 Mar 17	2019A	920	...	...	...
SDSS J110148.85+054815.5	1.589	16.22	15.52	15.33	2019 Dec 12	2019B	1800	...	1	...
SDSS J110516.68+200013.7	2.362	16.31	15.67	15.08	2019 Apr 15	2019A	1800	...	...	...
SDSS J110735.58+642008.6	2.330	16.21	15.74	15.08	2019 Dec 27	2019B	1800	...	...	...
SDSS J110810.87+014140.7	1.614	16.34	15.72	15.61	2019 Dec 28	2019B	1800	...	...	...
SDSS J111119.10+133603.8	3.475	15.89	15.51	15.03	2019 Mar 17	2019A	940	3	...	...
SDSS J111313.29+102212.4	2.261	16.02	15.48	14.62	2019 Jun 16	2019A	1800	...	1	...
SDSS J111352.53+104041.9	1.603	16.47	15.61	15.22	2019 Dec 29	2019B	1800	...	1	...
SDSS J111850.02+351311.7	2.175	16.47	15.77	15.32	2019 May 13	2019A	1800	...	...	...
SDSS J111920.98+232539.4	2.289	16.68	15.86	15.18	2019 Dec 29	2019B	1800	...	1	...
SDSS J112127.79+254758.9	1.587	16.26	15.41	15.38	2019 May 18	2019A	1800	...	1	...
SDSS J113048.45+225206.6	2.370	16.86	16.01	15.12	2020 Feb 04	2020A	1800	...	1	1

SDSS J113621.04+005021.2	3.428	16.45	15.81	15.48	2019 Mar 17	2019A	1800	...	...	...
SDSS J113740.61+630256.9	2.322	16.47	15.81	14.85	2019 Dec 16	2019B	1800	...	1	...
SDSS J113924.64+332436.9	2.314	16.38	15.95	14.85	2020 Mar 06	2020A	1800	...	1	...
SDSS J114212.25+233250.5	1.600	16.09	15.52	15.14	2020 Jan 04	2019B	1800	...	...	...
SDSS J114323.71+193448.0	3.348	16.10	15.72	15.31	2019 Mar 17	2019A	1800	...	1	...
SDSS J114350.30+362911.3	2.343	16.19	15.51	15.14	2019 Jun 18	2019A	1800	...	...	...
SDSS J114705.24+083900.6	1.604	16.08	15.18	14.79	2019 Nov 15	2019B	900	...	1	1
SDSS J114711.78+084029.6	2.333	16.64	15.79	15.21	2019 Jun 14	2019A	1800	...	...	...
SDSS J114738.35+301717.5	3.353	16.80	16.09	15.42	2019 Jun 17	2019A	1800	...	1	...
	...	...	...	...	2019 Dec 30	2019B	1920	...	...	...
SDSS J114902.70+144328.0	2.190	16.36	15.88	14.95	2019 Jun 14	2019A	1800	...	...	...
SDSS J114907.15+004104.3	2.301	16.85	15.47	14.95	2019 Jun 18	2019A	1800	...	...	...
SDSS J114927.90+432727.9	3.305	16.86	15.91	15.38	2019 Dec 18	2019B	1800	...	...	...
SDSS J115034.53+653928.2	2.224	15.32	14.82	14.08	2019 Mar 17	2019A	628	4	...	...
SDSS J115747.99+272459.6	2.206	16.14	15.43	14.48	2019 Jun 17	2019A	2025	...	1	...
SDSS J120452.82+354007.4	1.592	16.56	15.92	15.89	2019 Mar 01	2019A	1800	4	1	...
SDSS J121314.03+080703.6	2.376	16.63	15.88	15.30	2019 May 23	2019A	1800	...	...	...
SDSS J121404.11+330945.6	1.595	16.16	15.46	15.15	2019 Dec 28	2019B	900	...	...	...
SDSS J121423.01+024252.8	2.231	16.32	15.76	15.15	2019 Jun 13	2019A	1800	...	...	1
SDSS J121519.42+424851.0	2.314	16.45	15.80	14.50	2019 Feb 26	2019A	1800	3	...	...
SDSS J121736.65+515510.3	2.225	16.04	15.39	14.44	2019 Jun 16	2019A	1800	...	...	1
SDSS J121810.98+241410.9	2.381	15.78	15.13	14.33	2019 Mar 18	2019A	920	...	...	...
SDSS J121843.39+153617.2	2.268	15.27	14.52	13.83	2019 Mar 08	2019A	600	4	...	...
SDSS J121940.36−010007.4	1.575	15.60	15.06	14.84	2019 Mar 19	2019A	920	4	...	...
SDSS J122046.05+455442.1	2.220	15.71	15.07	14.23	2018 Jun 23	2018A	920	...	...	...
SDSS J122709.48+310749.3	2.190	16.57	15.59	14.93	2019 May 24	2019A	1800	...	...	...
SDSS J123514.64+462904.0	2.204	16.43	15.86	14.90	2019 May 22	2019A	1800	...	...	...
SDSS J124512.86+194727.5	2.173	15.95	15.26	14.73	2019 Jul 14	2019B	900	4	...	...
SDSS J125150.45+114340.7	2.195	16.46	15.70	14.83	2019 Apr 20	2019A	1800	3	...	...
SDSS J125159.90+500203.6	2.385	16.43	15.70	15.40	2019 Dec 12	2019B	1800	...	...	...
SDSS J132736.56+033128.3	1.594	15.61	14.87	14.84	2020 Jul 08	2020A	1200	4	1	...
SDSS J133342.56+123352.7	3.275	16.60	15.80	15.18	2019 May 18	2019A	1800	...	1	...
SDSS J133448.87+515743.6	3.240	16.77	16.04	15.62	2020 Jul 08	2020A	1800	4	1	...
SDSS J134341.99+255652.9	1.600	15.77	15.00	14.63	2019 Mar 19	2019A	1380	3	...	...
SDSS J135827.12+170510.3	2.233	16.71	15.82	14.96	2019 Mar 23	2019A	1800	4	...	...
SDSS J135908.35+305830.8	2.290	16.19	15.63	14.93	2019 May 14	2019A	1800	3	...	...
SDSS J140058.79+260619.4	2.351	16.43	15.70	14.95	2018 Jun 26	2018A	1800	...	1	...
SDSS J140704.43+273556.6	2.225	16.46	15.98	14.86	2020 Jun 30	2020A	1800	...	...	...
SDSS J141028.14+135950.2	2.213	16.21	15.52	14.67	2019 Mar 09	2019A	900	1,3	...	...

	...	...	...	...	2019 Mar 23	2019A	900	...	...	...
SDSS J141617.38+264906.1	2.299	16.39	15.68	14.84	2019 May 22	2019A	1800	...	...	1
SDSS J141925.48+074953.5	2.394	16.37	15.69	14.86	2019 May 19	2019A	1800	...	...	...
SDSS J141951.84+470901.3	2.296	15.72	15.05	14.30	2019 May 14	2019A	1800	3	...	...
SDSS J142013.03+253403.9	2.235	16.34	15.67	15.03	2019 Apr 17	2019A	1800	...	1	...
SDSS J142330.09+115951.2	1.613	16.22	15.43	15.27	2019 Mar 23	2019A	1800	4	...	1
SDSS J142435.97+421030.4	2.213	16.28	16.01	15.01	2020 Jul 10	2020A	1800	...	...	...
SDSS J142500.24+494729.2	2.260	16.52	15.80	15.22	2020 Mar 11	2020A	1800	...	1	...
SDSS J142502.62+274912.2	2.344	16.74	15.94	14.88	2020 Jun 29	2020A	1800	...	...	...
SDSS J142543.32+540619.3	3.247	16.06	15.50	15.24	2020 Mar 11	2020A	1800	...	...	...
SDSS J142903.03−014519.3	3.420	16.52	15.74	15.06	2019 May 14	2019A	1800	...	...	...
SDSS J144624.29+173128.8	2.196	16.56	15.76	15.42	2018 Jun 26	2018A	1800	...	...	...
SDSS J144706.29+350956.1	2.273	16.26	15.72	14.83	2019 Mar 21	2019A	1800	4	1	...
SDSS J144706.81+212839.2	3.235	16.47	15.82	15.29	2020 Jun 30	2020A	1800	...	...	...
SDSS J144948.62+123047.5	1.592	16.55	15.51	15.34	2019 Apr 23	2019A	1800	...	...	...
SDSS J145541.11−023751.0	1.613	16.58	16.05	14.78	2020 Jul 08	2020A	1800	...	...	...
SDSS J145608.33+111823.7	1.562	16.37	15.40	14.94	2019 Mar 22	2019A	1800	4	...	...
SDSS J150205.58−024038.5	2.215	16.49	15.84	15.14	2019 Apr 18	2019A	1800	...	1	...
SDSS J150226.60+180039.5	2.340	16.02	15.26	14.79	2020 Feb 23	2020A	1600	4	1	...
SDSS J150743.71+220928.8	3.236	16.57	16.06	15.35	2020 Jun 04	2020A	1800	...	...	...
SDSS J151123.30+495101.2	2.400	16.09	15.47	14.77	2019 Apr 24	2019A	1800	...	1	...
SDSS J151341.89+463002.8	1.579	16.60	15.62	15.57	2019 Apr 17	2019A	1800	...	1	...
SDSS J151507.82+612411.9	2.182	16.74	15.58	15.23	2020 Jun 14	2020A	1800	...	...	...
SDSS J151727.68+133358.6	2.235	16.48	15.84	14.94	2019 Apr 23	2019A	1800	...	...	...
SDSS J151733.09+435648.4	2.197	16.56	15.99	15.24	2020 Jun 04	2020A	1800	...	...	...
SDSS J152336.27+071325.7	1.586	16.43	15.42	15.36	2019 Mar 22	2019A	1800	4	1	...
SDSS J152929.55+230208.7	1.581	16.52	15.69	15.66	2019 Apr 16	2019A	1800	...	...	...
SDSS J153248.95+173900.8	2.350	16.69	15.70	15.37	2019 Apr 23	2019A	1800	...	1	...
SDSS J153551.23+373029.0	2.197	16.64	15.94	14.85	2020 Jul 01	2020A	1800	4	...	...
SDSS J154231.96+390854.8	2.356	17.01	15.74	15.24	2020 Jul 01	2020A	1720	4	...	...
SDSS J154550.37+554346.2	2.158	16.15	15.49	14.99	2018 Jul 31	2018A	920	3	1	...
SDSS J154907.47+565645.7	1.603	16.56	15.76	15.33	2020 Aug 01	2020A	1800	4	...	...
SDSS J155355.10+375844.1	2.369	16.89	15.96	15.19	2020 Jul 28	2020A	1800	...	...	...
SDSS J155934.26+590031.6	1.601	16.54	15.52	15.12	2020 Jun 14	2020A	1720	4	...	...
SDSS J160029.86+331806.9	1.593	16.61	15.83	15.27	2018 Jun 26	2018A	1800	...	...	...
SDSS J160137.90+172851.0	2.239	15.69	15.90	14.87	2020 Jun 04	2020A	1800	4	...	...
SDSS J160207.67+380743.0	1.593	15.29	14.51	14.39	2018 Jun 04	2018A	640	...	1	...
SDSS J160425.30+193929.1	3.313	16.55	16.05	15.15	2019 Jan 09	2018B	900	...	...	...
SDSS J160513.17+325829.9	2.276	16.49	15.97	15.42	2020 Jun 28	2020A	1800	...	...	...

SDSS J160552.97+292141.4	2.321	16.25	15.44	14.70	2019 Jan 10	2018B	920	...	1	...
SDSS J160637.57+173516.2	2.323	16.72	16.00	15.75	2020 Jul 11	2020A	1800	...	...	...
SDSS J160716.65+182649.4	2.323	16.48	15.83	14.97	2020 Jul 08	2020A	1800	4	...	...
SDSS J161435.70+372715.6	1.601	15.85	14.94	14.84	2020 Jun 30	2020A	1200	...	...	...
SDSS J161942.39+525613.4	2.345	15.55	14.83	13.95	2019 Apr 24	2019A	1800	...	...	1
SDSS J161942.58+325419.3	2.220	16.50	15.94	15.46	2020 Jun 29	2020A	1800	4	...	...
SDSS J162659.24+301535.0	1.578	16.45	15.81	15.43	2020 Jul 05	2020A	1800	...	...	1
SDSS J162701.94+313549.2	2.318	16.01	15.63	14.74	2018 Jun 26	2018A	1800	4	...	...
SDSS J163125.10+174810.0	2.180	16.15	15.38	14.44	2020 Jun 04	2020A	1600	...	1	...
SDSS J163433.42+265158.2	1.571	16.44	15.73	15.57	2020 Jul 05	2020A	1800	...	...	...
SDSS J164807.55+254407.1	2.191	15.71	15.16	14.35	2019 Apr 15	2019A	1800	...	...	...
SDSS J165321.03+271706.7	1.605	15.71	15.08	14.67	2020 Jun 15	2020A	1600	...	...	...
SDSS J165348.02+485019.0	2.249	16.18	15.44	15.01	2018 May 13	2018A	920	1,4	...	...
SDSS J174015.84+255457.1	2.220	16.61	16.01	15.46	2020 Jul 03	2020A	1800	4	...	...
SDSS J205900.36−064309.5	2.280	16.55	15.86	15.40	2018 Jun 29	2018B	1800	...	...	...
SDSS J210831.56−063022.5	2.345	16.43	15.78	15.08	2018 Jun 06	2018A	1800	...	...	...
SDSS J214611.80−085857.4	2.182	16.67	15.86	15.30	2018 Jun 29	2018B	1800	4	...	...
SDSS J214657.66−023946.3	2.283	16.44	16.09	15.32	2019 Oct 31	2019B	1800	4	...	...
SDSS J214901.21−073141.6	2.211	16.86	15.92	15.69	2018 Jul 19	2018A	1800	2	...	...
SDSS J220344.98+235729.3	2.187	17.54	16.08	15.52	2019 Sep 08	2019B	1800	...	1	...
SDSS J222621.45+251545.0	2.385	14.88	14.31	13.51	2017 Nov 05	2017B	600	...	...	...
SDSS J223934.45−004707.2	2.221	16.91	15.97	15.70	2018 Jul 28	2018A	1800	3	1	...
SDSS J225608.48+010557.8	2.268	16.78	15.86	15.23	2018 Jul 19	2018A	1800	...	1	...
SDSS J225627.12+092313.3	2.290	16.67	15.86	15.42	2018 Jul 01	2018B	1800	...	...	...
SDSS J230722.21+253803.8	1.594	16.40	15.53	15.46	2018 Jul 12	2018A	1800	...	...	...
SDSS J231450.12+182402.8	2.284	16.58	15.95	15.14	2018 Jul 01	2018B	1800	...	...	...
SDSS J231706.96+323802.8	2.378	16.97	16.07	15.73	2019 Oct 18	2019B	1800	4	...	...
SDSS J233344.66+290251.5	3.201	16.81	16.04	15.76	2019 Oct 31	2019B	1800	...	...	...
SDSS J234817.55+193345.8	2.154	16.69	15.96	15.33	2018 Jun 30	2018B	1800	...	...	...
SDSS J235212.85−012029.6	2.376	16.85	15.84	15.36	2017 Sep 09	2017B	1800	...	...	...

Table 2.1. ^{a}Value based on best available measurement as stated by SDSS (Pâris et al. (2018; [70]), Table A1, column 9 "Z").

NOTE – Objects followed by an empty row aside from observation date, semester, and net exposure are additional observations made for that same object.

Comments:

(1) At least one exposure was taken under subpar observing conditions.

(2) All exposures were taken under supbar observing conditions.

(3) Supplemental data used from other observations to aid in reduction as described in Section 2.4.5.

(4) Observation failed to provide spectrum of the source due to bad weather, instrument artifacts, or other technical difficulties during the observation.

Our data processing procedure generally follows the XDGNIRS pipeline developed by the Gemini Observatory ([76][5]: see also [77]) with the Gemini package in PyRAF[6]. Following standard image cleaning for artifacts and other observational anomalies, we pair-subtract the images to remove the bulk of the background noise by directly combining the sky-subtracted object exposures. Quartz lamps and IR lamps were used to create flat fields to correct pixel-by-pixel variation across the detector. The flat-fielded images were corrected for optical distortions. Several objects required replacement flat fields due to pixel shifting of dead pixels in the detector into the GNIRS spectra directly (marked accordingly with a corresponding comment in Table 3.1), which produced a notable increase in the uncertainty of spectroscopic measurements for these objects, particularly in the bluer bands. On average, the increased flux uncertainty from these spectra is on the order of ∼3%. At this stage, of the 272 sources observed, 46 observations did not yield a meaningful spectrum due to bad weather, instrument artifacts, or other technical difficulties (Note 4 in Column 9 of Table 3.1),

[5] `http://www.gemini.edu/sciops/instruments/gnirs/data-format-and-reduction/reducing-xd-spectra`

[6] `https://www.gemini.edu/node/11823`

leaving the final sample at 226 sources.

Wavelength calibration was performed using two argon lamp exposures in order to assign wavelength values to the observed pixels. The uncertainties associated with this wavelength calibration are not larger than 0.5 Å RMS, corresponding to $\lesssim 10$ km s^{-1} at ~ 15000 Å.

Spectra of the telluric standards were processed in a similar fashion, followed by a careful removal of the stars' intrinsic hydrogen absorption lines. This process was performed by fitting Lorentzian profiles to the hydrogen absorption lines, and interpolating across these features to connect the continuum on each side of the line. Following the line cancellation, the quasar spectra were divided by the corrected stellar spectra. The corrected spectra were multiplied by an artificial blackbody curve with a temperature corresponding to the telluric standard star, which yielded a cleaned, observed-frame quasar spectrum. Each quasar spectrum was flux calibrated by comparing local flux densities to the J, H, and K 2MASS magnitudes from Table 3.1 and using the magnitude-to-flux conversion factors from Table A.2 of [78]. For the final spectra, we masked any noise present from cosmic rays, regions of high levels of atmospheric absorption, and band gap interference.

We chose this method as opposed to flux calibrating via the telluric standards to avoid any differences in atmospheric conditions between observations of the object and the telluric standard. This preference was also motivated by our use of a relatively narrow slit in order to prioritize spectral resolution at the cost of potentially larger slit losses in the observations. Although the 2MASS and Gemini observations are separated by several years in the quasars' rest frames, the cross-calibrations are subject to minimal uncertainties since $\sim 88\%$ of our sources are luminous radio-quiet quasars at high redshift. Such sources typically show UV-optical flux variations on the order of $\lesssim 10\%$ over such timescales [79, 80, 81]. In fact, the effects stemming from the differences in airmass between the quasars and their respective telluric standard stars, as well as the slit losses, are typically larger than the expected intrinsic quasar variability.

In order to further test the reliability of our flux calibration, we compared the flux densities in overlapping continuum regions, $\lambda_{\rm obs} \sim 8000 - 10000$ Å, between our GNIRS spectra and those of the respective SDSS spectra; this test was feasible for $\sim 90\%$ of our sources that have both high-quality GNIRS and SDSS spectral data where we can obtain meaningful comparisons that avoid reductions in quality that can occur in this region for both surveys. We found that the flux densities in the SDSS spectra are, on average, smaller than the GNIRS flux densities by $\sim 40\%$ ($\mu = -0.155$), with a 1σ scatter of $\sim 60\%$ ($\sigma = 0.2013$) (see, Fig. 2.4, where μ and σ are the logarithms of the mean and standard deviation, respectively). Therefore, the flux densities when directly comparing both spectral sets are consistent at the 1σ level, despite the presence of this systematic offset. This systematic offset should be taken into account when comparing fluxes between SDSS and GNIRS spectra, however, it does not affect the emission-line measurements presented in this survey. This scatter may include discrepancies such as those due to intrinsic quasar variability, fiber light loss in SDSS spectra, and differences in airmass between quasars and their respective standard star observations. Examples of prominent emission lines in final, flux-calibrated spectra appear in Figure 2.5.

2.4. Spectral Fitting

The final GNIRS quasar spectra were fit by using multiple localized linear continua, explained in Section 2.4.1, constrained by no less than six narrow ($\sim$ 200 Å-wide, rest-frame) line-free regions, and performed Gaussian fits to the emission lines. The Fe II and Fe III emission complexes were modeled via empirical templates from Boroson, & Green [82] and Vestergaard & Wilkes [83] for the rest-frame optical and UV band, respectively. These templates were scaled and broadened by convolving a Gaussian with a full width at half maximum (FWHM) value that was free to vary between 1300 and 10000 km s^{-1}. Given that the Fe II, Fe III, and Hβ lines likely originate from different physical regions [84], we kept the FWHM of the iron templates as a free parameter. The FWHM values selected to broaden each template were determined using a least squares analysis on each fitted region.

For the [O III] lines, the widths of each line were restricted to be identical to each other, and their flux ratios were kept constant at $I_{5007}/I_{4959} = 3$ ([85] and references therein);

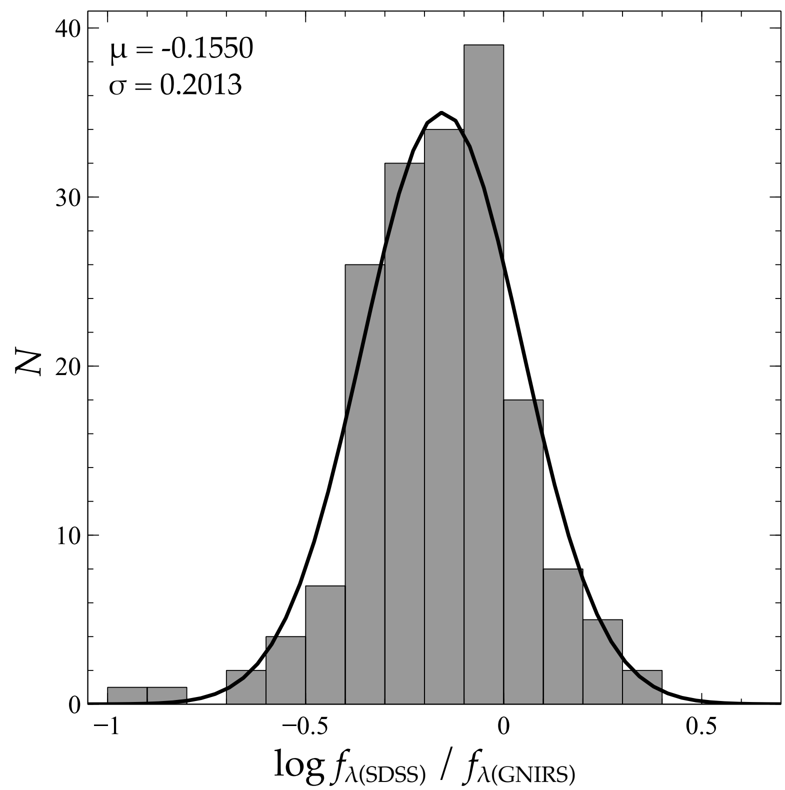

FIGURE 2.4. Flux-density ratio distribution between SDSS and GNIRS spectra from the overlapping continuum regions ($\lambda_{obs} \sim 8000 - 10000$ Å) with a lognormal distribution fit. The log of the mean ratio (μ) and its standard deviation (σ) indicate that the flux densities of the GNIRS spectra are consistent at the 1σ level with those from their respective SDSS spectra.

additionally, the rest-frame wavelength difference between the $\lambda5007$ and $\lambda4959$ lines was kept constant, which proved adequate for the fits of each object.

We fit two Gaussians to each broad emission line profile to accommodate possible asymmetry present in the profile due to, e.g., absorption, or outflows. We note that the two Gaussians fit per broad emission-line are adopted for fitting purposes only, and they do not represent physically distinct regions. Fitting the line profiles with more complex models was not warranted given the quality of our GNIRS spectra. The constraints on the Gaussian profiles for each emission line were that the peak wavelengths can differ from their known rest-frame values by up to $\pm$ 1500 km s^{-1}, on initial assessment (see, e.g., [86], Figure 5) with

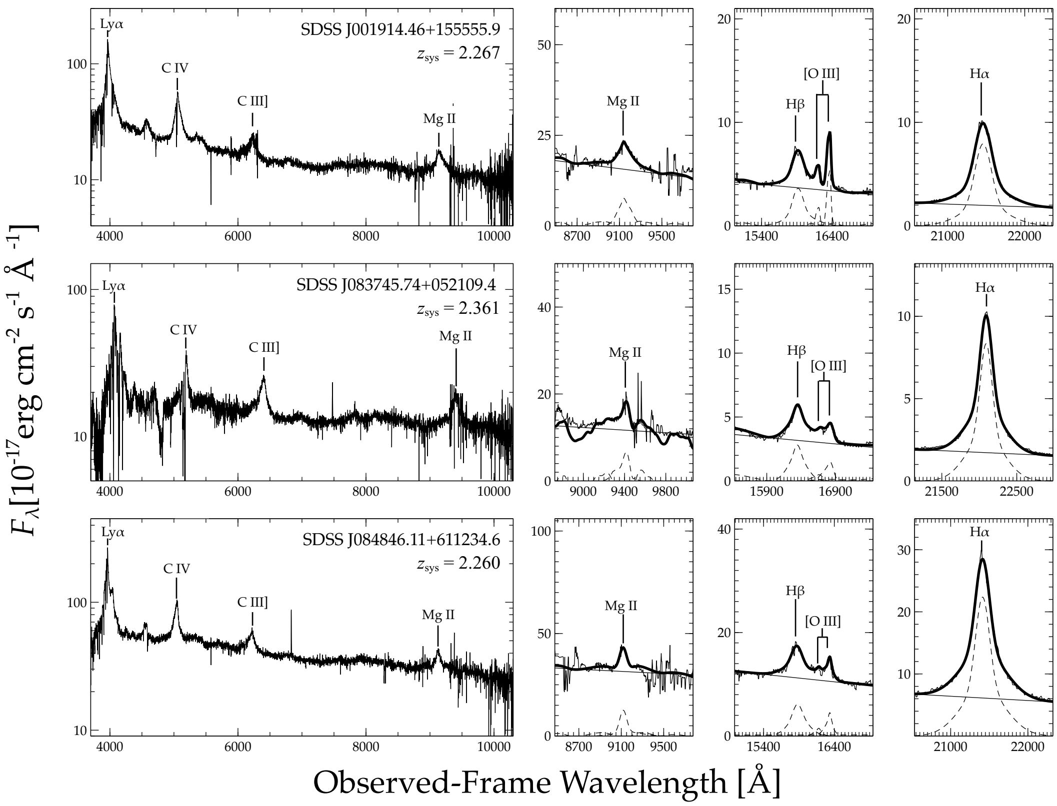

FIGURE 2.5. SDSS and GNIRS spectra and their best-fit models for three representative quasars in our sample (fitting of the SDSS spectra is deferred to a future publication). From left to right, panels show the corresponding SDSS spectra, followed by the GNIRS Mg II, Hβ, and Hα spectral regions, respectively. In the three rightmost panels, the spectrum is presented by a thin solid line, and best-fit models for the localized linear continua, Gaussian profiles, and iron emission blends are marked by dashed lines. Summed best-fit model spectra are overplotted with thick solid lines. Details of the spectral fitting procedure are given in Section 2.4. All of the GNIRS spectra and their best-fit models are available electronically at `https://datalab.noirlab.edu/gnirsdqs.php`. We note that SDSS J083745.74+052109.4 is flagged as a BAL quasar (see, Table 3.1, [69]), and will be discussed in a future publication.

a max flux value ranging from zero to a value calculated to be twice the maximum value of the emission line. Visual inspection yielded some exceptions beyond an offset of $\pm$ 1500 km s^{-1}, whereupon manual fitting was performed to compensate for the larger velocity offset.

2.4.1. Continuum Fitting

By using localized linear continuum fitting, we were able to achieve more accurate measurements by avoiding uncertainties stemming from a single power-law fit. There has been debate about an accurate model for quasar continua: a single power-law, a broken power-law [24], or whether the power-law description is appropriate at all in the rest-frame optical band; for example, in highly reddened quasar spectra a single power-law fitting will likely fail (see, e.g., [87]). Alternatively, quasar continua may be better described by accretion disk modeling [64]. This survey was primarily concerned with measuring emission-line properties as opposed to continua, and, through using a variety of fitting methods including our own investigations into the efficacy of power-law and broken power-law fits, we conclude that localized linear continua give, at worst, the same level of uncertainty as power-law fitting, and, at best, avoid large uncertainties inherent in modeling blended continuum features. Therefore, measurements of all the emission lines implemented localized linear continua where the windows for fitting were determined by the availability of the nearest continuum band segments as defined in [24].

2.4.2. Mg II

The Mg II doublet is detected in the bluer regions of our spectra, where the S/N is lower by roughly an order of magnitude than the redder regions where the Hβ line is detected. Since our survey was designed such that the S/N near the Hβ region would be roughly comparable to the S/N across the respective SDSS spectrum of each source (see, Section 2.2), the S/N around the Mg II region in our GNIRS spectra is roughly an order of magnitude lower than the corresponding values in the SDSS spectra. As a result, we were only able to obtain reliable Mg II and Fe II+Fe III fits for $\sim$31% of our sources (and we do not present measurements for Fe II+Fe III due to their considerable uncertainties). In this work, we only present Mg II line measurements based on the GNIRS spectra of our sources; in a future publication, we will complement these data with Mg II line measurements based on the sample's SDSS spectra (for ∼87% of our sample at $z \lesssim 2.4$). On average, the uncertainties on the measured Mg II properties are roughly an order of magnitude larger than those of Hβ. During the fitting process, we made a preliminary evaluation of the noise around the Hβ and Mg II lines. If the noise around Mg II was within a defined threshold ($S/N \sim 10$) when compared to that of the Hβ region ($S/N \sim 40$, see Section 2.3), the Mg II line was fit automatically. Otherwise, each spectrum was visually inspected to determine if it was possible to perform reliable measurements of the Mg II line. Due to the lower S/N in this region, the Fe II+Fe III complex was fit with narrow (~ 20 Å) continuum bands and often required further interactive adjustments in order to avoid noise spikes to ensure accurate fitting to the Mg II feature.

2.4.3. Hβ

The Hβ region, for most of our objects, provided reliable measurements given the survey was designed with this region in mind. However, in $\lesssim 2\%$ of our objects, the Hβ emission line was adjacent to the edge of the observing band, resulting in larger uncertainties when fitting the Fe II emission complex. This misalignment of Hβ stems from selecting our sample using UV-based redshifts, based primarily on the peak wavelength of the C IV emission line, which suffer from systematic biases due to outflows that can be as large as ≈ 5000 km s^{-1} ([54], Matthews et al. 2023, submitted). This misalignment also results in reduced coverage of the Fe II blends for these objects. Despite this complication, we were able to adequately fit two Gaussians to each of the Hβ emission lines.

By design, our survey targeted highly luminous quasars, biased toward having higher $L/L_{\rm Edd}$ values (see, Fig. 2.1, [88]), which typically also tend to have relatively strong Fe II emission. As a result, we relied on the broad iron bumps on either side of the Hβ line, rest-frame $\sim 4450 - 4750$ Å and $5100 - 5400$ Å [24], as our primary region for fitting the Fe II complex. While reasonable in most cases, these fits are likely affected by He II λ4686 emission-line contamination, however the He II emission line is unresolvable in this sample

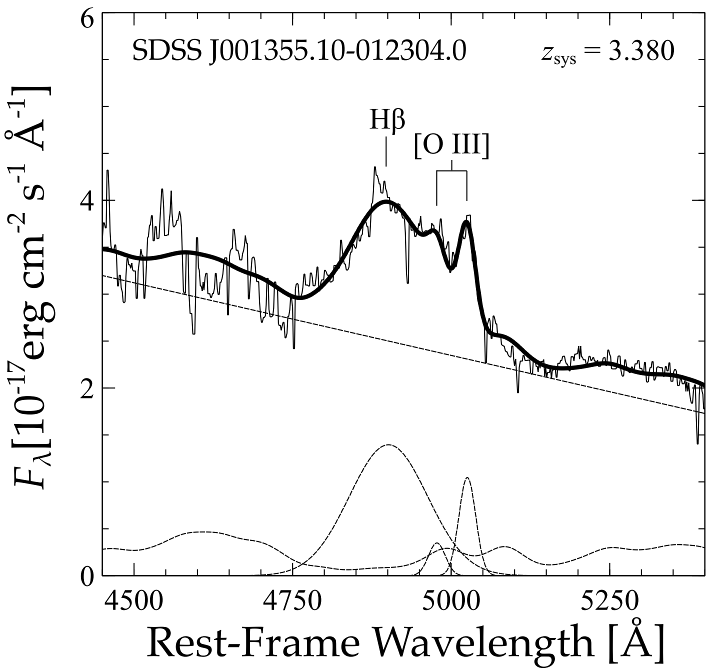

FIGURE 2.6. GNIRS spectrum of the Hβ region of SDSS J001355.10-012304.0, $z_{sys} = 3.380$. The "shelf" structure redward of the Hβ line appears to be a result of strong Fe II and mild [O III] emission. This differs from typical "Eigenvector 1" trends in Boroson, & Green [82], where sources with strong Fe II blends tend to have weak [O III] lines. Line styles are as in Fig. 2.5. These shelves may be a signature of binary quasar candidates (see, e.g., [89]).

due to uncertainties from a variety of factors (see Section 2.4.5). On average, the corresponding Fe II EW values in those sources is ~ 20 Å. Additionally, $\sim 5\%$ of our objects differed from the well-known trends of "Eigenvector 1" [82], having a blend of strong [O III] and Fe II emission, resulting in their spectra exhibiting "shelves" on the red side of the Hβ profile. These features required a more careful fitting, and we did not see any evidence of [O III] outflows directly contributing to this emission complex. An example of a shelf-like fit is presented in Figure 2.6.

Figure 2.7 shows the distribution of [O III] EWs in the GNIRS-DQS sample. As explained in Section 2.4.6 below, for those objects that do not have detectable [O III] emission,

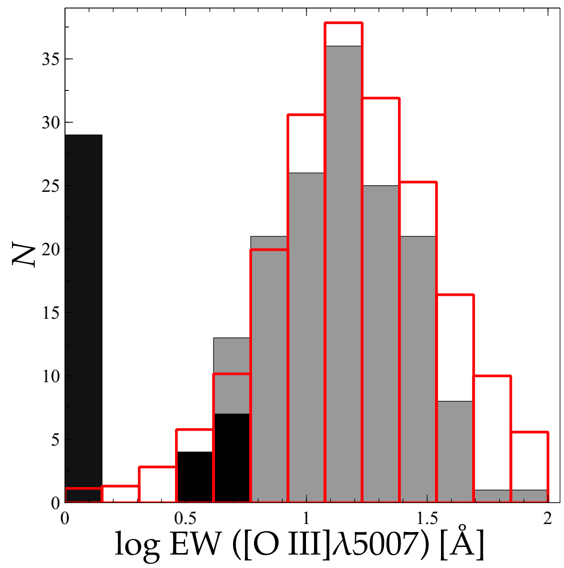

FIGURE 2.7. [O III] rest-frame EW distribution of the GNIRS-DQS sources (grey) overplotted with rest-frame [O III] EWs from [90] (red outline; scaled down by a factor of 100). For $\sim$ 19% of the GNIRS-DQS sources that lack detectable [O III] emission we are able to place strong upper limits on their EW values (black). When compared to [O III] measurements of low-redshift, low-luminosity sources from [90], the [O III] emission tends to become weaker as luminosity increases, consistent with the trends observed in previous studies of high-redshift quasars [91, 35].

we must use the Mg II line to determine systemic redshifts ($z_{\rm sys}$); for those objects that lack both [O III] and Mg II, we must utilize the Hβ line for that purpose, which is present in every GNIRS-DQS spectrum.

2.4.4. Hα

Being the most prominent feature in all the spectra of our sources at $z < 2.5$ (constituting $\sim$ 87% of the sample), Hα yielded the smallest uncertainties on all the emission-line parameters. We do not detect significant narrow [N II] emission-lines flanking the Hα line in any of our sources, which is expected given our selection of highly luminous quasars [92, 90].

2.4.5. Uncertainties in Spectral Measurements

The uncertainties inherent in the GNIRS spectra are contributed by a variety of factors. These include (but are not limited to) sub-par observing conditions, the use of replacement flat fields in several of the spectra (see Section 2.3), and differences in airmass and/or atmospheric conditions between the standard star and the respective quasar observations. Moreover, modeling the telluric standard star continuum with a blackbody function fails to account for potential NIR excess emission from a circumstellar disk around the star. These factors lead to uncertainties on the flux density and shapes of the emission-line profiles, including the locations of their peaks. The uncertainties on these parameters are in the range $\approx$ 4-7%, $\approx$ 3-6%, $\approx$ 2-5%, and $\approx$ 2-4%, for each emission line, respectively. On average, these uncertainties result in general measurement errors across all parameters for an emission-line profile of up to $\sim$ 7%.

Emission-line fitting first relied on shifting the spectrum to the rest-frame using the best available SDSS redshift. However, due to inaccuracies with the SDSS redshift, the emission-lines in the GNIRS spectra often did not line up with the known rest-frame values. This offset led to uncertainties during fitting, and was ultimately mitigated by introducing a redshift iteration process. Emission-lines were fit for three different regimes separately, the Mg II, Hβ, and Hα regions, based off of the SDSS redshift. A systemic redshift, $z_{\rm sys}$, was then determined by the best fit of the most reliable emission-line for measuring redshift, as discussed in Section 2.4.6 below, and the spectrum was shifted according to this value. This process was repeated until the difference in consecutive redshifts was less than $z_{n-1} - z_n < 0.001$ for each region. Additionally, this redshift iteration allows more accurate measurements on z_{sys}, the flux density at rest-frame 5100 Å ($F_{\lambda,5100}$), and more accurate fitting of the broadened iron templates.

After identifying the most accurate redshift, final fits are performed on emission-line features. Using preliminary Gaussian and localized linear continuum fits, residuals are generated, which yield upper and lower values for uncertainties present across the fitting region. With these residual bounds, Gaussian noise is introduced, and a series of 50 fits is performed in order to generate upper and lower bound estimates on the final Gaussian fits. To quantify the error on best-fit parameters, each iterated fit value is stored, which is used to generate a distribution of principle measurements. These distributions are then fit using a Gaussian function in order to determine the final errors at a 1σ confidence level. The iron templates of the Hβ and Mg II regions also experience iterations of FWHM for the line profile, which allows for accurate Fe II and Fe III broadening error estimates. These various fitting iterations allow conservative error estimates on basic emission-line parameters, i.e., FWHM, EW, and line peaks. Finally, the best fit spectral model for each source was verified by visual inspection.

2.4.6. The Catalog

Table 2.2 describes the format of the data presented in the catalog. It contains basic emission line properties, particularly the FWHM and rest-frame EW, of the Mg II, Hβ, [O III], and Hα emission lines. The catalog also provides observed-frame wavelengths of emission-line peaks, as well as the asymmetry and kurtosis of each emission line, which were obtained from the Gaussian fits. A host of additional parameters are given, including the FWHM of the kernel Gaussian used for broadening the Fe II blends around the Hβ region and the EW of these blends in the $4434 - 4684$ Å region (following [82]), as well as the flux density and monochromatic luminosity (λL_λ) at 5100 Å. The catalog also provides $z_{\rm sys}$ values measured from observed-frame wavelengths of emission-line peaks. For determining $z_{\rm sys}$, we adopt the observed-frame wavelength of the peak of one of three emission lines with the highest degree of accuracy which is present in the GNIRS spectrum, where it is known that these three emission lines have uncertainties of $\simeq 50$ km s^{-1}, $\simeq 200$ km s^{-1}, and $\simeq 400$ km s^{-1} for [O III], Mg II, and Hβ, respectively [32].

In cases where the prominent emission lines (i.e., Mg II, Hβ, [O III], and Hα) have no significant detections, upper limits are placed on their EWs by assuming FWHM values for each line using the median value in the sample distributions, and taking the weakest feature detectable in the GNIRS spectra for each line. Additionally, we placed upper limits on the EW of the optical Fe II blends in cases where excess noise surrounding the Hβ+[O III] region would not enable us to fit the Fe II blends reliably; we found that a value of 2 Å for this parameter provides a conservative upper limit in all such cases.

Finally, additional, and typically weaker, emission line measurements follow the formatting presented in Table 2.3, and are reported in the supplemental features catalog for 106 sources from our sample where such features could be measured reliably. These emission lines were fit on a case-by-case basis after visually inspecting each GNIRS spectrum (and no upper limits are assigned in cases of non-detections). Where applicable, we performed fits on the following emission lines with two Gaussians per line, following the same methodology used for primary emission line measurements: Hδ λ4101, Hγ λ4340, and [Ne III] λ3871. The [O II] λ3727 doublet was fit in the same manner.

Column	Name	Bytes	Format	Units	Description
(1)	(2)	(3)	(4)	(5)	(6)
1	OBJ	(1-24)	A24	...	SDSS object designation
2	ZSYS	(26-29)	F4.3	...	Systemic redshifts
3	LC_MG II	(31-35)	F5.0	Å	Observed-frame wavelength of the emission line peak of Mg II based on peak fit value
4	LC_MG II_UPP	(37-39)	F3.0	Å	Upper uncertainty for the line peak of Mg II
5	LC_MG II_LOW	(41-43)	F3.0	Å	Lower uncertainty for the line peak of Mg II
6	FWHM_MG II	(45-48)	F4.0	km s^{-1}	FWHM of Mg II
7	FWHM_MG II_UPP	(50-52)	F3.0	km s^{-1}	Upper uncertainty of FWHM of Mg II
8	FWHM_MG II_LOW	(54-56)	F3.0	km s^{-1}	Lower uncertainty of FWHM of Mg II
9	EW_MG II	(58-59)	F2.0	Å	Rest-frame EW of Mg II
10	EW_MG II_UPP	(61-62)	F2.0	Å	Upper uncertainty of EW of Mg II
11	EW_MG II_LOW	(64-65)	F2.0	Å	Lower uncertainty of EW of Mg II
12	AS_MG II	(67-71)	E5.2	...	Asymmetry of the double Gaussian fit profile of Mg II
13	KURT_MG II	(73-75)	F3.2	...	Kurtosis of the double Gaussian fit profile of Mg II
14	LC_HB	(77-81)	F5.0	Å	Observed-frame wavelength of the emission line peak of Hβ based on peak fit value
15	LC_HB_UPP	(83-85)	F3.0	Å	Upper uncertainty for the line peak of Hβ
16	LC_HB_LOW	(87-89)	F3.0	Å	Lower uncertainty for the line peak of Hβ
17	FWHM_HB	(91-94)	F4.0	km s^{-1}	FWHM of Hβ
18	FWHM_HB_UPP	(96-98)	F3.0	km s^{-1}	Upper uncertainty of FWHM of Hβ
19	FWHM_HB_LOW	(100-102)	F3.0	km s^{-1}	Lower uncertainty of FWHM of Hβ
20	EW_HB	(104-105)	F2.0	Å	Rest-frame EW of Hβ
21	EW_HB_UPP	(107-108)	F2.0	Å	Upper uncertainty of EW of Hβ
22	EW_HB_LOW	(110-111)	F2.0	Å	Lower uncertainty of EW of Hβ
23	AS_HB	(113-17)	E5.2	...	Asymmetry of the double Gaussian fit profile of Hβ

24	KURT_HB	(119-121)	F3.2	...	Kurtosis of the double Gaussian fit profile of Hβ
25	LC_O III	(123-127)	F5.0	Å	Observed-frame wavelength of the emission line peak of [O III] λ5007 based on peak fit value
26	LC_O III_UPP	(129-131)	F3.0	Å	Upper uncertainty for the line peak of [O III] λ5007
27	LC_O III_LOW	(133-135)	F3.0	Å	Lower uncertainty for the line peak of [O III] λ5007
28	FWHM_O III	(137-140)	F4.0	km s^{-1}	FWHM of [O III] λ5007
29	FWHM_O III_UPP	(142-144)	F3.0	km s^{-1}	Upper uncertainty of FWHM of [O III] λ5007
30	FWHM_O III_LOW	(146-148)	F3.0	km s^{-1}	Lower uncertainty of FWHM of [O III] λ5007
31	EW_O III	(150-151)	F2.0	Å	Rest-frame EW of [O III] λ5007
32	EW_O III_UPP	(153-154)	F2.0	Å	Upper uncertainty of EW of [O III] λ5007
33	EW_O III_LOW	(156-157)	F2.0	Å	Lower uncertainty of EW of [O III] λ5007
34	AS_O III	(159-163)	E5.2	...	Asymmetry of the double Gaussian fit profile of [O III] λ5007
35	KURT_O III	(165-167)	F3.2	...	Kurtosis of the double Gaussian fit profile of [O III] λ5007
36	LC_HA	(169-173)	F5.0	Å	Observed-frame wavelength of the emission line peak of Hα based on peak fit value
37	LC_HA_UPP	(175-177)	F3.0	Å	Upper uncertainty for the line peak of Hα
38	LC_HA_LOW	(179-181)	F3.0	Å	Lower uncertainty for the line peak of Hα
39	FWHM_HA	(183-186)	F4.0	km s^{-1}	FWHM of Hα
40	FWHM_HA_UPP	(188-190)	F3.0	km s^{-1}	Upper uncertainty of FWHM of Hα
41	FWHM_HA_LOW	(192-194)	F3.0	km s^{-1}	Lower uncertainty of FWHM of Hα
42	EW_HA	(196-197)	F2.0	Å	Rest-frame EW of Hα
43	EW_HA_UPP	(199-200)	F2.0	Å	Upper uncertainty of EW of Hα
44	EW_HA_LOW	(202-203)	F2.0	Å	Lower uncertainty of EW of Hα
45	AS_HA	(205-209)	E5.2	...	Asymmetry of the double Gaussian fit profile of Hα
46	KURT_HA	(211-213)	F3.2	...	Kurtosis of the double Gaussian fit profile of Hα
47	FWHM_FE II	(215-218)	F4.0	km s^{-1}	FWHM of the kernel Gaussian used to broaden the Fe II template
48	EW_FE II [a]	(220-221)	F2.0	Å	Rest-frame EW of Fe II in the optical as defined by [82]

49	LOGFλ5100	(223-227)	E5.2	erg $s^{-1}cm^{-2}Å^{-1}$	Flux density at rest-frame 5100 Å
50	LOGL5100	(229-232)	F4.2	erg s^{-1}	Monochromatic luminosity at rest-frame 5100 Å

TABLE 2.2. [a]A value of 2 Å denotes an upper limit on this parameter.

NOTE – Data formatting used for the catalog. Asymmetry is defined here as the skewness of the Gaussian fits, i.e., a measure of the asymmetry of the distribution about its mean, $s = E(x-\mu)^3/\sigma^3$, where μ is the mean of x, σ is the standard deviation of x, and $E(t)$ is the expectation value. Kurtosis is the quantification of the "tails" of the Gaussian fits defined as $k = E(x-\mu)^4/\sigma^4$, where symbols are the same as for asymmetry.

Column	Name	Bytes	Format	Units	Description
(1)	(2)	(3)	(4)	(5)	(6)
1	OBJ	(1-24)	A24	...	SDSS object designation
2	LC_HD	(26-30)	F5.0	Å	Observed-frame wavelength of the emission line peak of Hδ based on peak fit value
3	LC_HD_UPP	(32-35)	F4.0	Å	Upper uncertainty for the line peak of Hδ
4	LC_HD_LOW	(37-40)	F4.0	Å	Lower uncertainty for the line peak of Hδ
5	FWHM_HD	(42-45)	F4.0	km s^{-1}	FWHM of Hδ
6	FWHM_HD_UPP	(47-49)	F3.0	km s^{-1}	Upper uncertainty of FWHM of Hδ
7	FWHM_HD_LOW	(51-53)	F3.0	km s^{-1}	Lower uncertainty of FWHM of Hδ
8	EW_HD	(55-56)	F2.0	Å	Rest-frame EW of Hδ
9	EW_HD_UPP	(58-59)	F2.0	Å	Upper uncertainty of EW of Hδ
10	EW_HD_LOW	(61-62)	F2.0	Å	Lower uncertainty of EW of Hδ
11	AS_HD	(64-68)	E5.2	...	Asymmetry of the double Gaussian fit profile of Hδ
12	KURT_HD	(70-72)	F3.2	...	Kurtosis of the double Gaussian fit profile of Hδ
13	LC_HG	(74-78)	F5.0	Å	Observed-frame wavelength of the emission line peak of Hγ based on peak fit value
14	LC_HG_UPP	(80-83)	F4.0	Å	Upper uncertainty for the line peak of Hγ
15	LC_HG_LOW	(85-88)	F4.0	Å	Lower uncertainty for the line peak of Hγ
16	FWHM_HG	(90-93)	F4.0	km s^{-1}	FWHM of Hγ
17	FWHM_HG_UPP	(95-97)	F3.0	km s^{-1}	Upper uncertainty of FWHM of Hγ
18	FWHM_HG_LOW	(99-101)	F3.0	km s^{-1}	Lower uncertainty of FWHM of Hγ
19	EW_HG	(103-104)	F2.0	Å	Rest-frame EW of Hγ
20	EW_HG_UPP	(106-107)	F2.0	Å	Upper uncertainty of EW of Hγ
21	EW_HG_LOW	(109-110)	F2.0	Å	Lower uncertainty of EW of Hγ
22	AS_HG	(112-116)	E5.2	...	Asymmetry of the double Gaussian fit profile of Hγ
23	KURT_HG	(118-120)	F3.2	...	Kurtosis of the double Gaussian fit profile of Hγ
24	LC_O II [a]	(122-126)	F5.0	Å	Observed-frame wavelength of the emission line peak of [O II] based on peak fit value
25	LC_O II_UPP	(128-131)	F4.0	Å	Upper uncertainty for the line peak of [O II]

26	LC_O II_LOW	(133-136)	F4.0	Å	Lower uncertainty for the line peak of [O II]
27	FWHM_O II	(138-141)	F4.0	km s^{-1}	FWHM of [O II]
28	FWHM_O II_UPP	(143-145)	F3.0	km s^{-1}	Upper uncertainty of FWHM of [O II]
29	FWHM_O II_LOW	(147-149)	F3.0	km s^{-1}	Lower uncertainty of FWHM of [O II]
30	EW_O II	(151-152)	F2.0	Å	Rest-frame EW of [O II]
31	EW_O II_UPP	(154-155)	F2.0	Å	Upper uncertainty of EW of [O II]
32	EW_O II_LOW	(157-158)	F2.0	Å	Lower uncertainty of EW of [O II]
33	AS_O II	(160-164)	E5.2	...	Asymmetry of the double Gaussian fit profile of [O II]
34	KURT_O II	(166-168)	F3.2	...	Kurtosis of the double Gaussian fit profile of [O II]
35	LC_NE III [b]	(170-174)	F5.0	Å	Observed-frame wavelength of the emission line peak of [Ne III] based on peak fit value
36	LC_NE III_UPP	(176-179)	F4.0	Å	Upper uncertainty for the line peak of [Ne III]
37	LC_NE III_LOW	(181-184)	F4.0	Å	Lower uncertainty for the line peak of [Ne III]
38	FWHM_NE III	(186-189)	F4.0	km s^{-1}	FWHM of [Ne III]
39	FWHM_NE III_UPP	(191-193)	F3.0	km s^{-1}	Upper uncertainty of FWHM of [Ne III]
40	FWHM_NE III_LOW	(195-197)	F3.0	km s^{-1}	Lower uncertainty of FWHM of [Ne III]
41	EW_NE III	(199-200)	F2.0	Å	Rest-frame EW of [Ne III]
42	EW_NE III_UPP	(202-203)	F2.0	Å	Upper uncertainty of EW of [Ne III]
43	EW_NE III_LOW	(205-206)	F2.0	Å	Lower uncertainty of EW of [Ne III]
44	AS_NE III	(208-212)	E5.2	...	Asymmetry of the double Gaussian fit profile of [Ne III]
45	KURT_NE III	(214-216)	F3.2	...	Kurtosis of the double Gaussian fit profile of [Ne III]

TABLE 2.3. [a][O II] λ 3727

[b][Ne III] λ 3870

NOTE – Data formatting used for the supplemental measurements in the supplemental features catalog.

2.5. Summary

We present a catalog of spectroscopic properties obtained from NIR observations of a uniform, flux-limited sample of 226 SDSS quasars at $1.5 \lesssim z \lesssim 3.5$, which is the largest, uniform inventory for such sources to date. The catalog includes basic spectral properties of Mg II, Hβ, [O III], Fe II, and Hα emission lines, as well as Hδ, Hγ, [O II], and [Ne III] emission lines for a subset of the sample. A spectral resolution of $R \sim 1,100$ was achieved for this data set, which is roughly comparable to the value of the corresponding SDSS spectra. These measurements provide a database to comprehensively analyze and investigate rest-frame UV-optical spectral properties for high-redshift, high-luminosity quasars in a manner consistent with studies of low-redshift quasars.

In particular, the catalog will enable future work on robust calibrations of UV-based proxies to systemic redshifts and black-hole masses in distant quasars. Such prescriptions are becoming increasingly more important as millions of quasar optical spectra will be obtained in the near future by, e.g., the Dark Energy Spectroscopic Instrument (DESI; [93, 94]) and the 4-metre Multi-Object Spectroscopic Telescope (4MOST; [95]), where reliable estimates of z_{sys} and $M_{\rm BH}$ will be crucial to extract the science value from these surveys. In forthcoming papers we will present, among other facets, redshift calibrations via indicative emission lines such as [O III] (Matthews et al. 2023, submitted), SMBH estimates using the Hβ and Mg II profiles measured in this survey (Dix et al. 2023, submitted), and correlations among UV-optical emission lines [82, 96, 56].

In the future, we should continue to push the redshift barrier for the Hβ and [O III] emission lines, as current investigations have been confined to $z \lesssim 3.5$, in order to gain an increased understanding of the co-evolution of SMBHs and their host galaxies, along with more reliable redshifts. However, at redshifts higher than $z \sim 3.5$, these observations cannot be obtained via ground-based telescopes. Future studies in this respect could include a two-pronged approach using small calibration surveys. The first survey, for example, can use higher resolution instruments such as Gemini's Spectrograph and Camera for Observations of Rapid Phenomena in the Infrared and Optical (SCORPIO; [97]) which will better measure weak emission-line profiles and obtain more accurate measurements of the prominent emission lines. This information will reinforce the measurements of this survey and allow for more confident applications to much higher redshifts, even beyond $z > 6$. The second survey would be a select sample of a few dozen highly luminous $z > 3.5$ objects using space-based observations from the James Webb Space Telescope (JWST; [98]) for optimal spectral quality, with the possibility for a contemporaneous SCORPIO survey to obtain measurements of lines such as C IV from the ground.

This work is supported by National Science Foundation grants AST-1815281 (B. M. M., O. S., C. D.), AST-1815645 (M. S. B., A. D. M.), AST-1516784 (W. N. B.), and AST-1715579 (Y. S.). A.D.M. was also supported, in part, by the Director, Office of Science, Office of High Energy Physics of the U.S. Department of Energy under Award No. DE-SC0019022. Y. S. acknowledges support from an Alfred P. Sloan Research Fellowship. We thank an anonymous referee for thoughtful and valuable comments that helped improve this manuscript. This research has made use of the NASA/IPAC Extragalactic Database (NED), which is operated by the Jet Propulsion Laboratory, California Institute of Technology, under contract with the National Aeronautics and Space Administration. We thank Jin Wu and the Gemini Observatory staff for helpful discussions, and providing assistance with data reduction for this project. This work was enabled by observations made from the Gemini North telescope, located within the Maunakea Science Reserve and adjacent to the summit of Maunakea. We are grateful for the privilege of observing the Universe from a place that is unique in both its astronomical quality and its cultural significance.

CHAPTER 3

GNIRS-DQS: AUGMENTED SPECTROSCOPIC CATALOG AND A PRESCRIPTION FOR CORRECTING UV-BASED QUASAR REDSHIFTS

3.1. Introduction

Obtaining systemic redshifts ($z_{\rm sys}$) for quasars to accuracies better than 1000 km s^{-1} is necessary for a variety of reasons. These include measuring the kinematics of outflowing material near the supermassive black hole (SMBH) that impact star formation rates in the quasar's host galaxy [49, 50, 51], and cosmological studies that utilize redshifts as distance indicators, such as quasar clustering and the proximity effect at high redshift [99, 100, 101, 102, 103, 104].

A quasar $z_{\rm sys}$ value is typically determined from spectroscopy in the optical band relying, particularly, on the wavelength of the peak of the narrow [O III] λ5007 emission line at $z \lesssim 0.8$, the Mg II $\lambda\lambda 2798, 2803$ doublet for $0.4 \lesssim z \lesssim 2.3$, or the Balmer lines up to $z \sim 1$, in order of increasing uncertainty on the derived $z_{\rm sys}$ value, ranging from ~ 50 km s^{-1} to ~ 600 km s^{-1} [105, 32, 106]. However, at higher redshifts, these $z_{\rm sys}$ indicators shift out of the optical band, and redshift determinations usually rely on shorter wavelength, and typically higher ionization emission lines such as C IV λ1549. Such emission lines are known to show additional kinematic offsets of up to several 10^3 km s^{-1} that add uncertainties of this magnitude to the derived redshift values [27, 33, 23, 32, 107]. The redshifts of distant quasars determined from large spectroscopic surveys (e.g., Sloan Digital Sky Survey, SDSS) [68, 108, 94, 109], that are limited to $\lambda_{\rm obs} \lesssim 1$ μm, therefore will have uncertainties on the order of tens of Mpc at $z = 2.5$, when converting from velocity space into comoving distance [110].

A direct comparison of SDSS Pipeline redshifts [111, 109] with $z_{\rm sys}$ values obtained from rest-frame optical indicators show that corrections to UV-based redshifts can be made despite the presence of potentially large uncertainties. Past investigations such as Hewett & Wild [52], Mason et al. [112] and Dix et al. [54], hereafter HW10, M17, and D20, respectively, have demonstrated that these uncertainties can be mitigated through corrections obtained from regression analyses based on pre-existing rest-frame optical spectral properties and used as prescriptions for correcting UV-based redshifts.

HW10 relied primarily on sampling methods wherein an average quasar spectrum was generated using a large sample of existing quasar spectra, and then statistical analysis was used to provide offsets for any given quasar with respect to this "master" spectrum in order to correct for any uncertainties. However, this offset correction becomes less reliable for high redshift quasars as important emission lines such as [O III] and Mg II leave the optical-UV regime, and so additional corrections are needed [113].

M17 and D20 used regression analyses that apply empirical corrections to UV-based redshifts involving the C IV spectroscopic parameter space, a diagnostic of quasar accretion power [86, 113, 114], which affects the wavelengths of emission-line peaks. Specifically, these parameters include the rest-frame equivalent width (EW) and full width at half maximum intensity (FWHM) of the C IV line[1] as well as the continuum luminosity at the base of this line. Such corrections have been applied to sources that lack broad absorption lines and are not radio-loud[2] in order to minimize the effects of absorption and continuum boosting, respectively, to the C IV line profile to mitigate potential complications arising from these sources and provide the most reliable results possible.

The D20 analysis, an extension of the M17 study, was based on a non-uniform sample of 55 SDSS sources with spectral coverage in the rest-frame optical and UV. Here, we use a much larger and more uniform sample of 154 sources with highly reliable $z_{\rm sys}$ values drawn from an augmentation of the Gemini Near Infrared Spectrograph - Distant Quasar Survey (GNIRS-DQS) near-infrared (NIR) spectral inventory (hereafter M21, [115]). Our results allow us to obtain significantly improved prescriptions for correcting UV-based redshifts. Section 5.2.2 describes the properties of the quasar sample and the respective redshift measurements, along with an augmentation of the M21 catalog of spectral properties from GNIRS-DQS. Section 5.2 presents prescriptions for UV-based quasar redshift corrections

[1]We discuss additional velocity width measurement methods in Appendix 3.5.

[2]We consider radio-loud quasars to have $R > 100$, where R is defined as $R = f_\nu(5\ \mathrm{GHz})\ /\ f_\nu\ (4400\ \text{Å})$, where $f_\nu(5\ \mathrm{GHz})$ and $f_\nu(4400\ \text{Å})$ are the flux densities at a rest-frame frequency of 5 GHz and a rest-frame wavelength of 4400 Å, respectively [17]

based on multiple regression analyses including several velocity width indicators, alongside discussion of the redshift dependence of the velocity offset corrections, and redshift estimates for quasars with extremely high velocity outflows. Our conclusions are presented in Section 3.4. Throughout this paper we adopt a flat ΛCDM cosmology with $\Omega_\Lambda = 1 - \Omega_\mathrm{M} = 0.7$ and $H_0 = 70$ km s^{-1} Mpc^{-1} [67].

3.2. Sample Selection

Our quasar sample is drawn from GNIRS-DQS, which comprises the largest, most uniform sample of optically selected high-redshift quasars having NIR spectroscopic coverage (M21). The GNIRS-DQS sources were selected from all SDSS quasars [70, 109] having $m_i \lesssim 19.0$ mag at $1.55 \lesssim z \lesssim 3.50$ for which the Hβ and [O III] emission-lines can be covered in either the J, H, or K bands. We augment the original GNIRS-DQS sample with 34 additional sources, selected in a similar fashion as described below, and shown in Figure 3.1. Distributions of radio loudness and [O III] λ5007 EW for the GNIRS-DQS sources are shown in Figures 3.2 and 3.3, respectively.

3.2.1. The Augmented GNIRS-DQS Catalog

We add spectroscopic data for 31 sources that were observed in semester 2020B as part of our GNIRS-DQS campaign (see M21 for a detailed description of the observational strategy and the instrument configuration). In addition, we include spectroscopic data for 11 sources that were observed in a similar fashion, albeit with a narrower slit, 0.30″, in semester 2015A (program GN-2015A-Q-68; PI: Brotherton). Of these 42 sources, 34 (comprising 26 from GNIRS-DQS and 8 from GN-2015A-Q-68) had observations that produced useful spectra that we include in the augmented GNIRS-DQS catalog. This fraction is consistent with the overall success rate of $\sim 80\%$ for all the GNIRS-DQS observations. The observation log of these additional objects is given in Table 3.1.

The formatting for the basic spectral properties of all 260 GNIRS-DQS objects is presented in Tables 3.2 and 3.3 in a similar fashion to Tables 2 and 3 in M21. These Tables contain the most reliable measurements for the entire GNIRS-DQS sample. The GNIRS-

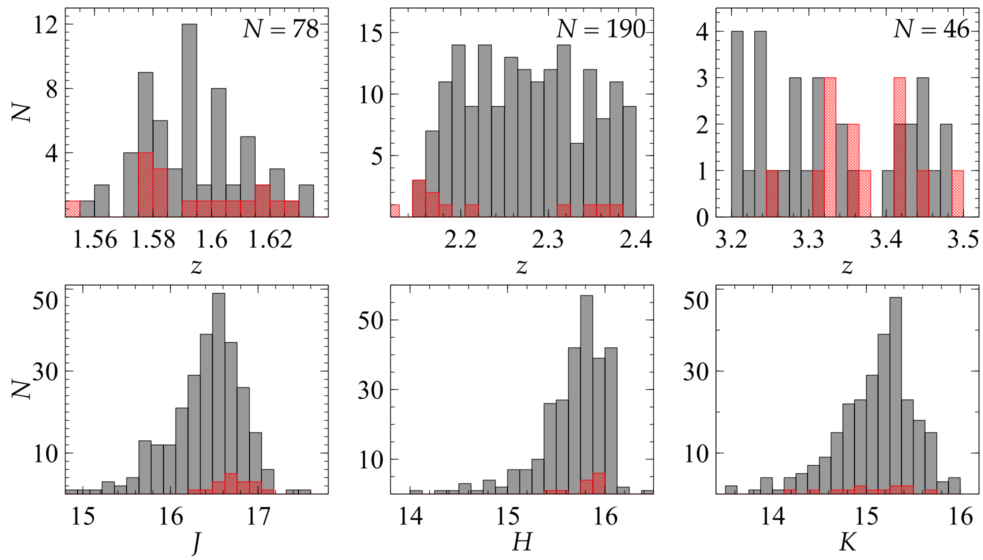

FIGURE 3.1. Distributions of the most reliable reported redshift estimate from SDSS (Table D1, column 27 "Z", [109]) in each redshift interval (top), and corresponding magnitude distributions (bottom). The initial GNIRS-DQS sample is marked in grey, and sources from the augmented sample are shown in red. The three redshift bins correspond to the Hβ and [O III] lines appearing at the center of the J, H, or K photometric bands. The number of sources observed in each redshift bin is marked in each of the top panels. Of a total of 314 sources observed, 272 of which were reported in M21, reliable NIR spectra were obtained for 260 sources; the NIR spectra of 226 of these were presented in M21 and the remaining 34 are presented in this work.

DQS sample was originally selected from the SDSS quasar catalogs for Data Release (DR) 12 and DR14 [69, 70]; the augmented GNIRS-DQS catalog presented here includes 26 sources that were selected from SDSS DR16 [109] which are marked appropriately in Table 3.1. DR16 measurements have been adopted for the full sample [109]. Table 3.4 presents the parameters used to model all of the emission lines, using Gaussian profiles, in the GNIRS-DQS spectra. For each profile, these parameters include the observed-frame wavelength of the line peak, velocity width (FWHM), and flux-density normalization (f_λ). All of the GNIRS spectra and

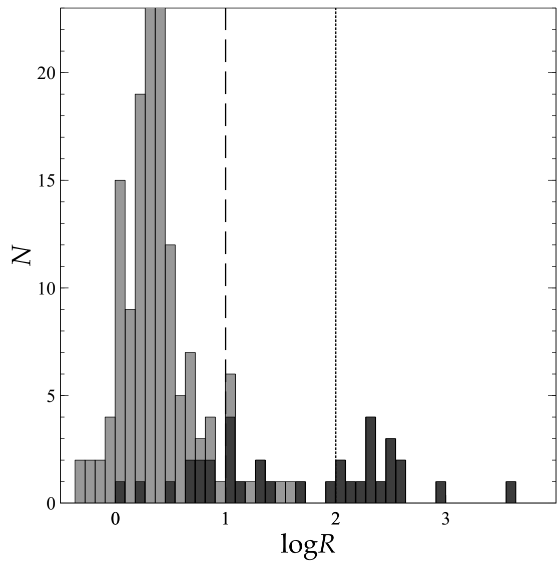

FIGURE 3.2. Radio-loudness distribution of the GNIRS-DQS sources. Darker shaded regions indicate new sources not in M21. The dashed line at log $R = 1$ indicates the threshold for radio-quiet quasars, and the dotted line at log $R = 2$ indicates the threshold for radio-loud quasars (see also M21).

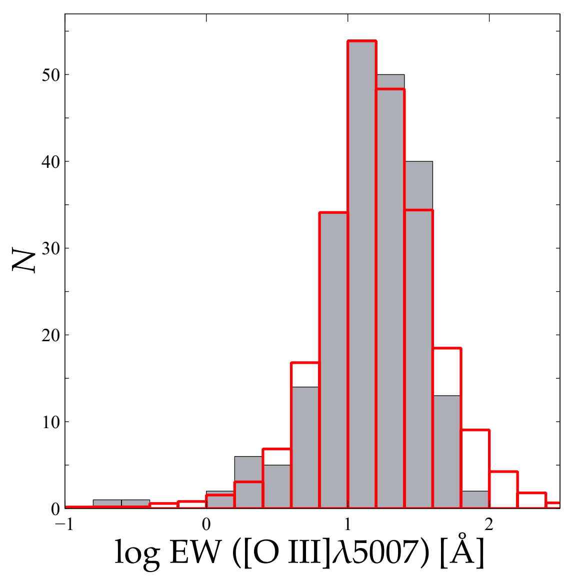

FIGURE 3.3. [O III] λ5007 rest-frame EW distribution of 222 GNIRS-DQS sources (solid gray histogram) and a similar distribution from Shen et al. [90] (red outline; scaled down by a factor of 500). See M21 for additional discussion. We define a threshold of reliability for an [O III] EW measurement at 0.1 Å.

their best-fit models are available electronically at NOIRLab[3].

Quasar	$z_{\rm SDSS}$ ^{a}	J	H	K	Obs. Date	Net Exp.	Comments	BAL	RL
		[mag]	[mag]	[mag]		[s]			
(1)	(2)	(3)	(4)	(5)	(6)	(7)	(8)	(9)	(10)
SDSS J001018.88+280932.5*	1.612	16.56	15.80	15.76	2020 Dec 09	1800	...	...	...
SDSS J003001.11−015743.5	1.582	17.08	15.96	15.76	2020 Sep 09	1800	...	...	...
SDSS J003853.15+333044.3	2.357	16.81	15.98	15.29	2020 Dec 25	1800	...	...	...
SDSS J004613.54+010425.7	2.150	16.44	15.85	15.02	2020 Dec 11	1800	...	1	...
SDSS J004710.48+163106.5	2.165	16.33	15.62	14.90	2020 Dec 11	1800	...	...	...
SDSS J005307.71+191022.7*	1.583	16.72	15.79	15.43	2020 Sep 08	1800	...	...	...
SDSS J020329.86-091020.3*	1.579	17.02	15.97	15.64	2020 Aug 23	900	2	...	...
	...	...	...	...	2020 Sep 11	900	2	...	...
SDSS J073132.18+461347.0*	1.578	16.71	15.83	15.31	2020 Sep 29	1350	...	...	...
SDSS J080117.91+333411.9*	1.598	16.73	15.99	15.79	2020 Oct 05	1350	...	...	...
SDSS J080429.61+113013.9*	2.165	16.64	15.99	15.13	2020 Nov 27	1800	...	...	...
SDSS J080636.81+345048.5*	1.553	16.45	15.88	16.58	2020 Sep 30	1800	...	...	...
SDSS J080707.37+260729.1*	2.312	16.84	15.99	15.53	2020 Sep 30	1800	2	...	...
SDSS J081520.94+323512.9*	1.584	16.90	15.85	15.55	2020 Nov 28	1800	2	...	...
SDSS J084017.87+103428.8	3.330	16.69	16.47	15.27	2015 Apr 23	1720	...	...	...
SDSS J084401.95+050357.9	3.350	15.39	14.93	14.19	2015 Apr 06	800	...	...	...
SDSS J084526.75+550546.8*	1.620	16.33	15.65	15.18	2020 Nov 27	1800	...	...	...
SDSS J091425.72+504854.9*	2.341	17.18	15.98	15.17	2020 Nov 29	1800	...	...	...
SDSS J092942.97+064604.1*	1.608	16.65	15.53	15.28	2020 Nov 30	1800	2	...	...
SDSS J094140.16+325703.2*	3.452	16.55	15.81	15.24	2020 Nov 29	1800	...	...	...
SDSS J094427.27+614424.6*	2.340	16.41	15.61	14.72	2020 Dec 09	1800	...	...	...
SDSS J095047.45+194446.1*	1.575	16.80	15.98	15.62	2020 Dec 12	900	...	...	...
	...	...	...	...	2020 Dec 21	900	...	...	...
SDSS J095555.68+351652.6*	1.616	16.99	15.97	15.85	2020 Dec 09	1800	...	...	...
SDSS J101724.26+333403.3*	1.579	16.49	15.84	15.40	2020 Nov 30	1800	...	...	...
SDSS J111127.43+293319.3*	2.178	16.42	15.88	15.10	2020 Dec 31	1800	2	...	...
SDSS J112726.81+601020.2*	2.159	16.60	15.79	15.40	2020 Dec 31	2250	2	...	...
SDSS J112938.46+440325.0*	2.213	16.99	15.88	15.11	2021 Jan 02	1800	...	...	...
SDSS J113330.17+144758.8*	3.248	16.90	15.88	15.64	2021 Jan 02	1800	...	...	...
SDSS J113924.64+332436.9*	2.314	16.38	15.95	14.85	2020 Dec 09	1800	...	...	...
SDSS J122343.15+503753.4	3.491	15.90	15.57	14.69	2015 Mar 30	1160	...	...	...
SDSS J122938.61+462430.5*	2.152	16.30	15.77	15.19	2020 Nov 30	1800	...	...	...
SDSS J130213.54+084208.6	3.305	16.12	15.64	15.02	2015 Apr 01	1720	2	...	...

[3]https://datalab.noirlab.edu/gnirs_dqs.php

SDSS J131048.17+361557.7	3.420	15.79	15.11	14.38	2015 Apr 05	800	2	...	...
SDSS J132845.00+510225.8	3.411	16.10	15.53	14.77	2015 Apr 05	1160	...	...	...
SDSS J141321.05+092204.8	3.327	16.16	15.63	15.05	2015 Apr 05	1160	...	...	...
SDSS J142123.97+463318.0	3.378	16.28	15.49	14.89	2015 Apr 07	1700	...	...	...
SDSS J142755.85−002951.1	3.362	16.60	15.91	15.27	2015 Apr 01	1720	...	...	...
SDSS J165523.09+184708.4	3.327	16.28	15.88	15.19	2015 Apr 08	1720	...	...	...
SDSS J173352.23+540030.4	3.424	15.87	15.72	14.95	2015 Mar 23	1190	...	...	...
	...	...	...	...	2015 Apr 01	680	...	...	...
SDSS J210558.29−011127.5	1.625	16.61	15.49	15.54	2020 Aug 21	2250	1	...	...
SDSS J211251.06+000808.3*	1.618	16.85	15.89	15.89	2020 Aug 19	1800	1	...	...
SDSS J213655.35−080910.1	1.591	16.96	15.56	15.74	2020 Aug 23	1800	...	...	...
SDSS J220139.99+114140.8*	2.382	16.87	15.76	15.84	2020 Aug 30	1800	1	...	...
SDSS J222310.76+180308.1*	1.602	16.70	15.99	15.60	2020 Sep 01	1800	1	...	...
SDSS J223934.45−004707.2	2.121	16.91	15.97	15.70	2020 Oct 03	1800	1	...	...
SDSS J233304.61−092710.9	2.121	16.17	15.41	14.83	2021 Jan 01	1800	1	...	...
	...	...	...	...	2021 Jan 02	900	...	...	...

TABLE 3.1. [a]Value based on best available measurement in SDSS DR16 ([109]; Table D1, column 27 "Z")

*Denotes object selected from Data Release 16.

Several sources have more than one observation, indicated by an empty source name. All SDSS data taken from DR16.

Comments in Column (8) represent:

[1] At least one exposure did not meet our observation conditions requirements.

[2] Observation failed to provide spectrum of the source due to bad weather, instrument artifacts, or other technical difficulties during the observation.

3.2.2. Improved Spectroscopic Inventory

Tables 3.2 and 3.3 include improved measurements of all spectral features. In particular, they include measurements of the rest-frame optical Fe II emission blend which was fitted for each source in the same manner as in M21; however, each such feature now has a measured EW value and errors, thus effectively removing all the upper limits on the EWs (cf. Table 2 of M21). We fit two Gaussians to each broad emission-line profile to accommodate a possible asymmetry arising from, e.g., absorption, or outflows. We note that the two Gaussian fit per broad emission line is adopted only to characterize the line shape; the two Gaussians do not imply two physically distinct regions. The errors on the spectral measurements were calculated in the same manner as the other uncertainties described in M21, with upper and lower values being derived from a distribution of values recorded during the iterative process of broadening the Fe II template (see M21 for a detailed description of the Fe II blend fitting process).

In addition to the inclusion of 34 new sources, Tables 3.2 and 3.3 contain the most reliable data following remeasurement of each source with additional vetting and visual inspection, particularly with respect to the [O III] and Fe II fitting. These values therefore supersede the corresponding values presented in M21.

Column	Name	Bytes	Format	Units	Description
(1)	(2)	(3)	(4)	(5)	(6)
1	OBJ	(1-24)	A24	...	SDSS object designation
2	ZSYS	(26-30)	F5.3	...	Systemic redshifts
3	LC_MG II	(32-36)	I5	Å	Mg II observed-frame wavelength[a]
4	LC_MG II_UPP	(38-39)	I2	Å	Upper uncertainty for the line peak of Mg II
5	LC_MG II_LOW	(41-42)	I2	Å	Lower uncertainty for the line peak of Mg II
6	FWHM_MG II	(44-47)	I4	km s^{-1}	FWHM of Mg II
7	FWHM_MG II_UPP	(49-52)	I4	km s^{-1}	Upper uncertainty of FWHM of Mg II
8	FWHM_MG II_LOW	(54-57)	I4	km s^{-1}	Lower uncertainty of FWHM of Mg II
9	EW_MG II	(59-60)	I2	Å	Rest-frame EW of Mg II
10	EW_MG II_UPP	(62-63)	I2	Å	Upper uncertainty of EW of Mg II
11	EW_MG II_LOW	(65-66)	I2	Å	Lower uncertainty of EW of Mg II
12	AS_MG II	(68-76)	E9.2	...	Asymmetry of the double Gaussian fit profile of Mg II
13	KURT_MG II	(78-81)	F4.2	...	Kurtosis of the double Gaussian fit profile of Mg II
14	LC_HB	(83-87)	I5	Å	Hβ observed-frame wavelength[a]
15	LC_HB_UPP	(89-90)	I2	Å	Upper uncertainty for the line peak of Hβ
16	LC_HB_LOW	(92-93)	I2	Å	Lower uncertainty for the line peak of Hβ
17	FWHM_HB	(95-99)	I5	km s^{-1}	FWHM of Hβ
18	FWHM_HB_UPP	(101-105)	I5	km s^{-1}	Upper uncertainty of FWHM of Hβ
19	FWHM_HB_LOW	(107-110)	I5	km s^{-1}	Lower uncertainty of FWHM of Hβ
20	EW_HB	(112-114)	I3	Å	Rest-frame EW of Hβ
21	EW_HB_UPP	(116-117)	I2	Å	Upper uncertainty of EW of Hβ
22	EW_HB_LOW	(119-120)	I2	Å	Lower uncertainty of EW of Hβ
23	AS_HB	(122-130)	E9.2	...	Asymmetry of the double Gaussian fit profile of Hβ
24	KURT_HB	(132-135)	F4.2	...	Kurtosis of the double Gaussian fit profile of Hβ
25	LC_O III	(137-141)	I5	Å	[O III] λ5007 observed-frame wavelength[a]

26	LC_O III_UPP	(143-144)	I2	Å	Upper uncertainty for the line peak of [O III] λ5007
27	LC_O III_LOW	(146-147)	I2	Å	Lower uncertainty for the line peak of [O III] λ5007
28	FWHM_O III	(149-152)	I4	km s^{-1}	FWHM of [O III] λ5007
29	FWHM_O III_UPP	(154-157)	I4	km s^{-1}	Upper uncertainty of FWHM of [O III] λ5007
30	FWHM_O III_LOW	(159-162)	I4	km s^{-1}	Lower uncertainty of FWHM of [O III] λ5007
31	EW_O III	(164-171)	E8.2	Å	Rest-frame EW of [O III] λ5007
32	EW_O III_UPP	(173-180)	E8.2	Å	Upper uncertainty of EW of [O III] λ5007
33	EW_O III_LOW	(182-189)	E8.2	Å	Lower uncertainty of EW of [O III] λ5007
34	AS_O III	(191-199)	E9.2	...	Asymmetry of the double Gaussian fit profile of [O III] λ5007
35	KURT_O III	(201-204)	F4.2	...	Kurtosis of the double Gaussian fit profile of [O III] λ5007
36	LC_HA	(206-210)	I5	Å	Hα observed-frame wavelength[a]
37	LC_HA_UPP	(212-213)	I2	Å	Upper uncertainty for the line peak of Hα
38	LC_HA_LOW	(215-216)	I2	Å	Lower uncertainty for the line peak of Hα
39	FWHM_HA	(218-221)	I4	km s^{-1}	FWHM of Hα
40	FWHM_HA_UPP	(223-226)	I4	km s^{-1}	Upper uncertainty of FWHM of Hα
41	FWHM_HA_LOW	(228-231)	I4	km s^{-1}	Lower uncertainty of FWHM of Hα
42	EW_HA	(233-235)	I3	Å	Rest-frame EW of Hα
43	EW_HA_UPP	(237-238)	I2	Å	Upper uncertainty of EW of Hα
44	EW_HA_LOW	(240-241)	I2	Å	Lower uncertainty of EW of Hα
45	AS_HA	(243-251)	E9.2	...	Asymmetry of the double Gaussian fit profile of Hα
46	KURT_HA	(253-256)	F4.2	...	Kurtosis of the double Gaussian fit profile of Hα
47	FWHM_FE II	(258-262)	F5.0	km s^{-1}	FWHM of the kernel Gaussian used to broaden the Fe II template
48	EW_FE II	(264-271)	E8.2	Å	Rest-frame EW of optical band Fe II as defined by [82]
49	EW_FE II_UPP	(273-280)	E8.2	Å	Upper uncertainty of EW of Fe II
50	EW_FE II_LOW	(282-289)	E8.2	Å	Lower uncertainty of EW of Fe II
51	LOGFλ5100	(291-296)	F6.2	erg $s^{-1}cm^{-2}Å^{-1}$	Flux density at rest-frame 5100 Å
52	LOGL5100	(298-302)	F5.2	erg s^{-1}	Monochromatic luminosity at rest-frame 5100 Å

Table 3.2. [a]The emission link peak based on the peak-fit value.

Data formatting used for the catalog. Asymmetry is defined here as the skewness of the Gaussian fits, i.e., a measure of the asymmetry of the distribution about its mean, $s = E(x-\mu)^3/\sigma^3$, where μ is the mean of x, σ is the standard deviation of x, and $E(t)$ is the expectation value. Kurtosis is the quantification of the "tails" of the Gaussian fits defined as $k = E(x-\mu)^4/\sigma^4$. All of the GNIRS spectra and their best-fit models are available electronically at https://datalab.noirlab.edu/gnirs_dqs.php.

Column	Name	Bytes	Format	Units	Description
(1)	(2)	(3)	(4)	(5)	(6)
1	OBJ	(1-24)	A24	...	SDSS object designation
2	LC_HD	(26-30)	F5.0	Å	Hδ observed-frame wavelength[a]
3	LC_HD_UPP	(32-35)	F4.0	Å	Upper uncertainty for the line peak of Hδ
4	LC_HD_LOW	(37-40)	F4.0	Å	Lower uncertainty for the line peak of Hδ
5	FWHM_HD	(42-45)	F4.0	km s^{-1}	FWHM of Hδ
6	FWHM_HD_UPP	(47-49)	F3.0	km s^{-1}	Upper uncertainty of FWHM of Hδ
7	FWHM_HD_LOW	(51-53)	F3.0	km s^{-1}	Lower uncertainty of FWHM of Hδ
8	EW_HD	(55-56)	F2.0	Å	Rest-frame EW of Hδ
9	EW_HD_UPP	(58-59)	F2.0	Å	Upper uncertainty of EW of Hδ
10	EW_HD_LOW	(61-62)	F2.0	Å	Lower uncertainty of EW of Hδ
11	AS_HD	(64-68)	E5.2	...	Asymmetry of the double Gaussian fit profile of Hδ
12	KURT_HD	(70-72)	F3.2	...	Kurtosis of the double Gaussian fit profile of Hδ
13	LC_HG	(74-78)	F5.0	Å	Hγ observed-frame wavelength[a]
14	LC_HG_UPP	(80-83)	F4.0	Å	Upper uncertainty for the line peak of Hγ
15	LC_HG_LOW	(85-88)	F4.0	Å	Lower uncertainty for the line peak of Hγ
16	FWHM_HG	(90-93)	F4.0	km s^{-1}	FWHM of Hγ
17	FWHM_HG_UPP	(95-97)	F3.0	km s^{-1}	Upper uncertainty of FWHM of Hγ
18	FWHM_HG_LOW	(99-101)	F3.0	km s^{-1}	Lower uncertainty of FWHM of Hγ
19	EW_HG	(103-104)	F2.0	Å	Rest-frame EW of Hγ
20	EW_HG_UPP	(106-107)	F2.0	Å	Upper uncertainty of EW of Hγ
21	EW_HG_LOW	(109-110)	F2.0	Å	Lower uncertainty of EW of Hγ
22	AS_HG	(112-116)	E5.2	...	Asymmetry of the double Gaussian fit profile of Hγ
23	KURT_HG	(118-120)	F3.2	...	Kurtosis of the double Gaussian fit profile of Hγ
24	LC_O II[b]	(122-126)	F5.0	Å	[O II] observed-frame wavelength[a]
25	LC_O II_UPP	(128-131)	F4.0	Å	Upper uncertainty for the line peak of [O II]
26	LC_O II_LOW	(133-136)	F4.0	Å	Lower uncertainty for the line peak of [O II]
27	FWHM_O II	(138-141)	F4.0	km s^{-1}	FWHM of [O II]
28	FWHM_O II_UPP	(143-145)	F3.0	km s^{-1}	Upper uncertainty of FWHM of [O II]
29	FWHM_O II_LOW	(147-149)	F3.0	km s^{-1}	Lower uncertainty of FWHM of [O II]
30	EW_O II	(151-152)	F2.0	Å	Rest-frame EW of [O II]
31	EW_O II_UPP	(154-155)	F2.0	Å	Upper uncertainty of EW of [O II]
32	EW_O II_LOW	(157-158)	F2.0	Å	Lower uncertainty of EW of [O II]
33	AS_O II	(160-164)	E5.2	...	Asymmetry of the double Gaussian fit profile of [O II]
34	KURT_O II	(166-168)	F3.2	...	Kurtosis of the double Gaussian fit profile of [O II]
35	LC_NE III[c]	(170-174)	F5.0	Å	[Ne III] observed-frame wavelength[a]
36	LC_NE III_UPP	(176-179)	F4.0	Å	Upper uncertainty for the line peak of [Ne III]

37	LC_NE III_LOW	(181-184)	F4.0	Å	Lower uncertainty for the line peak of [Ne III]
38	FWHM_NE III	(186-189)	F4.0	km s^{-1}	FWHM of [Ne III]
39	FWHM_NE III_UPP	(191-193)	F3.0	km s^{-1}	Upper uncertainty of FWHM of [Ne III]
40	FWHM_NE III_LOW	(195-197)	F3.0	km s^{-1}	Lower uncertainty of FWHM of [Ne III]
41	EW_NE III	(199-200)	F2.0	Å	Rest-frame EW of [Ne III]
42	EW_NE III_UPP	(202-203)	F2.0	Å	Upper uncertainty of EW of [Ne III]
43	EW_NE III_LOW	(205-206)	F2.0	Å	Lower uncertainty of EW of [Ne III]
44	AS_NE III	(208-212)	E5.2	...	Asymmetry of the double Gaussian fit profile of [Ne III]
45	KURT_NE III	(214-216)	F3.2	...	Kurtosis of the double Gaussian fit profile of [Ne III]

TABLE 3.3. [a]The emission link peak based on the peak-fit value.

[b][O II] λ 3727

[c][Ne III] λ 3870

Data formatting used for the supplemental measurements in the supplemental features catalog.

Column (1)	Name (2)	Bytes (3)	Format (4)	Units (5)	Description (6)
1	OBJ	(1-24)	A24	...	SDSS object designation
2	MG II_LAM_PEAK_NARROW	(26-29)	I4	Å	Narrow Mg II peak[a]
3	MG II_STD_NARROW	(31-32)	I2	Å	Narrow Mg II width
4	MG II_F_LAM_NARROW	(34-37)	I4	erg $s^{-1}cm^{-2}Å^{-1}$	Narrow Mg II normalization
5	MG II_LAM_PEAK_BROAD	(39-42)	I4	Å	Broad Mg II peak[a]
6	MG II_STD_BROAD	(44-47)	I4	Å	Broad Mg II width
7	MG II_F_LAM_BROAD	(49-52)	I4	erg $s^{-1}cm^{-2}Å^{-1}$	Broad Mg II normalization
8	O II_LAM_PEAK_NARROW	(54-57)	I4	Å	Narrow [O II] peak[a]
9	O II_STD_NARROW	(59-60)	I2	Å	Narrow [O II] width
10	O II_F_LAM_NARROW	(62-65)	I4	erg $s^{-1}cm^{-2}Å^{-1}$	Narrow [O II] normalization
11	O II_LAM_PEAK_BROAD	(67-70)	I4	Å	Broad [O II] peak[a]
12	O II_STD_BROAD	(72-75)	I4	Å	Broad [O II] width
13	O II_F_LAM_BROAD	(77-78)	I2	erg $s^{-1}cm^{-2}Å^{-1}$	Broad [O II] normalization
14	NE III_LAM_PEAK_NARROW	(80-83)	I4	Å	Narrow [Ne III] peak[a]
15	NE III_STD_NARROW	(85-86)	I2	Å	Narrow [Ne III] width
16	NE III_F_LAM_NARROW	(88-89)	I2	erg $s^{-1}cm^{-2}Å^{-1}$	Narrow [Ne III] normalization
17	NE III_LAM_PEAK_BROAD	(91-94)	I4	Å	Broad [Ne III] peak[a]
18	NE III_STD_BROAD	(96-99)	I4	Å	Broad [Ne III] width
19	NE III_F_LAM_BROAD	(101-102)	I2	erg $s^{-1}cm^{-2}Å^{-1}$	Broad [Ne III] normalization

20	HD_LAM_PEAK_NARROW	(104-107)	I4	Å	Narrow Hδ peak[a]
21	HD_STD_NARROW	(109-110)	I2	Å	Narrow Hδ width
22	HD_F_LAM_NARROW	(112-113)	I2	erg $s^{-1}cm^{-2}Å^{-1}$	Narrow Hδ normalization
23	HD_LAM_PEAK_BROAD	(115-118)	I4	Å	Broad Hδ peak[a]
24	HD_STD_BROAD	(120-123)	I4	Å	Broad Hδ width
25	HD_F_LAM_BROAD	(125-127)	I3	erg $s^{-1}cm^{-2}Å^{-1}$	Broad Hδ normalization
26	HG_LAM_PEAK_NARROW	(129-132)	I4	Å	Narrow Hγ peak[a]
27	HG_STD_NARROW	(134-135)	I2	Å	Narrow Hγ width
28	HG_F_LAM_NARROW	(137-139)	I3	erg $s^{-1}cm^{-2}Å^{-1}$	Narrow Hγ normalization
29	HG_LAM_PEAK_BROAD	(141-144)	I4	Å	Broad Hγ peak[a]
30	HG_STD_BROAD	(146-149)	I4	Å	Broad Hγ width
31	HG_F_LAM_BROAD	(151-153)	I3	erg $s^{-1}cm^{-2}Å^{-1}$	Broad Hγ normalization
32	HB_LAM_PEAK_NARROW	(155-158)	I4	Å	Narrow Hβ peak[a]
33	HB_STD_NARROW	(160-162)	I3	Å	Narrow Hβ width
34	HB_F_LAM_NARROW	(164-166)	I3	erg $s^{-1}cm^{-2}Å^{-1}$	Narrow Hβ normalization
35	HB_LAM_PEAK_BROAD	(168-171)	I4	Å	Narrow Hβ peak[a]
36	HB_STD_BROAD	(173-175)	I3	Å	Broad Hβ width
37	HB_F_LAM_BROAD	(177-179)	I3	erg $s^{-1}cm^{-2}Å^{-1}$	Broad Hβ normalization
38	O III_1_LAM_PEAK_NARROW	(181-184)	I4	Å	Narrow [O III] 4959Å peak[a]
39	O III_1_STD_NARROW	(186-187)	I2	Å	Narrow [O III] 4959Å width
40	O III_1_F_LAM_NARROW	(189-191)	I3	erg $s^{-1}cm^{-2}Å^{-1}$	Narrow [O III] 4959Å normalization
41	O III_1_LAM_PEAK_BROAD	(193-196)	I4	Å	Broad [O III] 4959Å peak[a]
42	O III_1_STD_BROAD	(198-200)	I3	Å	Broad [O III] 4959Å width
43	O III_1_F_LAM_BROAD	(202-204)	I3	erg $s^{-1}cm^{-2}Å^{-1}$	Broad [O III] 4959Å normalization
44	O III_2_LAM_PEAK_NARROW	(206-209)	I4	Å	Narrow [O III] 5007Å peak[a]
45	O III_2_STD_NARROW	(211-212)	I2	Å	Narrow [O III] 5007Å width
46	O III_2_F_LAM_NARROW	(214-216)	I3	erg $s^{-1}cm^{-2}Å^{-1}$	Narrow [O III] 5007Å normalization
47	O III_2_LAM_PEAK_BROAD	(218-221)	I4	Å	Broad [O III] 5007Å peak[a]
48	O III_2_STD_BROAD	(223-225)	I3	Å	Broad [O III] 5007Å width
49	O III_2_F_LAM_BROAD	(227-229)	I3	erg $s^{-1}cm^{-2}Å^{-1}$	Broad [O III] 5007Å normalization
50	HA_LAM_PEAK_NARROW	(231-234)	I4	Å	Narrow Hα peak[a]
51	HA_STD_NARROW	(236-238)	I3	Å	Narrow Hα width
52	HA_F_LAM_NARROW	(240-243)	I4	erg $s^{-1}cm^{-2}Å^{-1}$	Narrow Hα normalization
53	HA_LAM_PEAK_BROAD	(245-248)	I4	Å	Broad Hα peak[a]
54	HA_STD_BROAD	(250-252)	I3	Å	Broad Hα width
55	HA_F_LAM_BROAD	(254-256)	I3	erg $s^{-1}cm^{-2}Å^{-1}$	Broad Hα normalization

Table 3.4. [a]The Gaussian profile peak based on the peak-fit value.

Independent Gaussian feature fit parameters for each emission line that was fit with both a narrow and broad Gaussian profile.

3.2.3. C iv Emission-Line Measurements

M17 and D20 found that the accuracy and precision of a source's UV-based redshift can be significantly improved when regressed against the FWHM and EW of its C iv line as well as the UV continuum luminosity at a rest-frame wavelength of 1350Å (L_{1350}).[4] The C iv emission line has been measured in the SDSS spectrum of each GNIRS-DQS source using the same fitting approach outlined in D20, which closely follows the methods utilized in both M21 and this work; the C iv emission-line properties of all the GNIRS-DQS sources appear in Dix et al. (2023, submitted).

3.3. Correcting UV-Based Redshifts

Our aim is to derive corrections that, on average, shift the velocity offsets of the UV-based redshifts as close as possible to a velocity offset of zero km s^{-1} from z_{sys} based on the [O iii] λ5007 line. We make this correction by applying a regression analysis to a calibration sample of 154 sources from GNIRS-DQS as described below.

The sample used for this analysis is a subset of the augmented GNIRS-DQS sample described in Section 5.2.2. Starting with the 260 GNIRS-DQS sources with useful NIR spectra, we chose to include only the 222 objects with [O iii] rest-frame EW measurements greater than 0.1 Å that can provide the most accurate values of z_{sys} (see Figure 3.3); i.e., 38 sources whose z_{sys} values were based on either Mg ii or Hβ were removed. We then remove 52 broad absorption line (BAL) quasars, as the BAL troughs degrade measurements of the EW and FWHM for C iv [116, 23]. These two parameters are of primary importance for our regression analysis. We also remove 17 radio-loud (RL) quasars (having $R > 100$; see

[4]Objects with redshifts $z < 1.65$ had L_{1350} extrapolated from L_{3000} assuming a continuum power-law of the form $f_\nu \propto \nu^{0.5}$ [24].

Figure 3.2) (one of which, SDSS J114705.24+083900.6, is also classified as a BAL quasar) due to potential continuum boosting, which may affect both EW (C IV) and L_{1350} measurements [117].

Finally, two additional sources, SDSS J073132.18+461347.0, and SDSS J141617.38+264906.1, were excluded due to the inability to measure the C IV line reliably (see Dix et al., 2023, submitted). The result of this selection process is a calibration sample of 154 objects, presented in Table 3.5, which is a representative sample of optically selected quasars (see Section 5.2.2) used to derive prescriptions for correcting UV-based redshifts through linear regression analysis.

Quasar	$z_{\rm sys}$ [a]	$z_{\rm C\,IV}$ [b]	Δv_i (km s^{-1})	$z_{\rm HW10}$ [c]	Δv_i (km s^{-1})	$z_{\rm Pipe}$ [d]	Δv_i (km s^{-1})
SDSS J001018.88+280932.5	1.613	1.611	-230	...	...	1.612	-110
SDSS J001453.20+091217.6	2.335	2.326	-770	2.344	820	2.308	-2360
SDSS J001813.30+361058.6	2.324	2.303	-1880	...	...	2.316	-720
SDSS J001914.46+155555.9	2.267	2.263	-370	2.276	830	2.271	350
SDSS J002634.46+274015.5	2.247	2.243	-340	2.247	50	2.267	1850
SDSS J003001.11-015743.5	1.59	1.579	-1260	1.59	-40	1.582	-950
SDSS J003416.61+002241.1	1.63	1.626	-500	1.63	10	1.627	-350
SDSS J003853.15+333044.3	2.361	2.365	360	...	...	2.357	-350
SDSS J004710.48+163106.5	2.184	2.162	-2060	...	...	2.165	-1780
SDSS J004719.71+014813.9	1.591	1.588	-340	1.59	-130	1.59	-50
SDSS J005233.67+014040.8	2.309	2.295	-1250	2.305	-370	2.291	-1620
SDSS J005307.71+191022.7	1.598	1.581	-1940	1.585	-1460	1.583	-1680
SDSS J010113.72+032427.0	1.579	1.577	-270	1.577	-280	1.579	0
SDSS J010500.72+194230.4	2.323	2.293	-2660	...	...	2.288	-3140
SDSS J010615.93+101043.0	2.353	2.33	-2070	2.35	-330	2.335	-1600
SDSS J010643.23-031536.4	2.248	2.232	-1480	2.249	40	2.242	-570
SDSS J011538.72+242446.0	2.401	2.369	-2810	2.39	-1010	2.374	-2370
SDSS J013113.25+085245.5	3.537	3.529	-550	3.538	10	3.542	300
SDSS J013136.44+130331.0	1.599	1.579	-2260	1.597	-240	1.594	-490
SDSS J013647.96-062753.6	3.288	3.239	-3430	3.311	1620	3.265	-1640
SDSS J014128.26+070606.1	2.262	2.256	-580	...	...	2.262	0
SDSS J014932.06+152754.0	2.384	2.384	40	...	...	2.39	540
SDSS J020329.86-091020.3	1.582	1.574	-930	...	...	1.579	-310
SDSS J021259.21+132618.8	1.617	1.613	-500	1.627	1050	1.623	650

SDSS J035150.97-061326.4	2.223	2.22	-300	2.228	440	2.22	-320
SDSS J072928.48+252451.8	2.311	2.304	-650	2.309	-230	2.308	-280
SDSS J073900.90+485159.0	1.627	1.611	-1850	1.621	-750	1.618	-1110
SDSS J073913.65+461858.5	1.574	1.577	320	1.587	1480	1.581	790
SDSS J074941.16+262715.9	1.594	1.585	-980	1.594	10	1.588	-640
SDSS J075136.36+432732.4	2.249	2.227	-2050	2.244	-510	2.232	-1570
SDSS J075405.08+280339.6	2.271	2.274	280	2.277	590	2.276	480
SDSS J075547.83+220450.1	2.314	2.315	100	2.329	1340	2.312	-150
SDSS J080117.91+333411.9	1.602	1.596	-630	1.598	-440	1.602	20
SDSS J080413.66+251633.9	2.301	2.298	-300	...	...	2.295	-610
SDSS J081019.48+095040.9	2.236	2.213	-2130	2.23	-590	2.212	-2260
SDSS J081056.96+120914.8	2.251	2.26	820	2.267	1460	2.262	1010
SDSS J081127.44+461812.9	2.237	2.243	590	2.263	2440	2.242	530
SDSS J081410.76+443706.9	2.274	2.266	-700	2.282	720	2.274	-10
SDSS J081558.35+154055.2	2.235	2.228	-620	2.238	270	2.232	-260
SDSS J081940.58+082357.9	3.204	3.193	-780	3.207	230	3.2	-270
SDSS J082507.67+360411.1	1.582	1.576	-700	1.582	30	1.579	-370
SDSS J082603.32+342800.6	2.306	2.296	-930	2.312	510	2.283	-2130
SDSS J082644.66+163549.0	2.188	2.188	30	2.194	620	2.189	120
SDSS J082736.89+061812.1	2.191	2.193	220	2.203	1190	2.195	440
SDSS J083417.12+354833.1	2.162	2.153	-820	2.166	370	2.153	-780
SDSS J084017.87+103428.8	3.333	3.328	-370	3.333	0	3.33	-210
SDSS J084029.97+465113.7	1.574	1.569	-580	1.578	460	1.572	-290
SDSS J084526.75+550546.8	1.616	1.614	-210	1.62	530	1.618	200
SDSS J084846.11+611234.6	2.259	2.256	-300	2.262	220	2.257	-210
SDSS J085344.17+354104.5	2.183	2.161	-2080	2.19	660	...	...
SDSS J085443.10+075223.2	1.612	1.599	-1460	1.607	-570	1.603	-960
SDSS J085856.00+015219.4	2.169	2.144	-2390	2.168	-150	2.159	-950
SDSS J085946.79+603702.1	2.279	2.259	-1800	...	...	2.264	-1320
SDSS J090247.57+304120.7	1.562	1.56	-170	1.562	70	0.064	-146280
SDSS J090646.98+174046.8	1.581	1.567	-1620	1.579	-290	1.574	-860
SDSS J090709.89+250620.8	3.316	3.304	-830	3.317	100	3.281	-2450
SDSS J090710.36+430000.2	2.193	2.181	-1160	2.197	300	2.188	-470
SDSS J091941.26+253537.7	2.266	2.263	-240	2.268	250	2.267	110
SDSS J092216.04+160526.4	2.371	2.369	-170	2.382	980	2.373	180
SDSS J092325.25+453222.2	3.473	3.441	-2120	3.459	-940	3.453	-1350
SDSS J092456.66+305354.7	3.448	3.429	-1280	3.447	-80	3.457	580
SDSS J092523.24+214119.8	2.361	2.358	-230	2.362	120	2.364	300
SDSS J092555.05+490338.2	2.34	2.334	-560	2.345	440	2.344	360

SDSS J093533.88+235720.5	2.304	2.295	-810	2.306	200	2.296	-750
SDSS J094140.16+325703.2	3.449	3.401	-3180	3.454	370	3.453	310
SDSS J094214.40+034100.3	1.581	1.583	240	1.584	350	1.583	280
SDSS J094347.02+690818.4	1.599	1.588	-1270	1.591	-970	1.593	-740
SDSS J094602.31+274407.0	2.488	2.383	-8910	2.383	-8930	2.408	-6830
SDSS J094637.83-012411.5	2.215	2.214	-50	2.219	410	2.212	-200
SDSS J094648.59+171827.7	2.298	2.294	-350	2.303	440	2.294	-400
SDSS J095047.45+194446.1	1.573	1.571	-260	1.575	160	1.582	1040
SDSS J095058.76+263424.6	2.404	2.371	-2860	2.392	-1020	2.387	-1460
SDSS J095544.25+182546.9	3.485	3.476	-570	3.494	620	3.482	-170
SDSS J095555.68+351652.6	1.616	1.617	70	1.617	20	1.617	120
SDSS J095707.82+184739.9	2.37	2.324	-4040	2.364	-550	2.385	1380
SDSS J095852.19+120245.0	3.307	3.297	-720	3.309	100	3.275	-2270
SDSS J100212.63+520800.2	1.619	1.611	-860	1.618	-50	1.614	-500
SDSS J100850.06-023831.6	2.272	2.255	-1550	...	...	2.259	-1160
SDSS J101106.74+114759.4	2.249	2.244	-420	2.254	470	2.245	-320
SDSS J101425.11+032003.7	2.165	2.142	-2190	2.156	-880	2.148	-1620
SDSS J101429.57+481938.4	1.569	1.554	-1710	1.569	60	1.562	-800
SDSS J101724.26+333403.3	1.579	1.572	-780	1.579	30	1.574	-520
SDSS J102537.69+211509.1	2.255	2.25	-420	2.248	-640	2.247	-720
SDSS J102731.49+541809.7	1.59	1.587	-290	1.594	460	1.592	270
SDSS J102907.09+651024.6	2.17	2.155	-1420	2.171	120	2.162	-760
SDSS J103209.78+385630.5	1.581	1.584	360	1.596	1720	1.59	1110
SDSS J103236.98+230554.1	2.378	2.376	-140	2.382	400	2.38	180
SDSS J104018.51+572448.1	3.411	3.395	-1080	3.413	110	3.411	0
SDSS J104330.09+441051.5	2.216	2.201	-1430	2.212	-460	2.206	-1010
SDSS J104336.73+494707.6	2.195	2.177	-1650	2.197	270	2.194	-90
SDSS J104716.50+360654.0	2.29	2.289	-120	2.294	290	2.291	70
SDSS J104743.57+661830.5	2.166	2.162	-370	2.168	230	2.171	460
SDSS J104911.34+495113.6	1.606	1.605	-110	1.607	120	1.606	-40
SDSS J105045.72+544719.2	2.173	2.163	-940	2.174	90	2.169	-370
SDSS J105902.04+580848.6	2.248	2.238	-920	2.253	460	2.246	-140
SDSS J105926.43+062227.4	2.198	2.195	-250	2.205	660	2.193	-480
SDSS J110516.68+200013.7	2.357	2.355	-140	2.364	660	2.361	400
SDSS J110735.58+642008.6	2.325	2.304	-1850	2.323	-100	2.307	-1580
SDSS J110810.87+014140.7	1.605	1.616	1260	1.618	1430	1.614	1010
SDSS J111119.10+133603.8	3.478	3.464	-910	3.486	580	3.227	-16330
SDSS J112726.81+601020.2	2.162	2.142	-1850	2.159	-270	2.146	-1440
SDSS J113621.05+005021.2	3.428	3.42	-540	3.434	410	3.43	120

SDSS J114212.25+233250.5	1.594	1.582	-1350	1.6	720	1.592	-220
SDSS J114350.30+362911.3	2.352	2.349	-290	2.358	550	2.341	-970
SDSS J114902.70+144328.0	2.204	2.187	-1630	2.192	-1130	2.2	-400
SDSS J114907.15+004104.3	2.301	2.29	-1010	2.307	520	2.29	-980
SDSS J121314.03+080703.6	2.391	2.362	-2530	2.371	-1740	2.31	-7050
SDSS J121519.42+424851.0	2.311	2.307	-330	2.317	600	2.314	300
SDSS J121810.98+241410.9	2.38	2.366	-1260	2.382	180	2.375	-440
SDSS J122938.61+462430.5	2.145	2.146	90	2.157	1160	2.152	640
SDSS J123514.64+462904.0	2.208	2.198	-910	2.207	-110	2.203	-420
SDSS J125150.45+114340.7	2.209	2.188	-1960	2.202	-680	2.191	-1630
SDSS J125159.90+500203.6	2.378	2.365	-1170	2.384	500	2.377	-130
SDSS J132845.00+510225.8	3.403	3.4	-200	3.408	340	3.411	540
SDSS J134341.99+255652.9	1.601	1.601	60	1.604	360	1.613	1490
SDSS J135908.35+305830.8	2.316	2.259	-5150	2.287	-2650	2.266	-4490
SDSS J140704.43+273556.6	2.22	2.209	-1000	2.224	360	2.216	-320
SDSS J141028.14+135950.2	2.216	2.201	-1350	2.216	80	2.205	-1010
SDSS J141925.48+074953.5	2.391	2.37	-1870	2.39	-110	2.384	-660
SDSS J141951.84+470901.3	2.311	2.277	-3030	2.29	-1830	2.276	-3100
SDSS J142435.97+421030.4	2.212	2.209	-250	2.224	1200	2.212	70
SDSS J142502.62+274912.2	2.346	2.346	0	2.35	330	2.344	-200
SDSS J142543.32+540619.3	3.261	3.25	-760	3.263	120	3.241	-1400
SDSS J142755.85-002951.1	3.365	3.375	640	...	...	3.357	-580
SDSS J142903.03-014519.3	3.42	3.392	-1890	3.425	370	3.432	810
SDSS J144624.29+173128.8	2.209	2.198	-1060	2.2	-870	2.194	-1460
SDSS J144706.81+212839.2	3.224	3.202	-1550	3.225	50	3.218	-400
SDSS J144948.62+123047.4	1.592	1.588	-460	1.588	-450	1.596	500
SDSS J145541.11-023751.0	1.612	1.609	-330	1.616	510	1.613	120
SDSS J150743.71+220928.8	3.23	3.224	-410	3.247	1220	3.236	440
SDSS J151507.82+612411.9	2.182	2.176	-560	2.187	510	2.182	10
SDSS J151727.68+133358.6	2.236	2.221	-1350	2.238	180	2.234	-180
SDSS J151733.09+435648.4	2.204	2.179	-2330	2.189	-1440	2.182	-2080
SDSS J152929.55+230208.7	1.581	1.576	-580	1.584	410	1.581	-30
SDSS J155355.10+375844.1	2.364	2.346	-1560	2.369	500	2.353	-940
SDSS J160029.86+331806.9	1.594	1.587	-750	1.593	-110	1.594	80
SDSS J160637.57+173516.2	2.331	2.31	-1880	2.322	-800	2.311	-1790
SDSS J161435.70+372715.6	1.599	1.597	-280	1.603	390	1.601	160
SDSS J162659.24+301535.0	1.58	1.58	0	1.579	-100	1.579	-130
SDSS J163433.42+265158.2	1.569	1.565	-490	1.575	700	1.572	280
SDSS J164807.55+254407.1	2.195	2.194	-130	2.203	710	2.196	60

SDSS J173352.23+540030.4	3.429	3.421	-560	3.435	420	3.425	-310
SDSS J210558.29-011127.5	1.637	1.614	-2630	1.624	-1520	1.62	-1970
SDSS J213655.35-080910.1	1.596	1.575	-2460	1.59	-750	1.592	-460
SDSS J214901.21-073141.6	2.203	2.198	-460	2.212	800	2.215	1170
SDSS J220139.99+114140.8	2.372	2.35	-1970	2.378	550	2.382	890
SDSS J222310.76+180308.1	1.604	1.596	-860	1.606	230	1.602	-170
SDSS J222621.45+251545.0	2.391	2.377	-1210	2.39	-20	2.385	-530
SDSS J225627.12+092313.3	2.293	2.281	-1110	2.296	220	2.273	-1790
SDSS J230722.21+253803.8	1.597	1.591	-640	1.595	-190	1.594	-240
SDSS J231450.12+182402.8	2.284	2.279	-450	2.291	610	2.284	-40
SDSS J233304.61-092710.9	2.12	2.113	-660	2.125	530	2.121	120
SDSS J233344.66+290251.5	3.233	3.183	-3510	3.203	-2070	3.187	-3200
SDSS J234817.55+193345.8	2.202	2.179	-2140	2.194	-730	2.154	-4440

TABLE 3.5. [a]Redshifts determined from the [O III] $\lambda_{\rm peak}$ as described in M21.
[b]Redshifts determined from the C IV $\lambda_{\rm peak}$ values given in Dix et al. (2023, submitted).
[c]Acquired from HW10 and/or from P. Hewett, priv. comm.
[d]Acquired from Lyke et al. (2020; [109]).

The redshift corrections are performed on redshifts obtained from three separate techniques: 1) measurements of the observed-frame wavelength of the peak of the C IV emission line, 2) HW10 redshifts (P. Hewett, priv. comm.), and 3) SDSS Pipeline redshifts (Table D1, column 29 "Z_PIPE", [111]). The HW10 redshifts are notable as they already have a primary redshift correction applied.

The principal metric under investigation in this work is the initial velocity offset (Δv_i) between each of the aforementioned three UV-based redshifts ($z_{\rm meas}$) and the $z_{\rm sys}$ value of a source determined from its [O III] λ5007 emission line by measuring the line peak in each spectra, which is presented in Table 3.2. This offset is computed using the following equation (see D20):

(1) $$\Delta v_i = c\left(\frac{z_{\rm meas} - z_{\rm sys}}{1 + z_{\rm sys}}\right).$$

These initial velocity offset values are presented in Table 3.5 and are shown in the top panels of Figure 3.4.

As shown in Table 3.5, there are three sources, SDSS J085344.17+354104.5, SDSS J090247.57+304120.7 and SDSS J111119.10+133603.8, where the SDSS Pipeline fails to produce reliable redshifts, resulting in either no produced redshift for the first of these, or unrealistically high velocity offsets of $|\Delta v_i| > 16000$ km s^{-1} for the latter two, while the velocity offsets for these two sources from the C IV and HW10 methods yield values that are only -170 and $+70$ km s^{-1}, and -910 and $+580$ km s^{-1}, respectively. As a result, these three sources are excluded from the SDSS Pipeline analysis, but are retained in the C IV and HW10 analyses.

The regression analysis follows the methods used by M17 and D20, where the correction to the velocity offset depends on the C IV emission-line properties and UV continuum luminosity such that:

$$\begin{aligned}(2)\quad \Delta v_{\rm corr}\ ({\rm km\ s^{-1}}) = {} & \alpha \log_{10}{\rm FWHM}_{\rm CIV}\ ({\rm km\ s^{-1}}) \\ & + \ \beta \log_{10}{\rm EW}_{\rm CIV}\ (\text{Å}) \\ & + \ \gamma \log_{10} L_{1350}\ (10^{-17}\ {\rm erg\ s^{-1}}\text{Å}^{-1})\end{aligned}$$

where $\Delta v_{\rm corr}$ is the velocity offset we subtract from the initial velocity offset calculated using Equation 1. The final, post-correction velocity offset, $\Delta v_f = \Delta v_i - \Delta v_{\rm corr}$, is displayed in the bottom panels of Figure 3.4. Since we fit the observed values of Δv_i to the model shown in Equation 2 and solved for the best fit coefficients, then, by definition, the mean (μ) of $\Delta v_i - \Delta v_{corr}$ is zero. This $\Delta v_{\rm corr}$ value is used to obtain a revised $z_{\rm sys}$ prediction by adjusting the initially measured redshift of a quasar. From Equation 1, solving for $z_{\rm meas}$, and substituting $z_{\rm meas} = z_{\rm sys}$ and $v_{\rm corr} = v_i$, we get

$$z_{\mathrm{rev}} = z_{\mathrm{meas}} + \frac{\Delta v_{\mathrm{corr}}(1 + z_{\mathrm{meas}})}{c} \tag{3}$$

where z_{rev} is the revised, more accurate, and more precise redshift.

Starting with our 154-object calibration sample, we run linear regressions using the three parameters defined in Equation 2. The results of this linear regression analysis provide the Δv_{corr} values from Equation 2 that are subtracted from the initial velocity offsets of the objects (from Table 3.5).

Distributions of the Δv_i and Δv_f values are plotted in the top and bottom panels in Figure 3.4, respectively. We see that the C IV-based Δv_i values are skewed toward negative values (blueshift) with a mean velocity offset of $\mu = -1034$ km s^{-1}, and a standard deviation of $\sigma = 1173$ km s^{-1}. The SDSS Pipeline-based Δv_i values have a considerably smaller negative initial velocity offset of $\mu = -564$ km s^{-1}, yet a larger standard deviation of $\sigma = 1268$ km s^{-1}. As expected, the HW10-based Δv_i values show a mean initial velocity offset much closer to zero ($\mu = 54$ km s^{-1}), however the standard deviation is only slightly smaller than that of the C IV-based Δv_i values ($\sigma = 1038$ km s^{-1}). Despite the improvements demonstrated by the HW10-based values, we are able to use our regression analysis to improve on UV-based redshift determinations further, as shown below.

As explained above, our redshift corrections yield mean Δv_f values of zero km s^{-1} using all three UV-based methods (see the bottom panels of Figure 3.4). The standard deviation of the Δv_f values, on the other hand, indicated by the standard deviation, σ, are reduced by $\sim 17\%$, $\sim 3\%$, and $\sim 5\%$ for the C IV, HW10, and SDSS Pipeline methods, respectively, with respect to the measured Δv_i values. The median velocity offsets are also reduced significantly for all three methods. The linear regression coefficients (Equation 2) used to achieve these corrections are presented in Table 3.6. Table 3.6 also gives the t-Value [118] for confidence statistics in determining the importance of each parameter (see also D20), where t-Values of $|t| \gtrsim 2$ denote a strong correlation, with decreasing confidence as $t \rightarrow 0$.

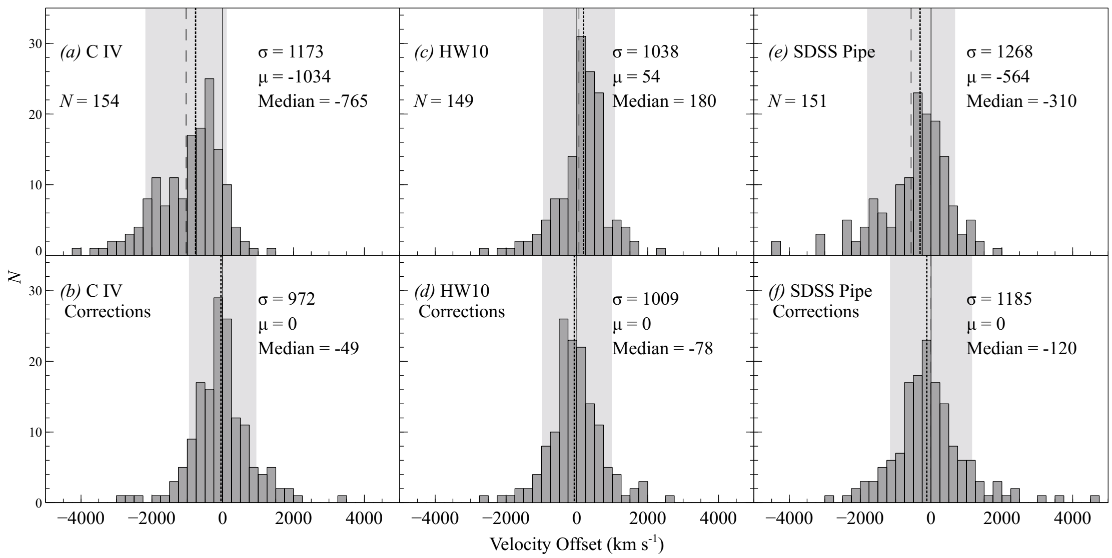

FIGURE 3.4. Velocity offsets relative to z_{sys} before (panels *a*, *c*, and *e*) and after (panels *b*, *d*, and *f*) the corrections using the linear regression coefficients given in Table 3.6. The standard deviation (shaded region), mean (dashed line), median (dotted line), and zero velocity offset (solid line) are marked in each panel. SDSS J090247.57+304120.7 and SDSS J111119.10+133603.8 do not appear on the SDSS Pipe panels because of their unreliable redshifts, and SDSS J085344.17+354104.5 does not appear as it lacks an SDSS Pipeline redshift.

UV-Based Redshift Method	Sample Size	Regression Coefficients	Value	Error	t-Value
C IV	154	α	-3268	537	-6.08
		β	1356	356	3.80
		γ	196	47	4.18
HW10	149	α	-1043	592	-1.76
		β	385	298	1.95
		γ	61	51	1.20
SDSS Pipe	151	α	-1696	661	-2.57
		β	452	461	3.17
		γ	79	57	1.37

Residuals of the 154 source sample both before and after our corrections are applied are presented in Figure 3.5. The residual distributions show the substantial reduction in the velocity offsets before and after each correction. The corrected velocity offsets for both the C IV and HW10-based methods are closer to zero than the corrected velocity offsets for the

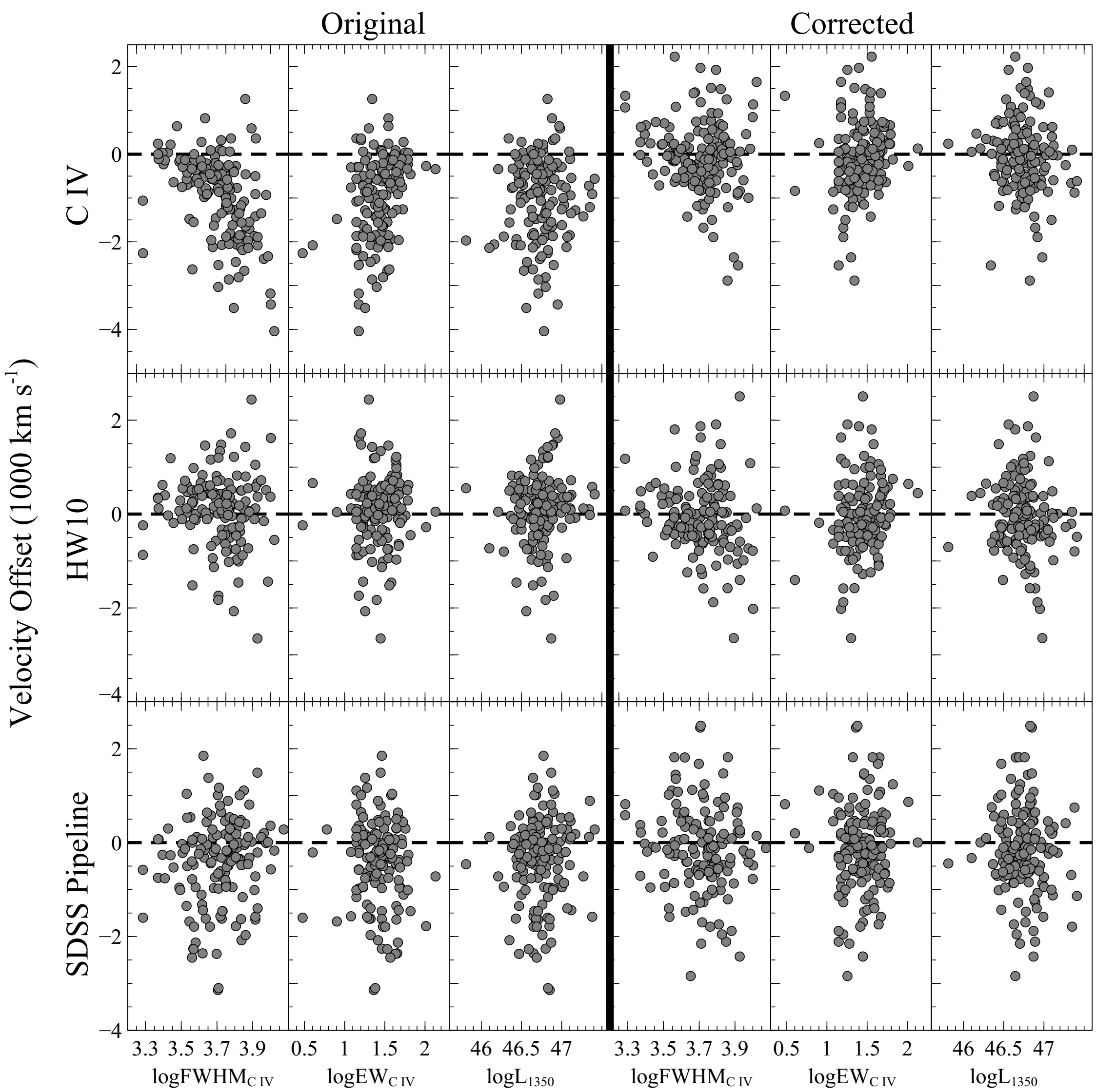

FIGURE 3.5. Residual velocity offsets with respect to z_{sys} before (three leftmost columns), and after (three rightmost columns), corrections are applied (see Equation 2) against our regression parameters. The outliers discussed in Section 5.2 do not appear in this plot.

offsets). Values of this magnitude, while high, are not unexpected due to the kinematics associated with luminous, rapidly accreting quasars that can directly affect the C IV emission line and cause large blueshifts [119, 120, 121]. Nevertheless, our method tends to correct even these large velocity offsets to more reasonable values as shown in Figures 3.4 and 3.6.

The results of our regression analysis, presented in Table 3.6, provide considerably

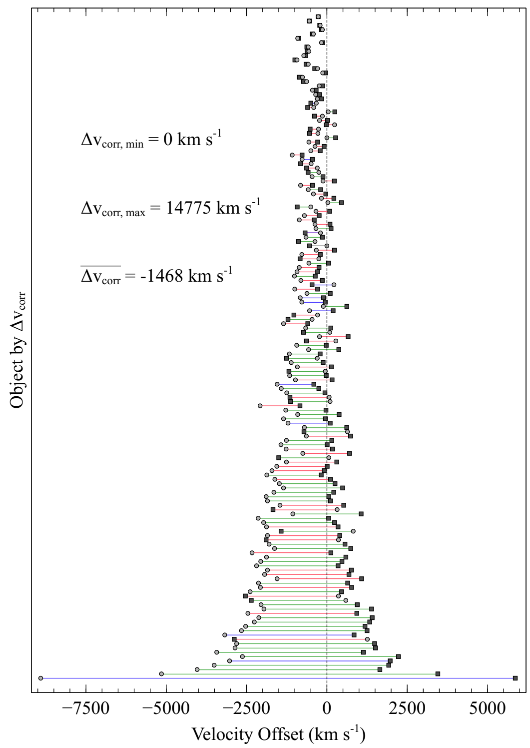

FIGURE 3.6. Initial velocity offsets (Δv_i; circles) compared to final velocity offsets (Δv_f; squares) for C IV-based redshifts of the calibration sample of 154 sources. The lines connecting the initial and final velocity offsets are sorted from top to bottom by the absolute value of the velocity offset correction ($|\Delta v_{\mathrm{corr}}|$), where the lines are color coded with respect to the monochromatic luminosity at rest-frame 5100 Å as such: $46.08 < \log(L_{5100}) < 46.41$, $46.42 < \log(L_{5100}) < 46.74$, and $46.75 < \log(L_{5100}) < 47.09$ are marked in red, green, and blue, respectively. While the majority of the Δv_i values, which are blueshifts, produce Δv_f values with the opposite sign, we also see Δv_i values which are redshifts that end up as blueshifts; however the overall effect of our regression analysis brings Δv_f values closer to zero. We find no trend between $|\Delta v_{\mathrm{corr}}|$ and the monochromatic luminosity at rest-frame 5100 Å.

improved redshifts over the regression coefficients used by D20. When we employ the D20 regression coefficients on our calibration sample of 154 sources, we obtain standard deviations on the distributions of Δv_f which are $\sim 8\%$ larger for the HW10 method, $\sim 31\%$ larger for

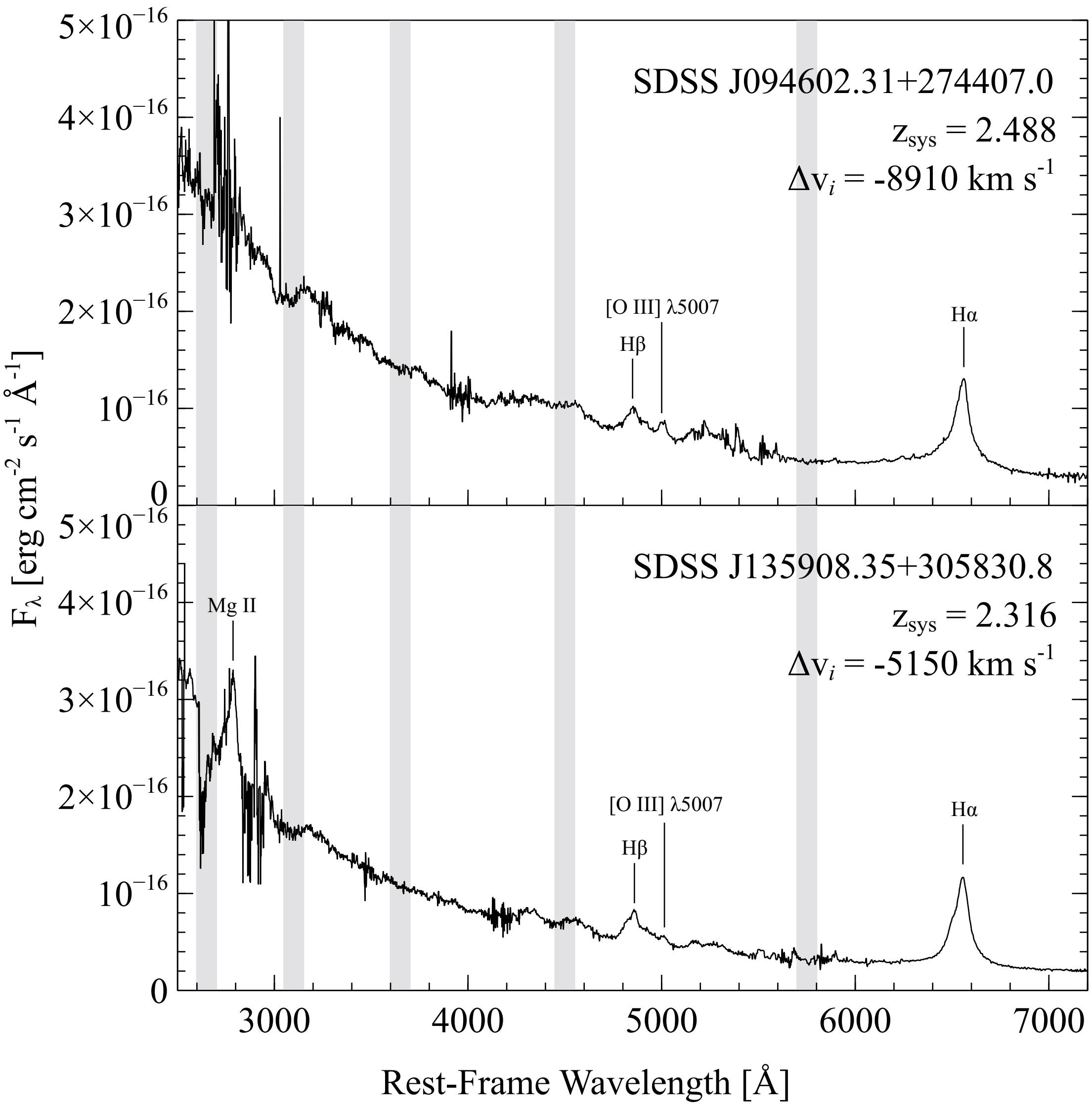

Figure 3.7. GNIRS-DQS spectra of SDSS J094602.31+274407.0 (top) and SDSS J135908.35+305830.8 (bottom). These two objects display the largest velocity offsets (C iv vs. [O iii]) in the 154 object calibration sample, with $\Delta v_i = -8910$ and $\Delta v_i = -5150$, respectively. For the GNIRS-DQS sample, we elected to fit Gaussians to residual spectral features after subtracting a localized linear continuum and a convolved Fe ii template (see M21 for further discussion).

the SDSS Pipeline method, and $\sim 2\%$ larger for the C IV-based redshifts than when using the coefficients from Table 3.6.

In summary, considering the four basic observables associated with the C IV emission line, one can derive the most accurate and precise prediction of the systemic redshift of a quasar.

3.3.1. Redshift and Luminosity Dependence

Typically, redshifts are determined either spectroscopically or photometrically from multiple features (i.e., HW10 and the SDSS Pipeline). When some of these features are no longer available in the spectra, our ability to determine the redshift is affected, and it is plausible that the initial velocity offsets depend also on source redshift. We search for such a dependence in our data by splitting our calibration sample into three redshift bins: $1.55 \lesssim z \lesssim 1.65$ (Bin 1), $2.10 \lesssim z \lesssim 2.40$ (Bin 2), and $3.20 \lesssim z \lesssim 3.50$ (Bin 3), which contain 43, 90, and 21 sources, respectively. These intervals ensure coverage of the [O III] $\lambda5007$ emission line in the J, H, or K bands (see Section 5.2.2).

We perform the regression analysis as described in Section 5.2 on each redshift bin separately. The results are presented in Table 3.7, and shown in Figure 3.8. The standard deviation (σ) of the velocity offsets has been reduced by factors of up to $\sim 32\%$ across all redshift bins compared with the respective standard deviations for the bulk sample. For the C IV-based method, the smallest improvement is in Bin 1 ($\sim 2\%$), compared to improvements of $\sim 22\%$ in Bin 2 and $\sim 32\%$ in Bin 3. This trend appears to follow the increase in the average Δv_i in each of those bins ($\mu = -703$ km s^{-1}, $\mu = -1161$ km s^{-1}, and $\mu = -1171$ km s^{-1}, respectively). Although the statistics in Bin 3 are limited, this trend may follow from the fact that the highest redshift bin tends to have higher luminosity quasars, which results in larger C IV blueshifts (e.g., due to outflows or winds) on average for more distant sources [86]. Since our regression analysis relies heavily on the C IV parameter space, it is not unexpected that our corrections to the C IV-based redshifts would be more important for the more powerful sources found preferentially at higher redshifts. It is therefore imperative to obtain rest-frame UV-optical spectra of as many quasars at the highest possible redshifts for

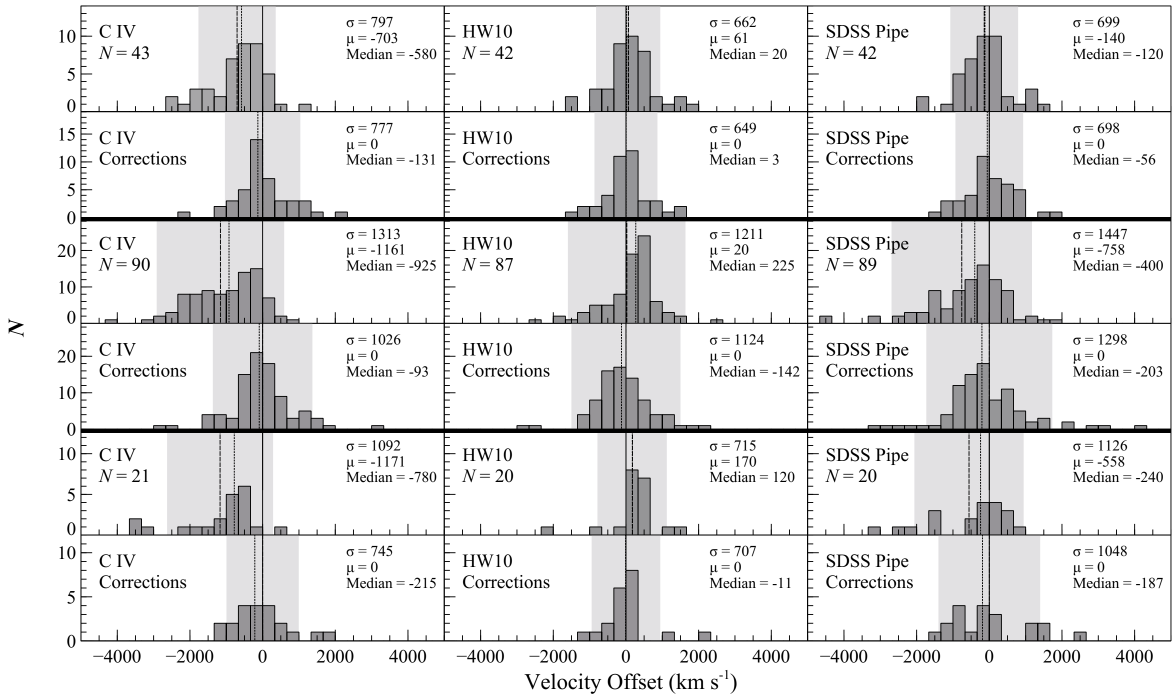

FIGURE 3.8. Same as Figure 3.4, but split into three redshift bins. Top six panels, middle six panels, and bottom six panels correspond to redshift Bin 1, Bin 2, and Bin 3, respectively, as described in the text.

this type of analysis.

Concerning the HW10-based method, our corrections produce improvements in standard deviation ranging from $\sim 2\%$ to $\sim 10\%$, with no apparent trend with redshift. Therefore, it seems that these improvements are not very sensitive to the coverage of the Mg II line, which is absent from Bin 3. This result may be indicative of the overall robustness of the HW10 method, as found from the entire sample (see Section 5.2 and Figure 3.4). Mild improvements, and no significant redshift dependence, are observed for the SDSS Pipeline method, and the overall standard deviations of velocity offset distributions stemming from this method remain high (> 1000 km s^{-1}) in Bins 2 and 3.

UV-Based Redshift Method	Redshift Bin[a]	Regression Coefficients	Value	Error	t-Value	Number of Sources
		α	-545	809	-0.67	
	1	β	611	475	1.29	43

		γ	9	66	0.13	
		α	-3976	758	-5.24	
C IV	2	β	1726	527	3.27	90
		γ	239	67	3.54	
		α	-5439	1474	-3.69	
	3	β	47	1078	0.04	21
		γ	239	138	2.95	
		α	494	710	0.81	
	1	β	-606	371	-1.55	42
		γ	-22	54	-0.39	
		α	-1831	942	-2.11	
HW10	2	β	1680	558	2.90	87
		γ	92	80	1.23	
		α	1721	1424	1.01	
	3	β	946	1100	0.86	20
		γ	-137	144	-1.10	
		α	108	741	0.15	
	1	β	-166	431	-0.38	42
		γ	-6	60	-0.11	
		α	-2310	959	-2.41	
SDSS Pipe	2	β	1943	668	2.91	89
		γ	108	85	1.27	
		α	2086	2114	0.99	
	3	β	2459	1520	1.62	20
		γ	-250	197	-1.27	

TABLE 3.7. [a]Bins 1, 2, and 3 correspond to redshift ranges of $1.55 \lesssim z \lesssim 1.65$, $2.10 \lesssim z \lesssim 2.40$, and $3.20 \lesssim z \lesssim 3.50$.

In general, the greatest limitation in our ability to search for a redshift dependence is the disparity in the number of sources in each bin. Predictably, Bin 2 yields results that are closer to those obtained for the entire sample, as $\sim 58\%$ of that sample is contained within that bin. A significantly larger sample size, particularly in Bin 3 ($z \sim 3$), may allow for a more definitive conclusion in this matter. This highest redshift bin is particularly important given the absence of the Mg II lines from the optical spectrum, and the need to reliably estimate redshifts of more distant sources.

In addition to exploring a possible redshift dependence, we also look to see if our ability to predict a quasar's $z_{\rm sys}$ value depends on source luminosity. We trisect the calibration sample into three equal L_{5100} bins: $46.08 - 46.41$, $46.42 - 46.74$, and $46.75 - 47.09$, and look for any significant statistical deviations with respect to the entire sample. The results are shown in Figure 3.6. We see that there appears to be no clear dependence on source luminosity. A possible explanation for this result is that our sample is flux limited, and therefore it is difficult to disentangle the strong redshift-luminosity dependence.

3.4. Summary and Conclusions

We present an augmented catalog of spectroscopic properties obtained from NIR observations of a uniform, flux-limited sample of 260 SDSS quasars at $1.55 \lesssim z \lesssim 3.50$. This catalog includes basic spectral properties of rest-frame optical emission lines, chiefly the Mg II, Hβ, [O III], Fe II, and Hα lines, depending on the availability of the line in the spectrum. These measurements provide an enhancement to the existing GNIRS-DQS database enabling one to more accurately analyze and investigate rest-frame UV-optical spectral properties for high-redshift, high-luminosity quasars in a manner consistent with studies of low-redshift quasars.

We also present prescriptions for correcting UV-based redshifts based on a subset of the GNIRS-DQS sample of 154 objects that are non-BAL, non-RL, have accurate C IV measurements, and have $z_{\rm sys}$ values obtained from [O III] measurements. We provide measurements of velocity offsets using three different UV-based methods compared to $z_{\rm sys}$ values. This 154 object sample is three times the size of the calibration sample used in D20, and is both a higher quality and more uniform dataset than M17 and D20.

We attempt to correct for these velocity offsets using a linear regression based on UV continuum luminosity and C IV emission-line properties. Using this approach, we can decrease the standard deviation of the distribution of velocity offsets in our calibration sample by $\sim 3\%$ with respect to the best available UV-based redshift method, and by $\sim 17\%$ using C IV-based redshifts. The SDSS Pipeline provides the least precise UV-based redshifts, as the standard deviation on the velocity offsets is larger by $\sim 20\%$ compared with the other two methods both before and after the correction. We find that the simplest, most reliable way to obtain an accurate and precise $z_{\rm sys}$ value is using the C IV parameter space alone via four basic observables associated with the C IV emission line, and applying the following methodology:

(1) Measure the observed peak wavelength, EW, and FWHM of C IV, and the monochromatic luminosity at 1350 Å (L_{1350}).

(2) Calculate an initial redshift measurement, $z_{\rm meas}$, with the observed peak wavelength of C IV.

(3) Use Equation 2 and the coefficients in Table 3.6 to calculate $\Delta v_{\rm corr}$.

(4) Use Equation 3 with the observed $z_{\rm meas}$ and calculated $\Delta v_{\rm corr}$ to obtain a revised, more accurate, and more precise redshift measurement.

Additionally, we explore whether our prescriptions depend on 1) velocity width measurement, of which we determine there is no overt discrepancy based on methodology, 2) source redshift, where we determine that additional data are needed, particularly at the highest redshifts under investigation, in order to obtain more robust results, and 3) source luminosity, where no clear trends are apparent, consistent with the flux-limited nature of our sample.

A primary interest going forward would be bolstering the sample with supplementary observations of quasars, primarily at $z \sim 3$, in order to obtain statistically meaningful results on a potential redshift dependence, and further improve UV-based redshift determinations. Another avenue of further investigation includes increasing the sample size of quasars with significantly higher spectral resolution, e.g., using Gemini's Spectrograph and Camera for Observations of Rapid Phenomena in the Infrared and Optical (SCORPIO, [122]), in order to further improve the UV-based redshift corrections by obtaining more accurate line peaks of spectral features. Machine learning can also play an important role as larger data sets will be produced that require redshift correction *en masse*. By utilizing the entire quasar UV spectrum, as opposed to a few key parameters, it will be possible to test if machine learning algorithms can produce more reliable estimates of $z_{\rm sys}$ much more efficiently than our prescriptions allow.

As future projects begin to produce data, we can expect that $\approx 10^6$ high-redshift ($z \gtrsim 0.8$) quasars will have redshifts determined through large spectroscopic surveys conducted in the rest-frame UV-optical regime from instruments such as the Dark Energy Spectroscopic Instrument (DESI, [93, 94]), the 4m Multi-Object Spectroscopic Telescope [95], and the Subaru Prime Focus Spectrograph (PFS, [108]). For those quasars at $1.5 \lesssim z \lesssim 5.0$, coverage of the C IV emission line will enable crucial redshift corrections, as has been demonstrated in this work. Instruments such as the James Webb Space Telescope (JWST, [98]) can provide simultaneous coverage of C IV, Mg II, and [O III] for $6 \lesssim z \lesssim 9$, allowing for similar investigations of redshift dependencies and corrections for the most distant known quasars.

This work is supported by National Science Foundation grants AST-1815281 (B. M. M., C. D., O. S.) and AST-1815645 (M. S. B., A. D. M.). W.N.B. acknowledges support from NSF grant AST-2106990. This work was enabled by observations made from the Gemini North telescope, located within the Maunakea Science Reserve and adjacent to the summit of Maunakea. We are grateful for the privilege of observing the Universe from a place that is unique in both its astronomical quality and its cultural significance. This research has made use of the NASA/IPAC Extragalactic Database (NED), which is operated by the Jet Propulsion Laboratory, California Institute of Technology, under contract with the National Aeronautics and Space Administration. We thank Paul Hewett for helpful contributions of redshift data.

3.5. Appendix: Comparing Different Velocity Widths of the C IV Line

In our regression analysis, we have elected to use the FWHM of the C IV line. However, there has been some debate in the literature concerning the overall reliability of using FWHM as the quantification of the velocity width of an emission line [123, 124]. While M17 and D20 used FWHM for their analyses, other methods for measuring velocity widths of emission-line profiles include Line Dispersion (σ) and Mean Absolute Deviation (MAD, [57, 124]). We therefore repeated our analysis by replacing FWHM with each of these two velocity width methods, measured from the Gaussian fits presented in Table 3.4, and compared the results obtained from all three velocity widths. We find that replacing FWHM with σ or MAD gave no notable improvement in the dispersion on the relevant corrections, as shown in Figure 3.9. We thus have elected to adopt the FWHM parameterization throughout this work.

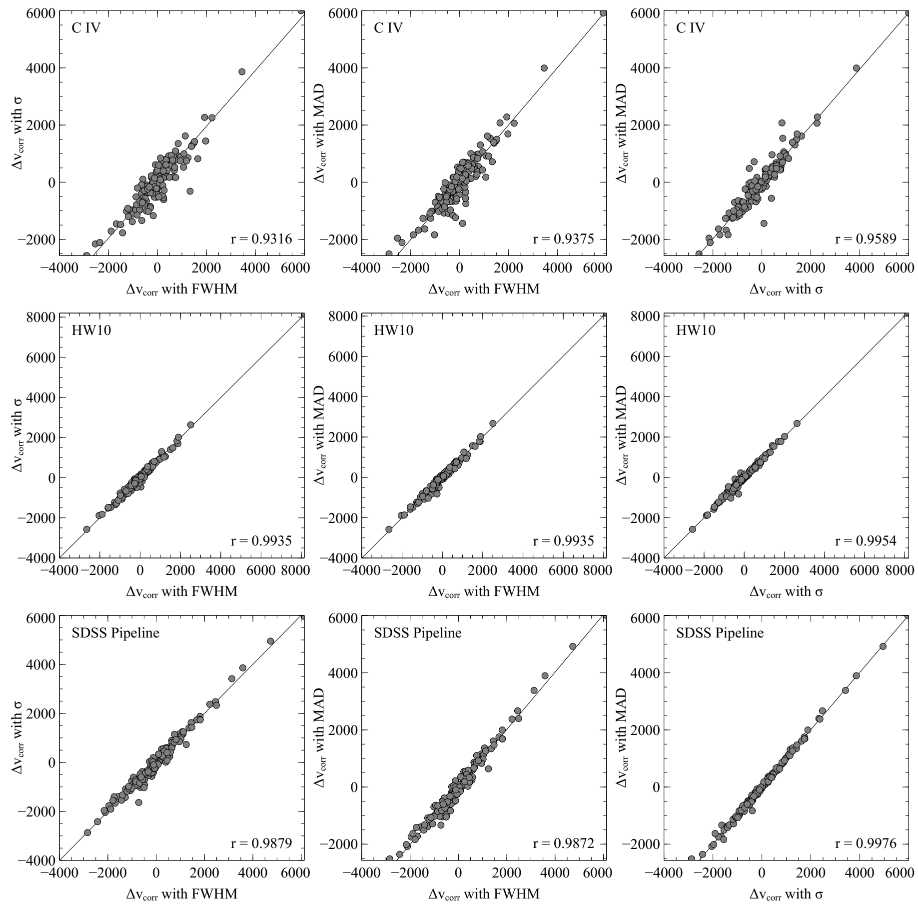

FIGURE 3.9. Comparison of the velocity offsets produced using C IV FWHM, σ, and MAD for each UV-based redshift method. Each panel displays the correlation between the corrected velocity offset values produced by our regression analysis when using either FWHM, σ, or MAD, along with a corresponding Pearson linear correlation coefficient r, where $r \to 1$ corresponds to a strong correlation. No significant difference exists in this regression analysis between the three different parameters.

CHAPTER 4

GEMINI NEAR INFRARED SPECTROGRAPH - DISTANT QUASAR SURVEY: PRESCRIPTIONS FOR CALIBRATING UV-BASED ESTIMATES OF SUPERMASSIVE BLACK HOLE MASSES IN HIGH-REDSHIFT QUASARS

4.1. Introduction

A persisting point of interest in astrophysics today is understanding the co-evolution of supermassive black holes (SMBHs) and their host galaxies through cosmic time [125, 36, 38, 51, 126, 127]. A fundamental ingredient in this research area is the SMBH mass ($M_{\rm BH}$). Over the past four decades, several methods have been employed for obtaining $M_{\rm BH}$ values in galaxies such as stellar kinematics, masers, interferometry and spectrophotometric monitoring campaigns of active galaxies, e.g., [40, 41, 128, 129, 130, 131, 132, 133]. Overall, the masses obtained from these methods are consistent with each other but deriving $M_{\rm BH}$ values in active galactic nuclei (AGN) have the best prospects of obtaining the SMBH mass function through cosmic time given the large luminosities of such sources and their mass observable indicators at all accessible redshifts [134, 135, 136, 55].

The $M_{\rm BH}$ values for AGN, or quasars, are usually determined through measurements of broad emission lines in the optical band. Specifically, following the virial assumption [137], we use measurements of the size of the broad emission line region (BELR), $R_{\rm BELR}$, and the velocity width of an emission line stemming from the BELR, ΔV, in order to estimate $M_{\rm BH}$ for AGN. Of these terms, estimating the value of $R_{\rm BELR}$ becomes the most pertinent for reliable estimates of $M_{\rm BH}$.

Ideally, measurements of $R_{\rm BELR}$ are derived from reverberation mapping (RM) of AGN or quasars, which uses time lags between continuum fluctuations and photoionized BELR emission line fluctuations to determine the size of the BELR [138, 139, 140]. To date, $M_{\rm BH}$ has been measured successfully using RM campaigns for ≈ 150 quasars primarily with the H$\beta\lambda$4861 emission line [141, 142, 143, 144]. One of the most important findings from these RM campaigns is the BELR size-luminosity ($R - L$) relation, where $R_{\rm BELR} \propto L^{\alpha}$ with $\alpha \sim 0.5$, in agreement with expectations from photoionization theory [145, 146, 147, 148, 149].

Since RM campaigns are currently impractical for $M_{\rm BH}$ measurements in $\approx 10^6$ of known quasars [131], [150] have proposed that the $R-L$ relation, in conjuction with the virial assumption, allows one to *estimate* single epoch (SE) $M_{\rm BH}$ values by substituting the continuum luminosity for $R_{\rm BELR}$. Estimates of $M_{\rm BH}$ values for $\approx 10^5$ quasars have been obtained in this fashion during the past two decades [90, 151, 152].

Nevertheless, estimating $M_{\rm BH}$ values using the SE method faces additional challenges, particularly at high redshift. First, the most reliable SE indicator for $M_{\rm BH}$ is obtained from spectroscopic measurements of low-ionization emission lines such as the Hβline, and at $z \gtrsim 1$, this line is shifted into the less accessible near-infrared (NIR) band. Second, recent Super-Eddington Accreting Massive Black Hole (SEAMBH) and Sloan Digital Sky Survey-RM campaigns discovered many highly accreting objects that lie below the $R-L$ relation [144, 153], suggesting that an additional correction to account for accretion rate is warranted for SE $M_{\rm BH}$ estimates.

To overcome the first of these, SE $M_{\rm BH}$ estimates using other prominent emission lines have been calibrated against Hβ-based $M_{\rm BH}$ estimates in the nearby universe. The two most common emission lines that are used for such calibrations are Mg II $\lambda\lambda 2798, 2803$ [154, 155, 62, 156, 157] and C IV $\lambda 1549$ [150, 158, 159, 160, 123, 65, 161, 124]. However, these emission lines have yielded relatively fewer successful $M_{\rm BH}$ measurements through RM campaigns [162, 32, 163, 132, 164, 165, 166], and each of these line profiles contains its own intrinsic measurement challenges [83, 167]. To address the second challenge, [168] have proposed to include a correction to the $R-L$ relationship based on the Fe II emission blend flanking the Hβ emission line, which is known to be an accretion-rate indicator. Recently, [169] implemented such a correction and found that $M_{\rm BH}$ estimates in highly accreting sources are overestimated.

In this work, we utilize a large spectroscopic inventory for high-redshift quasars that allows us to obtain the most reliable $M_{\rm BH}$ estimates using rest-frame ultraviolet (UV) emission lines. Our inventory includes high quality measurements of the Hβ, Fe II, Mg II, and C IV emission lines, which allows us to implement two separate accretion-rate based corrections to the estimated $M_{\rm BH}$ value while investigating the effects of using different BELR velocity width measurements.

This paper is organized as follows: In Section 5.2.2, we describe our sample and data analysis. In Section 4.3, we present the results of multiple regression analyses used for obtaining prescriptions for reliable $M_{\rm BH}$ estimates at high redshift. In Section 4.4 we discuss our results and in Section 5.4 we present our conclusions. Throughout this paper, we compute luminosity distances using $H_0 = 70$ km s^{-1} Mpc^{-1}, $\Omega_{\rm M} = 0.3$, and $\Omega_\Lambda = 0.7$ [67].

4.2. Sample Selection and Measurements

Our sample is drawn from the Gemini Near Infrared Spectrograph - Distant Quasar Survey (GNIRS-DQS; Matthews et al. 2023, hereafter M23). These quasars were selected from all the Sloan Digital Sky Survey [68] quasars [109] having $m_i \sim 19.0$ that lie in the redshift intervals $1.55 \lesssim z \lesssim 1.65$, $2.10 \lesssim z \lesssim 2.40$, and $3.20 \lesssim z \lesssim 3.50$; these redshift intervals assure that the Hβ spectral region is covered in either the J, H, or K bands.

From all 260 GNIRS-DQS sources, we were able to reliably measure C IV emission-line profiles for 177 sources from their respective SDSS spectra. Specifically, the C IV emission line is difficult to measure reliably in broad absorption line (BAL) quasars due to BAL troughs impacting the emission-line profile. Therefore, all 65 BAL quasars from the GNIRS-DQS sample were removed during our C IV-based $M_{\rm BH}$ estimate analysis. Since our analysis involves measurements of the rest-frame equivalent width (EW) of the C IV emission line, we further removed 16 radio-loud quasars (RLQs)[1] from the sample. This was done in order to avoid potential dilution of the C IV emission line by continuum emission originating in the radio jets. We note that one of the BAL quasars we removed, SDSS J114705.24+083900.6, is also radio loud. Finally, we removed two sources, SDSS J073132.18+461347.0 and SDSS J141617.38+264906.1, for which we were unable to measure the C IV emission line reliably from their SDSS spectra due to a poor signal-to-noise ratio (S/N). The remaining sample of 177 non-BAL, non-RL sources with reliable C IV measurements was used in the C IV-based $M_{\rm BH}$ estimate analysis below.

[1]We define radio loud quasars as sources having radio-loudness values of $R > 100$ (where R is the ratio of the flux densities at 5 GHz and 4400 Å; [17])

The GNIRS spectra provide reliable Mg II measurements for 99 of the GNIRS-DQS sources (see, M23): only 70 of these sources also have reliable C IV measurements following the removal of 22 BAL quasars and seven RLQs. From these 99 quasars, 65 (47 with reliable C IV measurements) lie in the redshift range of $2.10 \lesssim z \lesssim 2.40$, and 34 (23 with reliable C IV measurements) lie at $3.20 \lesssim z \lesssim 3.50$. In both of these redshift ranges Mg II and Hβ are covered in the same spectrum, however, in the latter range Mg II has the highest S/N [62].

Furthermore, we were able to reliably measure the Mg II profile in the SDSS spectra that adequately covered that emission line in 179 of the GNIRS-DQS sources: 34 and 13 of these sources do not have reliable C IV measurements given that these are BAL quasars and RLQs, respectively. From this sample of 179 quasars, 53 sources had a measurable Mg II profile in both the SDSS and the GNIRS-DQS spectra. When combining all available Mg II measurements, either from SDSS or GNIRS-DQS or both, we compiled a total sample of 225 sources: 47, 16, and 2 of these sources do not have reliable C IV measurements given that these are BAL quasars, RLQs, or sources with unreliable C IV measurements, respectively.

4.2.1. Fitting the SDSS Spectra

The SDSS spectra were fit utilizing a local linear continuum and two Gaussians for each broad emission line. We find that fitting two Gaussians to each of the C IV and Mg II emission lines is sufficient given the signal-to-noise (S/N) ratio across both the SDSS and GNIRS spectra. The Fe II and Fe III emission complex that blends with the Mg II emission line was modeled with the empirical template of [83]. This template was broadened with a Gaussian kernel having a full width at half maximum intensity (FWHM) value that was free to vary between $1300 - 10000$ km s^{-1} and was determined based on a least squares analysis of each fitted region.

The Gaussians were constrained such that the flux density would lie between zero and twice the value of the peak of the respective emission line and the widths between zero and 15000 km s^{-1}. The peaks of these Gaussians were also constrained to fit within ± 1500 km s^{-1} of the rest-frame value of the peak of the emission line based on the systemic redshift measured in M21. After the initial fitting was performed for each region, we visually inspected the fit to see if more lenient constraints with interactive fitting were warranted.

4.2.2. Measurements and Error

The SDSS spectra of the sources were fit utilizing a local linear continuum and two Gaussians for each broad emission line. We find that fitting two Gaussians to each of the C IV and Mg II emission lines is sufficient given the S/N of ~ 40 across both the SDSS and GNIRS spectra. The Fe II and Fe III emission complex that blends with the Mg II emission line was modeled with the empirical template of [83]. This template was broadened with a Gaussian kernel having a full width at half maximum (FWHM) intensity that was free to vary up to 10000 km s^{-1} and was determined based on a least squares analysis of each fitted region.

The Gaussians were constrained such that the flux density would lie between 0 and twice the value of the peak of the respective emission line and the FWHM was restricted to lie within 0 and 15000 km s^{-1}. The peaks of these Gaussians were also constrained to lie within ± 1500 km s^{-1} of the rest-frame wavelength of the peak of the emission line based on the systemic redshift from M23. After the initial fitting was performed for each region, we visually inspected the fit to see if more lenient constraints with interactive fitting were warranted.

Spectral properties stemming from these fits are reported in Table 4.1 for C IV and Mg II. In this Table, Column (1) reports the source's SDSS designation. Columns (2), (3), (4), (5), and (6) list the FWHM, mean absolute deviation (MAD; described below), line dispersion ($\sigma_{\rm line}$), EW, and the observed-frame wavelength of the emission-line peak, $\lambda_{\rm peak}$, respectively, for C IV. Columns (7), (8), (9), (10), and (11) list the same spectral properties for the Mg II emission line.

4.2.3. Measurements and Error

For each emission-line profile in either the GNIRS or SDSS spectra, we measured the values of the $\sigma_{\rm line}$ and MAD. The line dispersion is defined by

$$\sigma_{\text{line}} = \left[\frac{\int (\lambda - \lambda_0)^2 P(\lambda) d\lambda}{\int P(\lambda) d\lambda} \right]^{1/2} \tag{4}$$

where λ_0 is the line centroid and $P(\lambda)$ is the emission-line profile. The MAD is defined as

$$\text{MAD} = \int |\lambda - \lambda_{\text{med}}| P(\lambda) d\lambda \bigg/ \int P(\lambda) d\lambda \ , \tag{5}$$

where λ_{med} is the median wavelength of the emission-line profile, first suggested in [57] as an appropriate representation for the emission-line width. For each emission-line profile in the GNIRS spectra, we obtained the FWHM, EW, and observed-frame wavelength of the peak emission from M23.

We present three different values for the velocity widths (FWHM, MAD, σ_{line}) due to the uncertainties inherent in the accuracy of FWHM, the most popular of these parameters [123, 124, 157]. While σ_{line} is a dependable measurement to describe the emission-line velocity width, [57] suggest that MAD provides an accurate estimate of this quantity for low-quality data. Overall, we recognize that the best virial velocity width indicator is debatable, therefore, we provide calibrations for the M_{BH} estimates utilizing all of these parameters.

We have also derived the monochromatic luminosities, L_{1350} and L_{3000}, by measuring the continuum flux densities, at rest-frame λ1350 Å and λ3000 Å, respectively, and employing our chosen cosmology. All the flux densities and monochromatic luminosities (L_{5100}) at rest-frame λ5100 Å used in this work were obtained from the M23 catalog. The flux calibration for the GNIRS-DQS data is extensively discussed in [115]. In certain cases, the flux density at rest-frame wavelength 3000 Å was not measurable in the GNIRS-DQS spectrum due to this wavelength range falling outside of the J band. In these cases, the flux density was determined by extrapolating from the flux density at rest-frame wavelength 5100 Å using the canonical quasar optical-UV continuum of the form $f_\nu \propto \nu^{-0.5}$ [170, 24]. Similarly, there are SDSS spectra that do not have a reliable flux density value for the rest-frame wavelength

1350 Å due to low S/N at the blue end of the SDSS spectrum. In these cases, we employed the same model as described above extrapolating from the flux density at rest-frame 1450 Å.

The uncertainties for all emission line measurements reported in Table 1, were determined by following the methods described in M21 and M23. Briefly, we created mock spectra that introduced random Gaussian noise to the original spectra. We then fit these spectra as described above, and measured the newly fit profiles. This process was repeated 1000 times in order to obtain a distribution for each of our parameters, and the 68% range is reported as our measurement uncertainty.

4.3. UV-Based Black Hole Mass Calibration

4.3.1. Estimating Black Hole Masses

We obtain SE $M_{\rm BH}$ estimates for each emission line in this work by, first, following the virial assumption,

$$M_{\rm BH} = \frac{f R_{\rm BELR} \Delta V^2}{G}, \qquad (6)$$

where G is the gravitational constant and f is the virial factor which depends on the geometry and orientation of the system and is assumed to be on the order of ≈ 1 [171, 172]. Then, we substitute the continuum luminosity for $R_{\rm BELR}$ according to the $R-L$ relation (see, Section 5.1) as $R_{\rm BELR} \propto L^{0.5}$.

We estimate Hβ-based $M_{\rm BH}$ values by further correcting the $R_{\rm BELR}$ parameter in Equation 6 (hereafter, $R_{\rm H\beta}$) for the source accretion rate, based on the scaling relation presented in [168] in the following way

$$\log(R_{\rm H\beta}/{\rm lt-days}) = \delta + \beta \log \ell_{44} + \gamma \mathcal{R}_{\rm Fe} \qquad (7)$$

where $\ell_{44} = L_{5100}/10^{44}$ erg s^{-1}, $\delta = 1.65 \pm 0.06$, $\beta = 0.45 \pm 0.03$, $\gamma = -0.35 \pm 0.08$, and $\mathcal{R}_{\rm Fe}$ is an indicator of the strength of the Fe II emission defined as the ratio of the flux (F) or EW between Fe II (in the 4434-4684Å rest-frame band; [82]) and Hβ; $\mathcal{R}_{\rm Fe} = F_{\rm FeII}/F_{\rm H\beta} \approx {\rm EW_{FeII}/EW_{H\beta}}$. In this work we employ the ratio of EWs to determine $\mathcal{R}_{\rm Fe}$. For the virial factor in Equation 6, we adopt $f = 1.5$ and the FWHM as ΔV for Hβ-based $M_{\rm BH}$ values [169]. The value for the f factor introduces additional uncertainty, on the order of ~2-3 [173], in our estimation of $M_{\rm BH}$. Our adopted value is consistent with [174] and the emipirical best fit value obtained from the $M - \sigma_{\bigstar}$ correlation [175, 171, 176].

[169] have shown that this accretion-rate correction is necessary for adjusting $M_{\rm BH}$ values that are overestimated by a factor of 2 for typical luminous high-redshift quasars. We compare the accretion rate corrected Hβ-based $M_{\rm BH}$ estimates for our sample to the traditional approach of VP06 which uses the following equation to obtain Hβ-based $M_{\rm BH}$ values:

$$\log\left(\frac{M_{\rm BH}}{M_\odot}\right) = 0.91 + 2\log\left(\frac{\rm FWHM_{H\beta}}{\rm km\ s^{-1}}\right) + 0.5\log\left(\frac{\lambda L_\lambda(5100\text{Å})}{10^{44}\rm erg\ s^{-1}}\right), \tag{8}$$

utilizing a virial factor on the order of unity. Figure 4.1 presents the Hβ-based $M_{\rm BH}$ masses for our sample, based on the relation of VP06 against our accretion-rate-corrected values. We find that the masses, computed according to the VP06 approach, are systematically overestimated by 0.26 dex, consistent with the [169] finding.

Given that correcting for accretion-rate is necessary for reliable $M_{\rm BH}$ estimates, we explore whether additional accretion rate based corrections would further improve $M_{\rm BH}$ estimates for rest-frame UV emission lines. To accomplish this, we introduce a term into our UV-based $M_{\rm BH}$ estimates that includes the C IV EW, as this parameter has been shown to be generally anti-correlated with the quasar's accretion rate [167, 177].

Following Equation 6 with the addition of our C IV EW term, we derive C IV-based $M_{\rm BH}$ estimates as

$$\log\left(\frac{M_{\rm BH}}{M_\odot}\right) = 2\log\left(\frac{\Delta V}{1000\ \rm km\ s^{-1}}\right) + 0.5\log\left(\frac{\lambda L_\lambda(1350\text{Å})}{10^{44}\rm erg\ s^{-1}}\right) + \ a + b\log\left(\frac{\rm EW_{CIV}}{\text{Å}}\right). \tag{9}$$

The coefficients a and b were determined from a linear-regression analysis to the calibration set of Hβ-based $M_{\rm BH}$ estimates. By design, we allow a and b to freely vary during the regression analysis, resulting in a zero mean offset between the C IV-based and Hβ-based $M_{\rm BH}$ estimates.

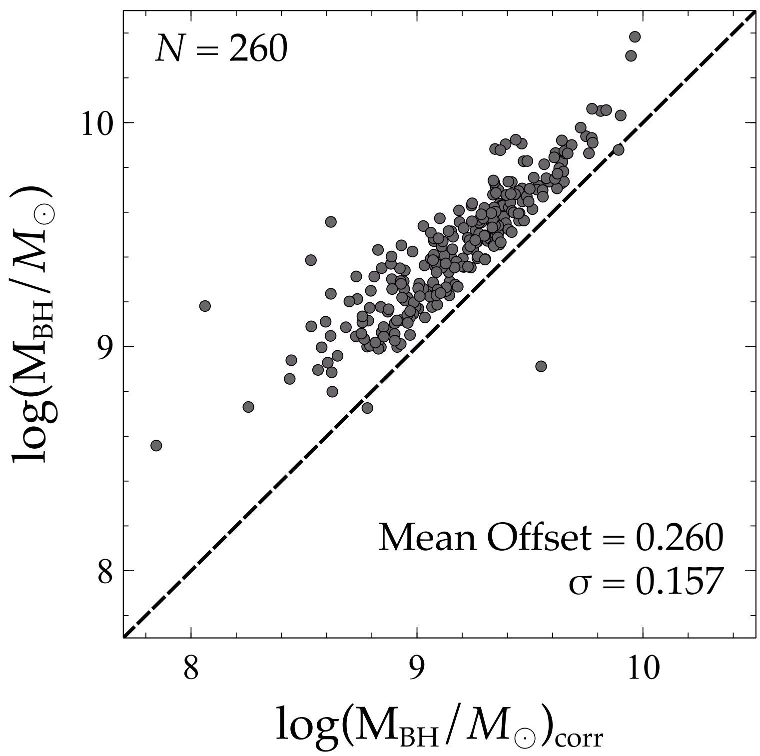

FIGURE 4.1. The Hβ-based $M_{\rm BH}$ estimates of all 260 quasars from the GNIRS-DQS sample calculated using the VP06 approach (y-axis) and correcting for accretion rate (x-axis). The dashed line represents a one-to-one relationship. This figure shows that Hβ-based $M_{\rm BH}$ esimates that were not corrected for accretion rate are systematically overestimated.

The linear-regression was performed such that the difference between our UV-based $M_{\rm BH}$ values and the Hβ-based $M_{\rm BH}$ values was minimized. Specifically, we subtracted the first two terms in Equation 9 from the derived Hβ-based $M_{\rm BH}$ estimates and fit the remaining coefficients, a and b, to this difference. This was accomplished utilizing the REGSTATS function in the Statistics Toolbox 11.4 of MATLAB 9.5. As the errors associated with SE $M_{\rm BH}$ values are large (on the order of 0.5-0.6 dex and 0.7 dex for relative and absolute uncertainty, respectively; see, Section 4.4), we did not include the errors as part of the linear-regression. Despite this, we also employed the LINMIX_ERR algorithm [178] where we adopted a 0.5 dex uncertainty to have a basis of comparison for our regression, and found the results were generally consistent. The uncertainty of the coefficients, presented in our equations below, stem directly from the linear fit.

Unlike the case for C IV above, for Mg II-based $M_{\rm BH}$ estimates, we calibrate our estimates in two separate runs using the following equation,

$$(10)\quad \log\left(\frac{M_{\rm BH}}{M_\odot}\right) = 2\log\left(\frac{\Delta V}{1000\ {\rm km\ s^{-1}}}\right) + 0.5\log\left(\frac{\lambda L_\lambda(3000{\rm \AA})}{10^{44}{\rm erg\ s^{-1}}}\right) + \ c + d\log\left(\frac{{\rm EW_{CIV}}}{\rm \AA}\right),$$

where ΔV is the velocity width of Mg II; the Mg II lines were measured from a combination of the SDSS and GNIRS spectra of the sources as described below. The coefficients c and d were determined differently in each run through a linear-regression analysis to the calibration set of Hβ-based $M_{\rm BH}$ estimates. The first run set the coefficient d to 0 in order to provide a prescription that only used the Mg II emission line while allowing c to be a free parameter. For this run we did not need any C IV measurements, allowing us to use all of the Mg II measurements in each subsample (see, Section 5.2.2). The second run allowed both c and d to be free parameters during the regression. This run required C IV measurements, reducing our Mg II sample as described in Section 5.2.2. In both runs, we used the same type of linear-regression as discussed for the C IV analysis, but using Equation 10 and coefficients c and d instead.

Given the considerably lower S/N ratio of the GNIRS spectra at $\lambda \lesssim 1.2\ \mu$m (M21), we split the analysis utilizing the Mg II line measured from the GNIRS spectra into three different parts based on source redshift (see Section 5.2.2). In addition to these subsamples, we analyzed the total of 160 and 225 sources for the subsample including SDSS and/or GNIRS Mg II measurements with and without C IV. For the subsample of 53 sources that have Mg II measurements available in both the GNIRS and SDSS spectra, the average of these measurements was used in the regression analyses (see Section 4.3.4).

4.3.2. Testing Different Velocity Width Parameters

We substitute the FWHM, MAD, and $\sigma_{\rm line}$ as the velocity width parameter in each of our $M_{\rm BH}$ estimates in Equations 9 and 10 to further investigate which of these parameters provides $M_{\rm BH}$ values closest to those obtained from Hβ. In each analysis described

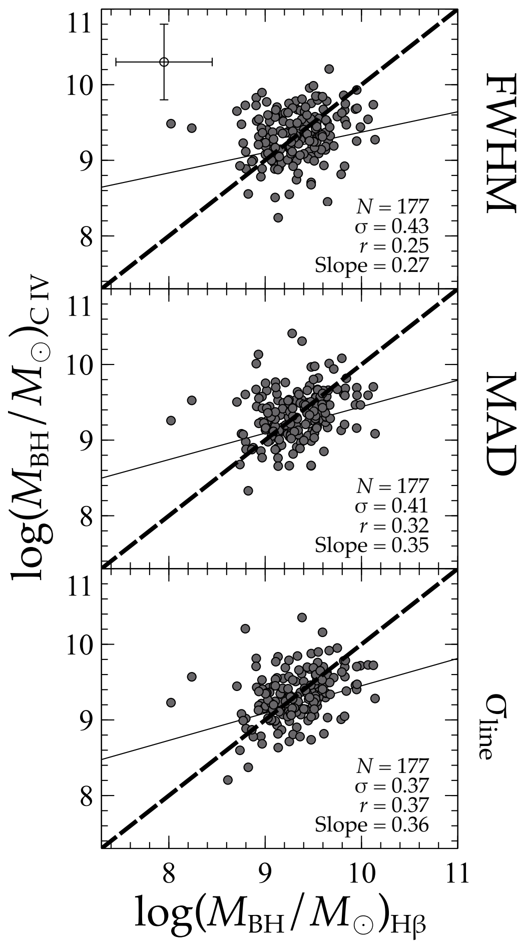

FIGURE 4.2. The calibrated C IV-based $M_{\rm BH}$ estimates using the three velocity width parameters, discussed in Section 4.3.1, against the calibration set of Hβ-based $M_{\rm BH}$ estimates. The dashed line in each panel represents a one-to-one relationship and the thin solid line in each panel represents the best linear fit to the data. The r value provided in each panel is the Pearson correlation coefficient and the slope is the slope of the best-fit line. Notably, using $\sigma_{\rm line}$ as the velocity width parameter provides the most precise C IV-based $M_{\rm BH}$ estimates with respect to the Hβ-based $M_{\rm BH}$ estimates. Additionally, using $\sigma_{\rm line}$ as the velocity width parameter leads to the largest Pearson correlation coefficient and steepest slope of the best fit relation. Typical uncertainty of 0.5 dex on the $M_{\rm BH}$ values is displayed in the top panel for reference.

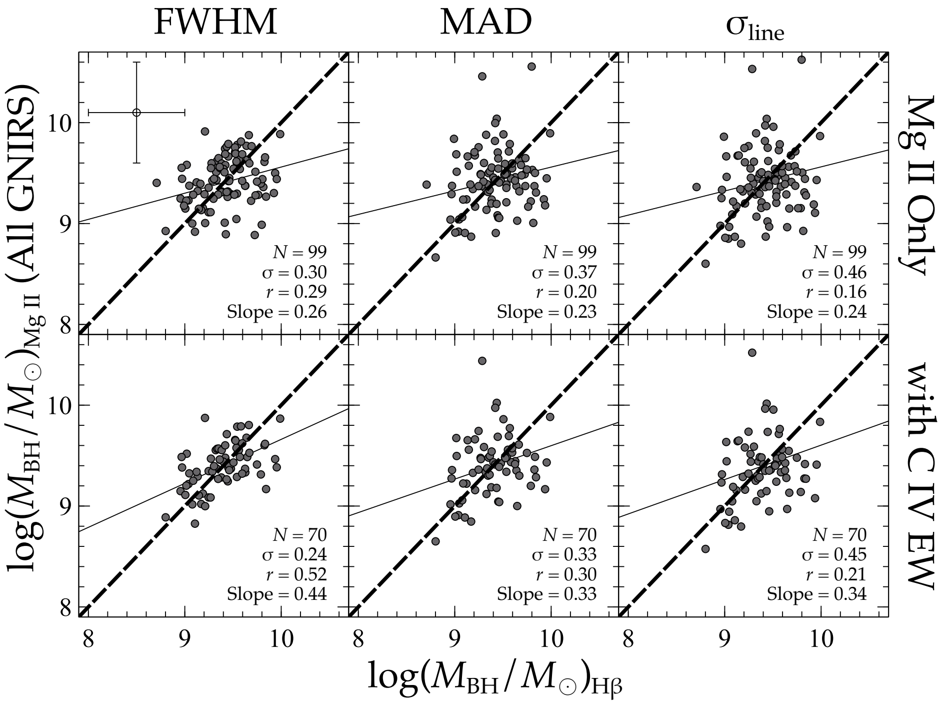

FIGURE 4.3. Calibrated Mg II-based $M_{\rm BH}$ estimates using the three velocity width parameters against the Hβ-based $M_{\rm BH}$ estimates; the bottom panels present the results when adding EW(C IV) to the analysis as discussed in Section 4.3.1. The symbols are the same as in Figure 4.2. For all the Mg II-based $M_{\rm BH}$ estimates, using the FWHM as the velocity width parameter provided the most accurate and precise results when compared to the Hβ-based $M_{\rm BH}$ estimates. As can be seen when comparing the standard deviations and r from the top panels and the bottom panels, including the C IV EW in the Mg II-based $M_{\rm BH}$ estimate resulted in a higher precision for each velocity width parameter. Typical uncertainty of 0.5 dex on the $M_{\rm BH}$ values is displayed in the top left panel for reference.

above, we calibrate the C IV- and Mg II-based $M_{\rm BH}$ estimates to the Hβ-based values that use the FWHM for the velocity width of Hβ [169]. For the C IV-based $M_{\rm BH}$ estimates, presented in Figure 4.2, $\sigma_{\rm line}$ produced the most reliable results when compared to the Hβ-based $M_{\rm BH}$ values. We determined which velocity width parameter was preferred based on the low-

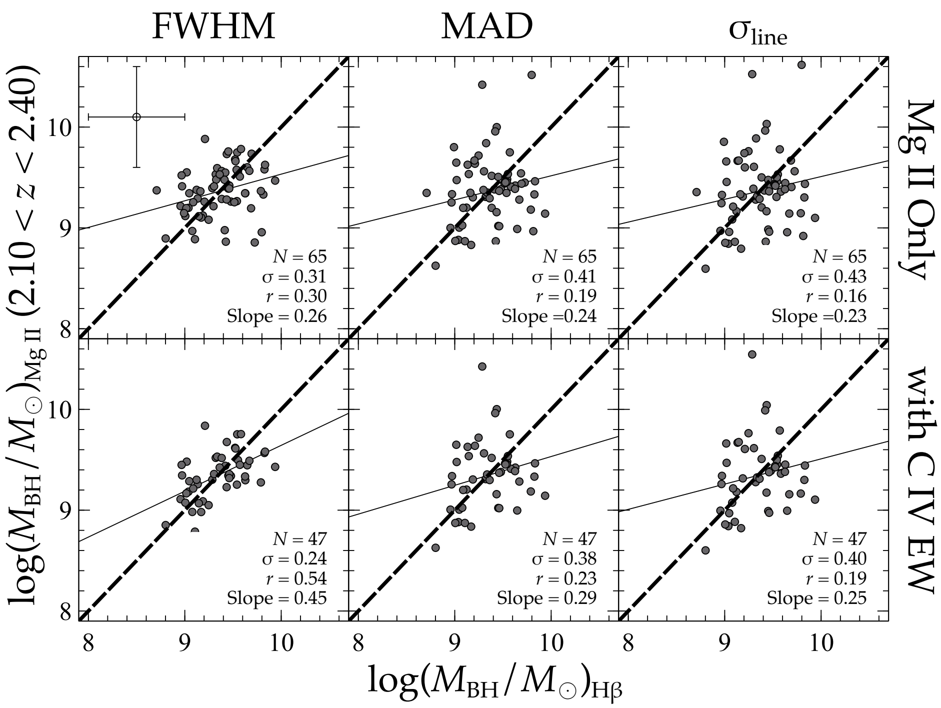

FIGURE 4.4. Same as Figure 4.3 but for the subset of sources in the range $2.10 \lesssim z \lesssim 2.40$. As observed for the entire redshift range (Figure 4.3), the FWHM of Mg II is the most reliable velocity width parameter and the inclusion of the C IV EW helped improve the accuracy and precision of the Mg II-based $M_{\rm BH}$ estimates with respect to the Hβ-based estimates.

est standard deviation, steepest slope of the best-fit relation and largest Pearson correlation coefficient when comparing the resulting UV- and Hβ-based $M_{\rm BH}$ values.

For each of the Mg II subsamples described above, we present the calibrated Mg II-based $M_{\rm BH}$ estimates in Figures 4.3, 4.4, 4.5, and 4.6 both with (bottom panels) and without (top panels) the inclusion of the C IV EW. Except for the subsample of sources at $3.20 \lesssim z \lesssim 3.50$, all the other Mg II-based subsamples showed the strongest corrrelation with the Hβ-based $M_{\rm BH}$ estimates when using the FWHM as the velocity width parameter for the Mg II line. For the subsample at $3.20 \lesssim z \lesssim 3.50$, we find that using the MAD for the velocity width parameter in $M_{\rm BH}$ estimates provides the best results when using only the Mg II emission line (see, Figure 4.5). We recognize that this discrepancy may be a result

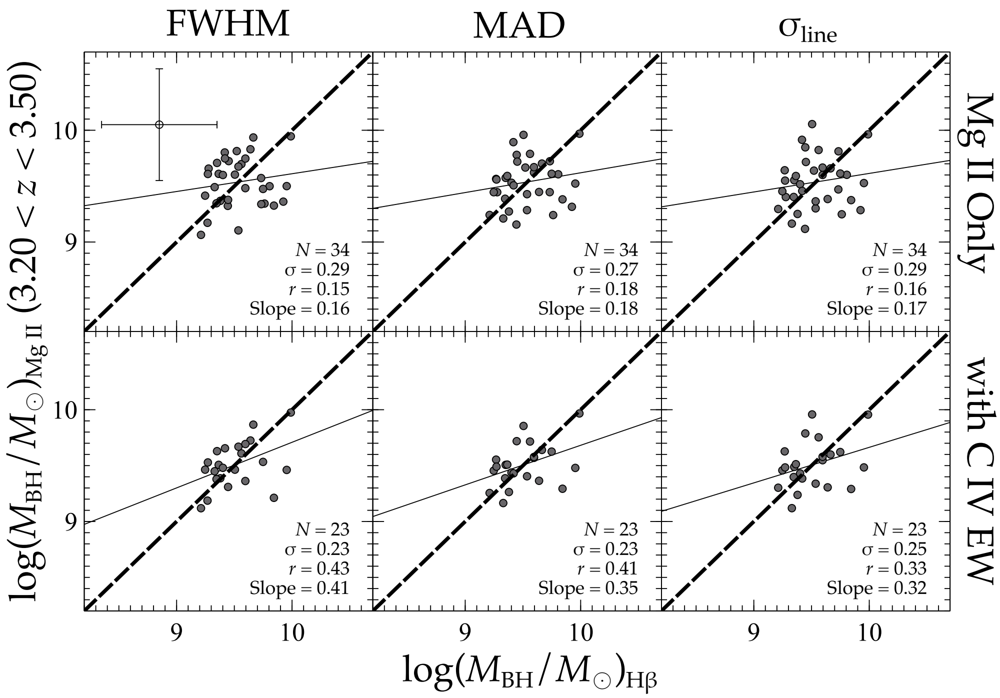

FIGURE 4.5. Same as Figure 4.3 but for the subset of sources in the range $3.20 \lesssim z \lesssim 3.50$. In this subset of sources the most reliable velocity width parameter for deriving Mg II only-based M_{BH} estimates is the MAD instead of the FWHM. This is determined from evaluating the standard deviations and r in each panel. This disparity suggests the importance of expanding the sample of quasars that lie in this redshift range. As we find for the entire redshift range, the inclusion of the EW of C IV (bottom panels) improves the accuracy and precision of these Mg II-based M_{BH} estimates.

of the limited sample size which may not provide meaningful statistics. In spite of this, the results from this subsample are considered to be the least uncertain given that Mg II and Hβ are measured in the same spectrum with the highest S/N ratio possible. The best fit coefficients stemming from our linear-regression analyses appear in Table 4.2.

4.3.3. Comparison with Previous Studies

In order to have a basis of comparison for this work, we provide estimates for the C IV-based M_{BH} values for our sample using the prescriptions provided in VP06, [123], and [65].

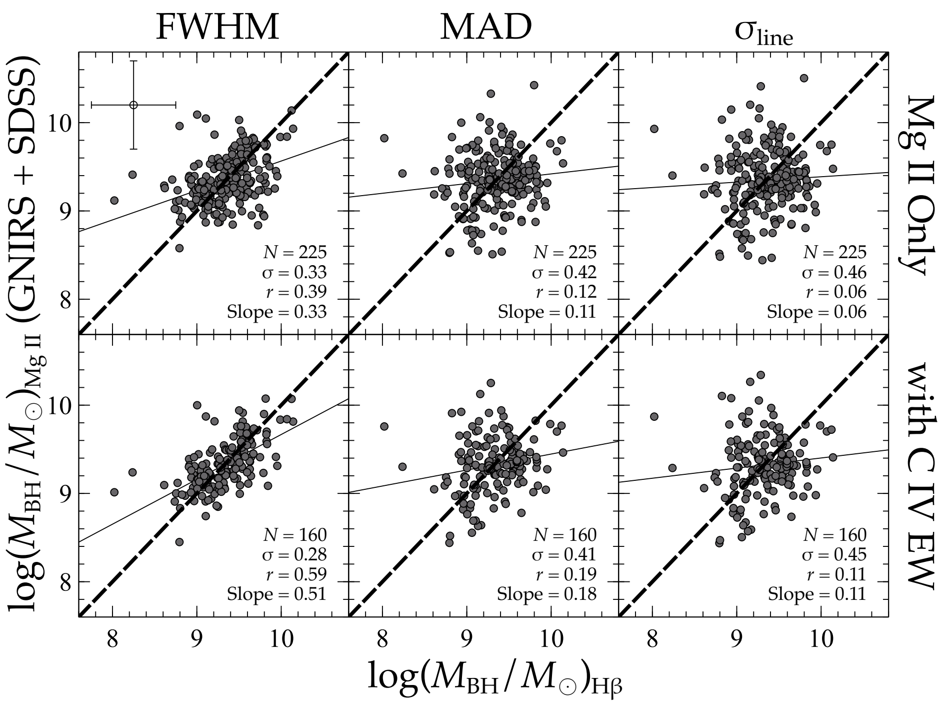

FIGURE 4.6. Same as Figure 4.3 but for the source sample having Mg II measurements taken from GNIRS-DQS and/or SDSS. From evaluating the standard deviations and Pearson correlation coefficients in each panel, we find that using the FWHM as the velocity width parameter in the calculation for Mg II-based M_{BH} estimates provides the most reliable M_{BH} estimates with respect to the Hβ-based M_{BH} values. As we find for each Mg II subsample, the inclusion of the EW of C IV (bottom panels) improves the accuracy and precision of our Mg II-based M_{BH} estimates.

VP06, P17, and C17, use the following Equations to determine C IV-based M_{BH} estimates, respectively,

$$(11) \qquad \log\left(\frac{M_{BH}}{M_\odot}\right) = 6.66 + 2.0\log\left(\frac{\mathrm{FWHM_{CIV}}}{1000\ \mathrm{km\ s^{-1}}}\right) + 0.53\log\left(\frac{\lambda L_\lambda(1350\text{Å})}{10^{44}\mathrm{erg\ s^{-1}}}\right),$$

$$(12) \qquad \log\left(\frac{M_{BH}}{M_\odot}\right) = 6.73 + 2.0\log\left(\frac{\sigma_{\mathrm{line,CIV}}}{1000\ \mathrm{km\ s^{-1}}}\right) + 0.43\log\left(\frac{\lambda L_\lambda(1350\text{Å})}{10^{44}\mathrm{erg\ s^{-1}}}\right),$$

$$\log\left(\frac{M_{\rm BH}}{M_\odot}\right) = 6.71 + 2.0\log\left(\frac{\rm FWHM_{CIV,Corr.}}{1000\ {\rm km\ s^{-1}}}\right) + 0.53\log\left(\frac{\lambda L_\lambda(1350\text{Å})}{10^{44}{\rm erg\ s^{-1}}}\right). \tag{13}$$

C17 uses a velocity width ($\rm FWHM_{CIV,Corr.}$) that has been adjusted by the blueshift of the C IV emission-line peak with respect to the line peak of Hβ [65].

In Figure 4.7 we present the C IV-based $M_{\rm BH}$ estimates for our sample based on the prescriptions from the literature. In comparison, our prescription,

$$\begin{aligned}\log\left(\frac{M_{\rm BH}}{M_\odot}\right) &= 6.299 \pm 0.169 + 2\log\left(\frac{\sigma_{\rm line}}{1000\ {\rm km\ s^{-1}}}\right) + \\ 0.5\log\left(\frac{\lambda L_\lambda(1350\text{Å})}{10^{44}{\rm erg\ s^{-1}}}\right) &+ 0.385 \pm 0.119\log\left(\frac{\rm EW_{CIV}}{\text{Å}}\right),\end{aligned} \tag{14}$$

which is plotted at the bottom panel of Figure 4.2, provides the smallest scatter, steepest slope of the best-fit relation, largest Pearson correlation coefficient, and, by design, corrects the mean offset[2] between previous C IV-based $M_{\rm BH}$ estimates and Hβ-based $M_{\rm BH}$ values.

To form a basis of comparison for our Mg II-based $M_{\rm BH}$ estimates, we followed the prescriptions provided in [155], [62], and [157]. VO09, Z15, and L20 use the following Equations to determine Mg II-based $M_{\rm BH}$ estimates, respectively,

$$\log\left(\frac{M_{\rm BH}}{M_\odot}\right) = 0.86 + 2.0\log\left(\frac{\rm FWHM_{MgII}}{\rm km\ s^{-1}}\right) + 0.5\log\left(\frac{\lambda L_\lambda(3000\text{Å})}{10^{44}{\rm erg\ s^{-1}}}\right), \tag{15}$$

$$\log\left(\frac{M_{\rm BH}}{M_\odot}\right) = 1.07 + 2.0\log\left(\frac{\rm FWHM_{MgII}}{\rm km\ s^{-1}}\right) + 0.48\log\left(\frac{\lambda L_\lambda(3000\text{Å})}{10^{44}{\rm erg\ s^{-1}}}\right), \tag{16}$$

$$\log\left(\frac{M_{\rm BH}}{M_\odot}\right) = 7.00 + 2.0\log\left(\frac{\rm FWHM_{MgII}}{1000\ {\rm km\ s^{-1}}}\right) + 0.5\log\left(\frac{\lambda L_\lambda(3000\text{Å})}{10^{44}{\rm erg\ s^{-1}}}\right). \tag{17}$$

In Figure 4.8, we present the Mg II-based $M_{\rm BH}$ estimates from Equations 15, 16, and 17. The three panels of Figure 4.8 that correspond to these three equations are almost

[2]The mean offset correction accounts for the bias introduced when not considering a source's accretion rate in their Hβ-based $M_{\rm BH}$ values [169].

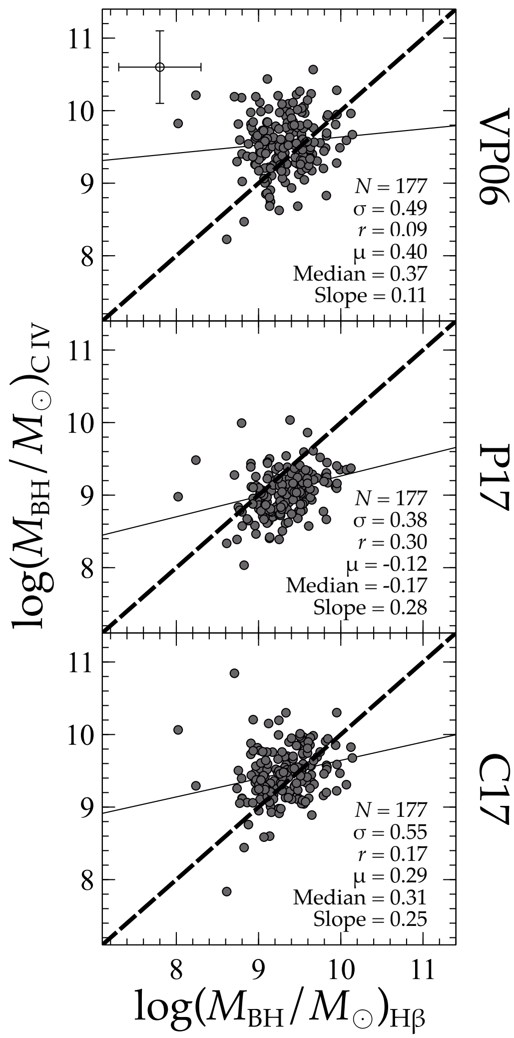

FIGURE 4.7. C IV-based $M_{\rm BH}$ estimates of our sample derived through the methodology of, from top to bottom: VP06, P17, and C17 against the Hβ-based $M_{\rm BH}$ estimates. The dashed lines represent one-to-one relationships and the thin solid lines represent the best linear fit to the data in each panel. The most reliable C IV-based $M_{\rm BH}$ values from this work were derived utilizing $\sigma_{\rm line}$ as the velocity width parameter (see the bottom panel of Figure 4.2). Our prescription shows a considerable improvement in the value of the Pearson correlation coefficient, r, albeit a modest improvement in the standard deviation, with respect to previous work. Additionally, our prescription corrects the mean offset due to considering the accretion rate when estimating Hβ-based $M_{\rm BH}$ values. Typical uncertainty of 0.5 dex on the $M_{\rm BH}$ values is displayed in the top panel for reference.

identical to each other given the similarities between these equations. For comparison, we elect to use the Mg II subsample that contains SDSS and/or GNIRS measurements as it is the largest and, therefore, provides the most meaningful statistics. From our comparison, we find that our Mg II-based $M_{\rm BH}$ estimates given by,

$$\log\left(\frac{M_{\rm BH}}{M_\odot}\right) = 7.000 \pm 0.022 + 2\log\left(\frac{\rm FWHM_{MgII}}{1000\ {\rm km\ s^{-1}}}\right) + 0.5\log\left(\frac{\lambda L_\lambda(3000{\rm \AA})}{10^{44}{\rm erg\ s^{-1}}}\right) \quad (18)$$

which is plotted at the top left panel of Figure 4.6, provides results that are consistent with those from the prescriptions of the previous studies except for the mean offset correction stemming from consideration of the accretion rate. The consistency between Equations 17 and 18 confirm the results derived in L20.

When the C IV EW is included in the regression analysis for the Mg II-based $M_{\rm BH}$ values, we obtain the following prescription (for 160 sources; see, Section 5.2.2),

$$\begin{aligned}\log\left(\frac{M_{\rm BH}}{M_\odot}\right) &= 6.793 \pm 0.047 + 2\log\left(\frac{\rm FWHM_{MgII}}{1000\ {\rm km\ s^{-1}}}\right)\\ &+0.5\log\left(\frac{\lambda L_\lambda(3000{\rm \AA})}{10^{44}{\rm erg\ s^{-1}}}\right) + 0.005 \pm 0.001\log\left(\frac{\rm EW_{CIV}}{\rm \AA}\right),\end{aligned} \quad (19)$$

which is plotted in the bottom left panel of Figure 4.6. In this case, we see a clear improvement in the scatter and the Pearson correlation coefficient and slope of the best-fit relation.

We report all the $M_{\rm BH}$ estimates for the Hβ, C IV and Mg II lines in Table 4.3 where Column (1) provides the SDSS designation of the object, Columns (2), (3), and (4) provide the Hβ-based $M_{\rm BH}$ estimates derived using the FWHM, MAD, and $\sigma_{\rm line}$ as the velocity width, respectively. Columns (5), (6), and (7) provide C IV-based $M_{\rm BH}$ estimates derived from VP06, P17, and C17, respectively. Columns (8), (9), and (10) are the C IV-based estimates derived using the regression analysis for each C IV velocity width parameter, FWHM, MAD, and $\sigma_{\rm line}$, respectively. We report in columns (11), (12), and (13) the Mg II-based $M_{\rm BH}$ estimates derived using the prescriptions of VO09, Z15, and L20. Lastly, in columns (14), (15), and

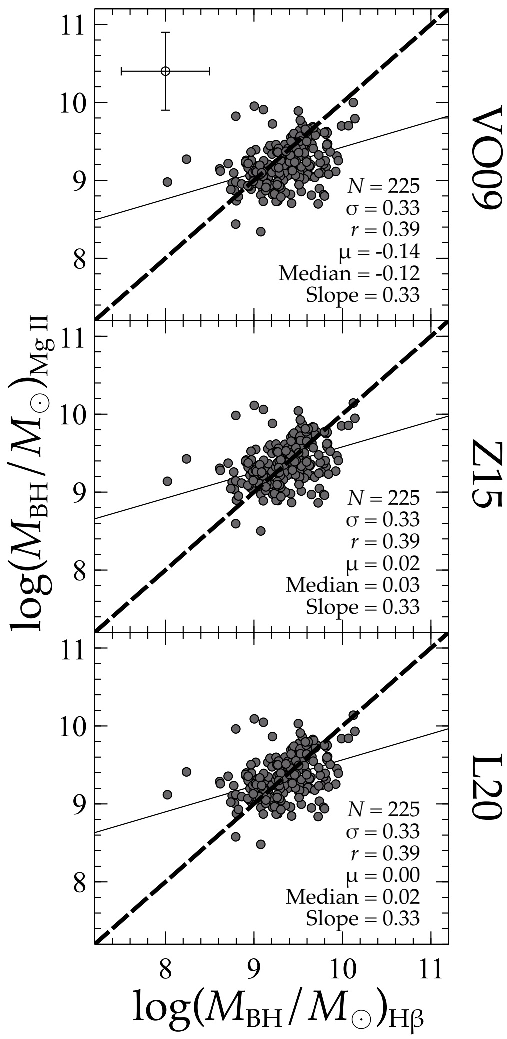

FIGURE 4.8. Mg II-based $M_{\rm BH}$ estimates of our sample derived through the methodology of, from top to bottom, VO09, Z15, and L20 against the Hβ-based $M_{\rm BH}$ estimates. The panels include all Mg II measurements available in SDSS and/or GNIRS. The dashed line in each panel represents a one-to-one relationship and the thin solid line in each panel represents the best linear fit to the data. We find that our results are consistent with those of previous work when only measuring Mg II, but are clearly improved with the inclusion of the C IV EW (see the left most panels of Figure 4.6). Our prescriptions, by design, correct the mean offsets between the Mg II- and Hβ-based $M_{\rm BH}$ values with or without the inclusion of the C IV EW. Typical uncertainty of 0.5 dex on the $M_{\rm BH}$ values is displayed in the top panel for reference.

(16), we report the Mg II-based $M_{\rm BH}$ estimates using each of the three Mg II velocity width parameters, FWHM, MAD, and $\sigma_{\rm line}$, respectively. For our Mg II-based $M_{\rm BH}$ estimates, values are provided with and without the C IV EW term.

4.3.4. Mg II Covered by both SDSS and GNIRS Spectra

For 53 sources from the GNIRS-DQS catalog of M23, in the $2.10 \lesssim z \lesssim 2.40$ redshift range, we have measurable Mg II profiles from both GNIRS and SDSS spectra. In order to confirm consistency across the SDSS and GNIRS spectra, we compare the effects of measuring these spectra in different epochs using different instruments by evaluating the differences in Mg II-based $M_{\rm BH}$ estimates stemming from each spectrum. In order to stay consistent, we used the VO09 method for calculating the Mg II-based $M_{\rm BH}$ estimates for all measurements in our comparison. This comparison is presented in Figure 4.9. Overall, we conclude that the two sets of measurements are consistent with each other and the mean offset between the $\log(M_{\rm BH})$ values is only -0.012.

4.4. Discussion

In this work, we perform calibrations between C IV- and Mg II-based $M_{\rm BH}$ estimates and those based on the Hβ line using the largest, homogeneous sample of luminous quasars at high redshift that cover these three emission lines. The Hβ-based $M_{\rm BH}$ estimates that we calibrate to are accretion-rate-corrected according to the scaling relation presented in [168] that involves the optical Fe II emission. We show that the inclusion of the C IV EW in our calibrations to these Hβ-based $M_{\rm BH}$ values allow for an additional accretion-rate correction in UV-based $M_{\rm BH}$ estimates. The inclusion of this term in our prescriptions leads to UV-based $M_{\rm BH}$ estimates that are closest to those obtained from Hβ.

Our results display improvements with respect to similar $M_{\rm BH}$ calibrations from previous studies that excluded such accretion-rate corrections. When utilizing $\sigma_{\rm line}$ as the velocity width parameter, we obtain the most reliable prescription (Equation 14) for C IV-based $M_{\rm BH}$ values, compared with previous studies of this kind. As shown in the bottom panel of Figure 4.2 we reduce the scatter of C IV-based $M_{\rm BH}$ estimates with respect to those from Hβ

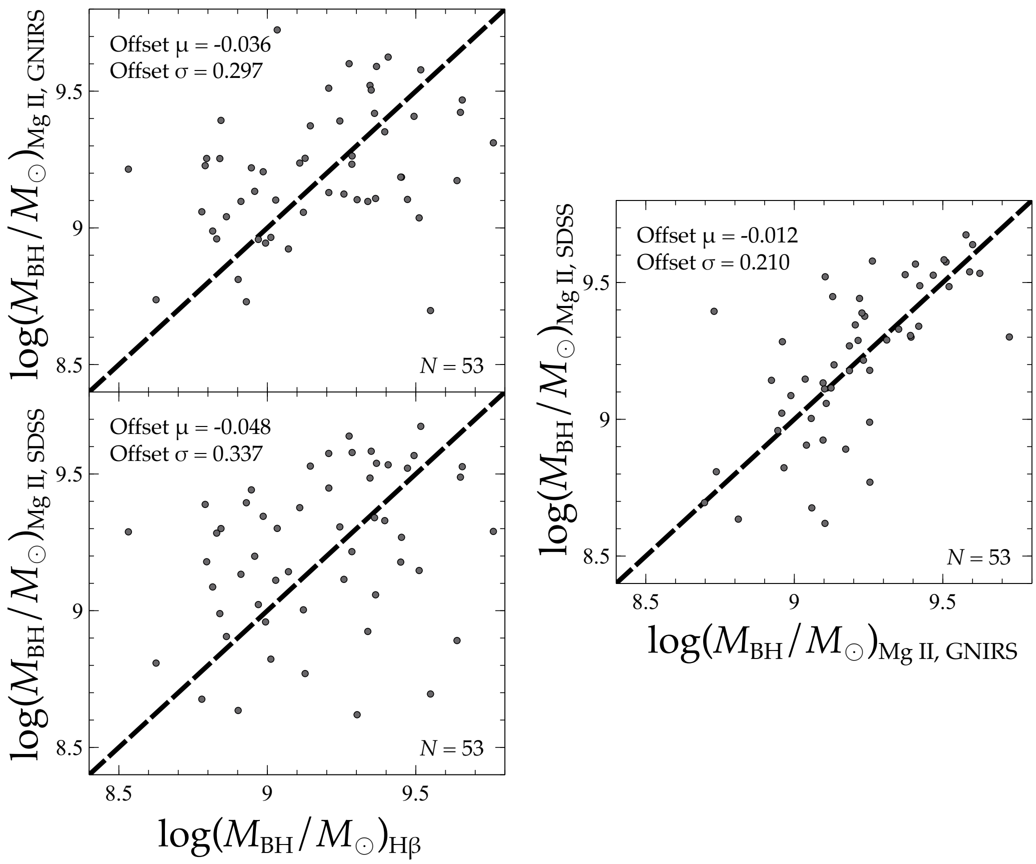

FIGURE 4.9. The upper leftmost and lower leftmost panel compare the GNIRS-DQS and SDSS, respectively, Mg II-based $M_{\rm BH}$ estimates based on the VO09 methodology using the Hβ-based masses. The rightmost panel presents the direct comparison of the SDSS- and GNIRS-DQS-based estimates to each other. In each panel, the mean and standard deviation of the residuals are reported. The dashed line in each panel represents a one-to-one relationship. Overall, we find that the measurements of the Mg II lines from the GNIRS spectra are consistent with the respective measurements from SDSS.

by $\sim 24\%$, $\sim 3\%$, and $\sim 33\%$ compared to the prescriptions of VP06, P17, and C17, respectively (see, Figure 4.7). Similarly, the Pearson correlation coefficient between C IV-based and Hβ-based $M_{\rm BH}$ values improves from 0.09, 0.30, and 0.17 to 0.37, respectively. The slope of the best-fit relation between C IV-based and Hβ-based $M_{\rm BH}$ values also improves from 0.11, 0.28, and 0.25 to 0.36, respectively.

We also present a prescription (Equation 18) for obtaining Mg II-based $M_{\rm BH}$ estimates when only the Mg II line is covered in the spectrum. This prescription is consistent with the findings of L20, confirming their results. This L20 prescription is recommended when only the Mg II emission line is available as there is no systematic mean offset present when compared to the accretion-rate corrected Hβ-based masses. We also note that for the subsample of 34 sources in the highest redshift bin ($3.20 \lesssim z \lesssim 3.50$), the scatter in our prescription is further reduced by $\sim$ 25% (see, Figures 4.5 and 4.6). A larger sample of sources in this redshift range is necessary in order to draw firm conclusions as to whether a larger improvement can be achieved.

When we introduce the additional accretion-rate correction factor, in the form of the EW of C IV, we obtain a significantly improved Mg II-based $M_{\rm BH}$ value using Equation 19. Compared to the Mg II-based $M_{\rm BH}$ estimates derived from Equation 18, this prescription reduces the scatter in the calibration with Hβ-based $M_{\rm BH}$ estimates, by $\sim$ 15%. Similarly, the Pearson correlation coefficient is increased by $\sim$ 51% (see, Figure 4.6). With respect to previous studies discussed throughout this work, our prescriptions, by design, correct the mean offset between UV-based and accretion-rate-corrected Hβ-based $M_{\rm BH}$ estimates. These corrections are critical, as manifested in Figures 4.7 and 4.8, where mean offsets of up to 0.40 and 0.14 appear in the μ values for C IV and Mg II, respectively.

We note that SE $M_{\rm BH}$ estimates, in general, have a 0.5-0.6 dex relative uncertainty and 0.7 dex absolute uncertainty [150]. Meanwhile, $M_{\rm BH}$ measurements that stem from RM campaigns have an inherent uncertainty of 0.3-0.5 dex due to their calibration against the $M - \sigma_\star$ relation [179, 180, 181, 171], and such observations are quite challenging at high redshift [166]. While not being able to completely bridge the gap between these two approaches, the improvements this work provides to the accuracy and precision of SE UV-based $M_{\rm BH}$ estimates are considerable. We find that even when significant outliers are removed from all the $M_{\rm BH}$ comparisons performed above, the resulting improvements in the scatter of up to $\sim$ 7% do not warrant the removal of otherwise ordinary looking sources from the sample. Overall, our work shows that when using a large, uniform calibration sample of quasars having coverage of C IV, Mg II, Fe II and Hβ, and when correcting for accretion rate both in the optical ($\mathcal{R}_{\rm Fe}$) and in the UV (EW(C IV)), one can obtain the most reliable prescriptions for obtaining SE UV-based $M_{\rm BH}$ estimates.

4.4.1. Hα-based $M_{\rm BH}$ values

The GNIRS-DQS spectral inventory of M23 also provides measurements for the Hα emission line where available. In order to test the applicability of using this emission line as a $M_{\rm BH}$ indicator [128], we ran the entire regression analyses presented in this paper substituting FWHM(Hα) for FWHM(Hβ). We find that the results based on Hα are consistent with those obtained from Hβ, thereby confirming the applicability of using Hα to estimate $M_{\rm BH}$ values in quasars.

4.5. Conclusions

We provide prescriptions for reliable rest-frame UV-based $M_{\rm BH}$ estimates with respect to $M_{\rm BH}$ estimates obtained from the Hβ line. Utilizing the GNIRS-DQS catalog (M23), we calibrate SE C IV- and Mg II-based $M_{\rm BH}$ estimates to Hβ-based $M_{\rm BH}$ estimates using a linear regression analysis that includes two basic accretion-rate observable indicators: the relative strength of the optical Fe II emission with respect to Hβ and the EW of the C IV emission line. We also investigate the use of different velocity width parameters for the C IV- and Mg II-based $M_{\rm BH}$ estimates and compare our results with previous studies. We summarize our main results as follows:

(1) The Hβ-based $M_{\rm BH}$ estimates in this work are overestimated by a factor of ~ 2 when the relative strength of the optical Fe II emission is not taken into account, consistent with the results of [169]. All of the $M_{\rm BH}$ prescriptions throughout this work take that correction into account.

(2) The inclusion of the C IV EW in our prescriptions considerably improves the accuracy and precision of UV-based $M_{\rm BH}$ estimates. With respect to previous studies, our most reliable UV-based $M_{\rm BH}$ values reduces the scatter by $\sim 15\%$ when compared to Hβ-based values.

(3) The preferred velocity width parameters for estimating $M_{\rm BH}$ using C IV and Mg II are $\sigma_{\rm line}$ and FWHM, respectively.

(4) Equation 14 presents the prescription for obtaining the most reliable C IV-based $M_{\rm BH}$ estimates, in the absence of Mg II coverage. Conversely, if the source's spectrum only covers the Mg II line, the prescription from L20 (Equation 17) is preferred. Otherwise, Equation 19 presents the most robust prescription for UV-based $M_{\rm BH}$ estimates when there is spectral coverage of both C IV and Mg II emission lines.

(5) NIR observations of additional sources at $3.20 \lesssim z \lesssim 3.50$ would allow us to test if further significant improvements can be achieved for UV-based $M_{\rm BH}$ estimates. Primarily, this redshift range reduces the uncertainty introduced when measuring Mg II by shifting the emission line further from the blue edge of the J-band. A larger sample with more reliable measurements at this range may reveal further discrepancies between low and high luminosity objects.

In the coming decade, we expect that millions of high-redshift ($z \gtrsim 0.8$) quasars will have $M_{\rm BH}$ estimates derived from rest-frame UV emission lines through large spectroscopic surveys, e.g., the Dark Energy Spectroscopic Instrument (DESI; [93]) and the 4m Multi-Object Spectroscopic Telescope [95]. It is therefore crucial to derive the most reliable $M_{\rm BH}$ estimates for future high-redshift quasar catalogs using the prescriptions provided in this work.

We gratefully thank the contributions to this work from Yue Shen and Michael A. Strauss. This work is supported by National Science Foundation grants AST-1815281 (C. D., O. S., B. M. M.), AST-1815645 (M. S. B., A. D. M.), and AST-2106990 (W. N. B.). I.A. acknowledges the support from Universidad Nacional de La Plata through grant 11/G153. This research has made use of the NASA/IPAC Extragalactic Database (NED), which is operated by the Jet Propulsion Laboratory, California Institute of Technology, under contract with the National Aeronautics and Space Administration.

	C IV					Mg II				
	FWHM	MAD	$\sigma_{\rm line}$	EW	$\lambda_{\rm peak}$	FWHM	MAD	$\sigma_{\rm line}$	EW	$\lambda_{\rm peak}$
Quasar	km s^{-1}	km s^{-1}	km s^{-1}	Å	Å	km s^{-1}	km s^{-1}	km s^{-1}	Å	Å
SDSS J001018.88+280932.5	2517^{+53}_{-78}	2274^{+37}_{-54}	3158^{+55}_{-82}	61^{+1}_{-1}	4045^{+0}_{-0}	...	...	...	...	...
SDSS J001249.89+285552.6	...	...	...	...	...	4195^{+188}_{-249}	2183^{+480}_{-757}	2956^{+637}_{-1017}	21^{+7}_{-9}	11874+3 −5
SDSS J001355.10-012304.0	...	...	...	...	...	2815^{+344}_{-455}	1249^{+260}_{-401}	1595^{+332}_{-515}	17^{+1}_{-2}	12274+4 −5
SDSS J001453.20+091217.6	6487^{+822}_{-1227}	3798^{+910}_{-1358}	5788^{+1383}_{-2064}	39^{+3}_{-5}	5152^{+5}_{-7}	...	...	...	...	...
SDSS J001813.30+361058.6	6079^{+197}_{-294}	3247^{+238}_{-356}	3861^{+369}_{-550}	26^{+1}_{-2}	5116^{+2}_{-3}	5129^{+983}_{-1301}	3354^{+1648}_{-2632}	4543^{+2198}_{-3511}	25^{+8}_{-11}	9303+13 −17
SDSS J001914.46+155555.9	4162^{+215}_{-320}	2329^{+81}_{-120}	3038^{+121}_{-180}	45^{+1}_{-1}	5054^{+1}_{-2}	4380^{+327}_{-433}	1628^{+821}_{-1235}	2061^{+1092}_{-1643}	23^{+1}_{-1}	9141+5 −6
SDSS J002634.46+274015.5	5196^{+739}_{-1103}	6331^{+868}_{-1295}	6701^{+1462}_{-2181}	135^{+10}_{-15}	5023^{+5}_{-7}	3158^{+150}_{-198}	1747^{+645}_{-979}	2373^{+934}_{-1418}	36^{+1}_{-1}	9097+2 −2
SDSS J003001.11-015743.5	6077^{+265}_{-396}	3339^{+251}_{-374}	3719^{+449}_{-669}	53^{+2}_{-3}	3995^{+1}_{-2}	...	...	...	...	...
SDSS J003416.61+002241.1	4213^{+107}_{-160}	2092^{+43}_{-65}	2710^{+66}_{-98}	29^{+0}_{-0}	4067^{+1}_{-1}	...	...	...	...	...
SDSS J003853.15+333044.3	8273^{+564}_{-841}	2485^{+403}_{-602}	3817^{+593}_{-884}	14^{+1}_{-1}	5213^{+11}_{-17}	...	...	...	...	...
SDSS J004613.54+010425.7	...	...	...	...	...	...	...	...	...	...
SDSS J004710.48+163106.5	6432^{+551}_{-822}	3074^{+210}_{-313}	4041^{+319}_{-476}	22^{+1}_{-1}	4898^{+3}_{-5}	...	...	...	...	...
SDSS J004719.71+014813.9	3805^{+102}_{-152}	2356^{+42}_{-62}	3152^{+68}_{-102}	49^{+0}_{-1}	4009^{+0}_{-1}	...	...	...	...	...
SDSS J005233.67+014040.8	6744^{+183}_{-273}	3020^{+55}_{-82}	3866^{+86}_{-128}	32^{+0}_{-1}	5103^{+1}_{-2}	3421^{+281}_{-372}	1128^{+368}_{-576}	1403^{+444}_{-696}	15^{+1}_{-2}	9248+6 −8
SDSS J005307.71+191022.7	6607^{+2423}_{-3614}	3611^{+862}_{-1287}	6109^{+1185}_{-1767}	38^{+4}_{-5}	3998^{+6}_{-9}	...	...	...	...	...
SDSS J010113.72+032427.0	6397^{+164}_{-245}	4160^{+133}_{-199}	6049^{+209}_{-312}	103^{+1}_{-2}	3992^{+0}_{-1}	...	...	...	...	...
SDSS J010328.71-110414.4	...	...	...	...	...	3744^{+607}_{-804}	2730^{+1272}_{-1931}	3764^{+1667}_{-2531}	20^{+2}_{-3}	8955+10 −13
SDSS J010447.39+101031.6	6798^{+537}_{-801}	4346^{+1108}_{-1654}	5892^{+1600}_{-2388}	22^{+2}_{-4}	5198^{+2}_{-3}	...	...	...	...	...
SDSS J010500.72+194230.4	7136^{+415}_{-620}	3764^{+1292}_{-1927}	6934^{+1901}_{-2835}	34^{+4}_{-5}	5102^{+4}_{-6}	3187^{+634}_{-839}	2253^{+462}_{-720}	3078^{+617}_{-967}	34^{+8}_{-11}	9290+5 −7
SDSS J010615.93+101043.0	5335^{+264}_{-394}	2246^{+305}_{-455}	3136^{+552}_{-824}	21^{+1}_{-2}	5159^{+4}_{-5}	...	...	...	...	...
SDSS J010643.23-031536.4	3515^{+343}_{-511}	2754^{+541}_{-807}	3357^{+820}_{-1223}	8^{+1}_{-1}	5007^{+2}_{-3}	4300^{+681}_{-901}	1022^{+352}_{-545}	1286^{+417}_{-650}	9^{+1}_{-1}	9066+4 −5
SDSS J011538.72+242446.0	6622^{+128}_{-191}	4305^{+225}_{-336}	5156^{+353}_{-527}	30^{+1}_{-1}	5219^{+1}_{-2}	5886^{+647}_{-856}	2133^{+414}_{-649}	2672^{+543}_{-851}	29^{+2}_{-2}	9530+17 −22
SDSS J013012.36+153157.9	...	...	...	...	...	2024^{+483}_{-640}	978^{+185}_{-287}	1271^{+233}_{-361}	14^{+8}_{-10}	9367+4 −5
SDSS J013113.25+085245.5	5075^{+471}_{-703}	2526^{+98}_{-146}	3010^{+147}_{-219}	23^{+0}_{-1}	7016^{+2}_{-3}	3212^{+258}_{-342}	1088^{+142}_{-221}	1364^{+176}_{-271}	18^{+1}_{-1}	12709+3 −4

SDSS J013136.44+130331.0	1932^{+1142}_{-1704}	543^{+2000}_{-2983}	2508^{+2524}_{-3765}	3^{+1}_{-2}	3995^{+8}_{-12}	...	...	...	...	...
SDSS J013417.81-005036.2	6403^{+746}_{-1113}	2053^{+723}_{-1079}	3209^{+1162}_{-1734}	7^{+1}_{-1}	5028^{+8}_{-12}	...	...	...	...	...
SDSS J013647.96-062753.6	10039^{+1927}_{-2874}	3456^{+181}_{-271}	4315^{+205}_{-306}	15^{+2}_{-2}	6566^{+29}_{-44}	4505^{+207}_{-274}	1358^{+202}_{-309}	1669^{+247}_{-379}	15^{+2}_{-3}	12045+6 −8
SDSS J013652.52+122501.5	...	...	...	...	...	...	...	...	...	...
SDSS J014018.20-013805.8	...	...	...	...	...	2924^{+191}_{-253}	925^{+367}_{-560}	1144^{+525}_{-801}	19^{+1}_{-1}	9053+6 −8
SDSS J014128.26+070606.1	4988^{+123}_{-183}	2724^{+434}_{-648}	4272^{+833}_{-1243}	43^{+2}_{-2}	5044^{+1}_{-1}	3151^{+353}_{-468}	1051^{+163}_{-252}	1314^{+200}_{-308}	20^{+7}_{-9}	9161+9 −12
SDSS J014206.86+025713.0	...	...	...	...	...	...	...	...	...	...
SDSS J014932.06+152754.0	2671^{+161}_{-240}	2795^{+176}_{-262}	4044^{+281}_{-419}	57^{+1}_{-2}	5242^{+1}_{-1}	...	...	...	...	...
SDSS J020329.86-091020.3	5817^{+309}_{-460}	5157^{+1173}_{-1750}	6124^{+1513}_{-2256}	29^{+4}_{-6}	3987^{+1}_{-2}	...	...	...	...	...
SDSS J021259.21+132618.8	8221^{+541}_{-807}	6506^{+640}_{-955}	6559^{+981}_{-1463}	44^{+4}_{-6}	4048^{+3}_{-5}	...	...	...	...	...
SDSS J022007.64-010731.1	...	...	...	...	...	2662^{+171}_{-227}	1028^{+505}_{-763}	1299^{+713}_{-1077}	18^{+1}_{-1}	12411+5 −6
SDSS J025042.45+003536.7	...	...	...	...	...	...	...	...	...	...
SDSS J035150.97-061326.4	3650^{+338}_{-504}	1685^{+114}_{-170}	2123^{+178}_{-266}	14^{+1}_{-1}	4987^{+3}_{-5}	2760^{+265}_{-351}	1034^{+215}_{-329}	1306^{+249}_{-384}	12^{+1}_{-1}	9033+6 −7
SDSS J072517.52+434553.4	7423^{+504}_{-752}	2724^{+93}_{-139}	3527^{+129}_{-192}	19^{+1}_{-1}	4014^{+2}_{-3}	...	...	...	...	...
SDSS J072928.48+252451.8	3556^{+468}_{-698}	2332^{+88}_{-132}	2741^{+129}_{-193}	17^{+1}_{-1}	5118^{+1}_{-2}	3290^{+701}_{-927}	1279^{+225}_{-343}	1603^{+262}_{-400}	11^{+2}_{-2}	9272+12 −15
SDSS J073132.18+461347.0	...	...	...	...	...	...	...	...	...	...
SDSS J073519.68+240104.6	...	...	...	...	...	2187^{+114}_{-150}	1261^{+153}_{-234}	1697^{+207}_{-315}	48^{+1}_{-2}	11989+2 −2
SDSS J073900.90+485159.0	5840^{+219}_{-327}	4629^{+353}_{-527}	4380^{+629}_{-938}	35^{+1}_{-2}	4044^{+2}_{-3}	...	...	...	...	...
SDSS J073913.65+461858.5	5291^{+226}_{-337}	2339^{+99}_{-147}	2852^{+158}_{-236}	16^{+0}_{-1}	3991^{+2}_{-3}	...	...	...	...	...
SDSS J074941.16+262715.9	4252^{+76}_{-114}	1948^{+40}_{-60}	2661^{+62}_{-92}	27^{+0}_{-0}	4004^{+0}_{-1}	...	...	...	...	...
SDSS J075115.43+505439.1	10208^{+724}_{-1080}	3738^{+1210}_{-1805}	5667^{+2229}_{-3326}	7^{+1}_{-1}	5027^{+3}_{-4}	...	...	...	...	...
SDSS J075136.36+432732.4	5874^{+237}_{-354}	3325^{+120}_{-179}	4573^{+192}_{-286}	34^{+1}_{-1}	4999^{+1}_{-2}	2616^{+495}_{-655}	1547^{+763}_{-1148}	2040^{+1053}_{-1584}	21^{+1}_{-1}	9092+3 −5
SDSS J075405.08+280339.6	4106^{+203}_{-303}	4284^{+97}_{-145}	5672^{+146}_{-218}	54^{+1}_{-1}	5071^{+1}_{-1}	5616^{+292}_{-386}	1988^{+880}_{-1330}	2529^{+1177}_{-1780}	25^{+1}_{-1}	9129+9 −11
SDSS J075547.83+220450.1	5207^{+87}_{-130}	2591^{+37}_{-56}	3431^{+60}_{-89}	28^{+0}_{-0}	5134^{+1}_{-1}	...	...	...	...	...
SDSS J075837.62+135733.7	...	...	...	...	...	...	...	...	...	...
SDSS J080036.01+501044.3	...	...	...	...	...	...	...	...	...	...
SDSS J080117.79+521034.5	10844^{+248}_{-370}	4142^{+82}_{-122}	4962^{+114}_{-170}	19^{+0}_{-0}	6525^{+6}_{-9}	4515^{+158}_{-209}	1615^{+660}_{-998}	2031^{+867}_{-1311}	21^{+1}_{-1}	11926+3 −4
SDSS J080117.91+333411.9	5550^{+463}_{-691}	2982^{+176}_{-263}	4271^{+253}_{-377}	19^{+1}_{-1}	4021^{+1}_{-2}	...	...	...	...	...

SDSS J080413.66+251633.9	5241^{+130}_{-193}	2024^{+40}_{-60}	2600^{+57}_{-85}	12^{+0}_{-0}	5109^{+2}_{-3}	2422^{+182}_{-241}	852^{+172}_{-263}	1066^{+214}_{-326}	17^{+2}_{-2}	9251+3 −4
SDSS J080636.81+345048.5	...	...	...	...	...	...	...	...	...	...
SDSS J081019.48+095040.9	6825^{+534}_{-796}	3331^{+176}_{-262}	3991^{+296}_{-441}	26^{+1}_{-1}	4976^{+3}_{-5}	3371^{+284}_{-376}	1094^{+200}_{-308}	1360^{+255}_{-390}	16^{+2}_{-2}	9053+9 −12
SDSS J081056.96+120914.8	4299^{+204}_{-304}	2939^{+201}_{-300}	4169^{+327}_{-488}	35^{+1}_{-2}	5050^{+1}_{-2}	2291^{+571}_{-755}	2293^{+2364}_{-2293}	3146^{+1895}_{-3007}	18^{+4}_{-5}	9099+4 −5
SDSS J081114.66+172057.4	...	...	...	...	...	...	...	...	...	...
SDSS J081127.44+461812.9	7825^{+293}_{-438}	3434^{+69}_{-104}	4292^{+104}_{-156}	20^{+0}_{-0}	5023^{+1}_{-2}	3299^{+399}_{-529}	1294^{+195}_{-301}	1623^{+219}_{-339}	19^{+1}_{-1}	9075+3 −4
SDSS J081410.76+443706.9	5243^{+384}_{-573}	4361^{+697}_{-1039}	3989^{+1139}_{-1700}	36^{+3}_{-5}	5059^{+4}_{-6}	3026^{+813}_{-1075}	2446^{+766}_{-1187}	3238^{+1043}_{-1616}	28^{+4}_{-5}	9169+7 −10
SDSS J081558.35+154055.2	3696^{+101}_{-151}	2381^{+79}_{-118}	3203^{+129}_{-193}	29^{+0}_{-1}	5000^{+1}_{-1}	3355^{+157}_{-208}	1053^{+3564}_{-1053}	1320^{+4443}_{-1320}	53^{+16}_{-21}	9057+2 −3
SDSS J081940.58+082357.9	5073^{+184}_{-274}	3184^{+305}_{-455}	5438^{+511}_{-762}	38^{+1}_{-2}	6495^{+2}_{-2}	4988^{+348}_{-460}	2399^{+499}_{-787}	3149^{+643}_{-1014}	21^{+1}_{-1}	11767+9 −12
SDSS J082507.67+360411.1	3414^{+99}_{-148}	2180^{+95}_{-142}	2883^{+167}_{-248}	47^{+1}_{-1}	3990^{+0}_{-1}	...	...	...	...	...
SDSS J082603.32+342800.6	9451^{+1813}_{-2704}	4874^{+1514}_{-2258}	6991^{+2266}_{-3380}	26^{+3}_{-5}	5105^{+7}_{-11}	4364^{+479}_{-634}	2054^{+400}_{-620}	2671^{+493}_{-778}	30^{+1}_{-2}	9231+5 −7
SDSS J082643.45+143427.6	...	...	...	...	...	3313^{+322}_{-427}	1439^{+300}_{-468}	1890^{+419}_{-652}	21^{+1}_{-1}	9257+2 −3
SDSS J082644.66+163549.0	2484^{+23}_{-35}	1949^{+27}_{-40}	2727^{+45}_{-67}	62^{+0}_{-0}	4939^{+0}_{-0}	...	...	...	...	...
SDSS J082736.89+061812.1	2755^{+56}_{-84}	2041^{+34}_{-51}	2805^{+54}_{-81}	23^{+0}_{-0}	4946^{+0}_{-1}	...	...	...	...	...
SDSS J083255.63+182300.7	7222^{+1290}_{-1925}	3601^{+1516}_{-2261}	6024^{+2513}_{-3749}	24^{+3}_{-5}	5041^{+8}_{-12}	3958^{+403}_{-533}	1441^{+1050}_{-1441}	1801^{+1408}_{-1801}	16^{+2}_{-3}	9194+12 −16
SDSS J083417.12+354833.1	5657^{+142}_{-212}	2393^{+42}_{-63}	3014^{+68}_{-101}	22^{+0}_{-0}	4884^{+1}_{-2}	3814^{+1524}_{-2017}	1679^{+473}_{-737}	2146^{+606}_{-945}	14^{+3}_{-4}	8823+9 −11
SDSS J083745.74+052109.4	...	...	...	...	...	3269^{+387}_{-512}	2517^{+523}_{-815}	3574^{+695}_{-1090}	26^{+2}_{-3}	9404+6 −8
SDSS J084017.87+103428.8	3808^{+64}_{-96}	2052^{+44}_{-66}	2729^{+74}_{-111}	46^{+0}_{-1}	6704^{+1}_{-1}	2094^{+155}_{-205}	1203^{+256}_{-395}	1691^{+332}_{-515}	24^{+9}_{-11}	12127+3 −4
SDSS J084029.97+465113.7	4814^{+202}_{-302}	1986^{+41}_{-62}	2480^{+62}_{-92}	19^{+0}_{-0}	3979^{+1}_{-2}	...	...	...	...	...
SDSS J084133.15+200525.7	...	...	...	...	...	...	...	...	...	...
SDSS J084401.95+050357.9	...	...	...	...	...	...	...	...	...	...
SDSS J084526.75+550546.8	4385^{+144}_{-215}	2588^{+86}_{-128}	3524^{+147}_{-219}	53^{+1}_{-1}	4050^{+1}_{-1}	...	...	...	...	...
SDSS J084729.52+441616.7	...	...	...	...	...	2282^{+1071}_{-1418}	736^{+164}_{-250}	909^{+177}_{-270}	10^{+2}_{-3}	9376+6 −7
SDSS J084846.11+611234.6	3641^{+78}_{-117}	2321^{+73}_{-109}	3196^{+119}_{-178}	29^{+0}_{-1}	5044^{+1}_{-1}	2683^{+303}_{-401}	1409^{+269}_{-427}	1894^{+379}_{-598}	12^{+6}_{-8}	9115+3 −4
SDSS J085046.17+522057.4	...	...	...	...	...	...	...	...	...	...
SDSS J085337.36+121800.3	6953^{+638}_{-952}	2238^{+1767}_{-2637}	5059^{+2900}_{-4327}	8^{+1}_{-2}	4933^{+4}_{-7}	...	...	...	...	...
SDSS J085344.17+354104.5	8456^{+1269}_{-1893}	2932^{+1320}_{-1969}	3956^{+1911}_{-2851}	4^{+1}_{-1}	4897^{+18}_{-27}	...	...	...	...	...
SDSS J085443.10+075223.2	4938^{+98}_{-146}	2506^{+76}_{-113}	3485^{+130}_{-194}	29^{+0}_{-1}	4026^{+1}_{-1}	...	...	...	...	...

SDSS J085726.94+331317.1	...	...	...	...	...	...	...	...	...	...
SDSS J085856.00+015219.4	9178^{+495}_{-738}	3529^{+151}_{-225}	4541^{+224}_{-334}	24^{+1}_{-1}	4871^{+5}_{-8}	...	...	...	...	...
SDSS J085946.79+603702.1	5925^{+207}_{-309}	2604^{+71}_{-106}	3306^{+121}_{-181}	28^{+0}_{-1}	5048^{+2}_{-2}	...	...	...	...	...
SDSS J090247.57+304120.7	3087^{+207}_{-308}	2492^{+133}_{-198}	3268^{+196}_{-292}	48^{+1}_{-2}	3966^{+1}_{-1}	...	...	...	...	...
SDSS J090444.33+233354.0	...	...	...	...	...	...	...	...	...	...
SDSS J090646.98+174046.8	6127^{+284}_{-423}	2504^{+75}_{-112}	3262^{+118}_{-176}	17^{+0}_{-1}	3976^{+2}_{-3}	...	...	...	...	...
SDSS J090709.89+250620.8	4140^{+407}_{-607}	2069^{+99}_{-148}	2561^{+152}_{-226}	19^{+0}_{-1}	6666^{+2}_{-3}	2538^{+71}_{-94}	1888^{+853}_{-1289}	2696^{+1205}_{-1821}	26^{+1}_{-1}	12089+1 −2
SDSS J090710.36+430000.2	5632^{+72}_{-107}	2681^{+60}_{-90}	3473^{+105}_{-157}	24^{+0}_{-0}	4927^{+1}_{-1}	...	...	...	...	...
SDSS J091054.17+375914.9	...	...	...	...	...	3557^{+436}_{-576}	1681^{+262}_{-409}	2158^{+341}_{-528}	32^{+3}_{-4}	8860+3 −4
SDSS J091118.02+202254.7	...	...	...	...	...	3025^{+472}_{-625}	1258^{+236}_{-370}	1676^{+278}_{-438}	17^{+9}_{-12}	11830+9 −12
SDSS J091301.01+422344.7	...	...	...	...	...	...	...	...	...	...
SDSS J091328.23+394443.9	...	...	...	...	...	...	...	...	...	...
SDSS J091425.72+504854.9	...	...	...	...	...	...	...	...	...	...
SDSS J091716.79+461435.3	...	...	...	...	...	...	...	...	...	...
SDSS J091941.26+253537.7	3636^{+124}_{-185}	2827^{+77}_{-116}	3721^{+115}_{-172}	37^{+1}_{-1}	5055^{+0}_{-1}	6096^{+220}_{-291}	1906^{+250}_{-379}	2353^{+305}_{-457}	28^{+1}_{-1}	9157+9 −12
SDSS J092216.04+160526.4	3705^{+55}_{-82}	1993^{+71}_{-106}	2754^{+121}_{-180}	44^{+1}_{-1}	5219^{+0}_{-1}	...	...	...	...	...
SDSS J092325.25+453222.2	4745^{+89}_{-133}	2799^{+80}_{-119}	3936^{+138}_{-206}	35^{+0}_{-1}	6879^{+1}_{-1}	2702^{+64}_{-84}	1133^{+251}_{-387}	1460^{+290}_{-449}	11^{+1}_{-1}	12524+2 −2
SDSS J092456.66+305354.7	5575^{+527}_{-787}	3087^{+912}_{-1361}	4426^{+1602}_{-2390}	18^{+1}_{-2}	6861^{+6}_{-9}	3970^{+262}_{-346}	1593^{+273}_{-421}	2055^{+357}_{-554}	25^{+31}_{-25}	12431+4 −5
SDSS J092523.24+214119.8	3385^{+205}_{-305}	1780^{+85}_{-127}	2572^{+151}_{-225}	44^{+1}_{-2}	5201^{+2}_{-3}	...	...	...	...	...
SDSS J092555.05+490338.2	4645^{+972}_{-1450}	6313^{+1884}_{-2811}	5262^{+2659}_{-3967}	32^{+8}_{-11}	5164^{+6}_{-8}	...	...	...	...	...
SDSS J092942.97+064604.1	6439^{+109}_{-163}	3184^{+160}_{-239}	4260^{+302}_{-450}	26^{+0}_{-1}	4016^{+1}_{-1}	...	...	...	...	...
SDSS J093251.98+023727.0	...	...	...	...	...	4288^{+910}_{-1204}	1583^{+1007}_{-1529}	1973^{+1317}_{-1973}	15^{+21}_{-15}	8874+12 −15
SDSS J093533.88+235720.5	5919^{+189}_{-281}	3823^{+121}_{-181}	5020^{+189}_{-282}	44^{+1}_{-1}	5104^{+1}_{-2}	4658^{+361}_{-477}	1683^{+238}_{-366}	2123^{+325}_{-499}	32^{+7}_{-9}	9249+6 −8
SDSS J094140.16+325703.2	9991^{+312}_{-465}	3601^{+97}_{-145}	4243^{+122}_{-182}	15^{+0}_{-1}	6817^{+16}_{-24}	3192^{+81}_{-107}	1462^{+286}_{-444}	1931^{+356}_{-555}	21^{+1}_{-1}	12365+2 −2
SDSS J094214.40+034100.3	2345^{+44}_{-65}	1574^{+24}_{-36}	2153^{+39}_{-58}	35^{+0}_{-0}	4001^{+0}_{-1}	...	...	...	...	...
SDSS J094328.94+140415.6	...	...	...	...	...	...	...	...	...	...
SDSS J094347.02+690818.4	6462^{+282}_{-421}	2829^{+69}_{-103}	3562^{+101}_{-150}	44^{+1}_{-1}	4009^{+3}_{-4}	...	...	...	...	...
SDSS J094427.27+614424.6	...	...	...	...	...	...	...	...	...	...

SDSS J094602.31+274407.0	11851^{+992}_{-1479}	4528^{+809}_{-1207}	5032^{+1575}_{-2349}	6^{+0}_{-1}	5240^{+0}_{-0}	...	...	...	...	...
SDSS J094637.83-012411.5	4885^{+206}_{-307}	2543^{+49}_{-73}	3270^{+69}_{-104}	19^{+0}_{-0}	4978^{+1}_{-1}	...	...	...	...	...
SDSS J094646.94+392719.0	8980^{+447}_{-667}	8840^{+1496}_{-2231}	12121^{+2321}_{-3462}	29^{+3}_{-4}	4935^{+3}_{-4}	4481^{+376}_{-498}	2039^{+814}_{-1219}	2616^{+1119}_{-1677}	19^{+1}_{-1}	9038^{+3}_{-4}
SDSS J094648.59+171827.7	4516^{+161}_{-239}	2242^{+65}_{-98}	2862^{+104}_{-155}	44^{+1}_{-1}	5103^{+1}_{-2}	3065^{+102}_{-134}	1834^{+1107}_{-1673}	2520^{+1552}_{-2345}	27^{+1}_{-1}	9241^{+1}_{-2}
SDSS J094902.38+531241.5	...	...	...	...	...	...	...	...	...	...
SDSS J095047.45+194446.1	4805^{+428}_{-638}	2121^{+179}_{-267}	3064^{+280}_{-418}	35^{+2}_{-2}	3983^{+3}_{-4}	...	...	...	...	...
SDSS J095058.76+263424.6	5841^{+264}_{-394}	3148^{+88}_{-132}	4188^{+130}_{-194}	22^{+0}_{-0}	5222^{+1}_{-2}	...	...	...	...	...
SDSS J095327.95+322551.5	...	...	...	...	...	...	...	...	...	...
SDSS J095330.36+353223.1	8282^{+650}_{-969}	3064^{+96}_{-143}	3971^{+129}_{-192}	13^{+0}_{-1}	5206^{+7}_{-10}	...	...	...	...	...
SDSS J095544.25+182546.9	3392^{+83}_{-125}	1761^{+72}_{-107}	2576^{+123}_{-183}	39^{+1}_{-1}	6933^{+1}_{-1}	2540^{+126}_{-166}	1246^{+617}_{-928}	1677^{+844}_{-1270}	14^{+1}_{-1}	12545^{+5}_{-7}
SDSS J095555.68+351652.6	5390^{+279}_{-416}	2738^{+59}_{-89}	3433^{+87}_{-129}	29^{+0}_{-1}	4054^{+1}_{-1}	...	...	...	...	...
SDSS J095707.82+184739.9	10500^{+787}_{-1174}	3951^{+2254}_{-3363}	10784^{+3566}_{-5320}	15^{+2}_{-3}	5149^{+0}_{-0}	...	...	...	...	...
SDSS J095746.75+565800.7	...	...	...	...	...	...	...	...	...	...
SDSS J095823.07+371218.3	6005^{+109}_{-163}	3236^{+50}_{-75}	4207^{+78}_{-116}	23^{+0}_{-0}	5050^{+1}_{-1}	3570^{+216}_{-286}	1569^{+231}_{-360}	2031^{+317}_{-493}	21^{+1}_{-1}	9187^{+2}_{-3}
SDSS J095852.19+120245.0	5862^{+186}_{-277}	2615^{+115}_{-172}	3130^{+163}_{-243}	17^{+0}_{-1}	6656^{+4}_{-6}	3762^{+100}_{-132}	1956^{+722}_{-1096}	2690^{+933}_{-1416}	15^{+1}_{-1}	12057^{+2}_{-2}
SDSS J100212.63+520800.2	4492^{+135}_{-201}	1810^{+62}_{-92}	2213^{+87}_{-129}	18^{+0}_{-1}	4045^{+2}_{-3}	...	...	...	...	...
SDSS J100610.55+370513.8	...	...	...	...	...	2969^{+687}_{-909}	1571^{+273}_{-429}	2065^{+360}_{-565}	21^{+2}_{-3}	11766^{+5}_{-7}
SDSS J100653.26+011938.7	...	...	...	...	...	...	...	...	...	...
SDSS J100850.06-023831.6	3707^{+73}_{-109}	2326^{+36}_{-54}	3044^{+54}_{-81}	34^{+0}_{-0}	5042^{+0}_{-1}	...	...	...	...	...
SDSS J101106.74+114759.4	3417^{+79}_{-117}	1901^{+70}_{-104}	2490^{+100}_{-149}	30^{+0}_{-1}	5025^{+1}_{-1}	2095^{+123}_{-162}	738^{+174}_{-272}	931^{+209}_{-324}	13^{+1}_{-1}	9093^{+2}_{-3}
SDSS J101211.44+330926.4	...	...	...	...	...	2244^{+136}_{-180}	2139^{+623}_{-946}	3178^{+819}_{-1243}	17^{+6}_{-8}	9104^{+2}_{-2}
SDSS J101353.43+244916.4	...	...	...	...	...	...	...	...	...	...
SDSS J101425.11+032003.7	6980^{+505}_{-754}	2464^{+381}_{-568}	3124^{+662}_{-988}	14^{+1}_{-1}	4867^{+7}_{-11}	3920^{+768}_{-1016}	3015^{+1465}_{-2258}	3975^{+1925}_{-2967}	35^{+24}_{-31}	8678^{+6}_{-8}
SDSS J101429.57+481938.4	7613^{+212}_{-316}	2303^{+84}_{-126}	3073^{+124}_{-185}	19^{+0}_{-0}	3956^{+6}_{-9}	...	...	...	...	...
SDSS J101542.04+430455.6	...	...	...	...	...	...	...	...	...	...
SDSS J101724.26+333403.3	4338^{+188}_{-281}	1913^{+44}_{-66}	2459^{+59}_{-89}	20^{+0}_{-1}	3985^{+1}_{-2}	...	...	...	...	...
SDSS J102154.00+051646.3	...	...	...	...	...	...	...	...	...	...
SDSS J102537.69+211509.1	5588^{+209}_{-311}	2821^{+60}_{-89}	3769^{+83}_{-124}	47^{+1}_{-1}	5035^{+1}_{-1}	...	...	...	...	...

SDSS J102731.49+541809.7	5686^{+1885}_{-2813}	6472^{+926}_{-1381}	4800^{+1216}_{-1814}	21^{+3}_{-5}	4007^{+9}_{-13}	...	...	...	...	...
SDSS J102907.09+651024.6	8220^{+105}_{-156}	3221^{+35}_{-52}	4032^{+51}_{-76}	24^{+0}_{-0}	4888^{+1}_{-2}	3228^{+267}_{-353}	975^{+534}_{-811}	1195^{+699}_{-1062}	12^{+1}_{-1}	8886+11 −15
SDSS J103209.78+385630.5	6008^{+574}_{-856}	2643^{+74}_{-110}	3302^{+107}_{-160}	16^{+0}_{-1}	4003^{+1}_{-2}	...	...	...	...	...
SDSS J103236.98+230554.1	2560^{+279}_{-415}	2611^{+86}_{-129}	3349^{+123}_{-184}	18^{+0}_{-0}	5230^{+1}_{-1}	...	...	...	...	...
SDSS J103246.19+323618.0	...	...	...	...	...	...	...	...	...	...
SDSS J103405.73+463545.4	...	...	...	...	...	5239^{+238}_{-315}	1788^{+300}_{-463}	2247^{+360}_{-555}	19^{+1}_{-1}	9012+5 −7
SDSS J103718.23+302509.1	...	...	...	...	...	3105^{+295}_{-391}	1858^{+285}_{-442}	2400^{+364}_{-558}	26^{+5}_{-7}	9247+3 −5
SDSS J104018.51+572448.1	7091^{+329}_{-491}	3224^{+130}_{-194}	4600^{+185}_{-276}	14^{+0}_{-0}	6808^{+2}_{-3}	3377^{+108}_{-143}	1459^{+454}_{-686}	1899^{+604}_{-913}	17^{+1}_{-1}	12338+2 −3
SDSS J104330.09+441051.5	6430^{+127}_{-190}	2795^{+45}_{-67}	3804^{+66}_{-99}	25^{+0}_{-0}	4959^{+1}_{-2}	4705^{+284}_{-376}	1757^{+282}_{-442}	2209^{+384}_{-592}	23^{+1}_{-1}	9017+5 −6
SDSS J104336.73+494707.6	7245^{+80}_{-119}	3755^{+545}_{-813}	5486^{+943}_{-1406}	30^{+1}_{-2}	4922^{+1}_{-1}	4414^{+468}_{-619}	1759^{+237}_{-368}	2228^{+322}_{-491}	27^{+1}_{-1}	8969+7 −10
SDSS J104621.57+483322.7	...	...	...	...	...	...	...	...	...	...
SDSS J104716.50+360654.0	3124^{+57}_{-85}	2049^{+44}_{-66}	2701^{+74}_{-110}	61^{+1}_{-1}	5094^{+0}_{-1}	2302^{+146}_{-194}	1180^{+216}_{-339}	1649^{+285}_{-450}	27^{+1}_{-2}	9218+1 −2
SDSS J104743.57+661830.5	6172^{+381}_{-569}	3666^{+766}_{-1142}	4676^{+1146}_{-1710}	29^{+2}_{-3}	4898^{+2}_{-3}	...	...	...	...	...
SDSS J104911.34+495113.6	2362^{+39}_{-59}	1401^{+22}_{-32}	1864^{+33}_{-50}	51^{+0}_{-1}	4035^{+0}_{-0}	...	...	...	...	...
SDSS J104941.58+522348.9	...	...	...	...	...	...	...	...	...	...
SDSS J105045.72+544719.2	5564^{+77}_{-115}	3143^{+67}_{-99}	4283^{+114}_{-171}	33^{+0}_{-0}	4900^{+1}_{-1}	...	...	...	...	...
SDSS J105902.04+580848.6	4397^{+163}_{-242}	2404^{+128}_{-191}	3212^{+193}_{-287}	30^{+1}_{-1}	5015^{+1}_{-2}	2692^{+205}_{-272}	974^{+218}_{-342}	1245^{+277}_{-435}	12^{+6}_{-8}	9094+3 −4
SDSS J105926.43+062227.4	5826^{+146}_{-218}	3310^{+89}_{-133}	4644^{+143}_{-213}	48^{+1}_{-1}	4949^{+1}_{-2}	...	...	...	...	...
SDSS J110148.85+054815.5	...	...	...	...	...	...	...	...	...	...
SDSS J110516.68+200013.7	4062^{+145}_{-216}	2215^{+64}_{-96}	3110^{+104}_{-156}	37^{+1}_{-1}	5196^{+1}_{-1}	...	...	...	...	...
SDSS J110735.58+642008.6	6870^{+111}_{-165}	3343^{+96}_{-143}	4607^{+166}_{-248}	24^{+0}_{-0}	5118^{+1}_{-2}	...	...	...	...	...
SDSS J110810.87+014140.7	7221^{+813}_{-1213}	2843^{+419}_{-624}	3894^{+663}_{-990}	22^{+2}_{-2}	4052^{+6}_{-9}	...	...	...	...	...
SDSS J111119.10+133603.8	8226^{+758}_{-1131}	3004^{+173}_{-258}	4072^{+239}_{-356}	19^{+1}_{-1}	6915^{+9}_{-13}	...	...	...	...	...
SDSS J111313.29+102212.4	...	...	...	...	...	4976^{+609}_{-806}	1789^{+202}_{-312}	2257^{+279}_{-432}	25^{+5}_{-6}	9124+7 −10
SDSS J111352.53+104041.9	...	...	...	...	...	...	...	...	...	...
SDSS J111850.02+351311.7	7898^{+209}_{-312}	2832^{+42}_{-63}	3618^{+62}_{-92}	22^{+0}_{-0}	4881^{+2}_{-3}	...	...	...	...	...
SDSS J111920.98+232539.4	...	...	...	...	...	...	...	...	...	...
SDSS J112127.79+254758.9	...	...	...	...	...	...	...	...	...	...

SDSS J112726.81+601020.2	6716^{+499}_{-744}	2973^{+113}_{-169}	3660^{+179}_{-266}	16^{+0}_{-1}	4867^{+4}_{-6}	...	...	...	...	...
SDSS J112938.46+440325.0	...	...	...	...	...	...	...	...	...	...
SDSS J113048.45+225206.6	...	...	...	...	...	...	...	...	...	...
SDSS J113330.17+144758.8	...	...	...	...	...	4151^{+216}_{-286}	1932^{+1129}_{-1706}	2544^{+1649}_{-2493}	25^{+1}_{-1}	11652+3 −5
SDSS J113621.05+005021.2	4184^{+258}_{-385}	3053^{+1671}_{-2492}	5305^{+2499}_{-3729}	47^{+7}_{-10}	6847^{+2}_{-3}	2798^{+159}_{-211}	1531^{+254}_{-393}	2029^{+324}_{-501}	29^{+1}_{-1}	12403+2 −2
SDSS J113740.61+630256.9	...	...	...	...	...	...	...	...	...	...
SDSS J113924.64+332436.9	...	...	...	...	...	...	...	...	...	...
SDSS J114212.25+233250.5	8865^{+221}_{-330}	2832^{+42}_{-62}	3517^{+53}_{-79}	19^{+0}_{-0}	3999^{+5}_{-8}	...	...	...	...	...
SDSS J114323.71+193448.0	...	...	...	...	...	3227^{+94}_{-124}	1306^{+334}_{-509}	1775^{+516}_{-788}	28^{+1}_{-1}	12179+3 −3
SDSS J114350.30+362911.3	3220^{+526}_{-785}	2008^{+185}_{-276}	3114^{+282}_{-421}	15^{+1}_{-1}	5188^{+3}_{-4}	...	...	...	...	...
SDSS J114705.24+083900.6	...	...	...	...	...	...	...	...	...	...
SDSS J114711.78+084029.6	7254^{+1205}_{-1798}	2553^{+161}_{-240}	3081^{+166}_{-247}	11^{+1}_{-2}	5078^{+7}_{-11}	...	...	...	...	...
SDSS J114738.35+301717.5	...	...	...	...	...	3633^{+196}_{-259}	1333^{+194}_{-302}	1676^{+233}_{-370}	22^{+3}_{-4}	12197+7 −9
SDSS J114902.70+144328.0	4817^{+290}_{-433}	3780^{+954}_{-1423}	5161^{+1505}_{-2246}	29^{+2}_{-3}	4937^{+1}_{-2}	...	...	...	...	...
SDSS J114907.15+004104.3	6024^{+389}_{-580}	2976^{+200}_{-298}	4168^{+307}_{-458}	24^{+1}_{-1}	5096^{+3}_{-4}	...	...	...	...	...
SDSS J114927.90+432727.9	6947^{+352}_{-525}	3203^{+201}_{-300}	3678^{+368}_{-549}	24^{+1}_{-1}	6674^{+4}_{-6}	2983^{+143}_{-190}	1433^{+289}_{-454}	1904^{+389}_{-603}	14^{+1}_{-1}	12121+2 −3
SDSS J115747.99+272459.6	...	...	...	...	...	2584^{+479}_{-634}	1497^{+384}_{-589}	1983^{+444}_{-693}	13^{+1}_{-2}	9018+5 −7
SDSS J121314.03+080703.6	5107^{+527}_{-785}	2828^{+394}_{-588}	4216^{+592}_{-883}	15^{+1}_{-1}	5207^{+2}_{-3}	1967^{+253}_{-334}	925^{+208}_{-322}	1199^{+279}_{-434}	20^{+2}_{-3}	9498+2 −3
SDSS J121404.10+330945.6	...	...	...	...	...	...	...	...	...	...
SDSS J121423.01+024252.8	...	...	...	...	...	...	...	...	...	...
SDSS J121519.42+424851.0	4356^{+130}_{-194}	2290^{+102}_{-153}	3358^{+182}_{-271}	29^{+0}_{-1}	5123^{+1}_{-1}	2640^{+174}_{-230}	2054^{+991}_{-1506}	3131^{+1130}_{-1724}	17^{+11}_{-15}	9276+2 −3
SDSS J121736.65+515510.3	...	...	...	...	...	2481^{+191}_{-253}	1778^{+2004}_{-1778}	2689^{+2617}_{-2689}	14^{+1}_{-1}	9036+2 −3
SDSS J121810.98+241410.9	5921^{+168}_{-250}	2559^{+88}_{-132}	3333^{+140}_{-209}	31^{+1}_{-1}	5214^{+2}_{-3}	...	...	...	...	...
SDSS J122046.05+455442.1	11952^{+677}_{-1010}	4844^{+904}_{-1349}	5643^{+1458}_{-2174}	22^{+2}_{-2}	4951^{+9}_{-14}	...	...	...	...	...
SDSS J122343.15+503753.4	...	...	...	...	...	2366^{+116}_{-154}	1723^{+822}_{-1281}	2522^{+1108}_{-1727}	11^{+1}_{-1}	12515+2 −3
SDSS J122709.48+310749.3	9055^{+1684}_{-2512}	3179^{+946}_{-1411}	4212^{+1590}_{-2372}	11^{+1}_{-1}	4885^{+12}_{-18}	...	...	...	...	...
SDSS J122938.61+462430.5	4622^{+118}_{-176}	2722^{+135}_{-201}	4395^{+237}_{-354}	43^{+1}_{-1}	4873^{+1}_{-1}	...	...	...	...	...
SDSS J123514.64+462904.0	4406^{+299}_{-446}	2842^{+191}_{-284}	4123^{+311}_{-464}	46^{+1}_{-2}	4953^{+1}_{-2}	3248^{+524}_{-694}	1642^{+307}_{-483}	2135^{+369}_{-582}	14^{+1}_{-1}	8976+4 −6

SDSS J125150.45+114340.7	4660^{+112}_{-168}	3030^{+80}_{-120}	4228^{+132}_{-196}	47^{+0}_{-1}	4939^{+0}_{-1}	...	...	...	...	...
SDSS J125159.90+500203.6	6835^{+208}_{-310}	3897^{+1669}_{-2490}	5522^{+2556}_{-3814}	29^{+4}_{-6}	5213^{+2}_{-3}	...	...	...	...	...
SDSS J132845.00+510225.8	4933^{+115}_{-171}	2771^{+204}_{-305}	3899^{+364}_{-543}	30^{+1}_{-1}	6816^{+1}_{-2}	3324^{+852}_{-1127}	1171^{+217}_{-339}	1438^{+270}_{-421}	24^{+23}_{-24}	12320+13 −17
SDSS J133342.56+123352.7	...	...	...	...	...	4243^{+216}_{-285}	1676^{+314}_{-487}	2146^{+408}_{-623}	20^{+2}_{-2}	11974+3 −4
SDSS J134341.99+255652.9	5911^{+1361}_{-2031}	2162^{+1019}_{-1521}	3673^{+1511}_{-2254}	17^{+3}_{-4}	4029^{+4}_{-6}	...	...	...	...	...
SDSS J135908.35+305830.8	8445^{+157}_{-234}	3302^{+59}_{-89}	4505^{+94}_{-140}	28^{+0}_{-0}	5049^{+2}_{-3}	4657^{+660}_{-873}	1756^{+304}_{-471}	2208^{+358}_{-558}	20^{+2}_{-2}	9238+7 −9
SDSS J140058.79+260619.4	...	...	...	...	...	...	...	...	...	...
SDSS J140704.43+273556.6	5627^{+242}_{-361}	2825^{+168}_{-251}	3905^{+323}_{-481}	20^{+0}_{-1}	4970^{+1}_{-2}	4554^{+242}_{-320}	1576^{+863}_{-1304}	1756^{+1149}_{-1737}	17^{+1}_{-1}	9038+8 −10
SDSS J141028.14+135950.2	5315^{+386}_{-576}	3448^{+288}_{-430}	5137^{+462}_{-688}	39^{+1}_{-2}	4959^{+2}_{-3}	...	...	...	...	...
SDSS J141321.05+092204.8	...	...	...	...	...	...	...	...	...	...
SDSS J141617.38+264906.1	...	...	...	...	...	...	...	...	...	...
SDSS J141925.48+074953.5	8128^{+256}_{-382}	3330^{+67}_{-100}	4312^{+105}_{-157}	14^{+0}_{-0}	5220^{+5}_{-7}	...	...	...	...	...
SDSS J141951.84+470901.3	5094^{+686}_{-1023}	3531^{+580}_{-866}	5080^{+905}_{-1350}	25^{+2}_{-3}	5076^{+3}_{-4}	3344^{+169}_{-224}	2120^{+957}_{-1491}	2865^{+1321}_{-2059}	23^{+1}_{-1}	9274+2 −3
SDSS J142013.03+253403.9	...	...	...	...	...	3232^{+187}_{-247}	1509^{+239}_{-375}	1989^{+282}_{-441}	15^{+1}_{-1}	9035+5 −6
SDSS J142435.97+421030.4	5113^{+210}_{-313}	3118^{+110}_{-164}	4380^{+192}_{-287}	24^{+0}_{-1}	4970^{+1}_{-1}	...	...	...	...	...
SDSS J142500.24+494729.2	...	...	...	...	...	...	...	...	...	...
SDSS J142502.62+274912.2	2346^{+242}_{-361}	1452^{+256}_{-383}	2850^{+390}_{-581}	42^{+3}_{-4}	5183^{+1}_{-2}	...	...	...	...	...
SDSS J142543.32+540619.3	5762^{+1058}_{-1579}	2707^{+243}_{-363}	3168^{+367}_{-548}	12^{+1}_{-1}	6583^{+7}_{-10}	3101^{+141}_{-186}	2186^{+1376}_{-2100}	3229^{+1828}_{-2789}	21^{+2}_{-2}	11900+2 −3
SDSS J142755.85-002951.1	2994^{+79}_{-118}	1759^{+67}_{-100}	2273^{+117}_{-175}	35^{+1}_{-1}	6748^{+1}_{-2}	2122^{+59}_{-78}	1561^{+1302}_{-1561}	2255^{+1832}_{-2255}	24^{+1}_{-1}	11979+1 −2
SDSS J142903.03-014519.3	8464^{+947}_{-1412}	3240^{+1364}_{-2034}	8043^{+2331}_{-3477}	21^{+2}_{-3}	6803^{+10}_{-15}	4037^{+162}_{-215}	1637^{+286}_{-444}	2109^{+365}_{-565}	17^{+3}_{-4}	12389+3 −4
SDSS J144624.29+173128.8	1929^{+55}_{-82}	1358^{+87}_{-129}	1802^{+136}_{-203}	15^{+0}_{-1}	4953^{+1}_{-1}	...	...	...	...	...
SDSS J144706.81+212839.2	7607^{+1324}_{-1975}	4845^{+975}_{-1455}	4016^{+1457}_{-2173}	14^{+2}_{-3}	6509^{+12}_{-19}	2460^{+163}_{-216}	1228^{+441}_{-663}	1610^{+633}_{-952}	25^{+1}_{-1}	11823+3 −4
SDSS J144948.62+123047.4	5370^{+572}_{-854}	6718^{+929}_{-1386}	4934^{+1368}_{-2041}	66^{+7}_{-10}	4009^{+3}_{-5}	...	...	...	...	...
SDSS J145541.11-023751.0	3625^{+144}_{-215}	2329^{+90}_{-134}	3437^{+154}_{-230}	60^{+1}_{-1}	4042^{+0}_{-1}	...	...	...	...	...
SDSS J150205.58-024038.5	...	...	...	...	...	3852^{+328}_{-434}	1659^{+261}_{-403}	2139^{+331}_{-507}	23^{+1}_{-1}	8992+2 −3
SDSS J150743.71+220928.8	6243^{+292}_{-436}	3111^{+1355}_{-2021}	5273^{+2183}_{-3257}	44^{+5}_{-7}	6543^{+2}_{-4}	2899^{+238}_{-315}	1406^{+286}_{-440}	1876^{+367}_{-566}	23^{+6}_{-8}	11877+5 −7
SDSS J151123.30+495101.2	...	...	...	...	...	...	...	...	...	...
SDSS J151341.89+463002.7	...	...	...	...	...	...	...	...	...	...

SDSS J151507.82+612411.9	3862^{+69}_{-102}	2030^{+45}_{-67}	2695^{+77}_{-115}	34^{+0}_{-1}	4919^{+0}_{-1}	...	...	...	...	...
SDSS J151727.68+133358.6	6686^{+149}_{-223}	2713^{+57}_{-86}	3555^{+92}_{-138}	27^{+0}_{-0}	4989^{+1}_{-2}	3089^{+245}_{-324}	1285^{+236}_{-368}	1696^{+302}_{-474}	18^{+1}_{-1}	9010+3 −4
SDSS J151733.09+435648.4	9673^{+380}_{-567}	3213^{+127}_{-190}	3676^{+181}_{-270}	17^{+1}_{-1}	4925^{+17}_{-26}	3666^{+199}_{-263}	5736^{+1309}_{-2019}	8458^{+1856}_{-2860}	27^{+23}_{-27}	8937+3 −4
SDSS J152929.55+230208.7	5710^{+129}_{-193}	2093^{+34}_{-50}	2744^{+49}_{-73}	25^{+0}_{-0}	3990^{+2}_{-3}	...	...	...	...	...
SDSS J153248.95+173900.8	...	...	...	...	...	...	...	...	...	...
SDSS J154550.37+554346.2	...	...	...	...	...	...	...	...	...	...
SDSS J155355.10+375844.1	6879^{+341}_{-509}	2696^{+103}_{-154}	3659^{+150}_{-223}	26^{+1}_{-1}	5183^{+3}_{-4}	...	...	...	...	...
SDSS J160029.86+331806.9	3197^{+1444}_{-2154}	3013^{+717}_{-1069}	3144^{+1006}_{-1501}	52^{+8}_{-12}	4008^{+6}_{-9}	...	...	...	...	...
SDSS J160207.67+380743.0	...	...	...	...	...	...	...	...	...	...
SDSS J160425.30+193929.1	10075^{+283}_{-422}	3428^{+61}_{-91}	4278^{+82}_{-122}	16^{+0}_{-0}	6608^{+10}_{-14}	4139^{+189}_{-250}	1468^{+262}_{-400}	1832^{+343}_{-523}	19^{+1}_{-1}	12029+6 −9
SDSS J160513.17+325829.9	10825^{+202}_{-301}	3704^{+309}_{-461}	4670^{+633}_{-944}	21^{+0}_{-1}	5016^{+7}_{-10}	4281^{+193}_{-255}	1510^{+1335}_{-1510}	1955^{+1800}_{-1955}	21^{+1}_{-1}	9165+3 −5
SDSS J160552.97+292141.4	...	...	...	...	...	...	...	...	...	...
SDSS J160637.57+173516.2	5640^{+101}_{-151}	2250^{+48}_{-72}	3024^{+81}_{-121}	17^{+0}_{-0}	5127^{+1}_{-2}	...	...	...	...	...
SDSS J161435.70+372715.6	4136^{+378}_{-564}	2180^{+266}_{-397}	3286^{+443}_{-661}	22^{+1}_{-1}	4022^{+1}_{-2}	...	...	...	...	...
SDSS J161942.39+525613.4	...	...	...	...	...	...	...	...	...	...
SDSS J162659.24+301535.0	3730^{+101}_{-151}	1839^{+28}_{-42}	2369^{+40}_{-59}	30^{+0}_{-1}	3996^{+0}_{-1}	...	...	...	...	...
SDSS J163125.10+174810.0	...	...	...	...	...	...	...	...	...	...
SDSS J163433.42+265158.2	4998^{+451}_{-673}	1723^{+49}_{-73}	2122^{+70}_{-105}	17^{+0}_{-1}	3974^{+4}_{-6}	...	...	...	...	...
SDSS J164807.55+254407.1	3320^{+72}_{-107}	2152^{+56}_{-84}	3033^{+97}_{-145}	40^{+0}_{-1}	4948^{+1}_{-1}	...	...	...	...	...
SDSS J165321.03+271706.7	8472^{+286}_{-426}	2945^{+52}_{-78}	3561^{+71}_{-106}	17^{+0}_{-0}	4010^{+2}_{-3}	...	...	...	...	...
SDSS J173352.23+540030.4	4727^{+203}_{-302}	2280^{+63}_{-94}	3049^{+94}_{-141}	14^{+0}_{-0}	6849^{+2}_{-2}	3022^{+149}_{-197}	1756^{+316}_{-489}	2311^{+391}_{-609}	23^{+1}_{-1}	12411+3 −4
SDSS J205900.36-064309.5	11381^{+502}_{-750}	3853^{+159}_{-237}	4987^{+211}_{-315}	12^{+0}_{-0}	5090^{+3}_{-4}	...	...	...	...	...
SDSS J210558.29-011127.5	3652^{+180}_{-268}	2316^{+61}_{-91}	2814^{+92}_{-138}	36^{+1}_{-1}	4050^{+1}_{-1}	...	...	...	...	...
SDSS J210831.56-063022.5	9363^{+470}_{-702}	3244^{+118}_{-175}	3976^{+147}_{-220}	11^{+0}_{-1}	5138^{+14}_{-21}	...	...	...	...	...
SDSS J211251.06+000808.3	7636^{+520}_{-776}	2937^{+242}_{-361}	3603^{+375}_{-559}	17^{+1}_{-1}	4024^{+7}_{-11}	...	...	...	...	...
SDSS J213655.35-080910.1	6387^{+813}_{-1212}	5763^{+1172}_{-1748}	4800^{+1612}_{-2405}	21^{+3}_{-5}	3989^{+3}_{-5}	...	...	...	...	...
SDSS J214901.21-073141.6	7251^{+737}_{-1100}	3610^{+864}_{-1289}	3924^{+1323}_{-1973}	21^{+2}_{-3}	4953^{+6}_{-10}	...	...	...	...	...
SDSS J220139.99+114140.8	7475^{+2239}_{-3339}	11789^{+1539}_{-2296}	4843^{+2064}_{-3079}	28^{+5}_{-8}	5189^{+10}_{-15}	...	...	...	...	...

SDSS J220344.98+235729.3	...	...	...	...	...	2271^{+235}_{-311}	6583^{+1119}_{-1754}	9644^{+1537}_{-2410}	32^{+3}_{-4}	8848+1 −1
SDSS J222310.76+180308.1	5145^{+149}_{-222}	2156^{+206}_{-307}	3040^{+442}_{-659}	19^{+0}_{-1}	4022^{+1}_{-1}	...	...	...	...	...
SDSS J222621.45+251545.0	5777^{+101}_{-151}	2974^{+58}_{-87}	3979^{+94}_{-141}	26^{+0}_{-0}	5231^{+1}_{-1}	...	...	...	...	...
SDSS J223934.45-004707.2	...	...	...	...	...	...	...	...	...	...
SDSS J225608.48+010557.8	...	...	...	...	...	2723^{+733}_{-969}	2782^{+1243}_{-1973}	3861^{+1624}_{-2577}	25^{+2}_{-3}	9137+7 −10
SDSS J225627.12+092313.3	5668^{+737}_{-1100}	2465^{+240}_{-358}	3404^{+440}_{-657}	27^{+1}_{-2}	5083^{+3}_{-4}	3618^{+416}_{-550}	2065^{+1019}_{-1540}	2839^{+1517}_{-2282}	27^{+2}_{-3}	9214+6 −8
SDSS J230722.21+253803.8	2863^{+121}_{-180}	1472^{+52}_{-78}	1944^{+87}_{-129}	49^{+1}_{-1}	4013^{+0}_{-0}	...	...	...	...	...
SDSS J231450.12+182402.8	4580^{+126}_{-189}	2160^{+143}_{-213}	3082^{+267}_{-398}	32^{+1}_{-1}	5079^{+1}_{-1}	3131^{+751}_{-994}	1411^{+256}_{-399}	1870^{+325}_{-510}	19^{+2}_{-3}	9198+7 −10
SDSS J233304.61-092710.9	3967^{+786}_{-1173}	10662^{+1276}_{-1904}	3207^{+1884}_{-2810}	37^{+5}_{-7}	4823^{+3}_{-4}	...	...	...	...	...
SDSS J233344.66+290251.5	6226^{+334}_{-498}	2246^{+136}_{-203}	3174^{+210}_{-314}	18^{+1}_{-1}	6479^{+5}_{-7}	3479^{+475}_{-628}	1538^{+237}_{-371}	2010^{+239}_{-382}	15^{+19}_{-15}	11742+8 −10
SDSS J234817.55+193345.8	7497^{+717}_{-1070}	2595^{+1204}_{-1796}	3130^{+1768}_{-2638}	14^{+2}_{-3}	4924^{+11}_{-16}	3835^{+358}_{-473}	1404^{+243}_{-373}	1820^{+351}_{-536}	19^{+16}_{-19}	8973+1 −1
SDSS J235212.85-012029.6	5664^{+290}_{-433}	3053^{+118}_{-176}	3905^{+181}_{-270}	21^{+0}_{-1}	5213^{+2}_{-2}	3401^{+313}_{-414}	1591^{+251}_{-388}	2067^{+299}_{-469}	21^{+2}_{-3}	9476+5 −7

TABLE 4.1. C IV and Mg II emission line measurements in our sample.

Emission Line	FWHM	MAD	$\sigma_{\rm line}$
C IV (a, b)	$(5.172 \pm 0.196, 0.960 \pm 0.138)$	$(6.727 \pm 0.187, 0.250 \pm 0.131)$	**(6.299±0.169, 0.385±0.119)**
Mg II only (c, d)	**(7.000±0.022, 0)**	$(7.562 \pm 0.028, 0)$	$(7.309 \pm 0.031, 0)$
Mg II & C IV (c, d)	**(6.793±0.047, 0.005±0.001)**	$(7.410 \pm 0.0.068, 0.005 \pm 0.002)$	$(7.168 \pm 0.074, 0.004 \pm 0.002)$

TABLE 4.2. Resulting regression coefficients from Equations 9 and 10 for each of our velocity width parameters. Bold coefficients are the recommended prescription for each emission line (see, Section 4.4).

	Hβ			C IV						Mg II					
Quasar	FWHM	MAD	$\sigma_{\rm line}$	VP06	P17	C17	FWHM	MAD	$\sigma_{\rm line}$	VO09	Z15	L20	FWHM[a]	MAD[a]	$\sigma_{\rm line}$
SDSS J001018.88+280932.5	8.97	8.41	8.64	8.74	8.77	9.01	8.72	8.92	9.02	...	...	...	...	...	...
SDSS J001249.89+285552.6	9.24	8.57	8.81	...	...	...	...	...	...	9.55	9.71	9.69	9.52	9.48	9.48
SDSS J001355.10-012304.0	9.75	9.04	9.26	...	...	...	...	...	...	9.11	9.27	9.25	9.05	8.92	8.88
SDSS J001453.20+091217.6	9.47	8.52	8.72	9.55	9.28	9.44	9.34	9.30	9.45	9.18	9.34	9.32	9.16	9.23	9.20
SDSS J001813.30+361058.6	9.26	8.43	8.65	9.71	9.10	9.29	9.31	9.32	9.23	9.57	9.73	9.71	9.56	9.68	9.68
SDSS J001914.46+155555.9	9.14	8.63	8.91	9.30	8.83	9.38	9.14	9.02	9.05	9.45	9.61	9.59	9.45	9.05	8.99
SDSS J002634.46+274015.5	9.30	8.68	8.92	9.26	9.33	9.48	9.58	9.79	9.70	8.86	9.03	9.00	8.87	8.99	9.04
SDSS J003001.11-015743.5	9.01	8.32	8.54	9.25	8.70	9.17	9.19	9.00	8.90	...	...	...	...	...	...
SDSS J003416.61+002241.1	9.15	8.54	8.78	9.16	8.61	9.13	8.82	8.73	8.73	9.29	9.45	9.43	9.32	8.98	8.94
SDSS J003853.15+333044.3	9.19	8.42	8.65	9.73	8.90	9.90	9.10	8.79	8.89	...	...	...	...	...	...
SDSS J004613.54+010425.7	9.09	8.54	8.77	...	...	...	...	...	...	8.67	8.83	8.81	8.67	9.69	9.84
SDSS J004710.48+163106.5	9.07	8.46	8.72	9.42	8.87	8.98	8.99	8.94	8.94	...	...	...	...	...	...
SDSS J004719.71+014813.9	9.31	8.52	8.73	9.12	8.78	9.12	9.01	8.94	9.00	9.21	9.37	9.35	9.21	9.10	9.10
SDSS J005233.67+014040.8	9.76	8.82	9.02	9.81	9.11	9.85	9.50	9.29	9.28	9.30	9.46	9.44	9.21	8.83	8.75
SDSS J005307.71+191022.7	9.77	8.84	9.03	9.28	9.09	9.22	9.08	8.98	9.23	...	...	...	...	...	...
SDSS J010113.72+032427.0	9.64	8.85	9.06	9.48	9.28	9.91	9.68	9.44	9.61	9.55	9.72	9.69	9.58	9.20	9.17
SDSS J010328.71-110414.4	9.15	8.45	8.68	...	...	...	...	...	...	9.32	9.48	9.46	9.28	9.54	9.57
SDSS J010447.39+101031.6	9.35	8.40	8.59	9.63	9.33	9.43	9.19	9.40	9.41	...	...	...	...	...	...
SDSS J010500.72+194230.4	8.96	8.49	8.73	9.71	9.50	9.26	9.44	9.35	9.66	9.17	9.32	9.31	9.17	9.17	9.16
SDSS J010615.93+101043.0	8.62	8.25	8.50	9.40	8.77	9.12	8.94	8.80	8.84	...	...	...	...	...	...
SDSS J010643.23-031536.4	9.47	9.36	9.60	9.17	8.93	8.89	8.27	8.99	8.85	9.48	9.64	9.62	9.44	8.85	8.79
SDSS J011538.72+242446.0	9.03	8.41	8.65	9.79	9.36	9.30	9.45	9.59	9.51	9.54	9.70	9.68	9.57	9.05	8.98
SDSS J013012.36+153157.9	9.25	8.66	8.92	...	...	...	...	...	...	8.71	8.87	8.85	8.63	8.60	8.58
SDSS J013113.25+085245.5	9.15	8.50	8.72	9.58	8.91	9.68	9.15	9.12	9.03	9.24	9.40	9.38	9.19	8.81	8.75
SDSS J013136.44+130331.0	8.44	7.94	8.17	8.23	8.34	7.84	6.93	7.07	8.03	9.07	9.23	9.21	9.00	8.94	8.94

SDSS J013417.81-005036.2	9.30	8.69	8.97	9.43	8.68	9.11	8.53	8.48	8.56	...	...	...	...	...	...
SDSS J013647.96-062753.6	9.46	8.52	8.72	10.23	9.27	9.57	9.61	9.40	9.33	9.58	9.74	9.72	9.51	9.07	8.99
SDSS J013652.52+122501.5	9.34	8.75	8.99	...	...	...	...	...	...	8.96	9.12	9.10	8.95	8.65	8.60
SDSS J014018.20-013805.8	9.64	8.80	9.01	...	...	...	...	...	...	9.04	9.19	9.18	9.01	9.17	9.17
SDSS J014128.26+070606.1	8.86	8.14	8.37	9.37	9.06	9.21	9.19	9.07	9.25	8.97	9.14	9.11	8.96	9.40	9.49
SDSS J014206.86+025713.0	9.37	8.55	8.78	...	...	...	...	...	...	9.09	9.24	9.23	9.07	9.60	9.68
SDSS J014932.06+152754.0	8.91	8.46	8.71	8.85	9.03	9.30	8.80	9.14	9.27	...	...	...	...	...	...
SDSS J020329.86-091020.3	9.48	8.58	8.78	9.40	9.29	9.34	9.07	9.48	9.40	9.39	9.56	9.53	9.37	9.00	8.94
SDSS J021259.21+132618.8	8.73	8.01	8.25	9.81	9.44	9.88	9.65	9.83	9.64	9.27	9.44	9.41	9.30	8.72	8.65
SDSS J022007.64-010731.1	9.27	8.82	9.08	...	...	...	...	...	...	9.08	9.23	9.22	9.02	8.76	8.70
SDSS J025042.45+003536.7	9.90	9.16	9.37	...	...	...	...	...	...	...	...	...	...	...	...
SDSS J035150.97-061326.4	8.78	8.51	8.79	9.26	8.58	9.47	8.61	8.68	8.61	8.90	9.06	9.04	8.76	8.62	8.57
SDSS J072517.52+434553.4	7.85	7.41	7.63	9.82	8.98	10.06	9.31	9.08	9.05	8.96	9.13	9.10	8.94	9.59	9.69
SDSS J072928.48+252451.8	9.61	8.67	8.87	9.20	8.77	9.16	8.64	8.95	8.83	9.21	9.37	9.35	9.10	8.94	8.89
SDSS J073132.18+461347.0	8.61	8.07	8.30	...	...	...	...	...	...	8.76	8.93	8.90	8.77	9.12	9.22
SDSS J073519.68+240104.6	9.36	8.54	8.75	...	...	...	...	...	...	8.86	9.01	9.00	8.90	8.79	8.78
SDSS J073900.90+485159.0	9.38	8.72	8.95	9.37	8.97	9.04	9.12	9.38	9.11	9.26	9.43	9.40	9.23	8.97	8.94
SDSS J073913.65+461858.5	8.94	8.28	8.50	9.46	8.74	9.26	8.87	8.87	8.77	...	...	...	...	...	...
SDSS J074941.16+262715.9	8.95	8.67	8.94	9.22	8.64	9.26	8.86	8.72	8.75	8.88	9.05	9.02	8.83	8.96	8.99
SDSS J075115.43+505439.1	8.06	7.29	7.50	10.21	9.48	9.29	9.25	9.35	9.39	9.35	9.51	9.49	9.26	9.35	9.33
SDSS J075136.36+432732.4	9.01	8.53	8.79	9.62	9.20	9.36	9.34	9.32	9.37	8.90	9.06	9.04	8.85	9.19	9.18
SDSS J075405.08+280339.6	9.37	8.90	9.13	9.21	9.31	9.97	9.14	9.50	9.55	9.57	9.73	9.71	9.57	9.10	9.04
SDSS J075547.83+220450.1	9.07	8.65	8.91	9.56	8.99	9.99	9.20	9.12	9.14	9.11	9.27	9.25	9.08	8.83	8.79
SDSS J075837.62+135733.7	9.32	8.76	9.01	...	...	...	...	...	...	9.00	9.16	9.14	8.97	9.50	9.56
SDSS J080036.01+501044.3	9.23	8.33	8.53	...	...	...	...	...	...	9.19	9.35	9.33	9.12	9.00	8.97
SDSS J080117.79+521034.5	9.49	9.08	9.34	10.57	9.61	9.98	10.03	9.84	9.74	9.69	9.84	9.83	9.65	9.29	9.23
SDSS J080117.91+333411.9	9.45	8.94	9.15	9.46	9.06	9.86	8.96	9.06	9.12	9.56	9.72	9.70	9.46	9.16	9.08
SDSS J080413.66+251633.9	8.99	8.42	8.65	9.50	8.70	9.76	8.79	8.76	8.69	8.95	9.11	9.09	8.91	8.95	8.97

SDSS J080636.81+345048.5	8.94	8.54	8.80	...	...	...	...	...	...	8.94	9.11	9.08	8.88	9.17	9.21
SDSS J081019.48+095040.9	8.87	8.44	8.68	9.73	9.07	9.39	9.34	9.27	9.19	9.19	9.35	9.33	9.12	8.73	8.66
SDSS J081056.96+120914.8	9.07	8.33	8.56	9.45	9.21	10.20	9.19	9.31	9.40	9.04	9.19	9.18	9.00	9.85	9.93
SDSS J081114.66+172057.4	9.64	8.90	9.12	...	...	...	...	...	...	9.65	9.81	9.79	9.62	9.32	9.26
SDSS J081127.44+461812.9	8.95	8.37	8.62	10.02	9.27	10.15	9.53	9.44	9.38	9.33	9.49	9.47	9.29	9.32	9.33
SDSS J081410.76+443706.9	8.84	8.20	8.43	9.44	9.02	9.34	9.19	9.48	9.18	9.02	9.18	9.16	9.02	9.41	9.43
SDSS J081558.35+154055.2	9.28	8.51	8.73	9.28	8.95	9.24	8.94	9.07	9.10	9.23	9.39	9.37	9.29	11.38	11.37
SDSS J081940.58+082357.9	9.81	8.99	9.21	9.49	9.35	9.47	9.26	9.29	9.54	9.70	9.85	9.84	9.66	9.56	9.53
SDSS J082507.67+360411.1	8.98	8.68	8.94	9.10	8.77	9.16	8.97	8.94	8.99	8.98	9.13	9.12	8.93	9.81	9.94
SDSS J082603.32+342800.6	9.38	8.44	8.63	10.06	9.59	9.91	9.67	9.65	9.72	9.39	9.55	9.53	9.39	9.20	9.16
SDSS J082643.45+143427.6	9.21	8.58	8.81	...	...	...	...	...	...	9.30	9.45	9.44	9.28	9.11	9.16
SDSS J082644.66+163549.0	8.97	8.63	8.89	8.90	8.78	9.33	8.88	8.95	9.06	8.95	9.10	9.09	8.96	9.41	9.52
SDSS J082736.89+061812.1	9.15	8.41	8.63	9.01	8.82	9.23	8.57	8.90	8.93	8.90	9.06	9.04	8.85	9.48	9.53
SDSS J083255.63+182300.7	9.16	9.09	9.36	9.92	9.54	9.59	9.49	9.46	9.67	9.44	9.59	9.58	9.37	9.08	9.01
SDSS J083417.12+354833.1	8.84	8.23	8.47	9.69	8.92	9.53	9.22	9.08	9.03	9.35	9.50	9.49	9.28	9.30	9.31
SDSS J083745.74+052109.4	9.03	8.35	8.57	...	...	...	...	...	...	9.11	9.27	9.25	9.08	9.29	9.36
SDSS J084017.87+103428.8	9.04	8.53	8.78	9.34	8.84	9.52	9.19	9.02	9.07	8.82	8.97	8.96	8.79	8.82	8.85
SDSS J084029.97+465113.7	9.08	8.41	8.64	9.51	8.72	5.00	8.99	8.87	8.81	9.10	9.27	9.24	9.07	8.83	8.80
SDSS J084133.15+200525.7	9.39	8.38	8.55	...	...	...	...	...	...	...	...	...	...	...	...
SDSS J084401.95+050357.9	9.84	9.01	9.21	...	...	...	...	...	...	...	...	...	...	...	...
SDSS J084526.75+550546.8	9.35	8.57	8.78	9.18	8.82	9.48	9.10	8.97	9.04	9.22	9.38	9.36	9.22	8.96	8.96
SDSS J084729.52+441616.7	9.24	8.64	8.87	...	...	...	...	...	...	8.82	8.98	8.96	8.71	8.40	8.33
SDSS J084846.11+611234.6	9.45	8.71	8.94	9.35	9.01	9.57	9.01	9.13	9.18	9.23	9.38	9.37	9.15	9.36	9.40
SDSS J085046.17+522057.4	9.14	8.44	8.66	...	...	...	...	...	...	...	...	...	...	...	...
SDSS J085337.36+121800.3	9.30	9.08	9.34	9.76	9.29	9.85	8.87	8.81	9.21	9.26	9.41	9.40	9.09	9.22	9.25
SDSS J085344.17+354104.5	8.92	8.30	8.55	9.84	9.00	9.76	8.71	8.89	8.81	...	...	...	...	...	...
SDSS J085443.10+075223.2	8.84	8.15	8.37	9.39	8.91	9.11	9.06	8.98	9.04	8.95	9.11	9.09	8.87	9.21	9.29
SDSS J085726.94+331317.1	8.78	8.28	8.55	...	...	...	...	...	...	9.11	9.26	9.25	9.15	9.12	9.12

SDSS J085856.00+015219.4	9.14	8.20	8.39	10.03	9.22	9.54	9.61	9.35	9.33	9.04	9.20	9.18	9.00	9.16	9.21
SDSS J085946.79+603702.1	8.78	8.11	8.34	9.61	8.91	9.34	9.25	9.07	9.04	9.15	9.31	9.29	9.08	8.74	8.69
SDSS J090247.57+304120.7	9.38	8.53	8.73	9.05	8.90	9.56	8.91	9.09	9.13	...	...	...	...	...	...
SDSS J090444.33+233354.0	9.47	8.58	8.79	...	...	...	...	...	...	9.27	9.43	9.41	9.24	9.61	9.69
SDSS J090646.98+174046.8	8.76	8.13	8.37	9.71	8.95	10.21	9.14	9.05	9.01	9.21	9.37	9.35	9.16	9.86	10.01
SDSS J090709.89+250620.8	9.27	8.76	9.04	9.36	8.73	9.31	8.85	8.88	8.82	9.13	9.28	9.27	9.11	9.35	9.39
SDSS J090710.36+430000.2	8.74	8.07	8.31	9.77	9.12	9.44	9.34	9.27	9.25	9.36	9.51	9.50	9.33	9.58	9.70
SDSS J091054.17+375914.9	8.99	8.38	8.61	...	...	...	...	...	...	9.28	9.43	9.42	9.26	9.10	9.10
SDSS J091118.02+202254.7	9.59	8.64	8.83	...	...	...	...	...	...	9.10	9.26	9.24	9.04	8.85	8.84
SDSS J091301.01+422344.7	9.27	8.52	8.74	...	...	...	...	...	...	...	...	...	...	...	...
SDSS J091328.23+394443.9	8.25	7.92	8.19	...	...	...	...	...	...	...	...	...	...	...	...
SDSS J091425.72+504854.9	9.06	8.70	9.01	...	...	...	...	...	...	...	...	...	...	...	...
SDSS J091716.79+461435.3	8.62	7.73	7.93	...	...	...	...	...	...	9.89	10.05	10.03	9.78	9.50	9.45
SDSS J091941.26+253537.7	9.41	8.51	8.72	9.21	9.03	9.33	8.96	9.19	9.21	9.58	9.74	9.72	9.57	9.11	9.06
SDSS J092216.04+160526.4	8.90	8.36	8.60	9.21	8.75	9.42	9.04	8.89	8.97	8.56	8.71	8.70	8.53	9.02	9.07
SDSS J092325.25+453222.2	9.20	8.64	8.88	9.63	9.23	9.19	9.36	9.36	9.44	9.12	9.27	9.26	9.02	8.92	8.89
SDSS J092456.66+305354.7	9.17	8.69	8.94	9.83	9.39	9.70	9.28	9.43	9.48	9.46	9.61	9.60	9.44	9.14	9.10
SDSS J092523.24+214119.8	8.93	8.42	8.66	9.03	8.61	9.20	8.87	8.70	8.81	9.08	9.24	9.22	9.05	8.76	8.71
SDSS J092555.05+490338.2	9.54	8.60	8.80	9.30	9.24	9.69	9.01	9.76	9.38	9.75	9.91	9.89	9.73	9.29	9.23
SDSS J092942.97+064604.1	8.98	8.04	8.24	9.60	9.06	8.93	9.21	9.15	9.17	9.42	9.58	9.56	9.40	9.02	8.97
SDSS J093251.98+023727.0	9.36	8.49	8.70	...	...	...	...	...	...	9.38	9.54	9.52	9.33	9.15	9.12
SDSS J093533.88+235720.5	9.65	8.69	8.88	9.65	9.31	9.58	9.48	9.49	9.52	9.46	9.62	9.60	9.47	8.99	8.93
SDSS J094140.16+325703.2	9.19	8.52	8.74	10.10	9.15	9.41	9.48	9.31	9.19	9.36	9.51	9.50	9.32	9.18	9.16
SDSS J094214.40+034100.3	9.07	8.15	8.33	8.63	8.39	8.91	8.37	8.49	8.54	8.77	8.93	8.91	8.71	9.16	9.24
SDSS J094328.94+140415.6	9.34	8.48	8.69	...	...	...	...	...	...	...	...	...	...	...	...
SDSS J094347.02+690818.4	9.34	8.41	8.59	9.56	8.87	9.37	9.40	9.07	9.06	9.10	9.26	9.24	9.07	8.99	8.96
SDSS J094427.27+614424.6	9.30	8.60	8.82	...	...	...	...	...	...	...	...	...	...	...	...
SDSS J094602.31+274407.0	8.93	8.24	8.47	10.44	9.45	9.25	9.42	9.59	9.36	9.88	10.03	10.02	9.79	9.48	9.42

SDSS J094637.83-012411.5	9.06	8.58	8.83	9.33	8.81	9.47	8.83	8.90	8.87	8.68	8.84	8.82	8.66	9.23	9.29
SDSS J094646.94+392719.0	9.21	8.93	9.33	9.97	10.04	9.22	9.63	10.13	10.18	9.49	9.65	9.63	9.44	9.25	9.21
SDSS J094648.59+171827.7	9.36	8.57	8.79	9.39	8.79	9.59	9.22	9.00	9.01	9.08	9.24	9.22	9.07	9.10	9.12
SDSS J094902.38+531241.5	9.01	8.45	8.71	...	...	...	...	...	...	8.85	9.02	8.99	8.82	8.78	8.75
SDSS J095047.45+194446.1	9.14	8.51	8.75	9.41	8.83	9.69	9.15	8.90	9.00	9.18	9.34	9.32	9.15	8.69	8.61
SDSS J095058.76+263424.6	9.01	8.53	8.78	9.63	9.14	9.11	9.18	9.24	9.24	9.39	9.55	9.53	9.41	9.02	8.96
SDSS J095327.95+322551.5	9.20	8.47	8.70	...	...	...	...	...	...	9.05	9.21	9.19	9.06	9.40	9.52
SDSS J095330.36+353223.1	9.08	9.24	9.52	9.97	9.13	9.50	9.31	9.20	9.15	9.28	9.43	9.42	9.24	9.36	9.38
SDSS J095544.25+182546.9	9.17	8.58	8.82	9.26	8.80	9.51	9.04	8.90	9.01	9.10	9.25	9.24	9.02	9.01	9.02
SDSS J095555.68+351652.6	9.34	8.55	8.75	9.32	8.77	9.88	8.99	8.92	8.89	8.96	9.13	9.10	8.90	9.12	9.11
SDSS J095707.82+184739.9	8.62	8.03	8.26	10.18	9.99	9.40	9.55	9.43	10.03	8.46	8.61	8.60	8.33	8.41	8.41
SDSS J095746.75+565800.7	8.44	8.00	8.26	...	...	...	...	...	...	9.11	9.27	9.25	9.07	9.23	9.27
SDSS J095823.07+371218.3	8.80	8.17	8.42	9.63	9.13	9.37	9.19	9.25	9.23	9.22	9.38	9.36	9.18	9.04	9.01
SDSS J095852.19+120245.0	9.39	8.65	8.88	9.97	9.16	9.90	9.38	9.36	9.26	9.45	9.60	9.59	9.38	9.41	9.43
SDSS J100212.63+520800.2	8.79	8.11	8.34	9.25	8.46	9.23	8.71	8.59	8.51	8.84	9.01	8.98	8.82	8.78	8.78
SDSS J100610.55+370513.8	9.63	8.78	8.98	...	...	...	...	...	...	9.25	9.40	9.39	9.21	9.19	9.17
SDSS J100653.26+011938.7	9.41	8.49	8.69	...	...	...	...	...	...	9.17	9.33	9.31	9.16	9.28	9.29
SDSS J100850.06-023831.6	8.83	8.10	8.36	9.17	8.81	8.95	8.90	8.96	8.97	8.90	9.07	9.04	8.90	8.90	8.89
SDSS J101106.74+114759.4	8.63	8.27	8.54	9.02	8.57	9.11	8.71	8.70	8.71	8.77	8.93	8.91	8.71	8.85	8.93
SDSS J101211.44+330926.4	9.55	8.60	8.80	...	...	...	...	...	...	8.70	8.86	8.84	8.65	9.47	9.55
SDSS J101353.43+244916.4	9.42	8.71	8.93	...	...	...	...	...	...	9.25	9.40	9.39	9.19	9.40	9.48
SDSS J101425.11+032003.7	9.24	8.40	8.60	9.85	8.94	9.66	9.19	9.03	8.96	9.35	9.51	9.49	9.34	9.49	9.49
SDSS J101429.57+481938.4	8.58	8.06	8.33	9.81	8.83	9.50	9.30	8.91	8.90	8.94	9.10	9.08	8.88	9.03	9.07
SDSS J101542.04+430455.6	8.89	8.59	8.88	...	...	...	...	...	...	9.31	9.46	9.45	9.25	9.29	9.28
SDSS J101724.26+333403.3	9.43	8.50	8.69	9.24	8.57	9.12	8.76	8.67	8.64	9.00	9.17	9.14	8.96	8.90	8.87
SDSS J102154.00+051646.3	9.53	8.91	9.14	...	...	...	...	...	...	...	...	...	...	...	...
SDSS J102537.69+211509.1	9.45	8.66	8.87	9.49	8.97	9.96	9.36	9.13	9.18	9.34	9.50	9.48	9.30	9.35	9.34
SDSS J102731.49+541809.7	9.34	8.37	8.54	9.54	9.21	9.96	9.08	9.80	9.29	9.65	9.81	9.79	9.59	9.22	9.16

SDSS J102907.09+651024.6	9.29	8.81	9.14	10.22	9.35	9.85	9.78	9.54	9.50	9.42	9.58	9.56	9.36	9.19	9.16
SDSS J103209.78+385630.5	8.81	8.04	8.24	9.66	8.94	9.82	9.06	9.05	8.98	9.17	9.33	9.31	9.11	9.15	9.15
SDSS J103236.98+230554.1	8.93	8.51	8.75	8.86	8.90	9.23	8.33	9.01	8.97	8.97	9.13	9.11	8.94	9.03	9.05
SDSS J103246.19+323618.0	9.07	8.24	8.46	...	...	...	...	...	...	9.43	9.59	9.57	9.38	9.13	9.08
SDSS J103405.73+463545.4	9.52	8.67	8.87	...	...	...	...	...	...	9.63	9.78	9.77	9.58	9.22	9.16
SDSS J103718.23+302509.1	9.34	9.19	9.54	...	...	...	...	...	...	9.01	9.17	9.15	9.00	9.18	9.20
SDSS J104018.51+572448.1	9.22	8.60	8.85	9.90	9.30	9.95	9.23	9.30	9.33	9.35	9.50	9.49	9.29	9.14	9.11
SDSS J104330.09+441051.5	9.35	8.73	8.97	9.67	9.03	9.53	9.27	9.11	9.14	9.50	9.66	9.64	9.47	9.22	9.21
SDSS J104336.73+494707.6	9.66	8.71	8.90	9.91	9.45	9.55	9.57	9.51	9.61	9.50	9.65	9.64	9.48	9.28	9.26
SDSS J104621.57+483322.7	8.62	7.68	7.88	...	...	...	...	...	...	8.97	9.14	9.11	8.95	9.19	9.22
SDSS J104716.50+360654.0	8.90	8.33	8.56	9.00	8.69	9.28	8.97	8.90	8.95	8.72	8.89	8.86	8.72	8.82	8.88
SDSS J104743.57+661830.5	9.65	8.68	8.87	9.69	9.25	9.52	9.35	9.41	9.40	9.56	9.72	9.70	9.52	9.14	9.08
SDSS J104911.34+495113.6	8.96	8.51	8.76	8.80	8.40	9.07	8.70	8.59	8.64	8.80	8.96	8.94	8.82	8.23	8.16
SDSS J104941.58+522348.9	9.39	8.54	8.74	...	...	...	...	...	...	9.10	9.26	9.24	9.07	9.07	9.06
SDSS J105045.72+544719.2	9.43	8.75	8.98	9.80	9.33	9.90	9.50	9.48	9.53	9.62	9.77	9.76	9.58	9.41	9.41
SDSS J105902.04+580848.6	8.83	8.35	8.61	9.33	8.86	9.31	9.01	8.98	9.01	9.13	9.28	9.27	9.05	8.87	8.84
SDSS J105926.43+062227.4	9.37	8.43	8.63	9.76	9.33	9.72	9.62	9.49	9.58	9.82	9.97	9.96	9.84	9.38	9.32
SDSS J110148.85+054815.5	9.68	8.78	8.98	...	...	...	...	...	...	9.33	9.49	9.47	9.30	9.05	9.01
SDSS J110516.68+200013.7	9.36	8.54	8.75	9.31	8.88	9.44	9.07	8.98	9.06	9.04	9.21	9.18	9.01	8.87	8.83
SDSS J110735.58+642008.6	8.73	8.39	8.64	9.98	9.39	9.73	9.55	9.49	9.53	9.43	9.58	9.57	9.42	9.44	9.47
SDSS J110810.87+014140.7	9.16	8.34	8.55	9.77	9.04	10.30	9.32	9.11	9.13	9.01	9.17	9.15	8.98	9.34	9.37
SDSS J111119.10+133603.8	9.77	8.79	8.97	10.28	9.40	10.30	9.75	9.52	9.53	...	...	...	...	...	...
SDSS J111313.29+102212.4	9.28	8.95	9.21	...	...	...	...	...	...	9.62	9.77	9.76	9.59	9.27	9.22
SDSS J111352.53+104041.9	9.49	8.57	8.76	...	...	...	...	...	...	...	...	...	...	...	...
SDSS J111850.02+351311.7	8.93	8.62	8.92	9.84	8.97	9.52	9.40	9.10	9.07	9.05	9.21	9.19	9.03	9.16	9.18
SDSS J111920.98+232539.4	9.18	8.53	8.76	...	...	...	...	...	...	8.87	9.03	9.01	8.79	9.00	9.14
SDSS J112127.79+254758.9	9.34	8.72	8.94	...	...	...	...	...	...	8.99	9.15	9.13	8.97	9.55	9.61
SDSS J112726.81+601020.2	8.88	8.14	8.36	9.72	9.00	9.43	9.14	9.13	9.04	8.86	9.03	9.00	8.94	8.23	8.15

SDSS J112938.46+440325.0	9.13	8.91	9.18	...	...	...	...	...	...	8.70	8.86	8.84	8.62	8.25	8.19
SDSS J113048.45+225206.6	9.47	8.57	8.78	...	...	...	...	...	...	8.59	8.75	8.73	8.60	8.39	8.36
SDSS J113330.17+144758.8	9.27	8.74	8.99	...	...	...	...	...	...	9.48	9.63	9.62	9.46	9.29	9.27
SDSS J113621.05+005021.2	9.57	8.77	8.99	9.56	9.52	9.76	9.40	9.50	9.77	9.23	9.38	9.37	9.22	9.17	9.15
SDSS J113740.61+630256.9	9.64	8.69	8.88	...	...	...	...	...	...	...	...	...	...	...	...
SDSS J113924.64+332436.9	9.03	8.13	8.33	...	...	...	...	...	...	9.38	9.54	9.52	9.38	9.32	9.31
SDSS J114212.25+233250.5	8.84	8.43	8.71	10.11	9.09	9.78	9.60	9.25	9.18	9.26	9.41	9.40	9.19	9.43	9.49
SDSS J114323.71+193448.0	9.56	8.64	8.84	...	...	...	...	...	...	9.32	9.48	9.46	9.32	9.01	9.01
SDSS J114350.30+362911.3	9.17	8.66	8.91	9.27	9.01	9.48	8.65	8.95	9.07	9.33	9.48	9.47	9.26	9.66	9.69
SDSS J114705.24+083900.6	9.40	8.72	8.93	...	...	...	...	...	...	...	...	...	...	...	...
SDSS J114711.78+084029.6	8.70	8.41	8.67	9.54	8.65	8.76	8.83	8.72	8.60	...	...	...	...	...	...
SDSS J114738.35+301717.5	9.10	8.77	9.02	...	...	...	...	...	...	9.41	9.56	9.55	9.38	9.03	8.97
SDSS J114902.70+144328.0	9.26	8.54	8.76	9.52	9.37	9.28	9.17	9.48	9.52	9.18	9.34	9.32	9.11	9.19	9.18
SDSS J114907.15+004104.3	9.50	8.62	8.82	9.56	9.06	9.31	9.15	9.11	9.16	9.66	9.81	9.80	9.64	9.18	9.10
SDSS J114927.90+432727.9	9.78	9.54	9.95	9.95	9.16	9.59	9.51	9.42	9.30	9.25	9.40	9.39	9.17	9.15	9.14
SDSS J115747.99+272459.6	9.12	8.69	8.97	...	...	...	...	...	...	9.03	9.19	9.17	8.98	9.31	9.32
SDSS J121314.03+080703.6	8.93	8.35	8.58	9.61	9.23	9.14	8.99	9.20	9.28	9.10	9.26	9.24	9.04	8.90	8.87
SDSS J121404.10+330945.6	9.13	8.41	8.62	...	...	...	...	...	...	8.83	8.99	8.97	8.77	8.98	9.00
SDSS J121423.01+024252.8	8.89	8.38	8.62	...	...	...	...	...	...	9.29	9.44	9.43	9.15	8.81	8.72
SDSS J121519.42+424851.0	8.97	8.58	8.85	9.21	8.81	9.21	8.87	8.83	8.93	9.00	9.16	9.14	8.94	9.03	9.09
SDSS J121736.65+515510.3	9.51	8.85	9.07	...	...	...	...	...	...	9.09	9.25	9.23	9.02	9.27	9.34
SDSS J121810.98+241410.9	9.23	8.67	8.92	9.79	9.06	9.53	9.47	9.24	9.24	9.35	9.50	9.49	9.32	9.72	9.74
SDSS J122046.05+455442.1	9.33	8.86	9.12	10.27	9.41	9.98	9.81	9.63	9.51	9.87	10.03	10.01	9.81	9.59	9.55
SDSS J122343.15+503753.4	9.56	9.06	9.30	...	...	...	...	...	...	9.09	9.24	9.23	8.99	9.37	9.45
SDSS J122709.48+310749.3	9.35	8.74	8.97	9.98	9.12	9.05	9.24	9.14	9.10	9.76	9.92	9.90	9.67	9.52	9.49
SDSS J122938.61+462430.5	9.11	8.44	8.68	9.38	9.14	9.23	9.21	9.14	9.35	9.13	9.28	9.27	9.07	9.07	9.10
SDSS J123514.64+462904.0	9.45	8.91	9.16	9.34	9.09	9.26	9.19	9.18	9.30	9.18	9.34	9.32	9.12	9.25	9.26
SDSS J125150.45+114340.7	9.36	8.82	9.09	9.46	9.17	9.09	9.32	9.31	9.40	9.40	9.56	9.54	9.39	9.16	9.13

SDSS J125159.90+500203.6	8.93	8.34	8.58	9.84	9.44	9.59	9.49	9.52	9.59	9.35	9.50	9.49	9.33	9.60	9.67
SDSS J132845.00+510225.8	9.36	8.79	9.03	9.61	9.18	9.74	9.27	9.28	9.34	9.43	9.58	9.57	9.40	9.00	8.92
SDSS J133342.56+123352.7	9.34	8.67	8.89	...	...	...	...	...	...	9.57	9.72	9.71	9.52	9.26	9.21
SDSS J134341.99+255652.9	9.96	9.06	9.25	9.67	9.05	9.68	9.10	8.91	9.11	9.79	9.95	9.93	9.72	9.36	9.30
SDSS J135908.35+305830.8	9.35	8.44	8.64	10.04	9.27	9.36	9.67	9.38	9.42	9.54	9.70	9.68	9.52	9.17	9.12
SDSS J140058.79+260619.4	8.77	8.17	8.40	...	...	...	...	...	...	9.05	9.21	9.19	9.01	9.38	9.47
SDSS J140704.43+273556.6	9.49	8.61	8.81	9.76	9.21	9.64	9.26	9.29	9.32	9.49	9.65	9.63	9.45	9.13	9.05
SDSS J141028.14+135950.2	9.89	8.95	9.15	9.59	9.35	9.31	9.37	9.42	9.55	9.68	9.84	9.82	9.67	9.43	9.42
SDSS J141321.05+092204.8	9.34	8.89	9.16	...	...	...	...	...	...	...	...	...	...	...	...
SDSS J141617.38+264906.1	9.29	8.38	8.58	...	...	...	...	...	...	9.03	9.19	9.17	8.95	9.17	9.16
SDSS J141925.48+074953.5	9.30	8.72	8.96	10.01	9.24	9.55	9.37	9.33	9.28	9.52	9.67	9.66	9.47	9.32	9.29
SDSS J141951.84+470901.3	9.40	8.57	8.78	9.56	9.35	9.07	9.15	9.40	9.47	9.34	9.49	9.48	9.33	9.17	9.15
SDSS J142013.03+253403.9	8.53	8.27	8.53	...	...	...	...	...	...	9.25	9.41	9.39	9.19	9.15	9.14
SDSS J142435.97+421030.4	9.42	8.43	8.61	9.57	9.23	9.41	9.16	9.30	9.35	9.79	9.94	9.93	9.72	9.39	9.33
SDSS J142500.24+494729.2	9.08	8.61	8.87	...	...	...	...	...	...	9.46	9.61	9.60	9.41	9.29	9.26
SDSS J142502.62+274912.2	9.30	8.86	9.09	8.68	8.68	9.23	8.50	8.49	8.87	9.36	9.51	9.50	9.34	9.57	9.57
SDSS J142543.32+540619.3	9.33	8.65	8.88	9.80	9.04	10.01	9.07	9.21	9.06	9.35	9.50	9.49	9.32	9.54	9.62
SDSS J142755.85-002951.1	9.09	8.51	8.75	9.19	8.72	9.33	8.91	8.91	8.91	8.92	9.08	9.06	8.90	9.14	9.20
SDSS J142903.03-014519.3	9.42	8.78	9.01	10.14	9.86	9.74	9.67	9.44	9.98	9.50	9.65	9.64	9.44	9.23	9.19
SDSS J144624.29+173128.8	8.96	8.55	8.78	8.68	8.42	8.60	8.06	8.48	8.46	8.94	9.09	9.08	8.93	9.59	9.67
SDSS J144706.81+212839.2	9.67	8.85	9.06	9.94	9.17	9.94	9.29	9.64	9.21	9.08	9.23	9.22	9.06	8.95	8.93
SDSS J144948.62+123047.4	9.62	8.79	8.99	9.44	9.19	9.46	9.45	9.91	9.46	9.55	9.71	9.69	9.53	9.17	9.13
SDSS J145541.11-023751.0	9.23	8.40	8.61	8.93	8.74	9.11	8.91	8.82	8.97	9.22	9.38	9.36	9.21	9.02	9.04
SDSS J150205.58-024038.5	9.24	8.56	8.79	...	...	...	...	...	...	9.32	9.48	9.46	9.29	9.07	9.03
SDSS J150743.71+220928.8	9.07	8.73	9.01	9.75	9.39	9.50	9.58	9.36	9.61	9.17	9.32	9.31	9.14	9.02	9.01
SDSS J151123.30+495101.2	9.44	8.50	8.69	...	...	...	...	...	...	9.65	9.80	9.79	9.59	9.41	9.37
SDSS J151341.89+463002.7	9.01	8.10	8.30	...	...	...	...	...	...	...	...	...	...	...	...
SDSS J151507.82+612411.9	9.09	8.57	8.81	9.25	8.74	9.46	8.97	8.89	8.91	9.08	9.24	9.22	9.04	9.56	9.69

SDSS J151727.68+133358.6	9.26	8.56	8.78	9.80	9.04	9.53	9.42	9.18	9.18	9.12	9.28	9.26	9.07	9.08	9.11
SDSS J151733.09+435648.4	9.11	8.32	8.54	10.09	9.04	9.76	9.52	9.25	9.10	9.31	9.47	9.45	9.28	9.78	9.84
SDSS J152929.55+230208.7	8.87	8.38	8.64	9.53	8.71	9.76	9.13	8.82	8.82	9.10	9.27	9.24	9.07	9.27	9.34
SDSS J153248.95+173900.8	9.61	8.74	8.95	...	...	...	...	...	...	...	...	...	...	...	...
SDSS J154550.37+554346.2	9.09	8.96	9.22	...	...	...	...	...	...	8.90	9.06	9.04	8.88	9.17	9.21
SDSS J155355.10+375844.1	8.90	8.47	8.72	9.58	8.87	9.24	9.20	8.94	8.96	9.00	9.17	9.14	9.12	8.30	8.22
SDSS J160029.86+331806.9	9.65	8.72	8.91	8.83	8.67	9.20	8.75	9.03	8.87	9.28	9.45	9.42	9.26	8.94	8.88
SDSS J160207.67+380743.0	9.72	8.80	8.98	...	...	...	...	...	...	...	...	...	...	...	...
SDSS J160425.30+193929.1	9.24	8.59	8.82	10.11	9.16	9.70	9.53	9.28	9.21	9.50	9.65	9.64	9.45	9.10	9.04
SDSS J160513.17+325829.9	8.79	8.28	8.56	10.19	9.26	9.56	9.72	9.40	9.35	9.38	9.54	9.52	9.35	9.01	8.97
SDSS J160552.97+292141.4	9.37	8.66	8.88	...	...	...	...	...	...	...	...	...	...	...	...
SDSS J160637.57+173516.2	8.69	8.25	8.54	9.37	8.67	9.06	8.81	8.70	8.69	8.98	9.15	9.12	8.97	8.85	8.81
SDSS J161435.70+372715.6	9.33	8.53	8.74	9.26	8.87	9.43	8.82	8.85	8.97	8.86	9.02	9.00	8.84	9.23	9.35
SDSS J161942.39+525613.4	9.56	8.77	8.98	...	...	...	...	...	...	8.90	9.05	9.04	8.88	9.23	9.22
SDSS J162659.24+301535.0	9.11	8.29	8.49	9.07	8.51	9.41	8.75	8.64	8.63	8.90	9.06	9.04	8.87	9.07	9.12
SDSS J163125.10+174810.0	9.61	8.80	9.01	...	...	...	...	...	...	8.86	9.02	9.00	8.85	9.41	9.44
SDSS J163433.42+265158.2	8.56	8.19	8.45	9.30	8.39	9.26	8.75	8.50	8.42	8.79	8.95	8.93	8.71	8.90	8.98
SDSS J164807.55+254407.1	9.09	8.63	8.87	9.21	8.92	9.46	9.00	9.04	9.13	9.04	9.19	9.18	8.96	9.21	9.28
SDSS J165321.03+271706.7	8.85	8.58	8.85	9.99	9.03	9.61	9.42	9.18	9.09	9.14	9.30	9.28	9.10	9.28	9.31
SDSS J173352.23+540030.4	9.42	8.68	8.90	9.82	9.16	9.81	9.13	9.25	9.23	9.23	9.39	9.37	9.21	9.25	9.23
SDSS J205900.36-064309.5	8.53	7.59	7.79	10.19	9.28	10.84	9.47	9.33	9.27	...	...	...	...	...	...
SDSS J210558.29-011127.5	8.89	8.28	8.52	9.06	8.67	8.59	8.82	8.88	8.83	9.02	9.19	9.16	9.01	9.35	9.45
SDSS J210831.56-063022.5	9.06	8.57	8.84	10.21	9.23	9.66	9.45	9.35	9.24	...	...	...	...	...	...
SDSS J211251.06+000808.3	8.60	7.97	8.23	9.59	8.79	9.05	9.05	8.90	8.81	9.08	9.24	9.22	9.03	9.00	8.99
SDSS J213655.35-080910.1	8.83	7.91	8.08	9.51	9.10	9.25	9.06	9.58	9.17	9.82	9.99	9.96	9.75	9.41	9.35
SDSS J214901.21-073141.6	8.76	8.46	8.74	9.84	9.10	9.78	9.37	9.38	9.20	9.29	9.45	9.43	9.25	9.29	9.32
SDSS J220139.99+114140.8	8.75	8.44	8.73	9.37	8.88	9.06	9.03	9.96	8.95	8.84	9.01	8.98	8.77	9.23	9.35
SDSS J220344.98+235729.3	9.62	8.68	8.88	...	...	...	...	...	...	8.80	8.96	8.94	8.80	10.18	10.24

SDSS J222310.76+180308.1	8.85	8.27	8.50	9.42	8.78	9.37	8.92	8.80	8.85	...	...	...	...	...	...
SDSS J222621.45+251545.0	9.95	8.98	9.18	9.96	9.37	9.83	9.56	9.53	9.55	10.07	10.21	10.21	10.00	9.68	9.63
SDSS J223934.45-004707.2	9.40	8.47	8.66	...	...	...	...	...	...	9.55	9.71	9.69	9.57	9.09	9.03
SDSS J225608.48+010557.8	8.82	8.37	8.62	...	...	...	...	...	...	9.04	9.20	9.18	9.03	9.26	9.27
SDSS J225627.12+092313.3	9.13	8.41	8.64	9.49	8.86	9.48	9.12	8.94	8.98	9.01	9.18	9.15	8.99	8.86	8.86
SDSS J230722.21+253803.8	8.65	8.04	8.27	8.47	8.03	8.44	8.38	8.15	8.20	8.61	8.78	8.75	8.58	9.44	9.63
SDSS J231450.12+182402.8	8.91	8.32	8.56	9.41	8.86	9.64	9.10	8.94	9.02	9.12	9.27	9.26	9.07	9.19	9.21
SDSS J233304.61-092710.9	9.10	8.63	8.86	9.17	8.81	9.31	8.94	10.23	8.98	9.16	9.31	9.30	9.10	9.39	9.43
SDSS J233344.66+290251.5	9.09	8.48	8.70	9.60	8.83	8.98	9.06	8.84	8.89	9.36	9.51	9.50	9.29	9.18	9.15
SDSS J234817.55+193345.8	9.19	8.74	9.00	9.52	8.62	9.13	8.89	8.71	8.60	9.37	9.53	9.51	9.32	9.00	8.97
SDSS J235212.85-012029.6	9.28	9.16	9.43	9.55	9.04	9.33	9.08	9.16	9.12	9.24	9.40	9.38	9.19	8.93	8.88

TABLE 4.3. [a]$\log(M_{\rm BH})$ estimates derived with (top row) and without (bottom row) the inclusion of the C IV EW, where available.

Data in this Table are presented as $\log(M_{\rm BH}/M_{\odot})$.

CHAPTER 5

SHEDDING NEW LIGHT ON WEAK EMISSION-LINE QUASARS IN THE C IV–Hβ PARAMETER SPACE

5.1. Introduction

Weak emission-line quasars (WLQs) are a subset of Active Galactic Nuclei (AGN) with extremely weak or undetectable rest-frame optical–UV emission lines [182, 183, 184, 185]. The Sloan Digital Sky Survey (SDSS; [68]) has discovered $\approx 10^3$ Type 1 quasars with Lyα+N V λ1240 rest-frame equivalent widths (EWs) < 15.4 Å and/or C IV λ1549 EW < 10.0 Å [186, 187]. These numbers represent a highly significant concentration of quasars at $\gtrsim 3\sigma$ deviation from the log-normal EW distribution of the SDSS quasar population, with no corresponding "tail" at the opposite end of the distribution [186, 188]. Furthermore, the fraction of WLQs among the broader quasar population increases sharply at higher redshifts (and thus higher luminosities), from $\sim 0.1\%$ at $3 \lesssim z \lesssim 5$ to $\sim 10 - 15\%$ at $z \gtrsim 5.7$ [186, 189, 77].

Multi-wavelength observations of sources of this class have shown that they are unlikely to be high-redshift galaxies with apparent quasar-like luminosity due to gravitational-lensing amplification, dust-obscured quasars, or broad-absorption-line (BAL) quasars [190, 191], but that their UV emission-lines are intrinsically weak. Furthermore, WLQs are typically radio-quiet, and have X-ray and mid-infrared properties inconsistent with those of BL Lac objects [192, 193, 188, 194].

About half of WLQs have notably lower X-ray luminosities than expectations from their monochromatic luminosities at 2500 Å [195, 196, 197, 198]. One explanation for this phenomenon is that, at small radii, the geometrically thick accretion disks of these WLQs are 'puffed up' and prevent highly ionizing photons from reaching the broad emission-line region (BELR; [199, 188, 195, 196, 198]). The X-ray radiation is partially absorbed by the thick disk, resulting in low apparent X-ray luminosities at high inclinations (i.e., when these objects are viewed edge-on). When these objects are viewed at much lower inclinations, their notably steep X-ray spectra indicate accretion at high Eddington luminosity ratio ([$L_{\rm bol}/L_{\rm Edd}$, hereafter $L/L_{\rm Edd}$; [200, 195, 201]).

The indications of high Eddington ratios in WLQs may provide a natural explanation for the weakness of their emission lines in the context of the Baldwin Effect. In its classical form, this effect is an anti-correlation between the EW(C IV) and the quasar luminosity [202]. Subsequent studies, however, have found that this relation stems from a more fundamental anti-correlation between EW(C IV) and Hβ-based $L/L_{\rm Edd}$ ([203], hereafter BL04; [204]). This anti-correlation, coined the Modified Baldwin Effect (MBE), was extensively studied and built upon by [177], hereafter SL15, however, see also [205]. SL15 utilized a sample of nine WLQs and 99 non-radio-loud, non-BAL ('ordinary') quasars spanning wide ranges of luminosity and redshift to analyze the relative strength of the C IV emission-line and the Hβ-based Eddington ratio. They confirmed the findings of BL04 for the sample of ordinary quasars. However, all nine WLQs were found to possess relatively low $L/L_{\rm Edd}$ values, while the MBE predicts considerably higher Eddington ratios for these sources. This finding led SL15 to conclude that the Hβ-based $L/L_{\rm Edd}$ parameter cannot depend solely on EW(C IV) for all quasars. Such a conclusion may also be consistent with subsequent findings that WLQs possess strong Fe II emission and large velocity offsets of the C IV emission-line peak with respect to the systemic redshift (hereafter, Blueshift(C IV)) [206], and that $L/L_{\rm Edd}$ correlates with Blueshift(C IV) at high Blueshift(C IV) values (see Figure 14 of [113]).

In this work, we explore two possible explanations for the findings of SL15. The first of these is that the traditional estimation of Hβ-based black-hole mass ($M_{\rm BH}$) values, and therefore $L/L_{\rm Edd}$ values, fails to accurately predict $M_{\rm BH}$, particularly in quasars with strong optical Fe II emission [181, 169]. Such a case is typical for WLQs, and thus a correction via measurement of the strength of the Fe II emission-complex in the optical band is required [168, 174]. The second explanation is that EW(C IV), by itself, is not an ideal indicator of the quasar accretion rate. In addition to EW(C IV), we utilize a recently defined parameter, the 'C IV || Distance' [207] (hereafter R22), which represents a combination of the EW(C IV) and Blueshift(C IV) [86, 114, 208], and search for a correlation between that parameter and $L/L_{\rm Edd}$.

To investigate these explanations, we extend the WLQ sample of SL15 to nine additional sources available from the Gemini Near-IR Spectrograph - Distant Quasar Survey (GNIRS-DQS;[115], hereafter M23). Furthermore, we study the distribution of WLQs in $L/L_{\rm Edd}$ space versus a sample of ordinary quasars from SL15 and M23. We aim to investigate the underlying driver for the weak emission lines in WLQs and test the assertion that all WLQs have extremely high accretion rates.

The structure of this paper is as follows. In Section 5.2, we discuss our sample selection and the relevant equations used to estimate Hβ-based $L/L_{\rm Edd}$ values. In Section 5.3, we analyze the samples' spectroscopic properties as well as the sources' black-hole masses and accretion rates. Then, we discuss the correlation between the C IV parameter space and $L/L_{\rm Edd}$. In Section 5.4, we summarize our findings. Throughout this paper, we compute luminosity distances using a standard ΛCDM cosmology with $H_0 = 70$ km s^{-1} Mpc^{-1}, $\Omega_{\rm M} = 0.3$, and $\Omega_\Lambda = 0.7$ [67].

5.2. Sample Selection and Data Analysis

5.2.1. WLQ Sample

We compile a sample of 18 WLQs in this work. All these WLQs have accurate full-width-at-half-maximum intensity of the broad component of the Hβ λ4861 emission line (hereafter, FWHM(Hβ)), monochromatic luminosity at rest-frame 5100 Å (hereafter, νL_ν(5100 Å)), EW(Fe II $\lambda\lambda 4434-4684$), and EW(Hβ) measurements. Nine of these sources were obtained from SL15, seven from the GNIRS-DQS sample of M23 (see Section 5.2.2), and two from this work (see Appendix 5.5). SL15 compiled a sample of nine WLQs: SDSS J0836+1425, SDSS J1411+1402, SDSS J1417+0733, SDSS J1447−0203 [185, 209], SDSS J0945+1009 [210, 209], SDSS J1141+0219, SDSS J1237+6301 [186, 191], SDSS J1521+5202 [211, 199], and PHL 1811 [212].

Table 5.1 provides basic properties for the 18 WLQs in our sample. Column (1) provides the source name; Column (2) gives the systemic redshift determined from the peak of, in order of preference, the [O III]λ5007, Mg II λ2798, and Hβ emission lines; Column (3) gives $\log \nu L_\nu$ (5100 Å); Column (4) gives FWHM(Hβ); Column (5) gives $R_{\rm Fe\,II} \approx$ EW(Fe II)/EW(Hβ); Column (6) gives traditional Hβ-based $M_{\rm BH}$ estimates (following Equations 21 and 23); Column (7) gives Fe II-corrected Hβ-based $M_{\rm BH,\ corr}$ estimates (following Equations 22 and 23); Column (8) gives traditional Hβ-based $L/L_{\rm Edd}$ values (from Equation 24); Column (9) gives Fe II-corrected Hβ-based $L/L_{\rm Edd,\ corr}$ values (from Equation 24); Column (10) gives EW(C IV); Column (11) gives Blueshift(C IV); Columns (12) and (13) provide the references for the rest-frame optical and UV spectral measurements, respectively. All derived properties are discussed in detail in Section 5.2.3.

The two WLQs from [191] and the two introduced in Appendix 5.5 do not have a reliable C IV line measurement in the literature, hence we perform our own measurements from their SDSS spectra, following the procedure in Dix et al. (2023, hereafter D23). Briefly, we fit the C IV emission line with a local, linear continuum and two independent Gaussians. These Gaussians are constrained such that the flux densities lie between 0 and twice the value of the peak of the emission line; the FWHM is restricted to not exceed 15000 km s^{-1}. The EW of the line emission can then be measured, as well as the blueshift, which is calculated from the difference between λ1549 and the peak of the Gaussians (see Equation 20).

These WLQs possess stronger relative optical Fe II emission (indicated by the larger $R_{\rm Fe\,II}$ values) compared to ordinary quasars from the same samples. WLQs are only selected based on their C IV emission-line strength (EW(C IV) $<$ 10 Å), so we are unaware of any biases introduced by the rest-frame optical emission to the selection process of the WLQs in this work.

5.2.2. Ordinary Quasar Sample Selection

In order to create a comprehensive comparison sample of quasars for our analysis, which requires measurements of both the Hβ and C IV emission lines, we select two catalogs of ordinary quasars from the literature. For the high-redshift quasars ($1.5 \lesssim z \lesssim 3.5$), C IV emission properties can be obtained from SDSS, but the Hβ emission line lies outside of the SDSS range, and therefore it has to be measured with NIR spectroscopy. In this redshift range, we utilize the GNIRS-DQS catalog in M23. GNIRS-DQS is the largest and most comprehensive inventory of rest-frame optical properties for luminous quasars, notably the Hβ, [O III], and Fe II emission lines. To complement this sample of high-redshift, high-luminosity quasars, we include an archival sample of quasars in the low-redshift regime from the BL04 subsample also utilized in SL15. In this redshift range ($z < 0.5$), the Hβ emission properties can be obtained from optical spectra, but the C IV emission-line properties are more difficult to obtain, and are available primarily from the *Hubble Space Telescope* (HST) and the *International Ultraviolet Explorer* (IUE) archives. Below, we briefly discuss the selection process for our ordinary quasar sample.

The GNIRS-DQS sources were selected to lie in three narrow redshift intervals, $1.55 \lesssim z \lesssim 1.65$, $2.10 \lesssim z \lesssim 2.40$, and $3.20 \lesssim z \lesssim 3.50$ to center the Hβ+[O III]spectral complex in the NIR bands covered by GNIRS (i.e., the J, H, and K bands, respectively). In total, the survey comprises 260 sources with high-quality NIR spectra and comprehensive Hβ, [O III], and Fe II spectral measurements [115]. We exclude 64 BAL quasars, 16 radio-loud quasars (RLQs), and one quasar, SDSS J114705.24+083900.6 that is both BAL and radio loud. We define RLQs as sources having radio-loudness values of $R > 100$ (where R is the ratio between the flux densities at 5 GHz and 4400 Å; [17]). RLQs and BAL quasars are excluded to minimize the potential effects of continuum boosting from a jet [187] and absorption biases (e.g., see BL04), respectively. Two quasars, SDSS J073132.18+461347.0 and SDSS J141617.38+264906.1, are excluded due to a lack of C IV measurements from D23. In total, 177 GNIRS-DQS quasars are included in our analysis; of these, seven sources with EW(C IV) < 10 Å can be formally classified as WLQs (see Section 5.2.1). We adopt values of FWHM(Hβ), νL_ν(5100 Å), EW(Hβ), and EW(Fe II) values from M23. The latter two parameters are used to derive $R_{\mathrm{Fe\,II}}$.

Quasars in the M23 sample are crossmatched with the C IV emission-line measurements from D23, who also report the wavelengths of the C IV emission-line peaks. The Blueshift(C IV) values are derived following Equation (2) in [54]

$$\frac{\Delta v}{\mathrm{km\ s^{-1}}} = \left[\frac{c}{\mathrm{km\ s^{-1}}}\right]\left(\frac{z_{\mathrm{meas}} - z_{\mathrm{sys}}}{1 + z_{\mathrm{sys}}}\right), \quad (20)$$

where z_{meas} is the redshift measured from the wavelength of the C IV emission-line peak, and z_{sys} is the systemic redshift with respect to the [O III], the Mg II, or the Hβ emission lines reported in M23. In this work, we report the Blueshift(C IV) $\equiv -\Delta v$ values.

WLQs often have extremely weak or undetectable [O III]emission, so we must use alternative emission lines as the reference for $z_{\rm sys}$. Although there are known, non-negligible intrinsic uncertainties associated with using the Mg II and Hβ emission lines as $z_{\rm sys}$ indicators ($\sim$ 200 km s^{-1} and $\sim$ 400 km s^{-1}, respectively; [32]), WLQs often possess large Blueshift(C IV) values ($>$ 2000 km s^{-1} in $\sim$ 60% of the WLQs in our sample); therefore, the uncertainty associated with using, e.g., an Hβ-based $z_{\rm sys}$ value is relatively small compared to the quasar's Blueshift(C IV) value, and does not affect the conclusions of this work.

Sixty quasars at $z < 0.5$ from BL04 are added to our analysis from the 63 BL04 quasars in SL15. PG 0049+171, PG 1427+480, and PG 1415+451 are excluded due to a lack of published Fe II spectral measurements. The UV data in the BL04 sample comes, roughly equally, from both the *HST* and the *IUE* archives [167]. Throughout this work, we check whether including only one *HST* or *IUE* data changes the conclusion of the paper, but we find no statistical difference in the results of Section 5.3. Therefore, we include both subsets in the main body of this work. We obtain the FWHM(Hβ), νL_ν(5100 Å), and $R_{\rm Fe\,II}$ values for the BL04 sources from [82], and their EW(C IV) and Blueshift(C IV) values from [167]. Table 5.2 lists the basic properties of the ordinary quasars in our sample with the same formatting as Table 5.1.

5.2.3. $M_{\rm BH}$ and $L/L_{\rm Edd}$ Estimates

Traditional estimation of single-epoch $M_{\rm BH}$ values has made use of the reverberation-mapping (RM) scaling relationship between the size of the Hβ-emitting region ($R_{\rm H\beta}$) and νL_ν(5100 Å) [145, 213, 147, 149]. In this work, we use the empirical scaling relation established by [149] for consistency with other recent studies [169]:

$$\log\left[\frac{R_{\rm H\beta}}{\rm lt{-}days}\right] = (1.527 \pm 0.031) + (0.533 \pm 0.035)\ \log\,\ell_{44} \tag{21}$$

where $\ell_{44} \equiv \nu L_\nu(5100\ \text{Å})\ /10^{44}$ erg s^{-1}.

However, the Hβ RM sample was subsequently determined to be biased toward objects with strong, narrow [O III] emission-lines, and, in effect, is biased in favor of low-accretion-rate broad-line AGNs [214, 215]. Recent RM campaigns aimed at minimizing such bias, such as the Super-Eddington Accreting Massive Black Hole (SEAMBH; [216, 217, 144]) and the SDSS-RM project [131], found deviations from the traditional size-luminosity relationship. In particular, SEAMBH found a population of rapidly accreting AGNs with a BELR size up to 3-8 times smaller than predicted by Equation 21, which implies an overestimation of super-Eddington-accreting $M_{\rm BH}$ values from single-epoch spectra by the same factor. We apply a correction to the traditional Hβ-based $M_{\rm BH}$ estimation, developed by [168], which utilizes the $R_{\rm Fe\,II}$ parameter in addition to FWHM(Hβ) and νL_ν (5100 Å).

For the Fe II-corrected values of $M_{\rm BH}$ (hereafter, $M_{\rm BH,\ corr}$), we apply the size-luminosity scaling relation for $R_{\rm H\beta}$ following Equation (5) of [168]:

$$\begin{aligned}(22)\qquad &\log\left[\frac{R_{\rm H\beta,\ corr}}{\rm lt{-}days}\right]\\ &= (1.65 \pm 0.06) + (0.45 \pm 0.03)\ \log\ \ell_{44}\\ &+ (-0.35 \pm 0.08)\ R_{\rm Fe\ II}.\end{aligned}$$

Subsequently, $M_{\rm BH}$ ($M_{\rm BH,\ corr}$) can be estimated using the following relationship:

$$\begin{aligned}(23)\qquad &\frac{M_{\rm BH}\ (M_{\rm BH,\ corr})}{M_\odot}\\ &= f\left[\frac{R_{\rm BELR}}{\rm pc}\right]\left[\frac{\Delta V}{\rm km\ s^{-1}}\right]^2\left[\frac{G}{\rm pc\ M_\odot^{-1}\ (km\ s^{-1})^2}\right]^{-1}\\ &\approx 1.5\left[\frac{R_{\rm H\beta}\ (R_{\rm H\beta,\ corr})}{\rm pc}\right]\left[\frac{\rm FWHM(H\beta)}{\rm km\ s^{-1}}\right]^2\\ &\cdot\left[\frac{4.3\times10^{-3}}{\rm pc\ M_\odot^{-1}\ (km\ s^{-1})^2}\right]^{-1},\end{aligned}$$

where we adopt $f = 1.5$ for the virial coefficient, consistent with results from [171, 172, 218, 169], $R_{\rm BELR} \approx R_{\rm H\beta}$ is the size-luminosity relation from Equation 21 or 22, ΔV is the velocity width of the emission line, which is taken here as FWHM(Hβ), assuming Doppler broadening [213], and G is the gravitational constant.

The $L/L_{\rm Edd}$ parameter can be computed from the corresponding $M_{\rm BH}$ value following Equation (2) of [191] assuming that $L_{\rm Edd}$ is computed for the case of solar metallicity:

$$L/L_{\rm Edd}\ (L/L_{\rm Edd,\ corr})$$

(24)
$$= 1.06 f(L) \left[\frac{\nu L_\nu(5100\,\text{Å})}{10^{44}\,\text{ergs}\,\text{s}^{-1}}\right] \left[\frac{M_{\rm BH}\ (M_{\rm BH,\ corr})}{10^6 M}\right]^{-1},$$

where $f(L)$ is the luminosity-dependent bolometric correction to $\nu L_\nu(5100\ \text{Å})$, derived from Equation (21) of [219].

We note that a wide range of bolometric corrections for quasars is available in the literature [220, 221, 222, 223]. However, in general, the range of these corrections is not large enough to affect the conclusion of our work. For example, [169] recently used a constant bolometric correction of $L_{\rm Bol}/\nu L_\nu(5100\ \text{Å}) \sim 9$; the bolometric corrections we derive are in the range of $\sim$ 5-6, which results in a relatively small *systematic* offset in the derivation of the $L/L_{\rm Edd}$ parameter.

The uncertainties associated with the corrected $M_{\rm BH}$ and $L/L_{\rm Edd}$ values in this work are estimated to be at least ~ 0.3 dex [169], but could be much larger ($\sim 0.4 - 0.6$ dex) for high $L/L_{\rm Edd}$ objects such as WLQs (see also, SL15).

5.3. Results and Discussion

5.3.1. Black Hole Masses and Accretion Rates

For the 248 quasars included in this work, we determine the virial Hβ-based $M_{\rm BH,\ corr}$ and corresponding $L/L_{\rm Edd,\ corr}$ values from their derived optical properties, following the Fe II-corrected BELR size-luminosity relation of Equation 22, applied to Equations 23 and 24. We also calculate these quasars' $M_{\rm BH}$ and $L/L_{\rm Edd}$ values following the traditional BELR size-luminosity relation of Equation 21 to compare the two methods for estimating black-hole masses and accretion rates.

Figure 5.1 presents the traditional versus corrected $M_{\rm BH}$ and $L/L_{\rm Edd}$ values for the quasars in our sample, following the procedure of [169]. The Hβ-based $M_{\rm BH,\ corr}$ values of ordinary quasars show small systematic deviations from the traditional BELR size-luminosity relation estimates (less than a factor of two for 222 out of 230 quasars). On the other hand, for a majority of the WLQs, due to the relative weakness in Hβ emission compared to

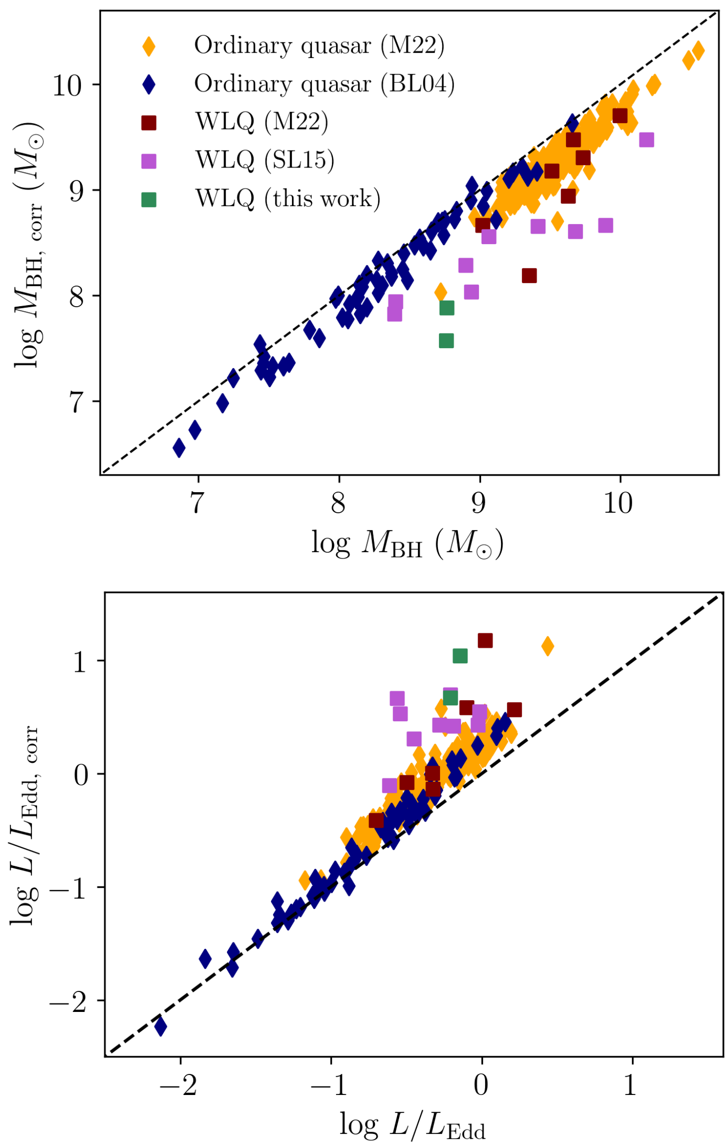

FIGURE 5.1. Black-hole mass (top panel) and accretion rate (bottom panel) calculated using the traditional (x-axis) and $R_{\rm Fe\,II}$-corrected (y-axis) BELR size-luminosity relation for all quasars in our analysis. Diamonds mark ordinary quasars and squares mark WLQs. The dashed lines represent a one-to-one relation between the two methods. The traditional relation overestimates $M_{\rm BH}$ in rapidly-accreting quasars by roughly an order of magnitude. In turn, the traditional relation underestimates $L/L_{\rm Edd}$ by a similar factor. In particular, the $R_{\rm Fe\,II}$-corrected accretion rates are much larger for a considerably larger fraction of sources in the WLQ subset than in the ordinary quasars, due to their larger $R_{\rm Fe\,II}$ values.

Fe II, $M_{\rm BH,\ corr}$ values deviate significantly from the traditional relation, by up to one order of magnitude. Since $L/L_{\rm Edd}$ is inversely proportional to $M_{\rm BH}$, the $L/L_{\rm Edd,\ corr}$ values are enhanced by a similar factor. This result is in line with the [169] finding of a larger deviation from the one-to-one relation in high-accretion-rate quasars.

5.3.2. The Anti-correlation between EW(C IV) and $L/L_{\rm Edd}$

We use our sample to explore the anti-correlation between EW(C IV) and Hβ-based $L/L_{\rm Edd}$ previously studied in SL15, as well as with $L/L_{\rm Edd,\ corr}$. Figure 5.2 shows EW(C IV) plotted against the traditional $L/L_{\rm Edd}$ values (left) and against the Fe II-corrected $L/L_{\rm Edd,\ corr}$ values (right). The first four rows of Table 5.3 present the respective Spearman-rank correlation coefficients ($r_{\rm S}$) and chance probabilities (p) of the ordinary quasar sample and the complete sample, including WLQs, for the correlation involving EW(C IV). We detect significant anti-correlations between EW(C IV) and $L/L_{\rm Edd}$ both with and without WLQs (i.e., $p \ll 1\%$). However, the anti-correlation for the sample including WLQs is slightly weaker than without WLQs (both p values are roughly similar, but $r_{\rm S}$ increases slightly). Our result reaffirms findings by SL15, who found WLQs to be outliers in this relation.

With a Fe II correction, the $L/L_{\rm Edd,\ corr}$ values provide a significantly stronger anti-correlation with EW(C IV) as the $r_{\rm S}$ value decreases from -0.36 (for the $L/L_{\rm Edd}$ case) to -0.48. Furthermore, the inclusion of WLQs no longer spoils the Spearman-rank correlation; in fact, the p value remains extremely low ($p = 4.02 \times 10^{-20}$ for the entire sample), and the $r_{\rm S}$ value decreases from -0.48 to -0.54, indicative of a stronger anti-correlation. Nevertheless, the $L/L_{\rm Edd,\ corr}$ values of most of the WLQs in our sample still appear considerably smaller than a linear model would suggest (see Figure 5.2). To quantify the deviation of WLQs from the MBE, we fit a simple linear model, without considering the errors, to the log EW(C IV) and log $L/L_{\rm Edd,\ corr}$ values of the ordinary quasar sample. Our WLQs deviate from the best-fit model by a mean of $\sim 3.4\sigma$, with a range in deviation from 1.08σ to 8.02σ. Such a discrepancy paints WLQs as significant outliers in this correlation.

We also explore whether a bolometric luminosity correction based on the peculiarity of WLQs could account for this discrepancy. Although several methods for correcting bolometric luminosity are available in the literature [220, 221, 222, 223], if WLQs were to be reliably predicted by the MBE, these corrections must be up to $\sim 10^5$ times larger than those of [219] (as in the case of SDSS J1141+0219 with EW(C IV) = 0.4 Å). Such a discrepancy is larger than the difference expected by any of the current bolometric correction methods in the literature. These results reveal that EW(C IV) is likely not the sole indicator of accretion rate in all quasars, in agreement with SL15.

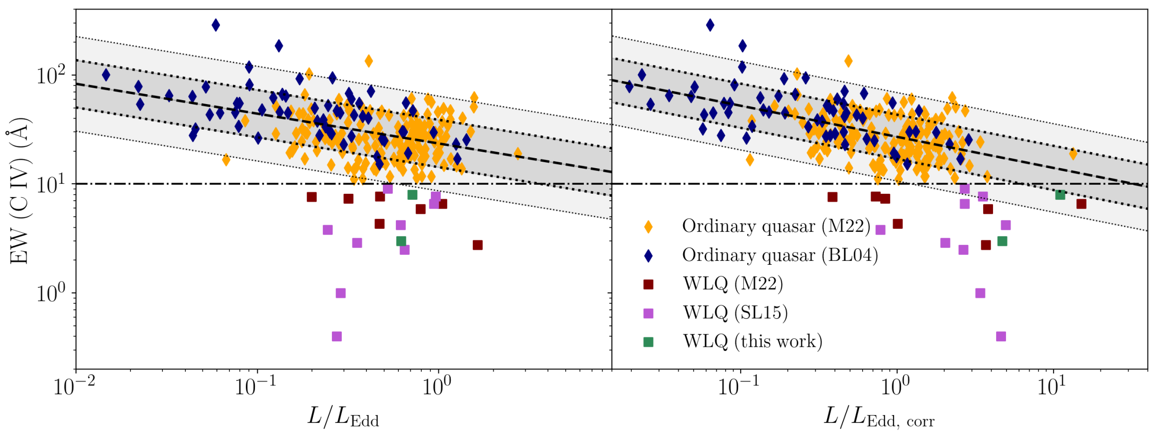

FIGURE 5.2. Correlation between EW(C IV) and $L/L_{\rm Edd}$ of ordinary quasars (diamonds) and WLQs from Table 5.1 (squares). The left panel presents the traditional $L/L_{\rm Edd}$ values, and the right panel displays the Fe II-corrected $L/L_{\rm Edd,\ corr}$ values. The dotted-dashed lines represent the EW threshold for quasars, below which objects are defined as WLQs. The correlation for the ordinary quasar sample, obtained by fitting a linear model, is shown as a dashed line. The shaded regions represent the 1- and 2-σ deviation from the fitted correlation. Correcting the traditional $L/L_{\rm Edd}$ values results in a stronger anti-correlation expected by the MBE (see Table 5.3); however, WLQs' $L/L_{\rm Edd,\ corr}$ values are still considerably (more than an order of magnitude) over-predicted by the MBE, suggesting that EW(C IV) is not the sole indicator of quasars' accretion rates.

5.3.3. The C IV || Distance as an Indicator of $L/L_{\rm Edd}$

[114] used an independent component analysis (ICA) technique to analyze the spectral properties of the C IV emission line in 133 quasars from the SDSS-RM project [131]. In particular, they fitted a curve to trace the positions of these sources on the EW(C IV) and the Blueshift(C IV) plane. The position of a quasar projected onto this curve is defined as its 'C IV || Distance' (for more details on how this parameter is calculated, see [208] and R22). This parameter essentially indicates the location along a non-linear first principal component of the C IV parameter space, and encodes information about the physics of the C IV-emitting gas [86, 224, 225].

The left panel of Figure 5.3 shows the distribution of EW(C IV) versus Blueshift(C IV) of the 248 quasars in our sample. The right panel of Figure 5.3 shows the same distribution in scaled space, following the procedure in [208], and the piece-wise polynomial best-fit curve from Figure 2 of R22. Even though our sources are drawn from samples that are different from those of R22, the best-fit curve traces the C IV parameter space of sources across wide ranges of redshifts and luminosities. Since all quasars in our sample are selected photometrically, either in optical (for GNIRS-DQS quasars) or UV (for BL04 quasars) surveys, and were not selected based on their spectroscopic characteristics, there are no known biases associated with their selection, and thus they are expected to trace the C IV parameter space in a similar manner to larger samples of quasars in other studies [113].

While the EW(C IV) parameter, on its own, is not an ideal accretion-rate indicator, the C IV || Distance parameter appears to provide a robust indication of the accretion rates for all quasars including WLQs. We plot the C IV || Distance versus Hβ-based $L/L_{\rm Edd}$ (left) and $L/L_{\rm Edd,\ corr}$ (right) for all quasars in our sample in Figure 5.4. The last four rows of Table 5.3 provide the Spearman-rank correlation coefficients and chance probabilities for the correlations involving the C IV || Distance. Both the $L/L_{\rm Edd}$ and $L/L_{\rm Edd,\ corr}$ are significantly correlated with the C IV || Distance parameter (i.e., $p \ll 1\%$).

In the case of C IV || Distance versus $L/L_{\rm Edd,\ corr}$, the correlation coefficient is considerably larger than the correlation involving $L/L_{\rm Edd}$ (0.56 versus 0.36), indicating the importance of the Fe II correction to $M_{\rm BH}$. Furthermore, the inclusion of WLQs in the sample both strengthens the correlation ($r_{\rm S}$ increases from 0.51 to 0.56 while the p value remains extremely small, $< 10^{-16}$), and allows the high-$L/L_{\rm Edd,\ corr}$ end of the correlation to be fully populated. There is also no significant deviation of the WLQs from this correlation, as opposed to their behavior in the MBE (see, Figure 5.2) as well as in the C IV $\|$ Distance versus traditional $L/L_{\rm Edd}$ (see left panel of Figure 5.4). To quantify this effect, we fit a linear model to the C IV $\|$ Distance and $L/L_{\rm Edd}$ ($L/L_{\rm Edd,\ corr}$) space, taken into account only the ordinary quasars. Then, we calculate the mean scatter of the WLQs from this line. In the case of $L/L_{\rm Edd}$, we find the deviation from the best-fit line to range from 0.97σ to 3.00σ, and the mean deviation to be $\sim 1.8\sigma$. Meanwhile, the deviation in the case of $L/L_{\rm Edd,\ corr}$ ranges from 0.01σ to 2.33σ, with a mean deviation of $\sim 1.1\sigma$. Thus, using $L/L_{\rm Edd,\ corr}$ not only results in a stronger correlation with C IV $\|$ Distance, but C IV $\|$ Distance also serves as a better predictor for $L/L_{\rm Edd,\ corr}$ than for $L/L_{\rm Edd}$.

The right panel of Figure 5.4 shows that WLQs are not a disjoint subset of quasars in the UV−optical space [206]. Our results indicate that WLQs possess relatively high accretion rates, due not only to their extremely weak C IV lines, but rather to their relatively large values of the C IV $\|$ Distance parameter. Similarly, we observe quasars with high accretion rates (and large values of C IV $\|$ Distance) that do not necessarily possess extremely weak C IV lines, some of which have Eddington ratios that are larger than those of several WLQs. Finally, while we are unaware of a large population of quasars that deviate significantly from the correlations of Figure 5.4, a future examination of, e.g., Hβ-based $L/L_{\rm Edd}$ values of quasars with very large EW(C IV) [226] is warranted to further test our results.

In this work, we show that the C IV and Hβ parameter space provides important diagnostics for quasar physics. In particular, we found that the C IV $\|$ Distance can serve as a robust predictor of quasar's accretion rate, especially after a correction based on $R_{\rm Fe\,II}$ is applied. Within the limits of our sample, we also find that WLQs are not a disjoint subset of the Type 1 quasar population, but instead lie preferentially towards the extreme end of the C IV-Hβ parameter space.

5.4. Conclusions

We compile a statistically meaningful sample of ordinary quasars and WLQs to study the dependence of quasar accretion rates, corrected for the relative strength of Fe II emission with respect to Hβ, upon source location in the C IV parameter space. Utilizing 18 WLQs, 16 of which are obtained from the literature and two of which are presented in this work, we confirm the findings of [169] that the traditional approach to estimating the Eddington ratio for rapidly-accreting quasars systematically underestimates this property by up to an order of magnitude compared to Fe II-corrected values of this parameter.

Using the Fe II-corrected values of Hβ-based $L/L_{\rm Edd}$, we investigate the correlation between this parameter and the C IV parameter space. We confirm and strengthen the SL15 results by finding that WLQs spoil the anti-correlation between EW(C IV) and Hβ-based $L/L_{\rm Edd}$ for quasars, whether the latter parameter is estimated using the traditional method, or whether a correction based on Fe II emission is employed in the $M_{\rm BH}$ estimate. In keeping with SL15, we conclude that the EW(C IV) cannot be the sole indicator of accretion rate in quasars.

We also investigate the relationships between a recently-introduced parameter, the C IV || Distance, which is a combination of EW(C IV) and Blueshift(C IV), and the traditional Hβ-based $L/L_{\rm Edd}$ and the Fe II-corrected $L/L_{\rm Edd,\ corr}$. Such relationships yield strong correlations, especially in the case of Fe II-corrected $L/L_{\rm Edd,\ corr}$, and can accommodate *all* the quasars in our sample. Our finding suggests that WLQs are not a disjoint subset of sources from the general population of quasars. We find that many WLQs have extremely high accretion rates which is indicated by their preferentially higher values of the C IV || Distance parameter. Similarly, we find several quasars in our sample that possess high Eddington ratios, and correspondingly large values of the C IV || Distance, that do not have extremely weak C IV lines; some of these sources display Eddington ratios that are larger than those of a subset of our WLQs.

In the context of the C IV parameter space, it will be interesting to investigate whether the extreme X-ray properties of WLQs are the result of extremely large C IV || Distance values rather than resulting only from extremely weak C IV lines. Such a test would require X-ray coverage of a large sample of sources with Hβ+Fe II data across the widest possible C IV parameter space such as the GNIRS-DQS sample of M23. It would also be useful to determine whether the weakness of the broad Lyα+N V emission line complex (from which the first high-redshift WLQs were identified) also correlates with C IV || Distance, which will require ultraviolet spectroscopy [227]. The results of these investigations will shed new light on the connection between the quasar accretion rate and the physics of the inner accretion disk and BELR.

This work is supported by National Science Foundation (NSF) grants AST-1815281 (B.M.M., O.S., C.D.), AST-1815645 (M.S.B., A.D.M.). G.T.R. was supported in part by NASA through a grant (HST-AR-15048.001-A) from the Space Telescope Science Institute, which is operated by the Association of Universities for Research in Astronomy, Incorporated, under NASA contract NAS5-26555. W.N.B. acknowledges support from NSF grant AST-2106990. B.L. acknowledges financial support from the National Natural Science Foundation of China grant 11991053. B.T. acknowledges support from the European Research Council (ERC) under the European Union's Horizon 2020 research and innovation program (grant agreement 950533) and from the Israel Science Foundation (grant 1849/19). This research has made use of the NASA/IPAC Extragalactic Database (NED), which is operated by the Jet Propulsion Laboratory, California Institute of Technology, under contract with the National Aeronautics and Space Administration.

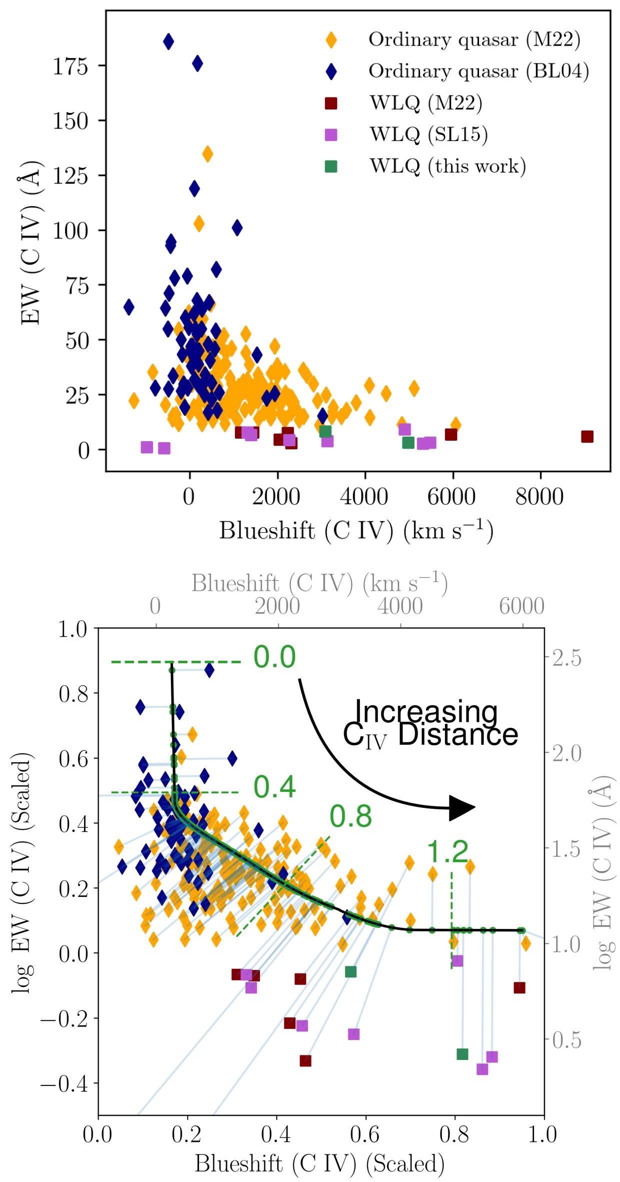

FIGURE 5.3. Top panel: distribution of EW(C IV) versus Blueshift(C IV) for our sample. Bottom panel: illustration of the C IV ∥ Distance parameter. The data are first scaled so that the two axes share the same limit, then each data point is projected onto the best-fit curve obtained from R22. The C IV ∥ Distance value of each quasar is defined as its projected position (green point) along the solid black curve. Three of the WLQs are out-of-range in the right panel, but only their projected positions onto the curve are relevant to our results.

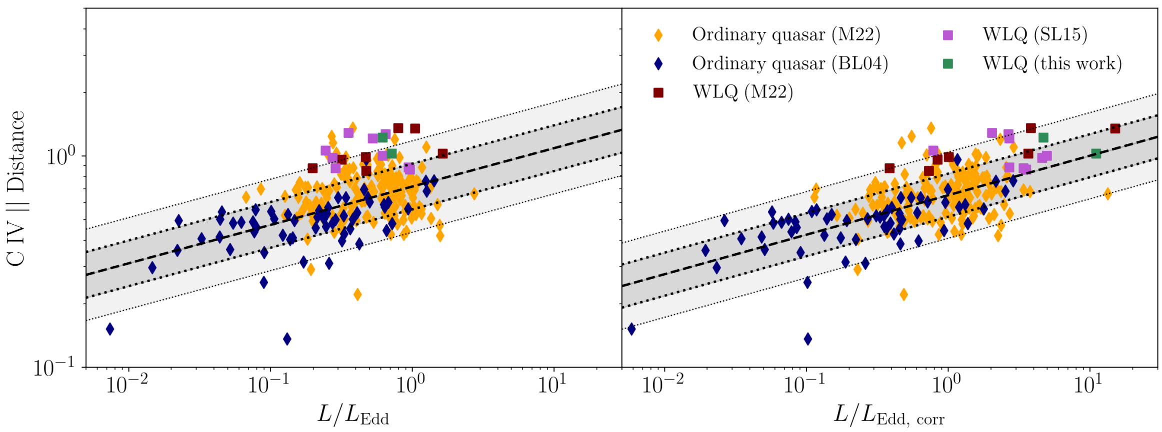

FIGURE 5.4. C IV ∥ Distance versus $L/L_{\rm Edd}$ of 248 quasars in our sample. In the left panel, the C IV ∥ Distance values are plotted against the traditional Hβ-based $L/L_{\rm Edd}$ parameter, and in the right panel, against the Fe II-corrected Hβ-based $L/L_{\rm Edd,\ corr}$ parameter. The correlation for the ordinary quasar sample, obtained by fitting a linear model, is shown as a dashed line. The shaded regions represent the 1- and 2-σ deviation from the fitted correlation. While using the traditional size-luminosity relation to estimate accretion rates already yields a strong correlation, the Fe II-corrected accretion rates show a much stronger correlation with the C IV ∥ Distance parameter for *all* quasars. Furthermore, this parameter serves as a better predictor for $L/L_{\rm Edd,\ corr}$ than for $L/L_{\rm Edd}$.

Quasar	$z_{\rm sys}$	$\log \nu L_\nu$(5100 Å) (erg s^{-1})	FWHM(Hβ) km s^{-1}	$R_{\rm Fe\,II}$	*log* $M_{\rm BH}$ ($M_\odot$)	log $M_{\rm BH,\ corr}$ ($M_\odot$)	$L/L_{\rm Edd}$	$L/L_{\rm Edd,\ corr}$	EW(C IV) Å	Blueshift(C IV) km s^{-1}	Optical Ref.[a]	C IV Ref.[b]
(1)	(2)	(3)	(4)	(5)	(6)	(7)	(8)	(9)	(10)	(11)	(12)	(13)
SDSS J010643.23−031536.4	2.248	46.51	6782	0.58	9.99	9.71	0.20	0.39	$7.6^{+0.6}_{-0.9}$	1451^{+119}_{-60}	1	2
SDSS J013136.44+130331.0	1.599	46.45	2294	0.78	9.02	8.67	1.63	3.67	$2.8^{+1.4}_{-2.0}$	2320^{+819}_{-521}	1	2
SDSS J013417.81−005036.2	2.270	46.45	5211	0.98	9.73	9.31	0.32	0.84	$7.3^{+0.7}_{-1.0}$	2233^{+651}_{-414}	1	2
SDSS J075115.43+505439.1	2.311	46.59	3077	3.05	9.35	8.19	1.05	15.04	$6.6^{+0.6}_{-1.0}$	5953^{+234}_{-117}	1	2
SDSS J083650.86+142539.0	1.749	45.93	2880	2.48	8.94	8.04	0.62	4.95	$4.2^{+0.3}_{-0.5}$	2266 ± 191	3	3
SDSS J085337.36+121800.3	2.197	46.56	4502	0.28	9.66	9.48	0.47	0.73	$7.7^{+1.1}_{-1.7}$	1166^{+363}_{-242}	1	2
SDSS J085344.17+354104.5	2.183	46.40	4168	0.72	9.51	9.18	0.47	1.00	$4.3^{+0.8}_{-1.2}$	2053^{+1580}_{-1094}	1	2
SDSS J094533.98+100950.1	1.683	46.17	4278	2.00	9.41	8.66	0.35	2.03	$2.9^{+0.3}_{-0.6}$	5485 ± 380	3	3
SDSS J094602.31+274407.0	2.488	46.75	3833	1.65	9.63	8.94	0.79	3.82	$5.9^{+0.4}_{-0.6}$	9062^{+16}_{-11}	1	2
SDSS J113747.64+391941.5	2.428	45.81	2518	3.31	8.76	7.57	0.72	10.99	8^{+6}_{-9}	3089^{+2050}_{-1236}	4	4
SDSS J114153.33+021924.4	3.550	46.55	5900	3.25	9.89	8.67	0.27	4.60	0.4^{+2}_{-4}	-577^{+2461}_{-1484}	5	6,4
SDSS J123743.07+630144.7	3.490	46.35	5200	2.86	9.68	8.61	0.29	3.39	1 ± 2	-970^{+1349}_{-845}	5	4
SDSS J141141.96+140233.9	1.754	45.64	3966	1.41	9.06	8.56	0.24	0.78	$3.8^{+0.8}_{-0.2}$	3142^{+370}_{-208}	1	2
SDSS J141730.92+073320.7	1.716	45.91	2784	1.65	8.90	8.29	0.65	2.64	$2.5^{+2.1}_{-0.7}$	5321^{+4178}_{-872}	1	2
SDSS J144741.76–020339.1	1.430	45.56	1923	1.60	8.39	7.83	0.96	3.52	$7.7^{+0.2}_{-1.3}$	1319^{+759}_{-381}	1	2
SDSS J152156.48+520238.5	2.190	47.14	5750	1.64	10.19	9.48	0.52	2.69	9.1 ± 0.6	4900 ± 300 [b]	7	7
SDSS J213742.25−003912.7	2.294	45.75	2630	2.45	8.77	7.89	0.62	4.68	3^{+1}_{-2}	4986^{+867}_{-535}	4	4
PHL 1811	0.192	45.56	1943	1.29 [c]	8.40	7.94	0.94	2.70	6.6	1400 ± 250	8	8

TABLE 5.1. [a]Source of rest-frame optical–UV data, Column (12): $z_{\rm sys}$, $\nu L_\nu(5100\,\text{Å})$, FWHM(H$\beta$), $R_{\rm Fe\,II}$; Column (13): EW(C IV), and Blueshift(C IV). (1) M23; (2) D23; (3) [209]; (4) this work; (5) [191]; (6) [90]; (7) [199];(8) [212].

[b][199] also reported Hβ-based Blueshift(C IV) = 9400 km s^{-1}. Here, we have opted to use a Mg II-based value of Blueshift(C IV).

[c][212] reported the $R_{\rm Fe\,II}$ value as being in the range 1.22−1.35. We have adopted a mean value of 1.29 for this work.

Quasar	$z_{\rm sys}$	$\log \nu L_\nu(5100\,\text{Å})$	FWHM(Hβ)	$R_{\rm Fe\ II}$	$L/L_{\rm Edd,\ corr}$	EW(C IV)	Blueshift(C IV)	Optical	C IV
		(erg s^{-1})	km s^{-1}			Å	km s^{-1}	Ref.[a]	Ref.[b]
(1)	(2)	(3)	(4)	(5)	(6)	(7)	(8)	(9)	(10)
SDSS J001018.88+280932.5	1.613	46.27	3189.0	0.06	1.29	61.0	203.0	1	2
SDSS J001453.20+091217.6	2.335	46.36	6428.0	0.72	0.60	39.0	825.0	1	2
SDSS J001813.30+361058.6	2.324	46.46	4896.0	0.55	1.02	25.8	1885.0	1	2
SDSS J001914.46+155555.9	2.267	46.34	4033.0	0.17	0.96	44.5	372.0	1	2
SDSS J002634.46+274015.5	2.247	46.38	4420.0	0.00	0.73	134.6	400.0	1	2
SDSS J003001.11-015743.5	1.590	46.10	4028.0	0.26	0.77	52.7	1279.0	1	2
SDSS J003416.61+002241.1	1.630	46.24	5527.0	0.44	0.56	28.5	483.0	1	2
SDSS J003853.15+333044.3	2.361	46.39	4297.0	0.50	1.17	13.8	-398.0	1	2
SDSS J004710.48+163106.5	2.184	46.51	3573.0	0.42	1.83	22.1	2080.0	1	2
SDSS J004719.71+014813.9	1.591	46.13	5605.0	0.24	0.41	48.9	341.0	1	2
SDSS J005233.67+014040.8	2.309	46.65	6518.0	0.63	0.77	31.7	1313.0	1	2
SDSS J005307.71+191022.7	1.598	46.23	8981.0	0.21	0.18	38.3	1989.0	1	2
SDSS J010113.72+032427.0	1.579	46.39	6484.0	0.00	0.34	102.8	208.0	1	2
SDSS J010447.39+101031.6	2.373	46.29	6754.0	0.61	0.46	22.1	1548.0	1	2
SDSS J010500.72+194230.4	2.323	46.42	3547.0	0.49	1.77	33.8	2663.0	1	2
SDSS J010615.93+101043.0	2.353	46.08	2936.0	0.54	1.79	21.1	2026.0	1	2
SDSS J011538.72+242446.0	2.401	46.53	3925.0	0.67	1.90	29.9	2820.0	1	2
SDSS J013113.25+085245.5	3.537	46.62	3874.0	0.42	1.78	23.3	508.0	1	2
SDSS J013647.96-062753.6	3.288	46.71	6617.0	0.97	1.05	15.0	3458.0	1	2
SDSS J014128.26+070606.1	2.262	46.25	3312.0	0.31	1.43	42.7	518.0	1	2
SDSS J014932.06+152754.0	2.384	46.33	2896.0	0.04	1.65	56.9	7.0	1	2
SDSS J020329.86-091020.3	1.582	46.13	7025.0	0.81	0.41	29.1	968.0	1	2
SDSS J021259.21+132618.8	1.617	46.11	4722.0	0.95	1.00	44.1	417.0	1	2
SDSS J035150.97-061326.4	2.223	46.51	2616.0	0.37	3.27	13.8	314.0	1	2

SDSS J072517.52+434553.4	1.595	46.37	1705.0	1.76	20.04	19.1	429.0	1	2
SDSS J072928.48+252451.8	2.311	46.51	7074.0	0.45	0.48	17.0	622.0	1	2
SDSS J073900.90+485159.0	1.627	46.27	5566.0	0.27	0.50	34.8	1851.0	1	2
SDSS J073913.65+461858.5	1.574	46.33	4060.0	0.74	1.48	15.9	-314.0	1	2
SDSS J074941.16+262715.9	1.594	46.37	3592.0	0.49	1.61	27.3	1023.0	1	2
SDSS J075136.36+432732.4	2.249	46.42	3736.0	0.58	1.71	33.5	1996.0	1	2
SDSS J075405.08+280339.6	2.271	46.34	4911.0	0.02	0.57	54.4	-256.0	1	2
SDSS J075547.83+220450.1	2.314	46.51	3207.0	0.24	1.97	28.0	-65.0	1	2
SDSS J080117.79+521034.5	3.259	46.92	5361.0	0.64	1.59	19.3	3267.0	1	2
SDSS J080117.91+333411.9	1.602	46.24	6795.0	0.59	0.42	19.4	729.0	1	2
SDSS J080413.66+251633.9	2.301	46.52	3188.0	0.37	2.24	11.8	273.0	1	2
SDSS J081019.48+095040.9	2.236	46.42	3297.0	0.83	2.69	25.8	2175.0	1	2
SDSS J081056.96+120914.8	2.251	46.57	3515.0	0.33	1.89	35.3	-851.0	1	2
SDSS J081127.44+461812.9	2.237	46.54	3804.0	0.54	1.84	20.4	-555.0	1	2
SDSS J081410.76+443706.9	2.274	46.32	2910.0	0.57	2.49	36.0	711.0	1	2
SDSS J081558.35+154055.2	2.235	46.53	4622.0	0.00	0.80	28.9	641.0	1	2
SDSS J081940.58+082357.9	3.204	46.76	7601.0	0.37	0.53	38.3	769.0	1	2
SDSS J082507.67+360411.1	1.582	46.60	2939.0	0.79	4.06	47.3	698.0	1	2
SDSS J082603.32+342800.6	2.306	46.40	5763.0	0.66	0.75	26.0	936.0	1	2
SDSS J082644.66+163549.0	2.188	46.72	2687.0	0.16	3.37	62.3	-24.0	1	2
SDSS J082736.89+061812.1	2.191	46.76	3400.0	0.33	2.54	22.8	-221.0	1	2
SDSS J083255.63+182300.7	2.279	46.64	4269.0	1.61	3.92	24.1	2265.0	1	2
SDSS J083417.12+354833.1	2.162	46.63	3654.0	1.11	3.52	22.0	835.0	1	2
SDSS J084017.87+103428.8	3.333	46.51	3038.0	0.26	2.23	45.7	371.0	1	2
SDSS J084029.97+465113.7	1.574	46.53	4447.0	0.86	1.72	19.1	596.0	1	2
SDSS J084526.75+550546.8	1.616	46.34	4971.0	0.26	0.68	53.3	199.0	1	2
SDSS J084846.11+611234.6	2.259	46.82	4180.0	0.52	2.11	29.2	231.0	1	2
SDSS J085443.10+075223.2	1.612	46.32	3138.0	0.47	1.96	29.1	1466.0	1	2

SDSS J085856.00+015219.4	2.169	46.50	3861.0	0.57	1.74	23.7	2320.0	1	2
SDSS J085946.79+603702.1	2.279	46.42	3148.0	0.81	2.89	27.6	1852.0	1	2
SDSS J090247.57+304120.7	1.562	46.52	5370.0	0.49	0.87	47.7	229.0	1	2
SDSS J090646.98+174046.8	1.581	46.39	3174.0	0.83	2.79	16.7	1677.0	1	2
SDSS J090709.89+250620.8	3.316	46.81	3498.0	0.06	2.06	19.4	851.0	1	2
SDSS J090710.36+430000.2	2.193	46.62	3136.0	1.20	5.08	24.4	1137.0	1	2
SDSS J091941.26+253537.7	2.266	46.28	6110.0	0.12	0.37	36.7	251.0	1	2
SDSS J092216.04+160526.4	2.371	46.37	3026.0	0.24	1.87	43.7	142.0	1	2
SDSS J092325.25+453222.2	3.473	46.67	3754.0	0.25	1.76	35.4	2167.0	1	2
SDSS J092456.66+305354.7	3.448	46.70	3628.0	0.29	2.01	18.0	1251.0	1	2
SDSS J092523.24+214119.8	2.361	46.22	3133.0	0.34	1.58	44.1	287.0	1	2
SDSS J092555.05+490338.2	2.340	46.34	6598.0	0.42	0.44	32.2	548.0	1	2
SDSS J092942.97+064604.1	1.632	46.23	5009.0	0.49	0.70	25.6	4476.0	1	2
SDSS J093533.88+235720.5	2.304	46.34	6736.0	0.13	0.33	44.1	820.0	1	2
SDSS J094140.16+325703.2	3.449	46.87	4034.0	0.69	2.76	15.2	3237.0	1	2
SDSS J094214.40+034100.3	1.581	46.14	5190.0	0.64	0.67	35.0	-250.0	1	2
SDSS J094347.02+690818.4	1.599	46.24	6247.0	0.60	0.50	44.1	1277.0	1	2
SDSS J094637.83-012411.5	2.215	46.52	3366.0	0.20	1.75	19.4	92.0	1	2
SDSS J094646.94+392719.0	2.230	46.37	5214.0	1.10	1.26	29.2	4085.0	1	2
SDSS J094648.59+171827.7	2.298	46.43	4627.0	0.17	0.81	44.5	346.0	1	2
SDSS J095047.45+194446.1	1.573	46.16	4163.0	0.02	0.64	35.1	201.0	1	2
SDSS J095058.76+263424.6	2.404	46.50	3550.0	0.73	2.35	22.3	2911.0	1	2
SDSS J095330.36+353223.1	2.389	46.39	4235.0	0.52	1.22	13.5	2488.0	1	2
SDSS J095544.25+182546.9	3.485	46.74	3151.0	0.22	2.64	39.1	629.0	1	2
SDSS J095555.68+351652.6	1.616	46.26	6595.0	0.74	0.52	29.2	-149.0	1	2
SDSS J095707.82+184739.9	2.370	46.53	2732.0	0.79	4.34	14.7	4102.0	1	2
SDSS J095823.07+371218.3	2.282	46.47	3566.0	0.92	2.62	22.5	1988.0	1	2
SDSS J095852.19+120245.0	3.307	46.76	4417.0	0.25	1.41	16.8	707.0	1	2

SDSS J100212.63+520800.2	1.619	46.21	3123.0	0.45	1.71	17.7	889.0	1	2
SDSS J100850.06-023831.6	2.272	46.31	2997.0	0.62	2.41	34.1	1557.0	1	2
SDSS J101106.74+114759.4	2.249	46.35	2275.0	0.41	3.71	30.4	483.0	1	2
SDSS J101425.11+032003.7	2.165	46.56	5309.0	0.81	1.20	13.6	2152.0	1	2
SDSS J101429.57+481938.4	1.569	46.36	2841.0	1.00	3.86	19.0	1799.0	1	2
SDSS J101724.26+333403.3	1.579	46.24	6689.0	0.60	0.44	20.0	763.0	1	2
SDSS J102537.69+211509.1	2.255	46.14	6420.0	0.18	0.30	46.9	416.0	1	2
SDSS J102731.49+541809.7	1.590	46.31	6892.0	0.76	0.51	21.2	382.0	1	2
SDSS J102907.09+651024.6	2.170	46.66	4545.0	0.48	1.42	23.8	1388.0	1	2
SDSS J103209.78+385630.5	1.581	46.28	4281.0	1.16	1.76	15.6	-385.0	1	2
SDSS J103236.98+230554.1	2.378	46.36	3267.0	0.30	1.66	18.3	144.0	1	2
SDSS J104018.51+572448.1	3.411	46.75	3984.0	0.44	2.00	13.5	1094.0	1	2
SDSS J104330.09+441051.5	2.216	46.51	7222.0	0.62	0.53	24.6	1353.0	1	2
SDSS J104336.73+494707.6	2.195	46.52	7025.0	0.43	0.48	29.7	1669.0	1	2
SDSS J104716.50+360654.0	2.290	46.34	2975.0	0.23	1.85	60.6	101.0	1	2
SDSS J104743.57+661830.5	2.166	46.53	7059.0	0.40	0.47	29.3	387.0	1	2
SDSS J104911.34+495113.6	1.606	46.73	2709.0	0.22	3.54	51.2	156.0	1	2
SDSS J105045.72+544719.2	2.173	46.66	4781.0	0.20	1.02	32.8	914.0	1	2
SDSS J105902.04+580848.6	2.248	46.37	2804.0	0.21	2.12	30.2	945.0	1	2
SDSS J105926.43+062227.4	2.198	46.72	6361.0	0.97	1.16	48.3	297.0	1	2
SDSS J110516.68+200013.7	2.357	46.38	5039.0	0.16	0.64	36.8	207.0	1	2
SDSS J110735.58+642008.6	2.325	46.40	2937.0	0.64	2.84	24.3	1887.0	1	2
SDSS J110810.87+014140.7	1.605	46.33	4784.0	0.75	1.07	22.2	-1275.0	1	2
SDSS J111119.10+133603.8	3.478	46.94	6936.0	0.33	0.76	19.5	922.0	1	2
SDSS J111850.02+351311.7	2.175	46.51	3664.0	0.77	2.31	22.3	2266.0	1	2
SDSS J112726.81+601020.2	2.162	46.44	4168.0	1.17	2.26	16.2	1869.0	1	2
SDSS J113621.05+005021.2	3.428	46.84	5139.0	0.19	1.10	46.8	523.0	1	2
SDSS J114212.25+233250.5	1.594	46.35	3518.0	0.72	1.98	19.3	1396.0	1	2

SDSS J114350.30+362911.3	2.352	46.44	4090.0	0.27	1.14	15.3	245.0	1	2
SDSS J114711.78+084029.6	2.332	46.46	3396.0	1.17	3.49	11.4	4831.0	1	2
SDSS J114902.70+144328.0	2.204	46.51	4461.0	0.25	1.02	28.5	1546.0	1	2
SDSS J114907.15+004104.3	2.301	46.50	5920.0	0.62	0.78	23.9	1029.0	1	2
SDSS J114927.90+432727.9	3.331	46.76	6459.0	0.19	0.63	23.8	1543.0	1	2
SDSS J121314.03+080703.6	2.391	46.44	3761.0	0.81	2.08	15.0	2600.0	1	2
SDSS J121519.42+424851.0	2.311	46.40	3345.0	0.27	1.63	28.9	353.0	1	2
SDSS J121810.98+241410.9	2.380	46.73	3981.0	0.41	1.91	30.8	1221.0	1	2
SDSS J122046.05+455442.1	2.219	46.79	4295.0	0.60	2.06	22.0	2112.0	1	2
SDSS J122709.48+310749.3	2.219	46.57	5057.0	0.59	1.13	11.2	6062.0	1	2
SDSS J122938.61+462430.5	2.145	46.46	4040.0	0.39	1.32	43.2	-86.0	1	2
SDSS J123514.64+462904.0	2.208	46.49	5243.0	0.15	0.67	46.2	953.0	1	2
SDSS J125150.45+114340.7	2.209	46.49	4635.0	0.10	0.82	47.0	1938.0	1	2
SDSS J125159.90+500203.6	2.378	46.51	3365.0	0.89	3.02	28.7	1113.0	1	2
SDSS J132845.00+510225.8	3.403	46.93	3821.0	0.25	2.31	30.0	209.0	1	2
SDSS J134341.99+255652.9	1.601	46.60	12197.0	0.39	0.17	16.7	-4.0	1	2
SDSS J135908.35+305830.8	2.316	46.50	5795.0	0.65	0.83	27.9	5112.0	1	2
SDSS J140704.43+273556.6	2.220	46.35	6045.0	0.44	0.54	20.4	1039.0	1	2
SDSS J141028.14+135950.2	2.216	46.67	6555.0	0.82	0.91	38.7	1353.0	1	2
SDSS J141925.48+074953.5	2.391	46.55	5214.0	0.64	1.08	14.3	1841.0	1	2
SDSS J141951.84+470901.3	2.311	46.76	4938.0	0.70	1.62	24.9	3100.0	1	2
SDSS J142435.97+421030.4	2.212	46.38	6177.0	0.63	0.62	24.5	295.0	1	2
SDSS J142502.62+274912.2	2.346	46.37	4436.0	0.04	0.74	41.7	-14.0	1	2
SDSS J142543.32+540619.3	3.261	46.91	4126.0	0.45	2.27	11.8	803.0	1	2
SDSS J142755.85-002951.1	3.365	46.70	3142.0	0.16	2.42	34.6	576.0	1	2
SDSS J142903.03-014519.3	3.420	46.74	5337.0	0.60	1.25	21.4	1908.0	1	2
SDSS J144624.29+173128.8	2.209	46.52	2938.0	0.22	2.34	14.9	1046.0	1	2
SDSS J144706.81+212839.2	3.224	46.76	6113.0	0.25	0.74	14.1	1566.0	1	2

SDSS J144948.62+123047.4	1.592	46.34	6505.0	0.09	0.35	66.2	471.0	1	2
SDSS J145541.11-023751.0	1.612	46.17	4798.0	0.18	0.56	59.6	295.0	1	2
SDSS J150743.71+220928.8	3.230	46.65	3764.0	0.61	2.27	43.9	410.0	1	2
SDSS J151507.82+612411.9	2.182	46.59	3663.0	0.42	1.92	33.6	585.0	1	2
SDSS J151727.68+133358.6	2.236	46.45	4680.0	0.53	1.08	26.8	1421.0	1	2
SDSS J151733.09+435648.4	2.204	46.38	4715.0	0.75	1.17	16.6	2301.0	1	2
SDSS J152929.55+230208.7	1.581	46.32	3536.0	0.59	1.71	25.1	583.0	1	2
SDSS J155355.10+375844.1	2.364	46.31	3307.0	0.34	1.57	25.7	1590.0	1	2
SDSS J160029.86+331806.9	1.594	46.25	7471.0	0.15	0.25	52.0	776.0	1	2
SDSS J160425.30+193929.1	3.296	46.71	4439.0	0.60	1.75	16.3	2073.0	1	2
SDSS J160513.17+325829.9	2.280	46.37	3460.0	0.85	2.33	21.3	3789.0	1	2
SDSS J160637.57+173516.2	2.331	46.26	3337.0	0.91	2.31	16.5	1878.0	1	2
SDSS J161435.70+372715.6	1.599	46.57	4662.0	0.34	1.08	22.5	250.0	1	2
SDSS J162659.24+301535.0	1.580	46.22	5308.0	0.78	0.79	29.6	47.0	1	2
SDSS J163433.42+265158.2	1.569	46.25	2695.0	0.71	2.98	17.3	428.0	1	2
SDSS J164807.55+254407.1	2.195	46.76	2949.0	0.14	2.89	40.4	82.0	1	2
SDSS J165321.03+271706.7	1.610	46.54	2843.0	0.73	3.84	17.1	2469.0	1	2
SDSS J173352.23+540030.4	3.429	46.71	4200.0	0.33	1.56	13.5	521.0	1	2
SDSS J205900.36-064309.5	2.283	46.50	4102.0	2.17	5.64	11.7	-261.0	1	2
SDSS J210558.29-011127.5	1.637	46.49	3557.0	0.78	2.40	36.2	2584.0	1	2
SDSS J210831.56-063022.5	2.350	46.42	4949.0	1.14	1.53	11.1	2949.0	1	2
SDSS J211251.06+000808.3	1.626	46.23	3493.0	0.61	1.59	17.2	3256.0	1	2
SDSS J213655.35-080910.1	1.596	46.33	4769.0	0.94	1.26	21.5	2379.0	1	2
SDSS J214901.21-073141.6	2.203	46.44	3181.0	0.75	2.77	21.1	486.0	1	2
SDSS J220139.99+114140.8	2.372	46.48	2846.0	0.60	3.21	27.6	1953.0	1	2
SDSS J222310.76+180308.1	1.604	46.20	3291.0	0.32	1.37	19.4	892.0	1	2
SDSS J222621.45+251545.0	2.391	47.09	8350.0	0.34	0.64	26.3	1225.0	1	2
SDSS J225627.12+092313.3	2.293	46.44	4175.0	1.00	1.96	26.8	1061.0	1	2

SDSS J230722.21+253803.8	1.597	46.36	2720.0	0.64	3.15	49.3	704.0	1	2
SDSS J231450.12+182402.8	2.284	46.37	3243.0	0.39	1.83	31.6	449.0	1	2
SDSS J233304.61-092710.9	2.120	46.65	3178.0	0.09	2.11	37.4	625.0	1	2
SDSS J233344.66+290251.5	3.233	46.71	4068.0	0.80	2.44	17.8	3567.0	1	2
SDSS J234817.55+193345.8	2.202	46.58	5058.0	1.41	2.20	13.9	2182.0	1	2
SDSS J235212.85-012029.6	2.387	46.50	5193.0	0.60	0.99	21.2	1906.0	1	2
PG 0003+199	0.026	44.07	1640.0	0.62	0.62	60.1	-102.0	3	4
PG 0026+129	0.145	45.13	1860.0	0.51	1.43	19.3	-120.0	3	4
PG 0050+124	0.059	44.61	1240.0	1.00	2.66	29.9	177.0	3	4
PG 0052+251	0.154	45.17	5200.0	0.23	0.15	119.0	107.0	3	4
PG 0157+001	0.163	44.99	2460.0	0.71	0.82	43.0	1524.0	3	4
PG 0804+761	0.100	45.28	3070.0	0.67	0.71	45.0	210.0	3	4
PG 0838+770	0.132	44.73	2790.0	0.89	0.55	50.0	-197.0	3	4
PG 0844+349	0.064	44.49	2420.0	0.89	0.56	28.0	-50.0	3	4
PG 0921+525	0.035	43.60	2120.0	0.14	0.15	186.0	-488.0	3	4
PG 0923+129	0.029	43.76	1990.0	0.53	0.28	93.0	-437.0	3	4
PG 0923+201	0.193	45.22	7610.0	0.72	0.11	28.0	-794.0	3	4
PG 0947+396	0.206	44.88	4830.0	0.23	0.13	55.0	266.0	3	4
PG 0953+414	0.234	45.56	3130.0	0.25	0.68	54.9	127.0	3	4
PG 1011-040	0.058	44.25	1440.0	0.73	1.07	25.0	337.0	3	4
PG 1012+008	0.186	45.00	2640.0	0.66	0.70	23.0	494.0	3	4
PG 1022+519	0.045	43.54	1620.0	1.00	0.49	38.0	39.0	3	4
PG 1048+342	0.167	44.80	3600.0	0.32	0.23	46.0	572.0	3	4
PG 1049-006	0.360	45.67	5360.0	0.56	0.33	67.0	436.0	3	4
PG 1114+445	0.144	44.73	4570.0	0.20	0.12	55.0	-494.0	3	4
PG 1115+407	0.154	44.61	1720.0	0.54	0.95	25.9	666.0	3	4
PG 1116+215	0.176	45.54	2920.0	0.47	0.90	40.5	462.0	3	4
PG 1119+120	0.050	44.02	1820.0	0.90	0.60	29.0	209.0	3	4

PG 1121+422	0.225	44.90	2220.0	0.37	0.69	41.7	92.0	3	4
PG 1126-041	0.060	44.37	2150.0	1.00	0.68	30.0	-143.0	3	4
PG 1149-110	0.049	44.02	3060.0	0.36	0.14	82.0	605.0	3	4
PG 1151+117	0.176	44.89	4300.0	0.24	0.16	26.6	-203.0	3	4
PG 1202+281	0.165	44.66	5050.0	0.29	0.10	290.0	689.0	3	4
PG 1211+143	0.081	45.10	1860.0	0.52	1.40	55.7	-20.0	3	4
PG 1216+069	0.332	45.65	5190.0	0.20	0.26	64.5	-562.0	3	4
PG 1229+204	0.064	44.41	3360.0	0.59	0.21	48.0	413.0	3	4
PG 1244+026	0.048	44.05	830.0	1.20	3.79	17.0	422.0	3	4
PG 1259+593	0.477	45.99	3390.0	1.00	1.74	15.3	3024.0	3	4
PG 1307+085	0.154	45.13	2360.0	0.19	0.69	71.2	-475.0	3	4
PG 1309+355	0.182	44.99	2940.0	0.28	0.41	33.5	-388.0	3	4
PG 1310-108	0.034	43.77	3630.0	0.38	0.08	78.0	-349.0	3	4
PG 1322+659	0.168	44.91	2790.0	0.59	0.53	52.6	164.0	3	4
PG 1341+258	0.086	44.34	3040.0	0.38	0.20	62.0	93.0	3	4
PG 1351+236	0.055	43.67	6540.0	1.00	0.03	101.0	1076.0	3	4
PG 1351+640	0.088	44.82	5660.0	0.24	0.09	43.3	-172.0	3	4
PG 1352+183	0.151	44.92	3600.0	0.46	0.29	45.1	164.0	3	4
PG 1402+261	0.164	45.11	1910.0	1.00	1.97	30.3	495.0	3	4
PG 1404+226	0.098	44.17	880.0	1.00	3.25	23.3	1754.0	3	4
PG 1425+267	0.364	45.35	9410.0	0.11	0.05	64.8	-1388.0	3	4
PG 1426+015	0.086	45.02	6820.0	0.39	0.09	32.0	103.0	3	4
PG 1435-067	0.129	45.12	3180.0	0.45	0.46	39.0	191.0	3	4
PG 1440+356	0.078	44.54	1450.0	1.00	1.79	30.1	316.0	3	4
PG 1444+407	0.268	45.32	2480.0	1.00	1.48	17.9	621.0	3	4
PG 1501+106	0.036	44.51	5470.0	0.35	0.07	64.0	273.0	3	4
PG 1519+226	0.136	44.70	2220.0	1.00	0.92	68.0	160.0	3	4
PG 1534+580	0.030	43.68	5340.0	0.27	0.03	79.0	-60.0	3	4

PG 1535+547	0.039	43.84	1480.0	0.47	0.53	27.6	-487.0	3	4
PG 1543+489	0.401	45.53	1560.0	0.86	4.29	25.6	1940.0	3	4
PG 1552+085	0.119	44.64	1430.0	1.00	2.06	47.0	24.0	3	4
PG 1612+261	0.131	44.75	2520.0	0.18	0.39	94.6	-434.0	3	4
PG 1613+658	0.129	44.73	8450.0	0.38	0.04	54.0	596.0	3	4
PG 1617+175	0.114	45.08	5330.0	0.60	0.18	34.0	342.0	3	4
PG 1626+554	0.132	44.67	4490.0	0.32	0.13	45.6	88.0	3	4
PG 2130+099	0.063	44.65	2330.0	0.64	0.59	47.0	62.0	3	4
PG 2214+139	0.066	44.49	4550.0	0.32	0.10	45.0	5.0	3	4
PG 2304+042	0.043	43.89	10100.0	0.09	0.01	176.0	178.0	3	4

TABLE 5.2. [a]Source of rest-frame optical data, including $z_{\rm sys}$, $\nu L_\nu(5100\,\text{Å})$, FWHM(H$\beta$), and $R_{\rm Fe\ II}$. (1) M23; (3) [82].

[b]Source of rest-frame UV data, including EW(C IV) and Blueshift(C IV). (2) D23; (4) [167]. Column (1) provides the source name; Column (2) gives the systemic redshift determined from the peak of, in order of preference, the [O III]λ5007 , Mg II λ2798, and Hβ λ4861 emission lines; Column (3) gives $\log \nu L_\nu$ (5100 Å); Column (4) gives FWHM(Hβ); Column (5) gives $R_{\rm Fe\ II} \equiv$ F(Fe II $\lambda\lambda 4434-4684$)/F(Hβ) $\approx$ EW(Fe II)/EW(Hβ); Column (6) gives Fe II-corrected Hβ-based $L/L_{\rm Edd}$ (from Equation 24); Column (7) gives EW(C IV λ1549); Column (8) gives C IV velocity offsets from the systemic redshift; Columns (9) and (10) provide the reference for the rest-frame optical and UV spectral measurements, respectively.

Correction	Sample	N	$r_{\rm S}$	p
EW(C IV)-$L/L_{\rm Edd}$	Ordinary	230	−0.38	3.27×10^{-9}
EW(C IV)-$L/L_{\rm Edd}$	All	247	−0.36	4.66×10^{-8}
EW(C IV)-$L/L_{\rm Edd,\ corr}$	Ordinary	230	−0.48	6.91×10^{-15}
EW(C IV)-$L/L_{\rm Edd,\ corr}$	All	247	−0.53	1.23×10^{-19}
C IV Distance-$L/L_{\rm Edd}$	Ordinary	230	0.39	7.23×10^{-10}
C IV Distance-$L/L_{\rm Edd}$	All	247	0.38	8.23×10^{-10}
C IV Distance-$L/L_{\rm Edd,\ corr}$	Ordinary	230	0.51	8.32×10^{-17}
C IV Distance-$L/L_{\rm Edd,\ corr}$	All	247	0.56	2.16×10^{-21}

TABLE 5.3. The last three columns represent the number of sources in each correlation, the Spearman-rank correlation coefficient, and the chance probability, respectively.

5.5. Appendix: NIR Spectroscopy of SDSS J113747.64+391941.5 and SDSS J213742.25−003912.7

SDSS J113747.64+391941.5 and SDSS J213742.25−003912.7 (hereafter, SDSS J1137+3919 and SDSS J2137−0039, respectively) are two WLQs with redshifts suitable for observing the Hβ line in the H-Band. Observations of these quasars were carried out by the *Gemini-North* Observatory using GNIRS throughout four observing runs between 2014 March 14 and 2014 August 4, under program GN-2014A-Q-47. The observation log appears in Table 5.4. For both targets, we used the Short Blue Camera, with spatial resolution $0.''15$ pix^{-1}, and a $1.0''$ slit to achieve a spectral resolution of $R \sim 600$. An H-filter was applied, producing a spectral range of 1.5 - 1.8 μm, corresponding to rest-frame $\sim 4500 - 5300$ Å. Exposure times for each subintegration were 238 s and 220 s, and the total integration times were 7140 s and 7040 s for SDSS J1137+3919 and SDSS J2137−0039, respectively. These observations were performed using the standard "ABBA" nodding pattern of the targets along the slit in order to obtain primary background subtraction.

The spectra were processed using the standard procedure of the IRAF *Gemini* package based on the PyRAF Python-based interface. Exposures from the same nodding position were added to boost the signal-to-noise ratio, then the sum of exposures from two different nodding positions were subtracted to remove background noise. Wavelength calibration was done against an Argon lamp in order to assign wavelength values to the observed pixels.

Spectra of telluric standard stars with $T_{\rm eff} \sim 9700$ K were taken immediately before or after the science exposures to remove telluric absorption features in the quasars' observed spectra. These spectra were processed in a similar fashion, followed by a removal of the stars' intrinsic hydrogen absorption lines by fitting a Lorentzian profile to each hydrogen absorption line, and interpolating across this feature to connect the continuum on each side of the line. The quasars' spectra were divided by the corrected stellar spectra. The corrected quasar spectra were then multiplied by an artificial blackbody curve with a temperature corresponding to the telluric standard star, which yielded a cleaned, observed-frame quasar spectrum.

Flux calibrations were obtained by taking the Wide-field Infrared Survey Explorer (WISE; [228]) $W1$-band (at 3.4 μm) apparent magnitudes, reported by SDSS Data Release 16 [109], and the $W1$ isophotal flux density $F_\lambda(\rm iso)$ given in Table 1 of [229]. Flux densities at 3.4 μm were derived according to:

$$F_\lambda(3.4\ \mu m) = F_\lambda(\rm iso) \cdot 10^{-\rm mag/2.5}. \quad (25)$$

The flux densities at 3.4 μm were extrapolated to flux densities at 1.63 μm, roughly corresponding to $\lambda_{\rm rest} = 5100$ Å, assuming an optical continuum of the form $F_\nu \propto \nu^{-0.5}$ [24].

We modeled the spectra following the methods of [58] and [191]. Our model consists of a linear continuum through the average flux densities of two narrow ($\sim$20 Å) rest-frame bands centered on 4750 Å and 4975 Å, a broadened Fe II emission template [82], and two Gaussian profiles for the Hβ λ4861 emission-line. No [O III]emission-lines are detectable in either spectrum, and we placed upper limits on their EWs by fitting a Gaussian feature where the [O III]emission-lines should be such that they are indistinguishable from the noise. The final, calibrated near infrared spectra of the two WLQs appear in Figure 5.5.

In both sources we detected weak and relatively narrow Hβ lines as well as strong Fe II features compared to quasars at similar luminosities and redshifts [60, 35]. We also determined the systemic redshifts ($z_{\rm sys}$) values from the observed-frame wavelength of the peak (λ_{peak}) of the Hβ emission-line, a similar treatment as in [115] for sources that lack [O III]emission. The z_{sys} values are larger than the redshifts reported by [109] by $\Delta z = 0.008$ in SDSS J1137+3919 and by $\Delta z = 0.013$ in SDSS J2137−0039, corresponding to velocity offsets (blueshifts) of 700 km s^{-1} and 1184 km s^{-1}, respectively, which is consistent with typical velocity offsets between SDSS Pipeline redshifts and z_{sys} values observed in luminous, high-redshift quasars (M23, [54]). The rest-frame spectra in Figure 5.5 have henceforth been corrected by z_{sys}. Rest-frame EWs of Hβ λ4861, Fe II $\lambda\lambda 4434-4684$, and the upper limit on the EWs of [O III] λ5007 were calculated for SDSS J1137+3919 to be 16 Å, 53 Å, and $\leq$ 4 Å, and for SDSS J2137−0039 to be 20 Å, 49 Å, and $\leq$ 5 Å, respectively. The flux densities at a rest-frame wavelength of 5100 Å are 7.77×10^{-18} ergs cm^{-2} s^{-1} Å^{-1} and 8.18×10^{-18} ergs cm^{-2} s^{-1} Å^{-1}, respectively.

Quasar	z [a]	z_{sys} [b]	$\log \nu L_\nu$ (5100 Å)	Observation Dates	Exp. Time (s)
SDSS J113747.64+391941.5	2.420	2.428	45.8	2014 Mar 14, 20	7140
SDSS J213742.25−003912.7	2.281	2.294	45.8	2014 Jun 29, Aug 04	7040

TABLE 5.4. [a]Obtained from visually-inspected redshifts (zvis) reported in SDSS Data Release 16 [109].

[b]Systemic redshifts (see § 5.5 for details).

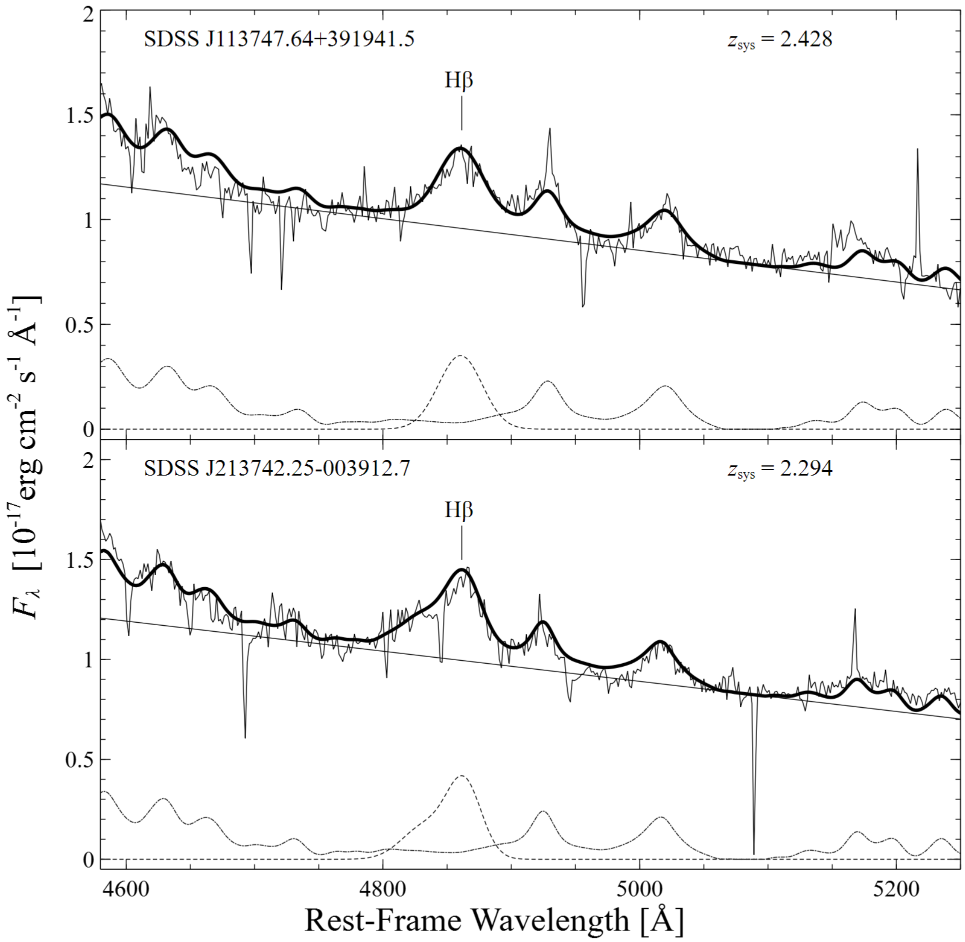

FIGURE 5.5. The NIR spectra of SDSS J1137+3919 (top) and SDSS J2137−0039 (bottom). In each panel, the continuous line is the observed spectrum of each quasar. The continuous straight line below the spectrum is the linear continuum fit. The dashed line is the Hβ λ4861 profile modelled with two Gaussians. The dotted-dashed line is the Fe II template from [82], which was broadened by 1500 km s^{-1} for SDSS J1137+3919, and 1400 km s^{-1} for J2137−0039. The bold solid line is the entire fitted spectrum.

CHAPTER 6

CONCLUSION

We present near-infrared spectroscopic measurements of 260 high redshift quasars between $1.5 \lesssim z \lesssim 3.5$. These measurements include important diagnostic emission lines such as Mg II, Hβ, and [O III], along with supplementary emission lines such as Hδ and Hγ, when present, for use in future investigations. This spectral inventory will not only serve as a reference point for investigations into high redshift quasars, but will also enable investigation into a variety of avenues including co-evolution of quasars and their host galaxies, and redshift evolution of spectral properties.

Using this spectral inventory, we take a sub-sample of 154 "ordinary" quasars with highly reliable [O III] measurements in order to explore relationships between accurate systemic redshift measurements and prominent observed-frame UV-optical lines in high redshift quasars, namely C IV, and whether we might be able to accurate correct redshifts using the properties of only a single emission line. Our results suggest that not only is this a feasible practice, but that it, in fact, yields the most accurate results, on average, barring direct [O III] measurement.

Also with this spectral inventory, we use a sub-sample of 177 sources to explore two different regimes in quasar understanding. The first was a similar exploration to the redshift analysis, only applied to correcting black hole masses. By using Hβ and Mg II measurements from GNIRS-DQS, we are able to explore how different black hole mass estimators work on our survey sample, and further explore our own corrections in this regard. We find that, using our black hole mass corrections, we can gain the most accurate black hole mass estimations using both the C IV and Mg II emission lines. While not as robust as reverberation mapped data, this single epoch analysis will prove invaluable for quick, reliable black hole mass estimations for bulk quasar observations.

The other exploration was into weak line quasars. Historically, there has been a definite distinction in the community as to what constitutes a weak line quasar based on emission line strength via measurements such as equivalent width. As a result, astronomers have been inclined to consider weak line quasars a sub-type of quasar. However, our investigation shows that, while weak line quasars might stick out a bit with respect to accretion rate, they still roughly follow the general distribution of "ordinary" quasars, and appear to not be notably distinct objects on their own.

As we push to higher and higher redshifts and obtain spectra of millons of quasars via a variety of sky surveys, establishing relationships and prescriptions using proven baseline methodologies will be crucial in interpreting large data sets in an efficient, accurate, and precise manner. By applying the tools and knowledge we have garnered, we will be able to ensure that future explorations into quasars will take advantage of the full parameter space available across a large of wavelength ranges, and across a large span of redshifts. Future avenues of investigation include high resolution radio spectroscopy of specific diagnostic line such as [O III] in order to gain a more complete understanding of outflows in the narrow line region, follow-up mini surveys of currently existing near-infrared inventory using next generation instruments such as SCORPIO to more accurately refine Fe II emission and Mg II measurements in order to investigate quasar metallicity, and how it evolves over cosmic time, and continuing to push to higher redshifts using such instruments as the Keck Observatory and the soon-to-be operational James Webb Space Telescope and explore the origins of these mysterious objects.

REFERENCES

[1] Bradley M. Peterson, *An Introduction to Active Galactic Nuclei*, 1997.

[2] Hagai Netzer, *The Physics and Evolution of Active Galactic Nuclei*, 2013.

[3] K. T. Korista, D. Alloin, P. Barr, J. Clavel, R. D. Cohen, D. M. Crenshaw, I. N. Evans, K. Horne, A. P. Koratkar, G. A. Kriss, J. H. Krolik, M. A. Malkan, S. L. Morris, H. Netzer, P. T. O'Brien, B. M. Peterson, G. A. Reichert, P. M. Rodriguez-Pascual, W. Wamsteker, K. S. J. Anderson, D. J. Axon, E. Benitez, P. Berlind, R. Bertram, Jr. Blackwell, J. H., N. G. Bochkarev, C. Boisson, M. Carini, R. Carrillo, T. E. Carone, F. Z. Cheng, J. A. Christensen, K. K. Chuvaev, M. Dietrich, J. J. Dokter, V. Doroshenko, D. Dultzin-Hacyan, M. N. England, B. R. Espey, A. V. Filippenko, C. M. Gaskell, M. R. Goad, L. C. Ho, J. P. Huchra, X. J. Jiang, S. Kaspi, W. Kollatschny, A. Laor, J. P. Luminet, G. M. MacAlpine, J. W. MacKenty, Yu. F. Malkov, D. Maoz, P. G. Martin, T. Matheson, B. McCollum, N. Merkulova, L. Metik, M. Mignoli, H. R. Miller, M. G. Pastoriza, D. Pelat, J. Penfold, M. Perez, G. C. Perola, J. L. Persaud, J. Peters, R. Pitts, R. W. Pogge, I. Pronik, V. I. Pronik, R. L. Ptak, L. Rawley, M. C. Recondo-Gonzalez, J. M. Rodriguez-Espinosa, W. Romanishin, A. C. Sadun, I. Salamanca, M. Santos-Lleo, K. Sekiguchi, S. G. Sergeev, A. I. Shapovalova, J. C. Shields, C. Shrader, J. M. Shull, N. A. Silbermann, M. L. Sitko, D. R. Skillman, H. A. Smith, S. M. Smith, M. A. J. Snijders, L. S. Sparke, G. M. Stirpe, R. E. Stoner, W. H. Sun, U. Thiele, S. Tokarz, Z. I. Tsvetanov, D. A. Turnshek, S. Veilleux, R. M. Wagner, S. J. Wagner, I. Wanders, T. Wang, W. F. Welsh, R. J. Weymann, R. J. White, B. J. Wilkes, B. J. Wills, C. Winge, H. Wu, and Z. L. Zou, *Steps toward Determination of the Size and Structure of the Broad-Line Region in Active Galactic Nuclei. VIII. an Intensive HST, IUE, and Ground-based Study of NGC 5548*, 97 (1995), 285.

[4] M. J. Page, J. A. Stevens, R. J. Ivison, and F. J. Carrera, *The Evolutionary Sequence of Active Galactic Nuclei and Galaxy Formation Revealed*, 611 (2004), no. 2, L85–L88.

[5] Carl K. Seyfert, *Nuclear Emission in Spiral Nebulae.*, 97 (1943), 28.

[6] C. Megan Urry and Paolo Padovani, *Unified Schemes for Radio-Loud Active Galactic Nuclei*, 107 (1995), 803.

[7] Guinevere Kauffmann, Timothy M. Heckman, Christy Tremonti, Jarle Brinchmann, Stéphane Charlot, Simon D. M. White, Susan E. Ridgway, Jon Brinkmann, Masataka Fukugita, Patrick B. Hall, Željko Ivezić, Gordon T. Richards, and Donald P. Schneider, *The host galaxies of active galactic nuclei*, 346 (2003), no. 4, 1055–1077.

[8] Diego F. Torres and Luis A. Anchordoqui, *Astrophysical origins of ultrahigh energy cosmic rays*, Reports on Progress in Physics 67 (2004), no. 9, 1663–1730.

[9] Heber D. Curtis, *Novae in the Spiral Nebulae and the Island Universe Theory*, 29 (1917), no. 171, 206–207.

[10] E. Opik, *An estimate of the distance of the Andromeda Nebula.*, 55 (1922), 406–410.

[11] Edwin Hubble, *A Relation between Distance and Radial Velocity among Extra-Galactic Nebulae*, Proceedings of the National Academy of Science 15 (1929), no. 3, 168–173.

[12] A. S. Bennett, *The revised 3C catalogue of radio sources.*, 68 (1962), 163.

[13] Cyril Hazard, *An investigation of extra-galactic radio-frequency radiation*, Ph.D. thesis, Victoria University of Manchester, United Kingdom, January 1953.

[14] M. Schmidt, *3C 273 : A Star-Like Object with Large Red-Shift*, nat 197(1963), *no.* 4872, 1040.

[15] Gregory A. Shields, *A Brief History of Active Galactic Nuclei*, 111 (1999), no. 760, 661–678.

[16] Feige Wang, Jinyi Yang, Xiaohui Fan, Joseph F. Hennawi, Aaron J. Barth, Eduardo Banados, Fuyan Bian, Konstantina Boutsia, Thomas Connor, Frederick B. Davies, Roberto Decarli, Anna-Christina Eilers, Emanuele Paolo Farina, Richard Green, Linhua Jiang, Jiang-Tao Li, Chiara Mazzucchelli, Riccardo Nanni, Jan-Torge Schindler, Bram Venemans, Fabian Walter, Xue-Bing Wu, and Minghao Yue, *A Luminous Quasar at Redshift 7.642*, 907 (2021), no. 1, L1.

[17] K. I. Kellermann, R. Sramek, M. Schmidt, D. B. Shaffer, and R. Green, *VLA Observations of Objects in the Palomar Bright Quasar Survey*, 98 (1989), 1195.

[18] Linhua Jiang, Xiaohui Fan, Željko Ivezić, Gordon T. Richards, Donald P. Schneider, Michael A. Strauss, and Brandon C. Kelly, *The Radio-Loud Fraction of Quasars is a Strong Function of Redshift and Optical Luminosity*, 656 (2007), no. 2, 680–690.

[19] Martin J. Rees, *Black Hole Models for Active Galactic Nuclei*, 22 (1984), 471–506.

[20] D. M. Worrall and M. Birkinshaw, *Multiwavelength Evidence of the Physical Processes in Radio Jets*, Physics of Active Galactic Nuclei at all Scales (Danielle Alloin, ed.), vol. 693, 2006, p. 39.

[21] Jesse L. Greenstein and Maarten Schmidt, *The Quasi-Stellar Radio Sources 3C 48 and 3C 273.*, 140 (1964), 1.

[22] Ray J. Weymann, Simon L. Morris, Craig B. Foltz, and Paul C. Hewett, *Comparisons of the Emission-Line and Continuum Properties of Broad Absorption Line and Normal Quasi-stellar Objects*, 373 (1991), 23.

[23] Robert R. Gibson, Linhua Jiang, W. N. Brandt, Patrick B. Hall, Yue Shen, Jianfeng Wu, Scott F. Anderson, Donald P. Schneider, Daniel Vanden Berk, S. C. Gallagher, Xiaohui Fan, and Donald G. York, *A Catalog of Broad Absorption Line Quasars in Sloan Digital Sky Survey Data Release 5*, 692 (2009), no. 1, 758–777.

[24] Daniel E. Vanden Berk, Gordon T. Richards, Amanda Bauer, Michael A. Strauss, Donald P. Schneider, Timothy M. Heckman, Donald G. York, Patrick B. Hall, Xiaohui Fan, G. R. Knapp, Scott F. Anderson, James Annis, Neta A. Bahcall, Mariangela Bernardi, John W. Briggs, J. Brinkmann, Robert Brunner, Scott Burles, Larry Carey, Francisco J. Castander, A. J. Connolly, J. H. Crocker, István Csabai, Mamoru Doi, Douglas Finkbeiner, Scott Friedman, Joshua A. Frieman, Masataka Fukugita, James E. Gunn, G. S. Hennessy, Željko Ivezić, Stephen Kent, Peter Z. Kunszt, D. Q. Lamb, R. French Leger, Daniel C. Long, Jon Loveday, Robert H. Lupton, Avery Meiksin, Aronne Merelli, Jeffrey A. Munn, Heidi Jo Newberg, Matt Newcomb, R. C. Nichol, Russell Owen, Jeffrey R. Pier, Adrian Pope, Constance M. Rockosi, David J. Schlegel, Walter A. Siegmund, Stephen Smee, Yehuda Snir, Chris Stoughton, Christopher Stubbs, Mark SubbaRao, Alexander S. Szalay, Gyula P. Szokoly, Christy Tremonti, Alan Uomoto,

Patrick Waddell, Brian Yanny, and Wei Zheng, *Composite Quasar Spectra from the Sloan Digital Sky Survey*, 122 (2001), no. 2, 549–564.

[25] J. Frank, A. King, and D. Raine, *Accretion power in astrophysics.*, vol. 21, 1992.

[26] Gordon T. Richards, Patrick B. Hall, Daniel E. Vanden Berk, Michael A. Strauss, Donald P. Schneider, Michael A. Weinstein, Timothy A. Reichard, Donald G. York, G. R. Knapp, Xiaohui Fan, Željko Ivezić, J. Brinkmann, Tamás Budavári, István Csabai, and R. C. Nichol, *Red and Reddened Quasars in the Sloan Digital Sky Survey*, 126 (2003), no. 3, 1131–1147.

[27] C. M. Gaskell, *A redshift difference between high and low ionization emission-line regions in QSO's-evidence for radial motions.*, 263 (1982), 79–86.

[28] B. J. Wilkes, *Studies of broad emission line profiles in QSOs - II. Properties of alarge, predominantly radio selected sample.*, 218 (1986), 331–361.

[29] M. S. Brotherton, Beverley J. Wills, Charles C. Steidel, and Wallace L. W. Sargent, *Statistics of QSO Broad Emission-Line Profiles. II. The C IV lambda 1549, C iii] lambda 1909, and MG II lambda 2798 Lines*, 423 (1994), 131.

[30] D. H. McIntosh, M. J. Rieke, H. W. Rix, C. B. Foltz, and R. J. Weymann, *A Statistical Study of Rest-Frame Optical Emission Properties in Luminous Quasars at 2.0¡=z¡=2.5*, 514 (1999), no. 1, 40–67.

[31] Gordon T. Richards, Daniel E. Vanden Berk, Timothy A. Reichard, Patrick B. Hall, Donald P. Schneider, Mark SubbaRao, Anirudda R. Thakar, and Donald G. York, *Broad Emission-Line Shifts in Quasars: An Orientation Measure for Radio-Quiet Quasars?*, 124 (2002), no. 1, 1–17.

[32] Yue Shen, W. N. Brandt, Gordon T. Richards, Kelly D. Denney, Jenny E. Greene, C. J. Grier, Luis C. Ho, Bradley M. Peterson, Patrick Petitjean, Donald P. Schneider, Charling Tao, and Jonathan R. Trump, *The Sloan Digital Sky Survey Reverberation Mapping Project: Velocity Shifts of Quasar Emission Lines*, 831 (2016), no. 1, 7.

[33] David Tytler and Xiao-Ming Fan, *Systematic QSO Emission-Line Velocity Shifts and New Unbiased Redshifts*, 79 (1992), 1.

[34] B. M. Peterson, L. Ferrarese, K. M. Gilbert, S. Kaspi, M. A. Malkan, D. Maoz, D. Merritt, H. Netzer, C. A. Onken, R. W. Pogge, M. Vestergaard, and A. Wandel, *Central Masses and Broad-Line Region Sizes of Active Galactic Nuclei. II. A Homogeneous Analysis of a Large Reverberation-Mapping Database*, 613 (2004), no. 2, 682–699.

[35] Yue Shen, *Rest-frame Optical Properties of Luminous 1.5 ¡ Z ¡ 3.5 Quasars: The Hβ-[O III] Region*, 817 (2016), no. 1, 55.

[36] Tiziana Di Matteo, Jörg Colberg, Volker Springel, Lars Hernquist, and Debora Sijacki, *Direct Cosmological Simulations of the Growth of Black Holes and Galaxies*, 676 (2008), no. 1, 33–53.

[37] A. Merloni, A. Bongiorno, M. Bolzonella, M. Brusa, F. Civano, A. Comastri, M. Elvis, F. Fiore, R. Gilli, H. Hao, K. Jahnke, A. M. Koekemoer, E. Lusso, V. Mainieri, M. Mignoli, T. Miyaji, A. Renzini, M. Salvato, J. Silverman, J. Trump, C. Vignali, G. Zamorani, P. Capak, S. J. Lilly, D. Sanders, Y. Taniguchi, S. Bardelli, C. M. Carollo, K. Caputi, T. Contini, G. Coppa, O. Cucciati, S. de la Torre, L. de Ravel, P. Franzetti, B. Garilli, G. Hasinger, C. Impey, A. Iovino, K. Iwasawa, P. Kampczyk, J. P. Kneib, C. Knobel, K. Kovač, F. Lamareille, J. F. Le Borgne, V. Le Brun, O. Le Fèvre, C. Maier, R. Pello, Y. Peng, E. Perez Montero, E. Ricciardelli, M. Scodeggio, M. Tanaka, L. A. M. Tasca, L. Tresse, D. Vergani, and E. Zucca, *On the Cosmic Evolution of the Scaling Relations Between Black Holes and Their Host Galaxies: Broad-Line Active Galactic Nuclei in the zCOSMOS Survey*, 708 (2010), no. 1, 137–157.

[38] Volker Bromm and Naoki Yoshida, *The First Galaxies*, 49 (2011), no. 1, 373–407.

[39] Timothy M. Heckman and Philip N. Best, *The Coevolution of Galaxies and Supermassive Black Holes: Insights from Surveys of the Contemporary Universe*, 52 (2014), 589–660.

[40] Laura Ferrarese and David Merritt, *A Fundamental Relation between Supermassive Black Holes and Their Host Galaxies*, 539 (2000), no. 1, L9–L12.

[41] Karl Gebhardt, Ralf Bender, Gary Bower, Alan Dressler, S. M. Faber, Alexei V. Filippenko, Richard Green, Carl Grillmair, Luis C. Ho, John Kormendy, Tod R. Lauer,

John Magorrian, Jason Pinkney, Douglas Richstone, and Scott Tremaine, *A Relationship between Nuclear Black Hole Mass and Galaxy Velocity Dispersion*, 539 (2000), no. 1, L13–L16.

[42] Jong-Hak Woo, Tommaso Treu, Aaron J. Barth, Shelley A. Wright, Jonelle L. Walsh, Misty C. Bentz, Paul Martini, Vardha N. Bennert, Gabriela Canalizo, Alexei V. Filippenko, Elinor Gates, Jenny Greene, Weidong Li, Matthew A. Malkan, Daniel Stern, and Takeo Minezaki, *The Lick AGN Monitoring Project: The M_{BH}-σ_* Relation for Reverberation-mapped Active Galaxies*, 716 (2010), no. 1, 269–280.

[43] John Kormendy and Luis C. Ho, *Coevolution (Or Not) of Supermassive Black Holes and Host Galaxies*, 51 (2013), no. 1, 511–653.

[44] Nicholas J. McConnell and Chung-Pei Ma, *Revisiting the Scaling Relations of Black Hole Masses and Host Galaxy Properties*, 764 (2013), no. 2, 184.

[45] Amy E. Reines and Marta Volonteri, *Relations between Central Black Hole Mass and Total Galaxy Stellar Mass in the Local Universe*, 813 (2015), no. 2, 82.

[46] Darren J. Croton, Volker Springel, Simon D. M. White, G. De Lucia, C. S. Frenk, L. Gao, A. Jenkins, G. Kauffmann, J. F. Navarro, and N. Yoshida, *The many lives of active galactic nuclei: cooling flows, black holes and the luminosities and colours of galaxies*, 365 (2006), no. 1, 11–28.

[47] Philip F. Hopkins and Eliot Quataert, *How do massive black holes get their gas?*, 407 (2010), no. 3, 1529–1564.

[48] Omer Blaes, *General Overview of Black Hole Accretion Theory*, 183 (2014), no. 1-4, 21–41.

[49] Philip F. Hopkins and Martin Elvis, *Quasar feedback: more bang for your buck*, 401 (2010), no. 1, 7–14.

[50] R. Maiolino, S. Gallerani, R. Neri, C. Cicone, A. Ferrara, R. Genzel, D. Lutz, E. Sturm, L. J. Tacconi, F. Walter, C. Feruglio, F. Fiore, and E. Piconcelli, *Evidence of strong quasar feedback in the early Universe*, 425 (2012), no. 1, L66–L70.

[51] Stefano Carniani, R. Maiolino, A. Marconi, G. Venturi, G. Cresci, M. Brusa,

A. Fluetsch, A. Ferrara, S. Gallerani, F. Fiore, C. Cicone, S. Ohad, H. Netzer, R. Schneider, B. Balmaverde, T. Nagao, F. La Franca, A. Comastri, F. Mannucci, G. Risaliti, E. Piconcelli, C. Feruglio, M. Cano-Diaz, V. Mainieri, L. Testi, and E. Sani, *AGN-driven outflows in the early Universe*, AGN13: Beauty and the Beast, vol. 13, October 2018, p. 68.

[52] Paul C. Hewett and Vivienne Wild, *Improved redshifts for SDSS quasar spectra*, 405 (2010), no. 4, 2302–2316.

[53] K. D. Denney, Keith Horne, W. N. Brandt, C. J. Grier, Luis C. Ho, B. M. Peterson, J. R. Trump, and J. Ge, *The Sloan Digital Sky Survey Reverberation Mapping Project: Biases in z ¿ 1.46 Redshifts Due to Quasar Diversity*, 833 (2016), no. 1, 33.

[54] Cooper Dix, Ohad Shemmer, Michael S. Brotherton, Richard F. Green, Michelle Mason, and Adam D. Myers, *Prescriptions for Correcting Ultraviolet-based Redshifts for Luminous Quasars at High Redshift*, 893 (2020), no. 1, 14.

[55] Benny Trakhtenbrot and Hagai Netzer, *Black hole growth to z = 2 - I. Improved virial methods for measuring* M_{BH} *and* L/L_{Edd}, 427 (2012), no. 4, 3081–3102.

[56] Yue Shen and Xin Liu, *Comparing Single-epoch Virial Black Hole Mass Estimators for Luminous Quasars*, 753 (2012), no. 2, 125.

[57] K. D. Denney, Keith Horne, Yue Shen, W. N. Brandt, Luis C. Ho, B. M. Peterson, Gordon T. Richards, J. R. Trump, and J. Ge, *The Sloan Digital Sky Survey Reverberation Mapping Project: An Investigation of Biases in C IV Emission Line Properties*, 224 (2016), no. 2, 14.

[58] O. Shemmer, H. Netzer, R. Maiolino, E. Oliva, S. Croom, E. Corbett, and L. di Fabrizio, *Near-Infrared Spectroscopy of High-Redshift Active Galactic Nuclei. I. A Metallicity-Accretion Rate Relationship*, 614 (2004), no. 2, 547–557.

[59] J. W. Sulentic, G. M. Stirpe, P. Marziani, R. Zamanov, M. Calvani, and V. Braito, *VLT/ISAAC spectra of the Hβ region in intermediate redshift quasars*, 423 (2004), 121–132.

[60] Hagai Netzer, Paulina Lira, Benny Trakhtenbrot, Ohad Shemmer, and Iara Cury, *Black Hole Mass and Growth Rate at High Redshift*, 671 (2007), no. 2, 1256–1263.

[61] Benny Trakhtenbrot, Hagai Netzer, Paulina Lira, and Ohad Shemmer, *Black Hole Mass and Growth Rate at z ~= 4.8: A Short Episode of Fast Growth Followed by Short Duty Cycle Activity*, 730 (2011), no. 1, 7.

[62] Wenwen Zuo, Xue-Bing Wu, Xiaohui Fan, Richard Green, Ran Wang, and Fuyan Bian, *Black Hole Mass Estimates and Rapid Growth of Supermassive Black Holes in Luminous z ~3.5 Quasars*, 799 (2015), no. 2, 189.

[63] S. López, V. D'Odorico, S. L. Ellison, G. D. Becker, L. Christensen, G. Cupani, K. D. Denney, I. Pâris, G. Worseck, T. A. M. Berg, S. Cristiani, M. Dessauges-Zavadsky, M. Haehnelt, F. Hamann, J. Hennawi, V. Iršič, T. S. Kim, P. López, R. Lund Saust, B. Ménard, S. Perrotta, J. X. Prochaska, R. Sánchez-Ramírez, M. Vestergaard, M. Viel, and L. Wisotzki, *XQ-100: A legacy survey of one hundred* $3.5 \lesssim z \lesssim 4.5$ *quasars observed with VLT/X-shooter*, 594 (2016), A91.

[64] J. E. Mejía-Restrepo, B. Trakhtenbrot, P. Lira, H. Netzer, and D. M. Capellupo, *Active galactic nuclei at* $z \sim 1.5$ *- II. Black hole mass estimation by means of broad emission lines*, 460 (2016), no. 1, 187–211.

[65] Liam Coatman, Paul C. Hewett, Manda Banerji, Gordon T. Richards, Joseph F. Hennawi, and J. Xavier Prochaska, *Correcting C IV-based virial black hole masses*, 465 (2017), no. 2, 2120–2142.

[66] Jonathan H. Elias, Richard R. Joyce, Ming Liang, Gary P. Muller, Edward A. Hileman, and James R. George, *Design of the Gemini near-infrared spectrograph*, Society of Photo-Optical Instrumentation Engineers (SPIE) Conference Series (Ian S. McLean and Masanori Iye, eds.), Society of Photo-Optical Instrumentation Engineers (SPIE) Conference Series, vol. 6269, June 2006, p. 62694C.

[67] D. N. Spergel, R. Bean, O. Doré, M. R. Nolta, C. L. Bennett, J. Dunkley, G. Hinshaw, N. Jarosik, E. Komatsu, L. Page, H. V. Peiris, L. Verde, M. Halpern, R. S. Hill, A. Kogut, M. Limon, S. S. Meyer, N. Odegard, G. S. Tucker, J. L. Weiland, E. Wol-

lack, and E. L. Wright, *Three-Year Wilkinson Microwave Anisotropy Probe (WMAP) Observations: Implications for Cosmology*, 170 (2007), no. 2, 377–408.

[68] Donald G. York, J. Adelman, Jr. Anderson, John E., Scott F. Anderson, James Annis, Neta A. Bahcall, J. A. Bakken, Robert Barkhouser, Steven Bastian, Eileen Berman, William N. Boroski, Steve Bracker, Charlie Briegel, John W. Briggs, J. Brinkmann, Robert Brunner, Scott Burles, Larry Carey, Michael A. Carr, Francisco J. Castander, Bing Chen, Patrick L. Colestock, A. J. Connolly, J. H. Crocker, István Csabai, Paul C. Czarapata, John Eric Davis, Mamoru Doi, Tom Dombeck, Daniel Eisenstein, Nancy Ellman, Brian R. Elms, Michael L. Evans, Xiaohui Fan, Glenn R. Federwitz, Larry Fiscelli, Scott Friedman, Joshua A. Frieman, Masataka Fukugita, Bruce Gillespie, James E. Gunn, Vijay K. Gurbani, Ernst de Haas, Merle Haldeman, Frederick H. Harris, J. Hayes, Timothy M. Heckman, G. S. Hennessy, Robert B. Hindsley, Scott Holm, Donald J. Holmgren, Chi-hao Huang, Charles Hull, Don Husby, Shin-Ichi Ichikawa, Takashi Ichikawa, Željko Ivezić, Stephen Kent, Rita S. J. Kim, E. Kinney, Mark Klaene, A. N. Kleinman, S. Kleinman, G. R. Knapp, John Korienek, Richard G. Kron, Peter Z. Kunszt, D. Q. Lamb, B. Lee, R. French Leger, Siriluk Limmongkol, Carl Lindenmeyer, Daniel C. Long, Craig Loomis, Jon Loveday, Rich Lucinio, Robert H. Lupton, Bryan MacKinnon, Edward J. Mannery, P. M. Mantsch, Bruce Margon, Peregrine McGehee, Timothy A. McKay, Avery Meiksin, Aronne Merelli, David G. Monet, Jeffrey A. Munn, Vijay K. Narayanan, Thomas Nash, Eric Neilsen, Rich Neswold, Heidi Jo Newberg, R. C. Nichol, Tom Nicinski, Mario Nonino, Norio Okada, Sadanori Okamura, Jeremiah P. Ostriker, Russell Owen, A. George Pauls, John Peoples, R. L. Peterson, Donald Petravick, Jeffrey R. Pier, Adrian Pope, Ruth Pordes, Angela Prosapio, Ron Rechenmacher, Thomas R. Quinn, Gordon T. Richards, Michael W. Richmond, Claudio H. Rivetta, Constance M. Rockosi, Kurt Ruthmansdorfer, Dale Sandford, David J. Schlegel, Donald P. Schneider, Maki Sekiguchi, Gary Sergey, Kazuhiro Shimasaku, Walter A. Siegmund, Stephen Smee, J. Allyn Smith, S. Snedden, R. Stone, Chris Stoughton, Michael A. Strauss, Christopher Stubbs, Mark SubbaRao, Alexander S.

Szalay, Istvan Szapudi, Gyula P. Szokoly, Anirudda R. Thakar, Christy Tremonti, Douglas L. Tucker, Alan Uomoto, Dan Vanden Berk, Michael S. Vogeley, Patrick Waddell, Shu-i. Wang, Masaru Watanabe, David H. Weinberg, Brian Yanny, Naoki Yasuda, and SDSS Collaboration, *The Sloan Digital Sky Survey: Technical Summary*, 120 (2000), no. 3, 1579–1587.

[69] Isabelle Pâris, Patrick Petitjean, Nicholas P. Ross, Adam D. Myers, Éric Aubourg, Alina Streblyanska, Stephen Bailey, Éric Armengaud, Nathalie Palanque-Delabrouille, Christophe Yèche, Fred Hamann, Michael A. Strauss, Franco D. Albareti, Jo Bovy, Dmitry Bizyaev, W. Niel Brandt, Marcella Brusa, Johannes Buchner, Johan Comparat, Rupert A. C. Croft, Tom Dwelly, Xiaohui Fan, Andreu Font-Ribera, Jian Ge, Antonis Georgakakis, Patrick B. Hall, Linhua Jiang, Karen Kinemuchi, Elena Malanushenko, Viktor Malanushenko, Richard G. McMahon, Marie-Luise Menzel, Andrea Merloni, Kirpal Nandra, Pasquier Noterdaeme, Daniel Oravetz, Kaike Pan, Matthew M. Pieri, Francisco Prada, Mara Salvato, David J. Schlegel, Donald P. Schneider, Audrey Simmons, Matteo Viel, David H. Weinberg, and Liu Zhu, *The Sloan Digital Sky Survey Quasar Catalog: Twelfth data release*, 597 (2017), A79.

[70] Isabelle Pâris, Patrick Petitjean, Éric Aubourg, Adam D. Myers, Alina Streblyanska, Brad W. Lyke, Scott F. Anderson, Éric Armengaud, Julian Bautista, Michael R. Blanton, Michael Blomqvist, Jonathan Brinkmann, Joel R. Brownstein, William Nielsen Brandt, Étienne Burtin, Kyle Dawson, Sylvain de la Torre, Antonis Georgakakis, Héctor Gil-Marín, Paul J. Green, Patrick B. Hall, Jean-Paul Kneib, Stephanie M. LaMassa, Jean-Marc Le Goff, Chelsea MacLeod, Vivek Mariappan, Ian D. McGreer, Andrea Merloni, Pasquier Noterdaeme, Nathalie Palanque-Delabrouille, Will J. Percival, Ashley J. Ross, Graziano Rossi, Donald P. Schneider, Hee-Jong Seo, Rita Tojeiro, Benjamin A. Weaver, Anne-Marie Weijmans, Christophe Yèche, Pauline Zarrouk, and Gong-Bo Zhao, *The Sloan Digital Sky Survey Quasar Catalog: Fourteenth data release*, 613 (2018), A51.

[71] Gordon T. Richards, Xiaohui Fan, Heidi Jo Newberg, Michael A. Strauss, Daniel E.

Vanden Berk, Donald P. Schneider, Brian Yanny, Adam Boucher, Scott Burles, Joshua A. Frieman, James E. Gunn, Patrick B. Hall, Željko Ivezić, Stephen Kent, Jon Loveday, Robert H. Lupton, Constance M. Rockosi, David J. Schlegel, Chris Stoughton, Mark SubbaRao, and Donald G. York, *Spectroscopic Target Selection in the Sloan Digital Sky Survey: The Quasar Sample*, 123 (2002), no. 6, 2945–2975.

[72] Paul C. Hewett, Craig B. Foltz, and Frederic H. Chaffee, *The Evolution of Bright, Optically Selected QSOs*, 406 (1993), L43.

[73] G. Hasinger, T. Miyaji, and M. Schmidt, *Luminosity-dependent evolution of soft X-ray selected AGN. New Chandra and XMM-Newton surveys*, 441 (2005), no. 2, 417–434.

[74] Gordon T. Richards, Michael A. Strauss, Xiaohui Fan, Patrick B. Hall, Sebastian Jester, Donald P. Schneider, Daniel E. Vanden Berk, Chris Stoughton, Scott F. Anderson, Robert J. Brunner, Jim Gray, James E. Gunn, Željko Ivezić, Margaret K. Kirkland, G. R. Knapp, Jon Loveday, Avery Meiksin, Adrian Pope, Alexander S. Szalay, Anirudda R. Thakar, Brian Yanny, Donald G. York, J. C. Barentine, Howard J. Brewington, J. Brinkmann, Masataka Fukugita, Michael Harvanek, Stephen M. Kent, S. J. Kleinman, Jurek Krzesiński, Daniel C. Long, Robert H. Lupton, Thomas Nash, Jr. Neilsen, Eric H., Atsuko Nitta, David J. Schlegel, and Stephanie A. Snedden, *The Sloan Digital Sky Survey Quasar Survey: Quasar Luminosity Function from Data Release 3*, 131 (2006), no. 6, 2766–2787.

[75] M. F. Skrutskie, R. M. Cutri, R. Stiening, M. D. Weinberg, S. Schneider, J. M. Carpenter, C. Beichman, R. Capps, T. Chester, J. Elias, J. Huchra, J. Liebert, C. Lonsdale, D. G. Monet, S. Price, P. Seitzer, T. Jarrett, J. D. Kirkpatrick, J. E. Gizis, E. Howard, T. Evans, J. Fowler, L. Fullmer, R. Hurt, R. Light, E. L. Kopan, K. A. Marsh, H. L. McCallon, R. Tam, S. Van Dyk, and S. Wheelock, *The Two Micron All Sky Survey (2MASS)*, 131 (2006), no. 2, 1163–1183.

[76] R. E. Mason, A. Rodríguez-Ardila, L. Martins, R. Riffel, O. González Martín, C. Ramos Almeida, D. Ruschel Dutra, L. C. Ho, K. Thanjavur, H. Flohic, A. Alonso-Herrero, P. Lira, R. McDermid, R. A. Riffel, R. P. Schiavon, C. Winge, M. D. Hoenig, and

E. Perlman, *The Nuclear Near-Infrared Spectral Properties of Nearby Galaxies*, 217 (2015), no. 1, 13.

[77] Yue Shen, Jin Wu, Linhua Jiang, Eduardo Bañados, Xiaohui Fan, Luis C. Ho, Dominik A. Riechers, Michael A. Strauss, Bram Venemans, Marianne Vestergaard, Fabian Walter, Feige Wang, Chris Willott, Xue-Bing Wu, and Jinyi Yang, *Gemini GNIRS Near-infrared Spectroscopy of 50 Quasars at* $z \gtrsim 5.7$, 873 (2019), no. 1, 35.

[78] M. S. Bessell, F. Castelli, and B. Plez, *Model atmospheres broad-band colors, bolometric corrections and temperature calibrations for O - M stars*, 333 (1998), 231–250.

[79] Daniel E. Vanden Berk, Brian C. Wilhite, Richard G. Kron, Scott F. Anderson, Robert J. Brunner, Patrick B. Hall, Željko Ivezić, Gordon T. Richards, Donald P. Schneider, Donald G. York, Jonathan V. Brinkmann, Don Q. Lamb, Robert C. Nichol, and David J. Schlegel, *The Ensemble Photometric Variability of ~25,000 Quasars in the Sloan Digital Sky Survey*, 601 (2004), no. 2, 692–714.

[80] Shai Kaspi, W. N. Brandt, Dan Maoz, Hagai Netzer, Donald P. Schneider, and Ohad Shemmer, *Reverberation Mapping of High-Luminosity Quasars: First Results*, 659 (2007), no. 2, 997–1007.

[81] Chelsea L. MacLeod, Željko Ivezić, Branimir Sesar, Wim de Vries, Christopher S. Kochanek, Brandon C. Kelly, Andrew C. Becker, Robert H. Lupton, Patrick B. Hall, Gordon T. Richards, Scott F. Anderson, and Donald P. Schneider, *A Description of Quasar Variability Measured Using Repeated SDSS and POSS Imaging*, 753 (2012), no. 2, 106.

[82] Todd A. Boroson and Richard F. Green, *The Emission-Line Properties of Low-Redshift Quasi-stellar Objects*, 80 (1992), 109.

[83] M. Vestergaard and B. J. Wilkes, *An Empirical Ultraviolet Template for Iron Emission in Quasars as Derived from I Zwicky 1*, 134 (2001), no. 1, 1–33.

[84] Aaron J. Barth, Anna Pancoast, Vardha N. Bennert, Brendon J. Brewer, Gabriela Canalizo, Alexei V. Filippenko, Elinor L. Gates, Jenny E. Greene, Weidong Li, Matthew A. Malkan, David J. Sand, Daniel Stern, Tommaso Treu, Jong-Hak Woo,

Roberto J. Assef, Hyun-Jin Bae, Tabitha Buehler, S. Bradley Cenko, Kelsey I. Clubb, Michael C. Cooper, Aleksandar M. Diamond-Stanic, Sebastian F. Hönig, Michael D. Joner, C. David Laney, Mariana S. Lazarova, A. M. Nierenberg, Jeffrey M. Silverman, Erik J. Tollerud, and Jonelle L. Walsh, *The Lick AGN Monitoring Project 2011: Fe II Reverberation from the Outer Broad-line Region*, 769 (2013), no. 2, 128.

[85] P. J. Storey and C. J. Zeippen, *Theoretical values for the [OIII] 5007/4959 line-intensity ratio and homologous cases*, 312 (2000), no. 4, 813–816.

[86] Gordon T. Richards, Nicholas E. Kruczek, S. C. Gallagher, Patrick B. Hall, Paul C. Hewett, Karen M. Leighly, Rajesh P. Deo, Rachael M. Kratzer, and Yue Shen, *Unification of Luminous Type 1 Quasars through C IV Emission*, 141 (2011), no. 5, 167.

[87] Yue Shen, Patrick B. Hall, Keith Horne, Guangtun Zhu, Ian McGreer, Torben Simm, Jonathan R. Trump, Karen Kinemuchi, W. N. Brandt, Paul J. Green, C. J. Grier, Hengxiao Guo, Luis C. Ho, Yasaman Homayouni, Linhua Jiang, Jennifer I-Hsiu Li, Eric Morganson, Patrick Petitjean, Gordon T. Richards, Donald P. Schneider, D. A. Starkey, Shu Wang, Ken Chambers, Nick Kaiser, Rolf-Peter Kudritzki, Eugene Magnier, and Christopher Waters, *The Sloan Digital Sky Survey Reverberation Mapping Project: Sample Characterization*, 241 (2019), no. 2, 34.

[88] Hagai Netzer, *The Largest Black Holes and the Most Luminous Galaxies*, 583 (2003), no. 1, L5–L8.

[89] Michael Eracleous and Jules P. Halpern, *Double-peaked Emission Lines in Active Galactic Nuclei*, 90 (1994), 1.

[90] Yue Shen, Gordon T. Richards, Michael A. Strauss, Patrick B. Hall, Donald P. Schneider, Stephanie Snedden, Dmitry Bizyaev, Howard Brewington, Viktor Malanushenko, Elena Malanushenko, Dan Oravetz, Kaike Pan, and Audrey Simmons, *A Catalog of Quasar Properties from Sloan Digital Sky Survey Data Release 7*, 194 (2011), no. 2, 45.

[91] H. Netzer, O. Shemmer, R. Maiolino, E. Oliva, S. Croom, E. Corbett, and L. di

Fabrizio, *Near-Infrared Spectroscopy of High-Redshift Active Galactic Nuclei. II. Disappearing Narrow-Line Regions and the Role of Accretion*, 614 (2004), no. 2, 558–567.

[92] B. J. Wills and I. W. A. Browne, *Relativistic Beaming and Quasar Emission Lines*, 302 (1986), 56.

[93] Michael Levi, Chris Bebek, Timothy Beers, Robert Blum, Robert Cahn, Daniel Eisenstein, Brenna Flaugher, Klaus Honscheid, Richard Kron, Ofer Lahav, Patrick McDonald, Natalie Roe, David Schlegel, and representing the DESI collaboration, *The DESI Experiment, a whitepaper for Snowmass 2013*, arXiv e-prints (2013), arXiv:1308.0847.

[94] DESI Collaboration, Amir Aghamousa, Jessica Aguilar, Steve Ahlen, Shadab Alam, Lori E. Allen, Carlos Allende Prieto, James Annis, Stephen Bailey, Christophe Balland, Otger Ballester, Charles Baltay, Lucas Beaufore, Chris Bebek, Timothy C. Beers, Eric F. Bell, José Luis Bernal, Robert Besuner, Florian Beutler, Chris Blake, Hannes Bleuler, Michael Blomqvist, Robert Blum, Adam S. Bolton, Cesar Briceno, David Brooks, Joel R. Brownstein, Elizabeth Buckley-Geer, Angela Burden, Etienne Burtin, Nicolas G. Busca, Robert N. Cahn, Yan-Chuan Cai, Laia Cardiel-Sas, Raymond G. Carlberg, Pierre-Henri Carton, Ricard Casas, Francisco J. Castander, Jorge L. Cervantes-Cota, Todd M. Claybaugh, Madeline Close, Carl T. Coker, Shaun Cole, Johan Comparat, Andrew P. Cooper, M. C. Cousinou, Martin Crocce, Jean-Gabriel Cuby, Daniel P. Cunningham, Tamara M. Davis, Kyle S. Dawson, Axel de la Macorra, Juan De Vicente, Timothée Delubac, Mark Derwent, Arjun Dey, Govinda Dhungana, Zhejie Ding, Peter Doel, Yutong T. Duan, Anne Ealet, Jerry Edelstein, Sarah Eftekharzadeh, Daniel J. Eisenstein, Ann Elliott, Stéphanie Escoffier, Matthew Evatt, Parker Fagrelius, Xiaohui Fan, Kevin Fanning, Arya Farahi, Jay Farihi, Ginevra Favole, Yu Feng, Enrique Fernandez, Joseph R. Findlay, Douglas P. Finkbeiner, Michael J. Fitzpatrick, Brenna Flaugher, Samuel Flender, Andreu Font-Ribera, Jaime E. Forero-Romero, Pablo Fosalba, Carlos S. Frenk, Michele Fumagalli, Boris T. Gaensicke, Giuseppe Gallo, Juan Garcia-Bellido, Enrique Gaztanaga, Nicola Pietro Gentile Fusillo, Terry Gerard, Irena Gershkovich, Tommaso Giannan-

tonio, Denis Gillet, Guillermo Gonzalez-de-Rivera, Violeta Gonzalez-Perez, Shelby Gott, Or Graur, Gaston Gutierrez, Julien Guy, Salman Habib, Henry Heetderks, Ian Heetderks, Katrin Heitmann, Wojciech A. Hellwing, David A. Herrera, Shirley Ho, Stephen Holland, Klaus Honscheid, Eric Huff, Timothy A. Hutchinson, Dragan Huterer, Ho Seong Hwang, Joseph Maria Illa Laguna, Yuzo Ishikawa, Dianna Jacobs, Niall Jeffrey, Patrick Jelinsky, Elise Jennings, Linhua Jiang, Jorge Jimenez, Jennifer Johnson, Richard Joyce, Eric Jullo, Stéphanie Juneau, Sami Kama, Armin Karcher, Sonia Karkar, Robert Kehoe, Noble Kennamer, Stephen Kent, Martin Kilbinger, Alex G. Kim, David Kirkby, Theodore Kisner, Ellie Kitanidis, Jean-Paul Kneib, Sergey Koposov, Eve Kovacs, Kazuya Koyama, Anthony Kremin, Richard Kron, Luzius Kronig, Andrea Kueter-Young, Cedric G. Lacey, Robin Lafever, Ofer Lahav, Andrew Lambert, Michael Lampton, Martin Landriau, Dustin Lang, Tod R. Lauer, Jean-Marc Le Goff, Laurent Le Guillou, Auguste Le Van Suu, Jae Hyeon Lee, Su-Jeong Lee, Daniela Leitner, Michael Lesser, Michael E. Levi, Benjamin L'Huillier, Baojiu Li, Ming Liang, Huan Lin, Eric Linder, Sarah R. Loebman, Zarija Lukić, Jun Ma, Niall MacCrann, Christophe Magneville, Laleh Makarem, Marc Manera, Christopher J. Manser, Robert Marshall, Paul Martini, Richard Massey, Thomas Matheson, Jeremy McCauley, Patrick McDonald, Ian D. McGreer, Aaron Meisner, Nigel Metcalfe, Timothy N. Miller, Ramon Miquel, John Moustakas, Adam Myers, Milind Naik, Jeffrey A. Newman, Robert C. Nichol, Andrina Nicola, Luiz Nicolati da Costa, Jundan Nie, Gustavo Niz, Peder Norberg, Brian Nord, Dara Norman, Peter Nugent, Thomas O'Brien, Minji Oh, Knut A. G. Olsen, Cristobal Padilla, Hamsa Padmanabhan, Nikhil Padmanabhan, Nathalie Palanque-Delabrouille, Antonella Palmese, Daniel Pappalardo, Isabelle Pâris, Changbom Park, Anna Patej, John A. Peacock, Hiranya V. Peiris, Xiyan Peng, Will J. Percival, Sandrine Perruchot, Matthew M. Pieri, Richard Pogge, Jennifer E. Pollack, Claire Poppett, Francisco Prada, Abhishek Prakash, Ronald G. Probst, David Rabinowitz, Anand Raichoor, Chang Hee Ree, Alexandre Refregier, Xavier Regal, Beth Reid, Kevin Reil, Mehdi Rezaie, Constance M. Rockosi, Natalie

Roe, Samuel Ronayette, Aaron Roodman, Ashley J. Ross, Nicholas P. Ross, Graziano Rossi, Eduardo Rozo, Vanina Ruhlmann-Kleider, Eli S. Rykoff, Cristiano Sabiu, Lado Samushia, Eusebio Sanchez, Javier Sanchez, David J. Schlegel, Michael Schneider, Michael Schubnell, Aurélia Secroun, Uros Seljak, Hee-Jong Seo, Santiago Serrano, Arman Shafieloo, Huanyuan Shan, Ray Sharples, Michael J. Sholl, William V. Shourt, Joseph H. Silber, David R. Silva, Martin M. Sirk, Anze Slosar, Alex Smith, George F. Smoot, Debopam Som, Yong-Seon Song, David Sprayberry, Ryan Staten, Andy Stefanik, Gregory Tarle, Suk Sien Tie, Jeremy L. Tinker, Rita Tojeiro, Francisco Valdes, Octavio Valenzuela, Monica Valluri, Mariana Vargas-Magana, Licia Verde, Alistair R. Walker, Jiali Wang, Yuting Wang, Benjamin A. Weaver, Curtis Weaverdyck, Risa H. Wechsler, David H. Weinberg, Martin White, Qian Yang, Christophe Yeche, Tianmeng Zhang, Gong-Bo Zhao, Yi Zheng, Xu Zhou, Zhimin Zhou, Yaling Zhu, Hu Zou, and Ying Zu, *The DESI Experiment Part I: Science,Targeting, and Survey Design*, arXiv e-prints (2016), arXiv:1611.00036.

[95] Roelof S. de Jong, Olga Bellido-Tirado, Cristina Chiappini, Éric Depagne, Roger Haynes, Diana Johl, Olivier Schnurr, Axel Schwope, Jakob Walcher, Frank Dionies, Dionne Haynes, Andreas Kelz, Francisco S. Kitaura, Georg Lamer, Ivan Minchev, Volker Müller, Sebastián. E. Nuza, Jean-Christophe Olaya, Tilmann Piffl, Emil Popow, Matthias Steinmetz, Ugur Ural, Mary Williams, Roland Winkler, Lutz Wisotzki, Wolfgang R. Ansorge, Manda Banerji, Eduardo Gonzalez Solares, Mike Irwin, Robert C. Kennicutt, Dave King, Richard G. McMahon, Sergey Koposov, Ian R. Parry, David Sun, Nicholas A. Walton, Gert Finger, Olaf Iwert, Mirko Krumpe, Jean-Louis Lizon, Mainieri Vincenzo, Jean-Philippe Amans, Piercarlo Bonifacio, Mathieu Cohen, Patrick Francois, Pascal Jagourel, Shan B. Mignot, Frédéric Royer, Paola Sartoretti, Ralf Bender, Frank Grupp, Hans-Joachim Hess, Florian Lang-Bardl, Bernard Muschielok, Hans Böhringer, Thomas Boller, Angela Bongiorno, Marcella Brusa, Tom Dwelly, Andrea Merloni, Kirpal Nandra, Mara Salvato, Johannes H. Pragt, Ramón Navarro, Gerrit Gerlofsma, Ronald Roelfsema, Gavin B. Dalton, Kevin F. Middleton, Ian A. Tosh, Cor-

rado Boeche, Elisabetta Caffau, Norbert Christlieb, Eva K. Grebel, Camilla Hansen, Andreas Koch, Hans-G. Ludwig, Andreas Quirrenbach, Luca Sbordone, Walter Seifert, Guido Thimm, Trifon Trifonov, Amina Helmi, Scott C. Trager, Sofia Feltzing, Andreas Korn, and Wilfried Boland, *4MOST: 4-metre multi-object spectroscopic telescope*, Ground-based and Airborne Instrumentation for Astronomy IV (Ian S. McLean, Suzanne K. Ramsay, and Hideki Takami, eds.), Society of Photo-Optical Instrumentation Engineers (SPIE) Conference Series, vol. 8446, September 2012, p. 84460T.

[96] Beverley J. Wills, A. Laor, M. S. Brotherton, D. Wills, B. J. Wilkes, G. J. Ferland, and Zhaohui Shang, *The PG X-Ray QSO Sample: Links between the Ultraviolet-X-Ray Continuum and Emission Lines*, 515 (1999), no. 2, L53–L56.

[97] Massimo Robberto, Peter W. Roming, Alexander J. van der Horst, Susan Pope, Todd J. Veach, Marisa L. García Vargas, Ernesto Sánchez-Blanco, Manuel Maldonado Medina, Ana Perez, Antonina G. Brody, Kelly D. Smith, Ronnie L. Killough, Kristian B. Persson, Jason L. Stange, Amanda J. Bayless, Stephen Goodsell, Jeffrey Radwick, Morten Andersen, Ruben Diaz, Manuel Lazo, Thomas Hayward, and Scot Kleinman, *SCORPIO: the Gemini facility instrument for LSST follow-up*, Ground-based and Airborne Instrumentation for Astronomy VII (Christopher J. Evans, Luc Simard, and Hideki Takami, eds.), Society of Photo-Optical Instrumentation Engineers (SPIE) Conference Series, vol. 10702, July 2018, p. 107020I.

[98] Jonathan P. Gardner, John C. Mather, Mark Clampin, Rene Doyon, Matthew A. Greenhouse, Heidi B. Hammel, John B. Hutchings, Peter Jakobsen, Simon J. Lilly, Knox S. Long, Jonathan I. Lunine, Mark J. McCaughrean, Matt Mountain, John Nella, George H. Rieke, Marcia J. Rieke, Hans-Walter Rix, Eric P. Smith, George Sonneborn, Massimo Stiavelli, H. S. Stockman, Rogier A. Windhorst, and Gillian S. Wright, *The James Webb Space Telescope*, 123 (2006), no. 4, 485–606.

[99] C. Alcock and B. Paczynski, *An evolution free test for non-zero cosmological constant*, nat 281(1979), 358.

[100] David W. Hogg, *Distance measures in cosmology*, arXiv e-prints (1999), astro–ph/9905116.

[101] Yue Shen, Michael A. Strauss, Masamune Oguri, Joseph F. Hennawi, Xiaohui Fan, Gordon T. Richards, Patrick B. Hall, James E. Gunn, Donald P. Schneider, Alexander S. Szalay, Anirudda R. Thakar, Daniel E. Vanden Berk, Scott F. Anderson, Neta A. Bahcall, Andrew J. Connolly, and Gillian R. Knapp, *Clustering of High-Redshift (z ¿= 2.9) Quasars from the Sloan Digital Sky Survey*, 133 (2007), no. 5, 2222–2241.

[102] Kyle S. Dawson, David J. Schlegel, Christopher P. Ahn, Scott F. Anderson, Éric Aubourg, Stephen Bailey, Robert H. Barkhouser, Julian E. Bautista, Alessandra Beifiori, Andreas A. Berlind, Vaishali Bhardwaj, Dmitry Bizyaev, Cullen H. Blake, Michael R. Blanton, Michael Blomqvist, Adam S. Bolton, Arnaud Borde, Jo Bovy, W. N. Brandt, Howard Brewington, Jon Brinkmann, Peter J. Brown, Joel R. Brownstein, Kevin Bundy, N. G. Busca, William Carithers, Aurelio R. Carnero, Michael A. Carr, Yanmei Chen, Johan Comparat, Natalia Connolly, Frances Cope, Rupert A. C. Croft, Antonio J. Cuesta, Luiz N. da Costa, James R. A. Davenport, Timothée Delubac, Roland de Putter, Saurav Dhital, Anne Ealet, Garrett L. Ebelke, Daniel J. Eisenstein, S. Escoffier, Xiaohui Fan, N. Filiz Ak, Hayley Finley, Andreu Font-Ribera, R. Génova-Santos, James E. Gunn, Hong Guo, Daryl Haggard, Patrick B. Hall, Jean-Christophe Hamilton, Ben Harris, David W. Harris, Shirley Ho, David W. Hogg, Diana Holder, Klaus Honscheid, Joe Huehnerhoff, Beatrice Jordan, Wendell P. Jordan, Guinevere Kauffmann, Eyal A. Kazin, David Kirkby, Mark A. Klaene, Jean-Paul Kneib, Jean-Marc Le Goff, Khee-Gan Lee, Daniel C. Long, Craig P. Loomis, Britt Lundgren, Robert H. Lupton, Marcio A. G. Maia, Martin Makler, Elena Malanushenko, Viktor Malanushenko, Rachel Mandelbaum, Marc Manera, Claudia Maraston, Daniel Margala, Karen L. Masters, Cameron K. McBride, Patrick McDonald, Ian D. McGreer, Richard G. McMahon, Olga Mena, Jordi Miralda-Escudé, Antonio D. Montero-Dorta, Francesco Montesano, Demitri Muna, Adam D. Myers, Tracy Naugle, Robert C. Nichol, Pasquier Noterdaeme, Sebastián E. Nuza, Matthew D. Olmstead, Audrey

Oravetz, Daniel J. Oravetz, Russell Owen, Nikhil Padmanabhan, Nathalie Palanque-Delabrouille, Kaike Pan, John K. Parejko, Isabelle Pâris, Will J. Percival, Ismael Pérez-Fournon, Ignasi Pérez-Ràfols, Patrick Petitjean, Robert Pfaffenberger, Janine Pforr, Matthew M. Pieri, Francisco Prada, Adrian M. Price-Whelan, M. Jordan Raddick, Rafael Rebolo, James Rich, Gordon T. Richards, Constance M. Rockosi, Natalie A. Roe, Ashley J. Ross, Nicholas P. Ross, Graziano Rossi, J. A. Rubiño-Martin, Lado Samushia, Ariel G. Sánchez, Conor Sayres, Sarah J. Schmidt, Donald P. Schneider, C. G. Scóccola, Hee-Jong Seo, Alaina Shelden, Erin Sheldon, Yue Shen, Yiping Shu, Anže Slosar, Stephen A. Smee, Stephanie A. Snedden, Fritz Stauffer, Oliver Steele, Michael A. Strauss, Alina Streblyanska, Nao Suzuki, Molly E. C. Swanson, Tomer Tal, Masayuki Tanaka, Daniel Thomas, Jeremy L. Tinker, Rita Tojeiro, Christy A. Tremonti, M. Vargas Magaña, Licia Verde, Matteo Viel, David A. Wake, Mike Watson, Benjamin A. Weaver, David H. Weinberg, Benjamin J. Weiner, Andrew A. West, Martin White, W. M. Wood-Vasey, Christophe Yeche, Idit Zehavi, Gong-Bo Zhao, and Zheng Zheng, *The Baryon Oscillation Spectroscopic Survey of SDSS-III*, 145 (2013), no. 1, 10.

[103] Ian D. McGreer, Sarah Eftekharzadeh, Adam D. Myers, and Xiaohui Fan, *A Constraint on Quasar Clustering at $z = 5$ from a Binary Quasar*, 151 (2016), no. 3, 61.

[104] Gong-Bo Zhao, Yuting Wang, Shun Saito, Héctor Gil-Marín, Will J. Percival, Dandan Wang, Chia-Hsun Chuang, Rossana Ruggeri, Eva-Maria Mueller, Fangzhou Zhu, Ashley J. Ross, Rita Tojeiro, Isabelle Pâris, Adam D. Myers, Jeremy L. Tinker, Jian Li, Etienne Burtin, Pauline Zarrouk, Florian Beutler, Falk Baumgarten, Julian E. Bautista, Joel R. Brownstein, Kyle S. Dawson, Jiamin Hou, Axel de la Macorra, Graziano Rossi, John A. Peacock, Ariel G. Sánchez, Arman Shafieloo, Donald P. Schneider, and Cheng Zhao, *The clustering of the SDSS-IV extended Baryon Oscillation Spectroscopic Survey DR14 quasar sample: a tomographic measurement of cosmic structure growth and expansion rate based on optimal redshift weights*, 482 (2019), no. 3, 3497–3513.

[105] Todd Boroson, *Blueshifted [O III] Emission: Indications of a Dynamic Narrow-Line Region*, 130 (2005), no. 2, 381–386.

[106] Nathen H. Nguyen, Paulina Lira, Benny Trakhtenbrot, Hagai Netzer, Claudia Cicone, Roberto Maiolino, and Ohad Shemmer, *ALMA Observations of Quasar Host Galaxies at z 4.8*, 895 (2020), no. 1, 74.

[107] G. Vietri, E. Piconcelli, M. Bischetti, F. Duras, S. Martocchia, A. Bongiorno, A. Marconi, L. Zappacosta, S. Bisogni, G. Bruni, M. Brusa, A. Comastri, G. Cresci, C. Feruglio, E. Giallongo, F. La Franca, V. Mainieri, F. Mannucci, F. Ricci, E. Sani, V. Testa, F. Tombesi, C. Vignali, and F. Fiore, *The WISSH quasars project. IV. Broad line region versus kiloparsec-scale winds*, 617 (2018), A81.

[108] Naoyuki Tamura, Naruhisa Takato, Atsushi Shimono, Yuki Moritani, Kiyoto Yabe, Yuki Ishizuka, Akitoshi Ueda, Yukiko Kamata, Hrand Aghazarian, Stéphane Arnouts, Gabriel Barban, Robert H. Barkhouser, Renato C. Borges, David F. Braun, Michael A. Carr, Pierre-Yves Chabaud, Yin-Chang Chang, Hsin-Yo Chen, Masashi Chiba, Richard C. Y. Chou, You-Hua Chu, Judith Cohen, Rodrigo P. de Almeida, Antonio C. de Oliveira, Ligia S. de Oliveira, Richard G. Dekany, Kjetil Dohlen, Jesulino B. dos Santos, Leandro H. dos Santos, Richard Ellis, Maximilian Fabricius, Didier Ferrand, Décio Ferreira, Mirek Golebiowski, Jenny E. Greene, Johannes Gross, James E. Gunn, Randolph Hammond, Albert Harding, Murdock Hart, Timothy M. Heckman, Christopher M. Hirata, Paul Ho, Stephen C. Hope, Larry Hovland, Shu-Fu Hsu, Yen-Shan Hu, Ping-Jie Huang, Marc Jaquet, Yipeng Jing, Jennifer Karr, Masahiko Kimura, Matthew E. King, Eiichiro Komatsu, Vincent Le Brun, Olivier Le Fèvre, Arnaud Le Fur, David Le Mignant, Hung-Hsu Ling, Craig P. Loomis, Robert H. Lupton, Fabrice Madec, Peter Mao, Lucas S. Marrara, Claudia Mendes de Oliveira, Yosuke Minowa, Chaz Morantz, Hitoshi Murayama, Graham J. Murray, Youichi Ohyama, Joseph Orndorff, Sandrine Pascal, Jefferson M. Pereira, Daniel Reiley, Martin Reinecke, Andreas Ritter, Mitsuko Roberts, Mark A. Schwochert, Michael D. Seiffert, Stephen A. Smee, Laerte Sodre, David N. Spergel, Aaron J. Steinkraus, Michael A. Strauss, Christian

Surace, Yasushi Suto, Nao Suzuki, John Swinbank, Philip J. Tait, Masahiro Takada, Tomonori Tamura, Yoko Tanaka, Laurence Tresse, Orlando Verducci, Didier Vibert, Clement Vidal, Shiang-Yu Wang, Chih-Yi Wen, Chi-Hung Yan, and Naoki Yasuda, *Prime Focus Spectrograph (PFS) for the Subaru telescope: overview, recent progress, and future perspectives*, Ground-based and Airborne Instrumentation for Astronomy VI (Christopher J. Evans, Luc Simard, and Hideki Takami, eds.), Society of Photo-Optical Instrumentation Engineers (SPIE) Conference Series, vol. 9908, August 2016, p. 99081M.

[109] Brad W. Lyke, Alexandra N. Higley, J. N. McLane, Danielle P. Schurhammer, Adam D. Myers, Ashley J. Ross, Kyle Dawson, Solène Chabanier, Paul Martini, Nicolás G. Busca, Hélion du Mas des Bourboux, Mara Salvato, Alina Streblyanska, Pauline Zarrouk, Etienne Burtin, Scott F. Anderson, Julian Bautista, Dmitry Bizyaev, W. N. Brandt, Jonathan Brinkmann, Joel R. Brownstein, Johan Comparat, Paul Green, Axel de la Macorra, Andrea Muñoz Gutiérrez, Jiamin Hou, Jeffrey A. Newman, Nathalie Palanque-Delabrouille, Isabelle Pâris, Will J. Percival, Patrick Petitjean, James Rich, Graziano Rossi, Donald P. Schneider, Alexander Smith, M. Vivek, and Benjamin Alan Weaver, *The Sloan Digital Sky Survey Quasar Catalog: Sixteenth Data Release*, 250 (2020), no. 1, 8.

[110] Andreu Font-Ribera, Eduard Arnau, Jordi Miralda-Escudé, Emmanuel Rollinde, J. Brinkmann, Joel R. Brownstein, Khee-Gan Lee, Adam D. Myers, Nathalie Palanque-Delabrouille, Isabelle Pâris, Patrick Petitjean, James Rich, Nicholas P. Ross, Donald P. Schneider, and Martin White, *The large-scale quasar-Lyman α forest cross-correlation from BOSS*, 2013 (2013), no. 5, 018.

[111] Adam S. Bolton, David J. Schlegel, Éric Aubourg, Stephen Bailey, Vaishali Bhardwaj, Joel R. Brownstein, Scott Burles, Yan-Mei Chen, Kyle Dawson, Daniel J. Eisenstein, James E. Gunn, G. R. Knapp, Craig P. Loomis, Robert H. Lupton, Claudia Maraston, Demitri Muna, Adam D. Myers, Matthew D. Olmstead, Nikhil Padmanabhan, Isabelle Pâris, Will J. Percival, Patrick Petitjean, Constance M. Rockosi, Nicholas P.

Ross, Donald P. Schneider, Yiping Shu, Michael A. Strauss, Daniel Thomas, Christy A. Tremonti, David A. Wake, Benjamin A. Weaver, and W. Michael Wood-Vasey, *Spectral Classification and Redshift Measurement for the SDSS-III Baryon Oscillation Spectroscopic Survey*, 144 (2012), no. 5, 144.

[112] Michelle Mason, Michael S. Brotherton, and Adam Myers, *Evaluating and improving the redshifts of z ¿ 2.2 quasars*, 469 (2017), no. 4, 4675–4682.

[113] Amy L. Rankine, Paul C. Hewett, Manda Banerji, and Gordon T. Richards, *BAL and non-BAL quasars: continuum, emission, and absorption properties establish a common parent sample*, 492 (2020), no. 3, 4553–4575.

[114] Angelica B. Rivera, Gordon T. Richards, Paul C. Hewett, and Amy L. Rankine, *Characterizing Quasar C IV Emission-line Measurements from Time-resolved Spectroscopy*, 899 (2020), no. 2, 96.

[115] Brandon M. Matthews, Ohad Shemmer, Cooper Dix, Michael S. Brotherton, Adam D. Myers, I. Andruchow, W. N. Brandt, Gabriel A. Ferrero, S. C. Gallagher, Richard Green, Paulina Lira, Richard M. Plotkin, Gordon T. Richards, Jessie C. Runnoe, Donald P. Schneider, Yue Shen, Michael A. Strauss, and Beverley J. Wills, *Placing High-redshift Quasars in Perspective: A Catalog of Spectroscopic Properties from the Gemini Near Infrared Spectrograph-Distant Quasar Survey*, 252 (2021), no. 2, 15.

[116] Mitchell Begelman, Martijn de Kool, and Marek Sikora, *Outflows Driven by Cosmic-Ray Pressure in Broad Absorption Line QSOs*, 382 (1991), 416.

[117] B. P. Miller, W. N. Brandt, D. P. Schneider, R. R. Gibson, A. T. Steffen, and Jianfeng Wu, *X-ray Emission from Optically Selected Radio-intermediate and Radio-loud Quasars*, 726 (2011), no. 1, 20.

[118] D.J. Sheskin, *Handbook of Parametric and Nonparametric Statistical Procedures*, Chapman & Hall 469 (2007), no. 4, 4675–4682.

[119] N. Murray, J. Chiang, S. A. Grossman, and G. M. Voit, *Accretion Disk Winds from Active Galactic Nuclei*, 451 (1995), 498.

[120] Jack W. Sulentic, Rumen Bachev, Paola Marziani, C. Alenka Negrete, and Deborah

Dultzin, *C IV λ1549 as an Eigenvector 1 Parameter for Active Galactic Nuclei*, 666 (2007), no. 2, 757–777.

[121] Yue Shen, Jenny E. Greene, Michael A. Strauss, Gordon T. Richards, and Donald P. Schneider, *Biases in Virial Black Hole Masses: An SDSS Perspective*, 680 (2008), no. 1, 169–190.

[122] Massimo Robberto, Peter W. A. Roming, Alexander J. van der Horst, María. Luisa García-Vargas, Stephen A. Smee, Stephen Goodsell, Jeffrey Radwick, Thomas Hayward, Morten Andersen, Susan Pope, Ethan E. Chaffee, Todd J. Veach, Antonina G. Brody, Kelly D. Smith, Ronnie L. Killough, Kristian B. Persson, Jason L. Stange, Amanda J. Bayless, Rebecca R. Thibodeaux, Andrew L. Peterson, Alexa K. Mathias, Carl L. Schwendeman, Adam W. Thornton, Guy A. Grubbs, Ernesto R. Verastegui, Thomas Lechner, Manuel Maldonado-Medina, Ana Pérez-Calpena, Ernesto Sánchez-Blanco, Gerardo Veredas, Ruben Diaz, Manuel Lazo, Scot Kleinman, Landon Gelman, Robert H. Barkhouser, and Stephen C. Hope, *SCORPIO: Final design and performance estimates for time-domain astronomy*, Society of Photo-Optical Instrumentation Engineers (SPIE) Conference Series, Society of Photo-Optical Instrumentation Engineers (SPIE) Conference Series, vol. 11447, December 2020, p. 1144774.

[123] Daeseong Park, Aaron J. Barth, Jong-Hak Woo, Matthew A. Malkan, Tommaso Treu, Vardha N. Bennert, Roberto J. Assef, and Anna Pancoast, *Extending the Calibration of C IV-based Single-epoch Black Hole Mass Estimators for Active Galactic Nuclei*, 839 (2017), no. 2, 93.

[124] Elena Dalla Bontà, Bradley M. Peterson, Misty C. Bentz, W. N. Brandt, S. Ciroi, Gisella De Rosa, Gloria Fonseca Alvarez, Catherine J. Grier, P. B. Hall, Juan V. Hernández Santisteban, Luis C. Ho, Y. Homayouni, Keith Horne, C. S. Kochanek, Jennifer I. Hsiu Li, L. Morelli, A. Pizzella, R. W. Pogge, D. P. Schneider, Yue Shen, J. R. Trump, and Marianne Vestergaard, *The Sloan Digital Sky Survey Reverberation Mapping Project: Estimating Masses of Black Holes in Quasars with Single-epoch Spectroscopy*, 903 (2020), no. 2, 112.

[125] Philip F. Hopkins, Brant Robertson, Elisabeth Krause, Lars Hernquist, and Thomas J. Cox, *An Upper Limit to the Degree of Evolution between Supermassive Black Holes and Their Host Galaxies*, 652 (2006), no. 1, 107–111.

[126] Zhu Chen, S. M. Faber, David C. Koo, Rachel S. Somerville, Joel R. Primack, Avishai Dekel, Aldo Rodríguez-Puebla, Yicheng Guo, Guillermo Barro, Dale D. Kocevski, A. van der Wel, Joanna Woo, Eric F. Bell, Jerome J. Fang, Henry C. Ferguson, Mauro Giavalisco, Marc Huertas-Company, Fangzhou Jiang, Susan Kassin, Lin Lin, F. S. Liu, Yifei Luo, Zhijian Luo, Camilla Pacifici, Viraj Pandya, Samir Salim, Chenggang Shu, Sandro Tacchella, Bryan A. Terrazas, and Hassen M. Yesuf, *Quenching as a Contest between Galaxy Halos and Their Central Black Holes*, 897 (2020), no. 1, 102.

[127] Hyewon Suh, Francesca Civano, Benny Trakhtenbrot, Francesco Shankar, Günther Hasinger, David B. Sanders, and Viola Allevato, *No Significant Evolution of Relations between Black Hole Mass and Galaxy Total Stellar Mass Up to $z \sim 2.5$*, 889 (2020), no. 1, 32.

[128] Jenny E. Greene and Luis C. Ho, *Estimating Black Hole Masses in Active Galaxies Using the Hα Emission Line*, 630 (2005), no. 1, 122–129.

[129] Kayhan Gültekin, Douglas O. Richstone, Karl Gebhardt, Tod R. Lauer, Scott Tremaine, M. C. Aller, Ralf Bender, Alan Dressler, S. M. Faber, Alexei V. Filippenko, Richard Green, Luis C. Ho, John Kormendy, John Magorrian, Jason Pinkney, and Christos Siopis, *The M-σ and M-L Relations in Galactic Bulges, and Determinations of Their Intrinsic Scatter*, 698 (2009), no. 1, 198–221.

[130] Jenny E. Greene, Chien Y. Peng, Minjin Kim, Cheng-Yu Kuo, James A. Braatz, C. M. V. Impellizzeri, James J. Condon, K. Y. Lo, Christian Henkel, and Mark J. Reid, *Precise Black Hole Masses from Megamaser Disks: Black Hole-Bulge Relations at Low Mass*, 721 (2010), no. 1, 26–45.

[131] Yue Shen, W. N. Brandt, Kyle S. Dawson, Patrick B. Hall, Ian D. McGreer, Scott F. Anderson, Yuguang Chen, Kelly D. Denney, Sarah Eftekharzadeh, Xiaohui Fan, Yang Gao, Paul J. Green, Jenny E. Greene, Luis C. Ho, Keith Horne, Linhua Jiang, Bran-

don C. Kelly, Karen Kinemuchi, Christopher S. Kochanek, Isabelle Pâris, Christina M. Peters, Bradley M. Peterson, Patrick Petitjean, Kara Ponder, Gordon T. Richards, Donald P. Schneider, Anil Seth, Robyn N. Smith, Michael A. Strauss, Charling Tao, Jonathan R. Trump, W. M. Wood-Vasey, Ying Zu, Daniel J. Eisenstein, Kaike Pan, Dmitry Bizyaev, Viktor Malanushenko, Elena Malanushenko, and Daniel Oravetz, *The Sloan Digital Sky Survey Reverberation Mapping Project: Technical Overview*, 216 (2015), no. 1, 4.

[132] C. J. Grier, Yue Shen, Keith Horne, W. N. Brandt, J. R. Trump, P. B. Hall, K. Kinemuchi, David Starkey, D. P. Schneider, Luis C. Ho, Y. Homayouni, Jennifer I-Hsiu Li, Ian D. McGreer, B. M. Peterson, Dmitry Bizyaev, Yuguang Chen, K. S. Dawson, Sarah Eftekharzadeh, Yucheng Guo, Siyao Jia, Linhua Jiang, Jean-Paul Kneib, Feng Li, Zefeng Li, Jundan Nie, Audrey Oravetz, Daniel Oravetz, Kaike Pan, Patrick Petitjean, Kara A. Ponder, Jesse Rogerson, M. Vivek, Tianmeng Zhang, and Hu Zou, *The Sloan Digital Sky Survey Reverberation Mapping Project: Initial C IV Lag Results from Four Years of Data*, 887 (2019), no. 1, 38.

[133] GRAVITY Collaboration, R. Abuter, N. Aimar, A. Amorim, J. Ball, M. Bauböck, J. P. Berger, H. Bonnet, G. Bourdarot, W. Brandner, V. Cardoso, Y. Clénet, Y. Dallilar, R. Davies, P. T. de Zeeuw, J. Dexter, A. Drescher, F. Eisenhauer, N. M. Förster Schreiber, A. Foschi, P. Garcia, F. Gao, E. Gendron, R. Genzel, S. Gillessen, M. Habibi, X. Haubois, G. Heißel, T. Henning, S. Hippler, M. Horrobin, L. Jochum, L. Jocou, A. Kaufer, P. Kervella, S. Lacour, V. Lapeyrère, J. B. Le Bouquin, P. Léna, D. Lutz, T. Ott, T. Paumard, K. Perraut, G. Perrin, O. Pfuhl, S. Rabien, J. Shangguan, T. Shimizu, S. Scheithauer, J. Stadler, A. W. Stephens, O. Straub, C. Straubmeier, E. Sturm, L. J. Tacconi, K. R. W. Tristram, F. Vincent, S. von Fellenberg, F. Widmann, E. Wieprecht, E. Wiezorrek, J. Woillez, S. Yazici, and A. Young, *Mass distribution in the Galactic Center based on interferometric astrometry of multiple stellar orbits*, 657 (2022), L12.

[134] Brandon C. Kelly, Marianne Vestergaard, Xiaohui Fan, Philip Hopkins, Lars Hern-

quist, and Aneta Siemiginowska, *Constraints on Black Hole Growth, Quasar Lifetimes, and Eddington Ratio Distributions from the SDSS Broad-line Quasar Black Hole Mass Function*, 719 (2010), no. 2, 1315–1334.

[135] Brandon C. Kelly and Andrea Merloni, *Mass Functions of Supermassive Black Holes across Cosmic Time*, Advances in Astronomy 2012 (2012), 970858.

[136] Yue Shen and Brandon C. Kelly, *The Demographics of Broad-line Quasars in the Mass-Luminosity Plane. I. Testing FWHM-based Virial Black Hole Masses*, 746 (2012), no. 2, 169.

[137] A. Wandel, *The Black Hole-to-Bulge Mass Relation in Active Galactic Nuclei*, 519 (1999), no. 1, L39–L42.

[138] R. D. Blandford and C. F. McKee, *Reverberation mapping of the emission line regions of Seyfert galaxies and quasars.*, 255 (1982), 419–439.

[139] Bradley M. Peterson, *Reverberation Mapping of Active Galactic Nuclei*, 105 (1993), 247.

[140] Anna Pancoast, Brendon J. Brewer, Tommaso Treu, Daeseong Park, Aaron J. Barth, Misty C. Bentz, and Jong-Hak Woo, *Modelling reverberation mapping data - II. Dynamical modelling of the Lick AGN Monitoring Project 2008 data set*, 445 (2014), no. 3, 3073–3091.

[141] Aaron J. Barth, Vardha N. Bennert, Gabriela Canalizo, Alexei V. Filippenko, Elinor L. Gates, Jenny E. Greene, Weidong Li, Matthew A. Malkan, Anna Pancoast, David J. Sand, Daniel Stern, Tommaso Treu, Jong-Hak Woo, Roberto J. Assef, Hyun-Jin Bae, Brendon J. Brewer, S. Bradley Cenko, Kelsey I. Clubb, Michael C. Cooper, Aleksandar M. Diamond-Stanic, Kyle D. Hiner, Sebastian F. Hönig, Eric Hsiao, Michael T. Kandrashoff, Mariana S. Lazarova, A. M. Nierenberg, Jacob Rex, Jeffrey M. Silverman, Erik J. Tollerud, and Jonelle L. Walsh, *The Lick AGN Monitoring Project 2011: Spectroscopic Campaign and Emission-line Light Curves*, 217 (2015), no. 2, 26.

[142] Misty C. Bentz and Sarah Katz, *The AGN Black Hole Mass Database*, 127 (2015), no. 947, 67.

[143] C. J. Grier, J. R. Trump, Yue Shen, Keith Horne, Karen Kinemuchi, Ian D. McGreer, D. A. Starkey, W. N. Brandt, P. B. Hall, C. S. Kochanek, Yuguang Chen, K. D. Denney, Jenny E. Greene, L. C. Ho, Y. Homayouni, Jennifer I-Hsiu Li, Liuyi Pei, B. M. Peterson, P. Petitjean, D. P. Schneider, Mouyuan Sun, Yusura AlSayyad, Dmitry Bizyaev, Jonathan Brinkmann, Joel R. Brownstein, Kevin Bundy, K. S. Dawson, Sarah Eftekharzadeh, J. G. Fernandez-Trincado, Yang Gao, Timothy A. Hutchinson, Siyao Jia, Linhua Jiang, Daniel Oravetz, Kaike Pan, Isabelle Paris, Kara A. Ponder, Christina Peters, Jesse Rogerson, Audrey Simmons, Robyn Smith, and Ran Wang, *The Sloan Digital Sky Survey Reverberation Mapping Project: Hα and Hβ Reverberation Measurements from First-year Spectroscopy and Photometry*, 851 (2017), no. 1, 21.

[144] Pu Du, Zhi-Xiang Zhang, Kai Wang, Ying-Ke Huang, Yue Zhang, Kai-Xing Lu, Chen Hu, Yan-Rong Li, Jin-Ming Bai, Wei-Hao Bian, Ye-Fei Yuan, Luis C. Ho, Jian-Min Wang, and SEAMBH Collaboration, *Supermassive Black Holes with High Accretion Rates in Active Galactic Nuclei. IX. 10 New Observations of Reverberation Mapping and Shortened Hβ Lags*, 856 (2018), no. 1, 6.

[145] Ari Laor, *On Quasar Masses and Quasar Host Galaxies*, 505 (1998), no. 2, L83–L86.

[146] Shai Kaspi, Paul S. Smith, Hagai Netzer, Dan Maoz, Buell T. Jannuzi, and Uriel Giveon, *Reverberation Measurements for 17 Quasars and the Size-Mass-Luminosity Relations in Active Galactic Nuclei*, 533 (2000), no. 2, 631–649.

[147] Shai Kaspi, Dan Maoz, Hagai Netzer, Bradley M. Peterson, Marianne Vestergaard, and Buell T. Jannuzi, *The Relationship between Luminosity and Broad-Line Region Size in Active Galactic Nuclei*, 629 (2005), no. 1, 61–71.

[148] Misty C. Bentz, Bradley M. Peterson, Hagai Netzer, Richard W. Pogge, and Marianne Vestergaard, *The Radius-Luminosity Relationship for Active Galactic Nuclei: The Effect of Host-Galaxy Starlight on Luminosity Measurements. II. The Full Sample of Reverberation-Mapped AGNs*, 697 (2009), no. 1, 160–181.

[149] Misty C. Bentz, Kelly D. Denney, Catherine J. Grier, Aaron J. Barth, Bradley M.

Peterson, Marianne Vestergaard, Vardha N. Bennert, Gabriela Canalizo, Gisella De Rosa, Alexei V. Filippenko, Elinor L. Gates, Jenny E. Greene, Weidong Li, Matthew A. Malkan, Richard W. Pogge, Daniel Stern, Tommaso Treu, and Jong-Hak Woo, *The Low-luminosity End of the Radius-Luminosity Relationship for Active Galactic Nuclei*, 767 (2013), no. 2, 149.

[150] Marianne Vestergaard and Bradley M. Peterson, *Determining Central Black Hole Masses in Distant Active Galaxies and Quasars. II. Improved Optical and UV Scaling Relationships*, 641 (2006), no. 2, 689–709.

[151] Suvendu Rakshit, C. S. Stalin, and Jari Kotilainen, *Spectral Properties of Quasars from Sloan Digital Sky Survey Data Release 14: The Catalog*, 249 (2020), no. 1, 17.

[152] Qiaoya Wu and Yue Shen, *A Catalog of Quasar Properties from Sloan Digital Sky Survey Data Release 16*, 263 (2022), no. 2, 42.

[153] Gloria Fonseca Alvarez, Jonathan R. Trump, Y. Homayouni, C. J. Grier, Yue Shen, Keith Horne, Jennifer I. Hsiu Li, W. N. Brandt, Luis C. Ho, B. M. Peterson, and D. P. Schneider, *The Sloan Digital Sky Survey Reverberation Mapping Project: The Hβ Radius-Luminosity Relation*, 899 (2020), no. 1, 73.

[154] Ross J. McLure and James S. Dunlop, *The cosmological evolution of quasar black hole masses*, 352 (2004), no. 4, 1390–1404.

[155] M. Vestergaard and Patrick S. Osmer, *Mass Functions of the Active Black Holes in Distant Quasars from the Large Bright Quasar Survey, the Bright Quasar Survey, and the Color-selected Sample of the SDSS Fall Equatorial Stripe*, 699 (2009), no. 1, 800–816.

[156] Jong-Hak Woo, Huynh Anh N. Le, Marios Karouzos, Dawoo Park, Daeseong Park, Matthew A. Malkan, Tommaso Treu, and Vardha N. Bennert, *Calibration and Limitations of the Mg II Line-based Black Hole Masses*, 859 (2018), no. 2, 138.

[157] Huynh Anh N. Le, Jong-Hak Woo, and Yongquan Xue, *Calibrating Mg II-based Black Hole Mass Estimators Using Low-to-high-luminosity Active Galactic Nuclei*, 901 (2020), no. 1, 35.

[158] R. J. Assef, K. D. Denney, C. S. Kochanek, B. M. Peterson, S. Kozłowski, N. Ageorges, R. S. Barrows, P. Buschkamp, M. Dietrich, E. Falco, C. Feiz, H. Gemperlein, A. Germeroth, C. J. Grier, R. Hofmann, M. Juette, R. Khan, M. Kilic, V. Knierim, W. Laun, R. Lederer, M. Lehmitz, R. Lenzen, U. Mall, K. K. Madsen, H. Mandel, P. Martini, S. Mathur, K. Mogren, P. Mueller, V. Naranjo, A. Pasquali, K. Polsterer, R. W. Pogge, A. Quirrenbach, W. Seifert, D. Stern, B. Shappee, C. Storz, J. Van Saders, P. Weiser, and D. Zhang, *Black Hole Mass Estimates Based on C IV are Consistent with Those Based on the Balmer Lines*, 742 (2011), no. 2, 93.

[159] Jessie C. Runnoe, R. Ganguly, M. S. Brotherton, and M. A. DiPompeo, *Rest-frame optical properties of luminous, radio-selected broad absorption line quasars*, 433 (2013), no. 2, 1778–1788.

[160] Michael S. Brotherton, J. C. Runnoe, Zhaohui Shang, and M. A. DiPompeo, *Bias in C IV-based quasar black hole mass scaling relationships from reverberation mapped samples*, 451 (2015), no. 2, 1290–1298.

[161] Mouyuan Sun, Yongquan Xue, Gordon T. Richards, Jonathan R. Trump, Yue Shen, W. N. Brandt, and D. P. Schneider, *The Sloan Digital Sky Survey Reverberation Mapping Project: The C IV Blueshift, Its Variability, and Its Dependence Upon Quasar Properties*, 854 (2018), no. 2, 128.

[162] E. M. Cackett, K. Gültekin, M. C. Bentz, M. M. Fausnaugh, B. M. Peterson, J. Troyer, and M. Vestergaard, *Swift/UVOT Grism Monitoring of NGC 5548 in 2013: An Attempt at MgII Reverberation Mapping*, 810 (2015), no. 2, 86.

[163] Paulina Lira, Shai Kaspi, Hagai Netzer, Ismael Botti, Nidia Morrell, Julián Mejía-Restrepo, Paula Sánchez-Sáez, Jorge Martínez-Palomera, and Paula López, *Reverberation Mapping of Luminous Quasars at High z*, 865 (2018), no. 1, 56.

[164] J. K. Hoormann, P. Martini, T. M. Davis, A. King, C. Lidman, D. Mudd, R. Sharp, N. E. Sommer, B. E. Tucker, Z. Yu, S. Allam, J. Asorey, S. Avila, M. Banerji, D. Brooks, E. Buckley-Geer, D. L. Burke, J. Calcino, A. Carnero Rosell, D. Carollo, M. Carrasco Kind, J. Carretero, F. J. Castander, M. Childress, J. De Vicente,

S. Desai, H. T. Diehl, P. Doel, B. Flaugher, P. Fosalba, J. Frieman, J. García-Bellido, D. W. Gerdes, D. Gruen, G. Gutierrez, W. G. Hartley, S. R. Hinton, D. L. Hollowood, K. Honscheid, B. Hoyle, D. J. James, E. Krause, K. Kuehn, N. Kuropatkin, G. F. Lewis, M. Lima, E. Macaulay, M. A. G. Maia, F. Menanteau, C. J. Miller, R. Miquel, A. Möller, A. A. Plazas, A. K. Romer, A. Roodman, E. Sanchez, V. Scarpine, M. Schubnell, S. Serrano, I. Sevilla-Noarbe, M. Smith, R. C. Smith, M. Soares-Santos, F. Sobreira, E. Suchyta, E. Swann, M. E. C. Swanson, G. Tarle, S. A. Uddin, and DES Collaboration, *C IV black hole mass measurements with the Australian Dark Energy Survey (OzDES)*, 487 (2019), no. 3, 3650–3663.

[165] Y. Homayouni, Jonathan R. Trump, C. J. Grier, Keith Horne, Yue Shen, W. N. Brandt, Kyle S. Dawson, Gloria Fonseca Alvarez, Paul J. Green, P. B. Hall, Juan V. Hernández Santisteban, Luis C. Ho, Karen Kinemuchi, C. S. Kochanek, Jennifer I. Hsiu Li, B. M. Peterson, D. P. Schneider, D. A. Starkey, Dmitry Bizyaev, Kaike Pan, Daniel Oravetz, and Audrey Simmons, *The Sloan Digital Sky Survey Reverberation Mapping Project: Mg II Lag Results from Four Years of Monitoring*, 901 (2020), no. 1, 55.

[166] Shai Kaspi, W. N. Brandt, Dan Maoz, Hagai Netzer, Donald P. Schneider, Ohad Shemmer, and C. J. Grier, *Taking a Long Look: A Two-decade Reverberation Mapping Study of High-luminosity Quasars*, 915 (2021), no. 2, 129.

[167] Alexei Baskin and Ari Laor, *What controls the CIV line profile in active galactic nuclei?*, 356 (2005), no. 3, 1029–1044.

[168] Pu Du and Jian-Min Wang, *The Radius-Luminosity Relationship Depends on Optical Spectra in Active Galactic Nuclei*, 886 (2019), no. 1, 42.

[169] Jaya Maithil, Michael S. Brotherton, Ohad Shemmer, Pu Du, Jian-Min Wang, Adam D. Myers, Jacob N. McLane, Cooper Dix, and Brandon M. Matthews, *Systematically smaller single-epoch quasar black hole masses using a radius-luminosity relationship corrected for spectral bias*, 515 (2022), no. 1, 491–506.

[170] D. O. Richstone and M. Schmidt, *The spectral properties of a large sample of quasars.*, 235 (1980), 361–376.

[171] Luis C. Ho and Minjin Kim, *The Black Hole Mass Scale of Classical and Pseudo Bulges in Active Galaxies*, 789 (2014), no. 1, 17.

[172] Li-Ming Yu, Wei-Hao Bian, Chan Wang, Bi-Xuan Zhao, and Xue Ge, *Calibration of the virial factor f in supermassive black hole masses of reverberation-mapped AGNs*, 488 (2019), no. 2, 1519–1534.

[173] J. E. Mejía-Restrepo, B. Trakhtenbrot, P. Lira, and H. Netzer, *Can we improve C IV-based single-epoch black hole mass estimations?*, 478 (2018), no. 2, 1929–1941.

[174] Li-Ming Yu, Bi-Xuan Zhao, Wei-Hao Bian, Chan Wang, and Xue Ge, *An extended size-luminosity relation for the reverberation-mapped AGNs: the role of the accretion rate*, 491 (2020), no. 4, 5881–5896.

[175] Christopher A. Onken, Laura Ferrarese, David Merritt, Bradley M. Peterson, Richard W. Pogge, Marianne Vestergaard, and Amri Wandel, *Supermassive Black Holes in Active Galactic Nuclei. II. Calibration of the Black Hole Mass-Velocity Dispersion Relationship for Active Galactic Nuclei*, 615 (2004), no. 2, 645–651.

[176] Jong-Hak Woo, Yosep Yoon, Songyoun Park, Daeseong Park, and Sang Chul Kim, *The Black Hole Mass-Stellar Velocity Dispersion Relation of Narrow-line Seyfert 1 Galaxies*, 801 (2015), no. 1, 38.

[177] Ohad Shemmer and Sara Lieber, *Weak Emission-line Quasars in the Context of a Modified Baldwin Effect*, 805 (2015), no. 2, 124.

[178] Brandon C. Kelly, *Some Aspects of Measurement Error in Linear Regression of Astronomical Data*, 665 (2007), no. 2, 1489–1506.

[179] *Co-evolution of Central Black Holes and Galaxies*, vol. 267, August 2010.

[180] M. Vestergaard, K. Denney, X. Fan, J. J. Jensen, B. C. Kelly, P. S. Osmer, B. M. Peterson, and C. A. Tremonti, *Black hole mass estimations: limitations and uncertainties*, Narrow-Line Seyfert 1 Galaxies and their Place in the Universe (L. Foschini, M. Colpi, L. Gallo, D. Grupe, S. Komossa, K. Leighly, and S. Mathur, eds.), January 2011, p. 38.

[181] Yue Shen, *The mass of quasars*, Bulletin of the Astronomical Society of India 41 (2013), no. 1, 61–115.

[182] Xiaohui Fan, Michael A. Strauss, James E. Gunn, Robert H. Lupton, C. L. Carilli, M. P. Rupen, Gary D. Schmidt, Leonidas A. Moustakas, Marc Davis, James Annis, Neta A. Bahcall, J. Brinkmann, Robert J. Brunner, István Csabai, Mamoru Doi, Masataka Fukugita, Timothy M. Heckman, G. S. Hennessy, Robert B. Hindsley, Željko Ivezić , G. R. Knapp, D. Q. Lamb, Jeffrey A. Munn, A. George Pauls, Jeffrey R. Pier, Constance M. Rockosi, Donald P. Schneider, Alexander S. Szalay, Douglas L. Tucker, and Donald G. York, *The Discovery of a High-Redshift Quasar without Emission Lines from Sloan Digital Sky Survey Commissioning Data*, 526 (1999), no. 2, L57–L60.

[183] Scott F. Anderson, Xiaohui Fan, Gordon T. Richards, Donald P. Schneider, Michael A. Strauss, Daniel E. Vanden Berk, James E. Gunn, Gillian R. Knapp, David Schlegel, Wolfgang Voges, Brian Yanny, Neta A. Bahcall, Mariangela Bernardi, J. Brinkmann, Robert Brunner, Istvan Csabái, Mamoru Doi, Masataka Fukugita, G. S. Hennessy, Željko Ivezić, Peter Z. Kunszt, Donald Q. Lamb, Jon Loveday, Robert H. Lupton, Timothy A. McKay, Jeffrey A. Munn, R. C. Nichol, G. P. Szokoly, and Donald G. York, *High-Redshift Quasars Found in Sloan Digital Sky Survey Commissioning Data. VI. Sloan Digital Sky Survey Spectrograph Observations*, 122 (2001), no. 2, 503–517.

[184] Matthew J. Collinge, Michael A. Strauss, Patrick B. Hall, Željko Ivezić, Jeffrey A. Munn, David J. Schlegel, Nadia L. Zakamska, Scott F. Anderson, Hugh C. Harris, Gordon T. Richards, Donald P. Schneider, Wolfgang Voges, Donald G. York, Bruce Margon, and J. Brinkmann, *Optically Identified BL Lacertae Objects from the Sloan Digital Sky Survey*, 129 (2005), no. 6, 2542–2561.

[185] Richard M. Plotkin, Scott F. Anderson, W. N. Brandt, Aleksandar M. Diamond-Stanic, Xiaohui Fan, Patrick B. Hall, Amy E. Kimball, Michael W. Richmond, Donald P. Schneider, Ohad Shemmer, Wolfgang Voges, Donald G. York, Neta A. Bahcall, Stephanie Snedden, Dmitry Bizyaev, Howard Brewington, Viktor Malanushenko, Elena Malanushenko, Dan Oravetz, Kaike Pan, and Audrey Simmons, *Optically Se-*

lected BL Lacertae Candidates from the Sloan Digital Sky Survey Data Release Seven, 139 (2010), no. 2, 390–414.

[186] Aleksandar M. Diamond-Stanic, Xiaohui Fan, W. N. Brandt, Ohad Shemmer, Michael A. Strauss, Scott F. Anderson, Christopher L. Carilli, Robert R. Gibson, Linhua Jiang, J. Serena Kim, Gordon T. Richards, Gary D. Schmidt, Donald P. Schneider, Yue Shen, Paul S. Smith, Marianne Vestergaard, and Jason E. Young, *High-redshift SDSS Quasars with Weak Emission Lines*, 699 (2009), no. 1, 782–799.

[187] H. Meusinger and N. Balafkan, *A large sample of Kohonen-selected SDSS quasars with weak emission lines: selection effects and statistical properties*, 568 (2014), A114.

[188] Jianfeng Wu, W. N. Brandt, Scott F. Anderson, Aleksandar M. Diamond-Stanic, Patrick B. Hall, Richard M. Plotkin, Donald P. Schneider, and Ohad Shemmer, *X-Ray and Multiwavelength Insights into the Nature of Weak Emission-line Quasars at Low Redshift*, 747 (2012), no. 1, 10.

[189] E. Bañados, B. P. Venemans, R. Decarli, E. P. Farina, C. Mazzucchelli, F. Walter, X. Fan, D. Stern, E. Schlafly, K. C. Chambers, H. W. Rix, L. Jiang, I. McGreer, R. Simcoe, F. Wang, J. Yang, E. Morganson, G. De Rosa, J. Greiner, M. Baloković, W. S. Burgett, T. Cooper, P. W. Draper, H. Flewelling, K. W. Hodapp, H. D. Jun, N. Kaiser, R. P. Kudritzki, E. A. Magnier, N. Metcalfe, D. Miller, J. T. Schindler, J. L. Tonry, R. J. Wainscoat, C. Waters, and Q. Yang, *The Pan-STARRS1 Distant z ¿ 5.6 Quasar Survey: More than 100 Quasars within the First Gyr of the Universe*, 227 (2016), no. 1, 11.

[190] Ohad Shemmer, W. N. Brandt, Donald P. Schneider, Xiaohui Fan, Michael A. Strauss, Aleksandar M. Diamond-Stanic, Gordon T. Richards, Scott F. Anderson, James E. Gunn, and Jon Brinkmann, *Chandra Observations of the Highest Redshift Quasars from the Sloan Digital Sky Survey*, 644 (2006), no. 1, 86–99.

[191] Ohad Shemmer, Benny Trakhtenbrot, Scott F. Anderson, W. N. Brandt, Aleksandar M. Diamond-Stanic, Xiaohui Fan, Paulina Lira, Hagai Netzer, Richard M. Plotkin, Gordon T. Richards, Donald P. Schneider, and Michael A. Strauss, *Weak Line Quasars*

at High Redshift: Extremely High Accretion Rates or Anemic Broad-line Regions?, 722 (2010), no. 2, L152–L156.

[192] Ohad Shemmer, W. N. Brandt, Scott F. Anderson, Aleksandar M. Diamond-Stanic, Xiaohui Fan, Gordon T. Richards, Donald P. Schneider, and Michael A. Strauss, *X-Ray Insights into the Nature of Weak Emission-Line Quasars at High Redshift*, 696 (2009), no. 1, 580–590.

[193] Ryan A. Lane, Ohad Shemmer, Aleksandar M. Diamond-Stanic, Xiaohui Fan, Scott F. Anderson, W. N. Brandt, Richard M. Plotkin, Gordon T. Richards, Donald P. Schneider, and Michael A. Strauss, *The Ultraviolet-to-mid-infrared Spectral Energy Distribution of Weak Emission Line Quasars*, 743 (2011), no. 2, 163.

[194] F. Massaro, E. J. Marchesini, R. D'Abrusco, N. Masetti, I. Andruchow, and Howard A. Smith, *Radio-weak BL Lac Objects in the Fermi Era*, 834 (2017), no. 2, 113.

[195] B. Luo, W. N. Brandt, P. B. Hall, Jianfeng Wu, S. F. Anderson, G. P. Garmire, R. R. Gibson, R. M. Plotkin, G. T. Richards, D. P. Schneider, O. Shemmer, and Yue Shen, *X-ray Insights into the Nature of PHL 1811 Analogs and Weak Emission-line Quasars: Unification with a Geometrically Thick Accretion Disk?*, 805 (2015), no. 2, 122.

[196] Q. Ni, W. N. Brandt, B. Luo, P. B. Hall, Yue Shen, S. F. Anderson, R. M. Plotkin, Gordon T. Richards, D. P. Schneider, O. Shemmer, and Jianfeng Wu, *Connecting the X-ray properties of weak-line and typical quasars: testing for a geometrically thick accretion disk*, 480 (2018), no. 4, 5184–5202.

[197] John D. Timlin, W. N. Brandt, Q. Ni, B. Luo, Xingting Pu, D. P. Schneider, M. Vivek, and W. Yi, *The correlations between optical/UV broad lines and X-ray emission for a large sample of quasars*, 492 (2020), no. 1, 719–741.

[198] Q. Ni, W. N. Brandt, B. Luo, G. P. Garmire, P. B. Hall, R. M. Plotkin, O. Shemmer, J. D. Timlin, F. Vito, J. Wu, and W. Yi, *Sensitive Chandra coverage of a representative sample of weak-line quasars: revealing the full range of X-ray properties*, 511 (2022), no. 4, 5251–5264.

[199] Jianfeng Wu, W. N. Brandt, Patrick B. Hall, Robert R. Gibson, Gordon T. Richards,

Donald P. Schneider, Ohad Shemmer, Dennis W. Just, and Sarah J. Schmidt, *A Population of X-Ray Weak Quasars: PHL 1811 Analogs at High Redshift*, 736 (2011), no. 1, 28.

[200] Ohad Shemmer, W. N. Brandt, Hagai Netzer, Roberto Maiolino, and Shai Kaspi, *The Hard X-Ray Spectrum as a Probe for Black Hole Growth in Radio-Quiet Active Galactic Nuclei*, 682 (2008), no. 1, 81–93.

[201] Andrea Marlar, Ohad Shemmer, S. F. Anderson, W. N. Brandt, A. M. Diamond-Stanic, X. Fan, B. Luo, R. M. Plotkin, Gordon T. Richards, D. P. Schneider, and Jianfeng Wu, *Steep Hard-X-Ray Spectra Indicate Extremely High Accretion Rates in Weak Emission-line Quasars*, 865 (2018), no. 2, 92.

[202] Jack A. Baldwin, *Luminosity Indicators in the Spectra of Quasi-Stellar Objects*, 214 (1977), 679–684.

[203] Alexei Baskin and Ari Laor, *On the origin of the C IV Baldwin effect in active galactic nuclei*, 350 (2004), no. 2, L31–L35.

[204] Xiao-Bo Dong, Ting-Gui Wang, Jian-Guo Wang, Xiaohui Fan, Huiyuan Wang, Hongyan Zhou, and Weimin Yuan, *Eddington Ratio Governs the Equivalent Width of Mg II Emission Line in Active Galactic Nuclei*, 703 (2009), no. 1, L1–L5.

[205] Yongjiang Wang, Wanqing Liu, Zhaohui Shang, and Michael S. Brotherton, *Comparison of the active galactic nuclei Baldwin effect with the modified Baldwin effect of the ultraviolet-optical emission lines in a single sample*, 515 (2022), no. 4, 5836–5846.

[206] M. L. Martínez-Aldama, A. del Olmo, P. Marziani, J. W. Sulentic, C. A. Negrete, D. Dultzin, M. D'Onofrio, and J. Perea, *Extreme quasars at high redshift*, 618 (2018), A179.

[207] Angelica B. Rivera, Gordon T. Richards, Sarah C. Gallagher, Trevor V. McCaffrey, Amy L. Rankine, Paul C. Hewett, and Ohad Shemmer, *Exploring Changes in Quasar Spectral Energy Distributions across C IV Parameter Space*, 931 (2022), no. 2, 154.

[208] D. V. McCaffrey and G. T. Richards, *C IV Distance.*, GitHub repository (2021).

[209] Richard M. Plotkin, Ohad Shemmer, Benny Trakhtenbrot, Scott F. Anderson, W. N.

Brandt, Xiaohui Fan, Elena Gallo, Paulina Lira, Bin Luo, Gordon T. Richards, Donald P. Schneider, Michael A. Strauss, and Jianfeng Wu, *Detection of Rest-frame Optical Lines from X-shooter Spectroscopy of Weak Emission Line Quasars*, 805 (2015), no. 2, 123.

[210] K. Hryniewicz, B. Czerny, M. Nikołajuk, and J. Kuraszkiewicz, *SDSS J094533.99+100950.1 - the remarkable weak emission line quasar*, 404 (2010), no. 4, 2028–2036.

[211] D. W. Just, W. N. Brandt, O. Shemmer, A. T. Steffen, D. P. Schneider, G. Chartas, and G. P. Garmire, *The X-Ray Properties of the Most Luminous Quasars from the Sloan Digital Sky Survey*, 665 (2007), no. 2, 1004–1022.

[212] Karen M. Leighly, Jules P. Halpern, Edward B. Jenkins, and Darrin Casebeer, *The Intrinsically X-Ray-weak Quasar PHL 1811. II. Optical and UV Spectra and Analysis*, 173 (2007), no. 1, 1–36.

[213] A. Wandel, B. M. Peterson, and M. A. Malkan, *Central Masses and Broad-Line Region Sizes of Active Galactic Nuclei. I. Comparing the Photoionization and Reverberation Techniques*, 526 (1999), no. 2, 579–591.

[214] A. Robinson, *The LAG Spectroscopic Monitoring Campaign: an Overview*, Reverberation Mapping of the Broad-Line Region in Active Galactic Nuclei (P. M. Gondhalekar, K. Horne, and B. M. Peterson, eds.), Astronomical Society of the Pacific Conference Series, vol. 69, January 1994, p. 147.

[215] Yue Shen and Luis C. Ho, *The diversity of quasars unified by accretion and orientation*, $\mathrm{nat}\,513(2014), no.\ 7517, 210--213$.

[216] Pu Du, Chen Hu, Kai-Xing Lu, Fang Wang, Jie Qiu, Yan-Rong Li, Jin-Ming Bai, Shai Kaspi, Hagai Netzer, Jian-Min Wang, and SEAMBH Collaboration, *Supermassive Black Holes with High Accretion Rates in Active Galactic Nuclei. I. First Results from a New Reverberation Mapping Campaign*, 782 (2014), no. 1, 45.

[217] Pu Du, Jian-Min Wang, Chen Hu, Luis C. Ho, Yan-Rong Li, and Jin-Ming Bai, *The*

Fundamental Plane of the Broad-line Region in Active Galactic Nuclei, 818 (2016), no. 1, L14.

[218] Li-Ming Yu, Wei-Hao Bian, Xue-Guang Zhang, Bi-Xuan Zhao, Chan Wang, Xue Ge, Bing-Qian Zhu, and Yu-Qin Chen, *The Supermassive Black Hole Masses of Reverberation-mapped Active Galactic Nuclei*, 901 (2020), no. 2, 133.

[219] A. Marconi, G. Risaliti, R. Gilli, L. K. Hunt, R. Maiolino, and M. Salvati, *Local supermassive black holes, relics of active galactic nuclei and the X-ray background*, 351 (2004), no. 1, 169–185.

[220] Gordon T. Richards, Mark Lacy, Lisa J. Storrie-Lombardi, Patrick B. Hall, S. C. Gallagher, Dean C. Hines, Xiaohui Fan, Casey Papovich, Daniel E. Vanden Berk, George B. Trammell, Donald P. Schneider, Marianne Vestergaard, Donald G. York, Sebastian Jester, Scott F. Anderson, Tamás Budavári, and Alexander S. Szalay, *Spectral Energy Distributions and Multiwavelength Selection of Type 1 Quasars*, 166 (2006), no. 2, 470–497.

[221] Rodrigo S. Nemmen and Michael S. Brotherton, *Quasar bolometric corrections: theoretical considerations*, 408 (2010), no. 3, 1598–1605.

[222] Jessie C. Runnoe, Michael S. Brotherton, and Zhaohui Shang, *Updating quasar bolometric luminosity corrections*, 422 (2012), no. 1, 478–493.

[223] Hagai Netzer, *Bolometric correction factors for active galactic nuclei*, 488 (2019), no. 4, 5185–5191.

[224] Gordon T. Richards, Trevor V. McCaffrey, Amy Kimball, Amy L. Rankine, James H. Matthews, Paul C. Hewett, and Angelica B. Rivera, *Probing the Wind Component of Radio Emission in Luminous High-redshift Quasars*, 162 (2021), no. 6, 270.

[225] Margherita Giustini and Daniel Proga, *A global view of the inner accretion and ejection flow around super massive black holes. Radiation-driven accretion disk winds in a physical context*, 630 (2019), A94.

[226] Shuqi Fu, W. N. Brandt, Fan Zou, Ari Laor, Gordon P. Garmire, Qingling Ni, III

Timlin, John D., and Yongquan Xue, *The Nature of Luminous Quasars with Very Large C IV Equivalent Widths*, 934 (2022), no. 2, 97.

[227] Jeremiah D. Paul, Richard M. Plotkin, Ohad Shemmer, Scott F. Anderson, W. N. Brandt, Xiaohui Fan, Elena Gallo, Bin Luo, Qingling Ni, Gordon T. Richards, Donald P. Schneider, Jianfeng Wu, and Weimin Yi, *Connecting Low- and High-redshift Weak Emission-line Quasars via Hubble Space Telescope Spectroscopy of Lyα Emission*, 929 (2022), no. 1, 78.

[228] Edward L. Wright, Peter R. M. Eisenhardt, Amy K. Mainzer, Michael E. Ressler, Roc M. Cutri, Thomas Jarrett, J. Davy Kirkpatrick, Deborah Padgett, Robert S. McMillan, Michael Skrutskie, S. A. Stanford, Martin Cohen, Russell G. Walker, John C. Mather, David Leisawitz, III Gautier, Thomas N., Ian McLean, Dominic Benford, Carol J. Lonsdale, Andrew Blain, Bryan Mendez, William R. Irace, Valerie Duval, Fengchuan Liu, Don Royer, Ingolf Heinrichsen, Joan Howard, Mark Shannon, Martha Kendall, Amy L. Walsh, Mark Larsen, Joel G. Cardon, Scott Schick, Mark Schwalm, Mohamed Abid, Beth Fabinsky, Larry Naes, and Chao-Wei Tsai, *The Wide-field Infrared Survey Explorer (WISE): Mission Description and Initial On-orbit Performance*, 140 (2010), no. 6, 1868–1881.

[229] T. H. Jarrett, M. Cohen, F. Masci, E. Wright, D. Stern, D. Benford, A. Blain, S. Carey, R. M. Cutri, P. Eisenhardt, C. Lonsdale, A. Mainzer, K. Marsh, D. Padgett, S. Petty, M. Ressler, M. Skrutskie, S. Stanford, J. Surace, C. W. Tsai, S. Wheelock, and D. L. Yan, *The Spitzer-WISE Survey of the Ecliptic Poles*, 735 (2011), no. 2, 112.